May 2020

# Topological Excitations and Anomalous Transport Phenomena in Condensed Matter Systems

Chuanchang Zeng
*Clemson University*, hitwhzcc@hotmail.com

# TOPOLOGICAL EXCITATIONS AND ANOMALOUS TRANSPORT PHENOMENA IN CONDENSED MATTER SYSTEMS

---

A Dissertation
Presented to
the Graduate School of
Clemson University

---

In Partial Fulfillment
of the Requirements for the Degree
Doctor of Philosophy
Physics

---

by
Chuanchang Zeng
May 2020

---

Accepted by:
Dr. Sumanta Tewari, Committee Chair
Dr. Jian He
Dr. Murray Daw
Dr. Catalina Marinescu

# Abstract

Topological physics is a burgeoning new area of study in condensed matter systems, focusing on the topological excitations as well as the transport phenomena of systems with topologically non-trivial band structures. These systems being either gapped or gapless, are topologically protected and can support new phenomena which are absent in topologically trivial systems. The gapless topological superconductors can host Majorana zero modes, known as the interpretation of the Majorana fermions in condensed matter systems, which have been proposed as the ideal qubit for topological quantum computation due to their non-Abelian topological properties. The gapped topological insulators, on the other hand, can realize the non-dissipation transport charge and spin currents, which are immune to defects and directly related to the topologically non-trivial Berry curvature of the Bloch bands of the electrons. In this thesis, we will discuss the topological features of topological superconductors, higher-order superfluids, and topological insulators. For the studies on topological superconductors, we focus on investigating the properties of Majorana fermions using numerical modeling as well as theoretical methods. We also elucidate the formation of the so-called quasi-Majoranas or partially separated Andreev bound states in semiconductor-superconductor heterostructures, and discuss the feasibility of braiding in the quasi-Majorana regime. Using ultra-cold atoms in optical lattices, we propose a Hofstadter-Hubbard model to realize the higher-order topological superfluid capable of supporting the Majorana corner modes, which are degenerate and protected by time-reversal symmetry. In the aspect of the anomalous transport phenomena manifested by Berry phase effect, we propose the non-linear anomalous Nernst effect and the non-linear anomalous thermal Hall effect in time-reversal invariant systems. By analyzing the anomalous transport coefficients, we also propose the analog of the Wiedemann-Franz law and Mott formula for the non-linear transport phenomena.

# Acknowledgments

First and foremost, I would like to thank my advisor, Dr. Sumanta Tewari, for his support and guidance of my research projects. The discussions with him either on my studies or daily life, have helped inspire and motivate me many times. I am indebted to his patience and inculcation during the completion of my PhD. I must also thank my dissertation committee: Dr. Jian He, Dr. Murray Daw, and Dr. Catalina Marinescu. I am very grateful for the advice I have been given about doing research, presenting research, and most importantly, being a research scientist in physics. I would also like to acknowledge my collaborators, Dr. Tudor Stanescu, Dr. Chuanwei Zhang, Dr. Vito Scarola, Dr. Apparao M. Rao, Dr. Nandy Snehasish, Dr. Girish Sharma and Dr. Christopher Moore for all of their hard work and contributions to the research presented in this thesis. I am grateful for all of my Professors and friends for all of the help that they have offered during my last five years of being a graduate student at Clemson University. Additionally, I want to thank my grandma, my parents and my sister for their support and encouragement for all these years. Your support and understanding have always been and will always be my greatest motivation.

# Table of Contents

**Title Page** . . . . . **i**

**Abstract** . . . . . **ii**

**Acknowledgments** . . . . . **iii**

**List of Figures** . . . . . **vi**

**1 Introduction** . . . . . **1**
1.1 Majorana fermions in topological superconductors . . . . . 2
1.2 Topological quantum computation . . . . . 5
1.3 Higher-order topology . . . . . 10
1.4 Anomalous transport phenomena . . . . . 12

**2 Quantized zero bias conductance plateau in semiconductor-superconductor heterostructures without non-Abelian Majorana zero modes** . . . . . **16**
2.1 Introduction . . . . . 17
2.2 SM-SC heterostructure coupled to a quantum dot . . . . . 18
2.3 Results . . . . . 23
2.4 Summary and conclusion . . . . . 24

**3 Analytical solution of the finite length Kitaev chain coupled to a quantum dot** . . . . . **26**
3.1 Introduction . . . . . 27
3.2 Kitaev model preliminaries . . . . . 30
3.3 Finite length Kitaev chain and splitting oscillations . . . . . 32
3.4 Finite length Kitaev chain attached to a quantum dot . . . . . 36
3.5 Discussion and conclusion . . . . . 46

**4 Feasibility of measurement-based braiding in the quasi-Majorana regime in semiconductor-superconductor heterostructures** . . . . . **51**
4.1 Introduction . . . . . 52
4.2 Measurement-based braiding . . . . . 54
4.3 General properties of quasi-Majoranas . . . . . 55
4.4 Stability of quasi-Majoranas in the presence of local perturbations . . . . . 62
4.5 Discussion and conclusion . . . . . 79

**5 Majorana corner modes and higher order topological superfluidity in an attractive Hubbard-Hofstadter model of cold atom optical lattices** . . . . . **80**
5.1 Introduction . . . . . 81
5.2 Non-interacting model and Hofstadter bands . . . . . 82
5.3 Attractive interactions . . . . . 85

5.4 Soliton-induced Majorana zero-energy modes . . . 86
5.5 Connection with higher-order topological superconductors . . . 91
5.6 Discussion and conclusion . . . 94

**6 Non-linear Nernst effect in bilayer $WTe_2$ . . . 96**
6.1 Introduction . . . 96
6.2 Semiclassical Boltzmann formalism of non-linear Nernst response . . . 99
6.3 Angular dependence of non-linear anomalous Nernst response . . . 103
6.4 Model Hamiltonian of two-dimensional bilayer $WTe_2$ . . . 108
6.5 Results and discussions . . . 112
6.6 Conclusion . . . 119

**7 Wiedemann-Franz law and Mott relation for anomalous transport in the non-linear regime . 121**
7.1 Introduction . . . 121
7.2 Boltzmann theory and anomalous thermal Hall effect in the non-linear regime . . . 123
7.3 Analog of Wiedemann-Franz law and Mott relation in the non-linear regime . . . 125
7.4 Non-linear transport coefficients for 2D massive Dirac fermions . . . 128
7.5 Conclusions . . . 130

**8 Summary and conclusion . . . 132**

**Bibliography . . . 136**

# List of Figures

2.1 (a) Proximitized nanowire junction in which a portion of the semiconductor wire (SM) is not covered by the superconductor (SC), represented by a quantum dot (QD). (b) Quantum dot potential $V(x) = V_{barrier} + V_{dot}$ as described by Eq. 2.2 may form within the QD due to a combination of tunnel coupling to the metallic lead $(V_{barrier})$ as well as application of the tunnel gate potentials $(V_{dot})$. Parameters used here were, barrier potential height $Z = 16\Delta$ and width $x_t = 0.02\mu m$, a quantum dot of width $x_0 \sim 0.5\mu m$ with a potential height $V \sim 5.5\Delta$ which varies over a length scale of $\sigma_V \sim 27.5nm$. Induced pairing $\Delta(x)$ described by Eq. 2.3 is present within the proximitized region of the wire. Here we used $\Delta_{ind} \sim 0.25$meV which varies over a length scale of $\sigma_\Delta \sim 27.5nm$. Robustness of the zero bias peaks to different values of the barrier and dot potentials is shown in Fig. 2.2. (c)-(d) Vertical line cuts from the differential conductance spectra shown in (g) showing a ZBCP quantized to $2e^2/h$ due to the presence of a ps-ABS (blue, Zeeman field $\Gamma < \Gamma_c$ with $\Gamma_c$ the critical field) and a MZM (red, $\Gamma > \Gamma_c$). Temperature dependence of ZBCP from 20 mK to 440 mK in steps of 20 mK shows gradual decrease of the peak height. (e) Full width at half maximum (FWHM) as a function of temperature $T$ for ps-ABS (blue) and MZM (red) of curves taken from (c)-(d). (f) Low-energy spectra as a function of Zeeman field for a nanowire with the potential profile pictured in (b). The Zeeman field $\Gamma > \Gamma_c$ region is marked by the red zero energy mode (MZM), while the blue zero mode marks the region supporting ps-ABSs. (g) Differential conductance spectra as a function of Zeeman field corresponding to energy spectra in (f). (h)-(j) Profiles of lowest energy mode wave functions: (h) A standard ABS consisting of a pair of overlapping MBSs, (i) a ps-ABS consisting of two overlapping MBSs whose separation is on the order of the Majorana decay length $\zeta$, and (j) a pair of non-Abelian MZMs localized at opposite ends of the wire. (k) Zero bias line cuts from conductance spectra showing $2e^2/h$-quantized conductance plateaus against variation of the Zeeman field for two representative values of the chemical potential due to the presence of a ps-ABS (blue) and MZM (red). . . 19

2.2 (Color online) (a)-(c) Differential conductance as a function of barrier height $Z$ and bias potential associated with a standard ABS ($\Gamma = .25\Gamma_c$) (a), a ps-ABS ($\Gamma = .75\Gamma_c$) (b), and a pair of MZMs ($\Gamma = 1.05\Gamma_c$) (c).(d-f) Zero bias line cuts for (a-c) showing the MZMs and ps-ABSs forming nearly identical profiles which plateau at $2e^2/h$ for a wide range of barrier heights. The standard ABS peak height (d) may take any value between 0 and $4e^2/h$ and quickly goes to 0 with increased barrier height. (g-h) Vertical line cuts from (b) and (c) showing ZBCPs quantized at $2e^2/h$ over a large range of barrier potential heights $Z$ for both ps-ABS and MZM. (i-j) Low energy spectra as a function of quantum dot potential height $V$ associated with potential profile in Fig. 2.1(b) for ps-ABS (blue, $\Gamma < \Gamma_c$) and MZM (red, $\Gamma > \Gamma_c$). Here and in the following plots $V_c = 2\mu$ is taken as the reference dot potential, while the dot potential $V$ is varied between $.25V_c = 2\Delta$ and $V_c = 2\mu = 8\Delta$. (k-l) Plots of differential conductance as a function of dot potential height $V$ and bias potential for values consistent with energy-spectra shown in (i-j). (m) Horizontal zero bias line cuts with (m) corresponding to (k-l) showing a $2e^2/h$-quantized plateau for both ps-ABSs (blue) and MZMs (red). . . . . 21

2.3 (Color online)(a)Low-energy spectra as a function of chemical potential. The red line signifies the topological region supporting MZMs, the blue line shows a non-topological region supporting ps-ABSs which stick to zero energy for a wide range of chemical potential. (b) Zero bias line cut taken from (c) showing a robust $2e^2/h$ quantized conductance plateau forming in the topologically trivial regime due to the presence of a ps-ABS. (c) Differential conductance spectrum as a function of chemical potential for parameter values consistent with Fig. 2.1. . . . . 22
2.4 (Color online) Differential conductance as a function of the in plane angle of the Zeeman field for the ps-ABS (a) and the MZM (b) shown in Fig. 2.1(i)-(j). A ZBCP appears for a small angle in which the Zeeman field is almost aligned with the wire. As the angle between the wire and the direction of the Zeeman field is increased the ZBCP is destroyed in both cases due to splitting. . . . . 24

3.1 (Color online) Lowest-energy spectra for the finite length Kitaev chain in the topological phase $\mu > 0$ as a function of chemical potential $\mu$ in (a)–(b) and Length $L$ in (c)–(d). Analytical results (red dotted line) are based on Eq. (3.18), while the simulation results (blue solid line) are from direct diagonalization of the tight binding hamiltonian in Eq. (3.1) for a finite length $L$. The cyan dashed lines in (a)–(b) show the condition $\mu \geq \Delta^2/4$ discussed below Eq. (3.18), after which the analytical solutions are valid. It shows a lower hopping energy $t$ reduces the energy splitting in (a) relative to that in (b); a higer SC $\Delta$ offers a more effective exponential protection in (d) than that in (c). All of this can be explained by the dependence of the lowest energy $E$ on the parameters $\mu, L$, respectively, through Eq. (3.18). A slight shift of the analytical results relative to the simulation results is caused by the dropped terms for $q$ and $k$ in Eq. (3.18). The other model parameters are $L = 71$ in (a)–(b) and $\mu = 0.25t_0$ in (c)–(d), and $t_0 = 1$. . . . . 33
3.2 (Color online) Lowest energy wave functions $\phi_{\pm E}$ as defined in Eq. (3.19) and its counterpart by particle-hole transformation, for the lowest energy modes of a pure Kitaev chain in the topological regime ($\mu > 0$). The inset shows the corresponding MZMs as defined by Eq. (3.20). The dotted lines correspond to analytical results while the solid lines correspond to numerical simulation. The black dashed line shows the exponential decay envelope of the wave function which is proportional to $e^{-q_F L}$. Parameters used were $\Delta = t_0$, $t = 15t_0$, and $\mu = 2t_0$. In the topological phase the putative MZM wave functions are localized at the two ends of the chain as shown in the inset. No such near-zero-energy subgap state exists as low energy solution in the non-topological phase of the Kitaev chain *without* the quantum dot. . . 35

3.3 (Color online) (a) Schematic of a finite length Kitaev chain in which a fraction of the chain is not covered by the superconductor. This part of the chain (yellow) with vanishing superconducting pair potential $\Delta(x)$, and an effective electric potential $V(x)$ which may be induced by tunnel gates, is called a quantum dot. A proximitized region within the quantum dot (QD) with finite length $\delta_x$ is introduced. We also show the wave functions of the topological MZMs and the partially separated ABSs (in which the component MBSs are spatially separated over the length of the quantum dot), which are the generic lowest energy excitations in the topological and the non-topological phases of the Kitaev chain, respectively. (b) Numerically calculated spectrum of a specific finite length kitaev chain with a potential-well-like QD, where $V = -2.5t_0, \Delta = t_0, x_0 = 30$ , and $\delta_x = 20$ as defined in Eq. (3.21). The spectrum shows a robust near-zero-energy state even before the bulk gap closes around $\mu = 0$, which is present due to the potential-well like QD. The square of the amplitude of the wave functions at zero energy at $\mu = -t_0$ and $\mu = t_0$ (marked by black dots in 3(b)) are shown in (c) and (d), respectively. (c) shows the two component MBSs of the ps-ABS in the topologically trivial phase, while (d) shows the true MZMs in the topoloically non-trivial state that emerges after the bulk gap closing. The vertical black dashed lines in (c) and (d) indicate the boundaries at $x = x_0 - \delta x$ and $x = x_0$ respectively, indicating the spatial separation of the component MBSs of the ps-ABS. . . . . 37

3.4 (Color online) Wave functions for the lowest energy modes of a QD-Kitaev chain without a proximitized region in the QD ($\delta_x = 0$ in Fig. 3.3) (a) corresponding to Eq. (3.24) for the topologically trivial regime with $\mu = -0.5t_0$, showing a pair of BdG wave functions $\phi_{\pm\varepsilon}$ in which the constituent MBSs are sitting directly on top of each other (see inset); and (b) corresponding to Eq. (3.26) for the topological regime with $\mu = 3.5t_0$ in which a pair of MZMs are separated by the length of the wire (see inset). The insets show the MBSs associated with the low energy BdG wave functions. The dotted lines show the analytical results while the solid lines are from numerical simulations. Because the constituent MBSs are strongly overlapping in (a), there is no robust near-zero-energy ABS in the topologically trivial phase in the absence of a proximitized region ($\delta_x = 0$) in the QD. The black dashed lines mark the QD-SC boundary at $x = x_0$. Parameters used were $V = -1.5t_0$, $\Delta = t_0$ and $t = 10t_0$. . . . . 39

3.5 (Color online) Wave functions for the lowest energy mode of a Kitaev chain coupled to a QD where the QD contains a proximitized region of finite length $\delta_x$ (see Fig. 3.3)). (a) Wave functions for the lowest energy modes within the bare QD (yellow), the proximitized part of the QD (green), and the bulk Kitaev chian (orange), plotted using analytical results based on Eq. (3.28) (dotted lines) and direct numerical solutions using a tight binding Hamiltonian (solid lines). Here, the parameters are such that the proximitized region of the QD satisfies $\mu - V > 0$, with $V = -2.5t_0$, while the Kitaev chain is topologically trivial with $\mu = -1.25t_0$. (b)-(d) Spatial profiles of the component pair of MBSs of a partially separated ABS for the proximitized regions of various lengths $\delta_x$. (b) shows the MBSs corresponding to the wave functions in (a). Samples are taken for values corresponding to the crossed diamonds in Fig. 3.6(c). The MBSs are separated on the order of the length of the proximitized region $\delta_x$ within the QD, marked by the black dotted lines. The figures illustrate that the ps-ABSs form essentially because the proximitized region in the QD satisfies the effective chemical potential $\tilde{\mu} > 0$, partially decoupling the ABS into a pair component MBSs, which are then spatially separated by the width of the proximitized region. Here the dot length is $x_0 = 30$, the total length of the QD-Kitaev chain is $L = 100$, the hopping energy is $t = 2.5t_0$, and superconducting pairing potential is $\Delta = t_0$. . . . . 42

3.6 (Color online) Overlap between the left and right MBSs $\langle\phi_L|\phi_R\rangle$ of a partially separated ABS, as a function of the width of the proximitized region $\delta_x$ within the QD, and chemical potential $\mu$, for a potential well (a) and a potential barrier (b) in the QD region. Since the mechanism for the formation of the ps-ABS involves the effective chemical potential ($\tilde{\mu} = \mu - V$) in the proximitized part of the QD being in the topological regime, the potential well in the QD region ($V < 0$) works for the bare $\mu < 0$, while the potential barrier in the QD region works for the bare $\mu > 4t$. As the length of the proximitized region $\delta_x$ within the QD approaches zero, the overlap between the left and right MBSs dramatically increases (red). For finite values of the length of the proximitized region $\delta_x \geq 5$ minimal overlap between the left and right MBSs (blue) can be seen within the topologically trivial regime, $\mu \in \{-2.5t_0, 0\}$ (a) and $\mu \in \{10t_0, 12.5t_0\}$ (b) supporting the presence of ps-ABSs. Here $\delta_x = 30$, $L = 100$, and $t = |V| = 2.5t_0$. (c) Overlap between the left and right MBSs as a function of the length of the proximitized region within the dot. The red line corresponds with vertical line cuts taken from (a)(dotted red) and (b)(solid red), and the blue line represents identical values with decreased hopping energy $t$. The cyan diamonds and the magenta circles represent the analytical results. The wave modes for the three black crossed diamonds are given in Fig. 3.5 . . . . . 44

3.7 (Color online)(a) Overlap of the left and right MBSs $\langle\phi_L|\phi_R\rangle$ of a partially separated ABS as a function of chemical potential $\mu$ for a Kitaev chain of varying length $\delta_L$ coupled to a QD which with a finite proximitized region of length $\delta_x = 5$. Increasing the length of the Kitaev chain $\delta_L$ decreases the overlap between the left and right modes. The overlap value $0.1748$ is significantly reduced to $0.06$ for $\mu$ marked by the black dashed line. (b)-(c) Majorana wave functions for the lowest energy modes of a QD-Kitaev chain associated with red diamonds in (a) for numerical simulation (b) and analytical results based on Eq. (3.26c). Significant portions of the mode distribution leak into the Kitaev chain region $\delta_L$, reducing the overlap between the left and right modes, increasing the robustness of the ps-ABS. Here $t = 5t_0, x_0 = 30, \Delta = t_0, V = -2.5t_0$ were used. . . . . 45

3.8 (Color online) Lowest energy eigenvalues plotted with effective chemical potential for a Kitaev chain with QD in the topologically trivial phase (solid blue) and bare Kitaev chain of length equal to the QD in the topological phase (dashed red) with different parameters $t, \Delta$, and the length of the proximitized region $\delta_x$. The parameters $x_0 = 30, L = 100$ indicate a dot-chain system with a total length of $100$ sites attached to a QD with $30$ sites with the effective chemical potential in the QD $\tilde{\mu} = \mu - V$. The parameters $x_0 = 0, L = 30$ indicate a bare Kitaev chain of length $30$ sites (and no QD), with the effective chemical potential $\tilde{\mu} = \mu$ ($V = 0$ in the bare chain). We fix $\mu = -0.05t_0$ for the dot-chain system and vary the dot potential $V$ in a range such as $\tilde{\mu} > 0$ within the QD, which varies within the same range as that for the bare Kitaev chain. The lowest energy in the topologically trivial ($\mu < 0$) dot-chain system (i.e., the ps-ABS) shows a significantly suppressed energy splitting as compared to that of the topological ($\tilde{\mu} = \mu > 0$) Kitaev chain of length $x_0$. We have length of the proximitized region $\delta_x = 10$ in (a)-(c), and $\delta_x = 30$ in (d). Parameters $t, \Delta$ are as given. . . 47

3.9 (Color online) (a) Energy spectrum for an experimental SM-SC heterostructure attached to a potential well-like QD ($V(x) \leq 0$) where the QD potential and SC pairing potential are given schematically in the top panel in(b) with potential depth $|V(x)_{min}| = 5.5t_0$, and $\mu = -4t_0, \Delta_0 = t_0$. For these parameters the critical phase transition point is $B_c \sim |\mu| = 4t_0$, where the bulk gap closes signifying a topological transition. As can be seen, in the presence of the QD, a robust near-zero-energy state is also present in the topologically trivial phase, i.e., for $B < B_c$. The spatial profile for the amplitude of the square of the wave function at $\mu = 3.4t_0$ is shown in the bottom panel in (b), where we have the two MBS components of a ps-ABS state, separated by the QD size $x_0 \sim 50$. The spin density profile $\langle s_x \rangle$ for the ps-ABS state is plotted in (c), where we see that the two MBS components are characterized by the same spin polarization, i.e., the spin polarizations are mainly in the negative $s_x$ direction in both cases. Here length L=200 sites. . . . . 48

4.1 (Color online) (a) Dependence of the low energy spectrum on the applied Zeeman field for a system described by the Hamiltonian in Eq. (4.1) with chemical potential $\mu = 5\Delta$. The bulk gap has a minimum at $\Gamma_c \approx \mu = 5\Delta$, the critical field associated with the TQPT. (b) Potential profiles corresponding to Eq. (4.2) with $\Delta_0 = 0.25\ meV, V_{max} = 8\Delta$. (c), (d) Wave functions associated with the near-zero energy eigenstates marked as the green and black lines in panel (a), respectively. The component MBSs of ps-ABS are now separated by QD length scale ($L^* \sim x_\Delta$, the length of the bare SM segment), as shown in panel (c). Here a uniform Zeeman field is applied along the length of the wire and the other parameters are as follows: $m = 0.03m_e, \alpha(x) = \alpha = 0.4\ eV\text{Å}, x_V = 0.20\ \mu m, \delta x_V = 0.15\ \mu m, \delta x_\Delta = 0.10\ \mu m, x_\Delta = 0.50\ \mu m$. . . . . 58

4.2 (Color online) Lowest energy $E_0$ of Hamiltonian given in Eq. (4.3) as a function of Zeeman potential $\Gamma$ and the maximum potential height of the quantum dot $V_{max}$ with chemical potential $\mu = 3\Delta$ in (a) and $\mu = 5\Delta$ in (b). The green dotted lines represent the critical Zeeman potential of TQPT ($\Gamma/\Gamma_c = 1$). The dark blue regions indicate the ps-ABSs with energy splittings $E_0 \in (0, 20\ m\Delta) < \varepsilon_w$, which are also below the braiding energy scale $\varepsilon_m$. The insets show the lowest energy $E_0$ for system at $\mu = 3\Delta, 4\Delta$ with $V_{max} = 0, 1.5\mu$ respectively. The rest of the parameters used here are the same as in Fig. 4.1. . . . . 59

4.3 (Color online) (a) The logarithm of the lowest energy $E_0$ at $\Gamma = 4\Delta$ ($< \Gamma_c = 5\Delta$) as a function of effective mass ($m^*/m_e \in (0.01, 0.06)$) and spin-orbit coupling strength ($\alpha \in (0, 0.6)\ eV\text{Å}$). The dark blue region indicates the trivial states with near zero energy $E_0 \sim 0.1\ m\Delta \lesssim \varepsilon_m$, which in principle can be utilized in measurement-based braiding. Panel (b), (c) show the line-cuts from panel (a), with fixed spin-orbit couplings ($\alpha = 0.15, 0.30\ eV\text{Å}$) and fixed effective masses ($m^* = 0.02, 0.05m_e$), respectively. The other parameters used here are the same as in Fig. 4.1 . . . . . 60

4.4 (Color online) *Top panel*: spatial profile for spin-orbit coupling strength where the blue line represents a uniform SOC $\alpha$ and the envelop line of the green area represents the position-dependent $\alpha(x)$. *Middle panel*: spatial profile for Zeeman potential where the magenta line represents a uniform Zeeman field $\Gamma$ while the envelop line of the cyan area represents the position-dependent Zeeman potential $\Gamma(x)$. $\Gamma_0$ indicates the twisting amplitude of the Zeeman field (or amplitude of magnetic disorder), $\pi/\omega$ indicates the frequency and $x_\Gamma$ is taken to smoothly connect the twisted region with the uniform region along the direction of the nanowire (see Eq. (4.6)). Here the gray line represents another possible function $\Gamma(x)$. *Bottom panel*: spatial profile for confinement potential where $V(x), \Delta(x)$ are the same as that givn in Fig. 4.1(b) and the orange area represents a local potential disorder $\delta V(x)$ with localization center $x_0$. The length of the nanowire is $L = 2\ \mu m$, and the equations of the spatial profiles in this figure are given in Eqs. (4.5), (4.6), (4.7), respectively. . . . . 61

4.5 (Color online) Low-energy spectrum as a function of Zeeman potential for a system with spin-orbit coupling given as a constant $\alpha$ in panel (a) and a spatially varying function $\alpha(x)$ in panel (b), respectively. A schematic plot of the position-dependent SOC $\alpha(x)$ is given in the top panel of Fig. 4.4. Large energy splitting oscillations (panel (b)) are induced by the presence of the local perturbation in SOC, in contrast to a constant SOC (panel (a)). The wave function profiles associated with the marked lines are given in Fig. 4.6. We consider a system at $\mu = 5\Delta$ with $m^* = 0.03m_e, \alpha = 0.4\ eV\text{Å}, \Delta = 0.25\ meV$, and a confinement potential with $x_V = 0.2\ \mu m, \delta x_V = 0.15\mu m, V_{max} = 6\Delta$. The parameters for $\alpha(x)$ (Eq. (4.5)) in panel (b) is given as $x_\alpha = 0.25\ \mu m, dx_\alpha = 0.02\ \mu m$, $\alpha_1 = 0$, and a symmetric $\alpha(x)$ is applied here. The other parameters used here are: $x_\Delta = 0.5\ \mu m, \delta x_\Delta = 0.15\ \mu m$. . . . . 63

4.6 (Color online) (a), (b) Wave functions associated with the near-zero energy ps-ABS marked as the green and cyan lines in Fig. 4.5, respectively. Similarly, panel (c), (d) show the wave function profiles for the topological MZMs marked by the black and orange line in Fig. 4.5, respectively. In the presence of a step-like SOC, the splitting energy of the ps-ABS has been increased from $E = 6.4m\Delta$ in (a) to $E = 48.6m\Delta$ in (b), while the splitting energy of the topological MZMs has not been significantly changed ($E = 38.9m\Delta$ in (c) and $E = 25.6m\Delta$ in (d)). Note that, the energy splittings of topological MZMs can be reduced (hence satisfy $E_0 \lesssim \varepsilon_w, \varepsilon_m$) by extending the length of the nanowire, while that of the topologically trivial ps-ABSs can not be controlled externally. . . . . 64

4.7 (Color online) Low-energy spectrum as a function of applied Zeeman field for a system with SOC given as a constant $\alpha$ in (a) and a spatially varying function $\alpha(x)$ in (b). Panels (c), (d) show the wave functions along with the corresponding energy splittings associated with the green and cyan lines marked in panel (a), (b) respectively. In the presence of local perturbation in SOC, an obvious overlap appears between the two component MBSs, as shown in panel (d). Also, the corresponding energy splitting has been greatly increased from ($E = 0.1\ m\Delta \lesssim \varepsilon_m$) to ($E = 43.5\ m\Delta \sim \varepsilon_w$). In contrast to Fig. 4.5, here we have considered a smoother confinement potential with $\delta x_V = 0.3\ \mu m$, and a position-dependent SOC given with $x_\alpha = 0.55\,\mu m, dx_\alpha = 0.02\,\mu m, \alpha_1/\alpha = 0.2$. The other parameters used are $m^* = 0.05m_e, \alpha = 0.2\ eV\text{Å}, \Delta = 0.25\ meV, \mu = 6\Delta, V_{max} = 8\Delta, x_V = 0.20\,\mu m, \delta x_V = 0.30\ \mu m$. . . . . 66

4.8 (Color online) Dependence of low-energy spectrum on the strength of the applied Zeeman field for a) system with a uniform Zeeman field, b) system with a locally twisted Zeeman field (Eq. (4.6)) with $\Gamma_0/\Gamma = 0.3, \omega = -3\pi/100$, c) system with a locally twisted Zeeman field (Eq. (4.6)) with $\Gamma_0/\Gamma = 0.4, \omega = 4\pi/200$. The twisted Zeeman potentials used here are schematically shown in the middle panel of Fig. 4.4. The chemical potential here is $\mu = 5\Delta$ and the confinement potential is characterised by $x_V = 0.2\ \mu m, \delta x_V = 0.15\ \mu m$ and $V_{max} = 8\Delta$. The other parameters used here are the same are Fig. 4.7. . . . . 67

4.9 (Color online) Majorana wave functions associated with the near-zero energy ABS mode from Fig. 4.8 corresponding to the marked lines. The energy splitting of the trivial ps-ABS in the case of a uniform Zeeman field is small, with $E = 0.93\ m\Delta$ in (a); while as shown in panel (b), (c), in the presence of the twisted Zeeman fields as have been described in Fig. 4.8, the energy splitting has been increased to $E = 45\ m\Delta, 42.1\ m\Delta$, respectively. . . . . 68

4.10 (Color online) Dependence of low-energy spectrum on the applied Zeeman field for a) system with a confinement potential (Eq. (4.2)) and without any potential disorder, b) system with a confinement potential (Eq. (4.2)) as well as a local potential disorder, described by Eq. (4.7). Clearly, the trivial near-zero energy splittings in panel (a) have been lifted by the local potential perturbation in panel (b). The wave functions and their corresponding energy splitting associated with the green and cyan line in panel (a), (b) are shown in panel (c), (d) respectively. An obvious overlapping between the component MBSs has been induced by the local potential disorder for ps-ABS in panel (d). The chemical potential is $\mu = 5.5\Delta$, and the local potential disorder is characterized by $\delta V/V_{max} = 0.3, x_0 = 0.2\ \mu m, \delta x_0 = 0.05\ \mu m$. The other parameters used here are $m^* = 0.05m_e, \alpha = 0.15\ eV\text{Å}, V_{max} = 8\Delta$, and $x_\Delta = 0$. 70

4.11 (Color online) Dependence of the logarithm of $(E_0'/E_0)$ on the parameters $\alpha_0, x_\alpha$ that characterize the step-like SOC described by the function in Eq. (4.5). Here $E_0', E_0$ are the energy splitting of the system with and without the presence of a local SOC perturbation, respectively. The black dashed lines indicate $\log(E_0'/E_0) = 1$, before which the energy splittings $E_0'$ are considered still applicable for braiding ($E_0' \sim \varepsilon_m$). (a) Energy splittings of the trivial states for systems with a fixed $x_\alpha = 0.55\ \mu m$ for SOC perturbation, here $\log(E_0'/E_0)$ go over the black dashed line ($E_0' > \varepsilon_m$) even at a small perturbation strength $\alpha_0/\alpha \sim 0.05$. (b) Energy splittings of the trivial states for systems with a fixed SOC perturbation strength $\alpha_0/\alpha = 0.30$, in this case a perturbation length scale $x_\alpha \gtrsim 0.35\ \mu m$ is required to break the readout condition for braiding. In contrast, the energy splittings of the topological states satisfy $\log(E_0'/E_0) \approx 0$ for all different values of $\alpha_0$ and $x_\alpha$ of the SOC perturbations, as shown in Fig. (c), (d), respectively. The chemical potential is $\mu = 6\Delta$. The other parameters used here are $m^* = 0.05m_e, \alpha = 0.2\ eV\text{Å}, \Delta = 0.25\ meV$, and the confinement potential is given with $V_{max} = 8\Delta, x_V = 0.20\ \mu m, \delta x_V = 0.30\ \mu m$. . . . . 71

4.12 (Color online) The logarithm of $(E_0'/E_0)$ (indicated by the colors) as a function of the parameters $\alpha_0$ and $x_\alpha$ that characterize the step-like SOC described by the function in Eq. (4.5). The cyan dashed lines imply the energy splittings ($\log(E_0'/E_0) = 0$) for system without SOC perturbation ($\alpha_0 = 0$). The yellow color implies ps-ABSs with energy splittings $E_0'/E_0 \geq 10$ in the presence of SOC perturbations, which as assumed are not applicable for measurement-based braiding ($E_0' > \varepsilon_m$), as shown in the top panels. However, all of the energy splittings of the topological states satisfy $\log(E_0'/E_0) \lesssim 0$ ($E_0' \lesssim E_0 \sim \varepsilon_m$), as shown in the bottom panels, where nearly no region with yellow color are present. Note that, the threshold amplitude for $\varepsilon_m$ of SOC perturbation is as small as $\alpha_0/\alpha \sim 0.05$ (provided a length scale $x_\alpha \in (50, 80)$site and smoothness parameter $\delta x_\alpha = 0.02\ \mu m$), as shown in the top left panel. A higher threshold perturbation strength $\alpha_0/\alpha \sim 0.25$ (positive $\alpha_0$) is observed in the top right panel, where $\delta x_\alpha = 0.05\ \mu m$. The chemical potential is $\mu = 5\Delta$, the other parameters used here are the same as Fig. 4.11. . . . . 72

4.13 (Color online) Similar plot as Fig. 4.11, but is the dependence of the logarithm of $(E_0'/E_0)$ on the parameters $\Gamma_0, x_\Gamma$ that characterize the twisted Zeeman field described by the function in Eq. (4.6). Panels (a), (c) show the value of $\log(E_0'/E_0)$ as a function of $\Gamma_0/\Gamma$ for a system with fixed $x_\Gamma = 0.60\ \mu m$ in trivial states ($\Gamma = 3.5\Delta$) and topological states ($\Gamma = 7.5\Delta$), respectively. Here, two different values of $\delta x_V$, which defines the smoothness of the confinement potential $V(x)$ (Eq. (4.2), are considered. The energy splittings of trivial states, as shown in panel (a), are consistent for braiding ($E_0' \sim \varepsilon_m$) for perturbations in Zeeman field with $\Gamma_0/\Gamma \lesssim 0.30$. On the other hand, a threshold value with $\Gamma_0/\Gamma \sim 0.40$ is observed for measurement-based braiding in quasi-Majorana regime (with ps-ABSs) for topologically trivial systems ($\Gamma = 4.5\Delta$) with fixed $\delta x_V = 0.30\ \mu m$ but with two different length scales $x_\Gamma$, as shown in panel (b). Panel (d) shows the topological case ($\Gamma = 6.5\Delta$) of panel (b), where energy splittings are well below the black dashed line, as expected. The chemical potential is $\mu = 5.5\Delta$, and the other parameters used here are the same as Fig. 4.11. . . . . 73

4.14 (Color online) Similar plot as Fig. 4.12 for $\log(E_0'/E_0$ under the influence of a twisted Zeeman potential (Eq. (4.6)). Here $\Gamma_0/\Gamma$ indicates the perturbation strength from the twisting of the Zeeman field. Length scale $x_\Gamma$ and frequency $\omega$ are varied simultaneously to satisfy $2\omega x_\Gamma = 5\pi$ in the left panels and $\omega x_\Gamma = -3\pi$ in the left panels, respectively. A threshold perturbation amplitude for ps-ABSs admitting braiding is found to be $\Gamma_0/\Gamma \sim 0.25$ for both the two types of the twisted Zeeman field, as shown in the top panels. In addition, the ps-ABSs can not be significantly perturbed in the presence of Zeeman filed perturbation with length scale $x_\Gamma \lesssim 40$sites, in which case, their energy splittings are all consistently below the braiding energy scale $\varepsilon_m$. The chemical potential is $\mu = 5\Delta$, and the other parameters used here are the same as Fig. 4.12. . . . . 74

4.15 (Color online) Dependence of $\log(E_0'/E_0)$ on the perturbation strength $\delta V/V_{max}$ for system perturbed by a local potential perturbation, described by Eq. (4.7). As shown in panel (a) and (b), the energy splittings are generically increased (except for the decrease around $\delta V/V_{max} \approx 0.3$ ) with $\delta V \neq 0$ for the trivial ps-ABSs ($\Gamma = 4\Delta$). On the contrary, the energy splittings for the topological MZMs ($\Gamma = 6\Delta$) do not show this feature, as shown in panels (c), (d). For local perturbations with positive amplitude $\delta V/V_{max} \lesssim 0.40$, the energy splittings are well below the black dashed line, implying their applicability for braiding($E_0' \sim \varepsilon_m$), as shown in panel (a). In the case of a negative potential perturbation, as shown in panel (b), a smaller minimum perturbation strength with $-\delta V/V_{max} \sim 0.10$ is found to be able to increase the energy spitting as $\log(E_0'/E_0) \geq 1$. Panel (c), (d) give energy splittings in the topological case for the system in panel (a), (b), respectively, which are below the black dashed lines (though an enhancement might be present, as shown by the green dotted line in panel (c)). Here, the value of $x_0$ implies the location of the potential disorder, $\mu = 5\Delta$, and the confinement potential is characterized by the same parameters used in Fig. 4.11. . . . . 75

4.16 (Color online) The energy splittings ($\log(E_0'/E_0)$) under the influence of a local potential perturbation $\delta V(x)$ described by Eq. (4.7). As shown in the top left panel ($\delta x_0 = 0.02\ \mu m$), a threshold amplitude $\delta V/V_{max} \sim 0.10$ for $E_0' \sim \varepsilon_m$ is observed for both positive and negative $\delta V(x)$ if the perturbation is localized around $x_0 \sim (50, 80)$sites (where the component MBSs of ps-ABSs overlap with each other, consistent with the results found in Fig. 4.12). For the system perturbed by potential perturbation with $\delta x_0 = 0.10\ \mu m$, as shown in the top right panel, $\log(E_0'/E_0) \geq 1$ is satisfied at a relatively higher perturbation strength $\delta V/V_{max} \sim 0.3$ for a positive perturbation $\delta V(x)$. For both cases with different values of $\delta x_0$, the energy splittings in the topological states (bottom panels) do not show any significant enhancement ($E_0'/E_0 \geq 10$) as that observed for the trivial states. The parameters used here are the same as Fig. 4.15. . . . . 76

4.17 (Color online)The logarithm of the lowest energy $E_0$ of the Hamiltonian given in Eqs. (4.1, 4.3) as a function of the applied Zeeman potential ($\Gamma$, $x$-axis) and the smoothness parameter of the confinement potential ($\delta x_V$, $y$-aixs). The values of $\log(E_0)$ (unperturbed) or $\log(E_0')$ (perturbed by local perturbations) are indicated by the colors. Panel (a) shows the $\log(E_0)$ for a system with $m^* = 0.05m_e, \mu = 5\Delta, V_{max} = 8\Delta, \alpha = 0.2\ eV\text{Å}, \Delta = 0.25\ meV$ without the presence of any local perturbations. The dark blue color (with green index $-4$ ) represents energy splittings in the trivial state with $E_0 \lesssim \varepsilon_m$, which satisfy the readout condition in the measurement-based braiding scheme. The energy splittings in the presence of disorder from a local potential are shown in panels (b), (c), (d), where the dark blue region are greatly reduced. Similarly, the energy splittings of the trivial states are all unavoidably enhanced by the local perturbations either from a step-like SOC, as shown in panels (e), (f), or from a twisted Zeeman field, as shown in panels (g), (h). The topologically trivial states that satisfy $E_0 \lesssim \varepsilon_m$ in the unperturbed system in (a) (dark blue regions with index $(-4)$), generally obtain higher energy splittings that fail to meet braiding requirement. In contrast, the energy splittings for the topological states are not showing any evident changes in the presence of the local perturbations. Note that, for systems with a smoother confinement potential ($\delta x_V \gtrsim 0.40\ \mu m$), ps-ABSs in the trivial regime with energy splittings below the energy scale $\varepsilon_m$ for measurement-based braiding still exist in the presence of the local perturbations with relatively weaker strength, as shown in panel (b, c, e, g). . . . . 78

5.1 Band structure of the non-interacting two-component Hofstadter model, $H_0$, with $\alpha = 1/3$ and periodic boundary conditions in the y-direction. (a) System with $N_x = 92$ and hard confinement in the x-direction. (b) System with $N_x = 92$ and soft (Gaussian) confinement (see Eq. (5.2), (5.3)). The bulk states are shown in blue and the red curves represent the gapless edge modes. . . . . 84

5.2 (Color online) *Left*: The mean-field phase diagram obtained by plotting the self-consistent value of the pairing order parameter $\Delta$ for $k_BT = 10^{-4}t$. The dashed-white line indicates the phase boundary. *Center*: Chemical potential as function of the filling factor for $\Delta = 0$. *Right*: Mean-field $\Delta$ as function of the interaction strength for two different filling factors. The $n_0 = 1$ line shows $\Delta \neq 0$ (i.e. superfluid phase) all the way to $U \sim 0$, while for $n_0 = 2/3$ one needs $U \sim 3t$ to enter the superfluid phase.. The green dotted lines mark the band edges of the bulk spectrum in Fig. 5.1. . . . . 86

5.3 Position-dependent pairing potential $\Delta(x, y)$ for a strongly interacting system with $U = 3.5t$, i.e., in the SF phase. The pairing potential is obtained as the self-consistent solution of the mean-field equations (5.12-5.15) for a finite system with $N_x \times N_y = 50 \times 34$ and soft confinement (see Eqs. (5.2, 5.3)) at finite temperature, $k_BT = 0.01t$. The total number of particles is fixed, $N = 800$. *Top*: Self-consistent solution with constant phase. The (self-consistent) chemical potential is $\mu = -1.250t$. *Bottom*: Self-consistent solution with a line soliton. The chemical potential is $\mu = -1.248t$. Note that $\Delta(x, y)$ is nonzero in the bulk – consistent with phase diagram in Fig. 5.2(b) – as well as on the boundary of the system, except along the line soliton. . . . . 87

5.4 *Top*: Low-energy spectrum of the Hofstadter-Hubbard model with strong interaction ($U = 3.5t$) within the mean-field approximation for a system with constant phase pairing potential and parameters corresponding to Fig. 5.3 (top panel). *Bottom*: The same but for parameters corresponding to the bottom panel of Fig. 5.3. Note that in the presence of a line soliton the system hosts two pairs of zero-energy Majorana bound states (red dots). The insets plot the wave functions of the states marked by arrows. . . . . 89

5.5 The same as Fig. 5.3 but for weak pairing, $U = 2t$ (i.e. in the QSHI phase). *Top*: Self-consistent solution with constant phase. The (self-consistent) chemical potential is $\mu = -1.258t$. *Bottom*: Self-consistent solution with a line soliton associated with a $\pi$ phase change. The (self-consistent) chemical potential is $\mu = -1.255t$. Note that $\Delta(x, y)$ is nonzero only on the boundary of the system (where the low-lying edge modes are located), while the bulk $\Delta(x, y)$ vanished, in agreement with the phase diagram in Fig. 5.2(b). . . . . 90
5.6 Low-energy spectrum of the Hofstadter-Hubbard model within the mean-field approximation for a weakly interacting system ($U = 2t$) with constant phase pairing potential and all other parameters corresponding to Fig. 5.3 (top panel). The bottom plots the same but with a line soliton. The red circles in the bottom panel correspond to MKPs found at the soliton edges in the weak pairing phase. . . . . 90
5.7 Low energy spectrum of the Hamiltonian in Eq. 5.13 as a function of chemical potential in the presence of a soliton (see the initial value of the order parameter $\widetilde{\Delta}_{i,j}$ for the BdG Hamiltonian in Eq. 5.12) for a finite system with $N_x \times N_y = 50 \times 34$ and soft confinement (Eq. 5.3). The red line represents the robust degenerate Majorana zero modes. The rest of parameters used here are the same as in Fig. 5.1. . . . . 91
5.8 The same as Fig. 5.1(a) but with $\alpha = 0$, i.e., the energy eigenvalues for a zero-field hopping model. There is no magnetic field coupling with the spin components, rendering the system a non-interacting two-band Fermi gas. The two bands are separated by a gap of about $2t$, within which the blue lines represent trivial edge modes. . . . . 92
5.9 The same as Fig. 5.7 but for a trivial superfluid for which the parent system is a two-component Fermi gas, i.e., $\alpha = 0$. We see that this system reveals the same qualitative spectrum as the one in Fig. 5.7 for which the parent system is a QSHI but there is no Majorana zero mode (red line in Fig. 5.7). This shows that the soliton induces (D-2)-dimensional Majorana zero modes *only* when the parent system is a QSHI and not when the non-SF system is a Fermi gas. The parameters used are the same as in Fig. 5.7. . . . . 93
5.10 The same as Fig. 5.7 but with on-site disorder (with a disorder strength $V_0 = 0.8t$). Here we see that the Majorana zero mode (red line) remains in spite of the applied disorder. Compared with Fig. 5.7, the system now is clearly gapped within the whole range. The other parameters used are the same as in Fig. 5.7. . . . . 93

6.1 (Color online) (a) Schematic experimental setup for measuring the non-linear anomalous Nernst effect in a time-reversal symmetric but inversion symmetry broken system. $V_x$ is measured as the non-linear anomalous Nernst voltage when a temperature gradient ($-\boldsymbol{\nabla} T$, represented by the red arrow) is applied along $y-$direction forming an angle $\theta$ with the principal axis $a$ (black dashed line). (b) $M_a$ is the mirror line which takes $k_a$ to $-k_a$. Due to the mirror symmetry and time reversal symmetry, only the $a-$component (black arrow) of the non-linear anomalous Nernst coefficient ($\mathbf{\Lambda}$), which is perpendicular to the mirror line $M_a$, is non-zero. . . . . 104
6.2 (Color online) Energy dispersions of bilayer $WTe_2$ (a) without spin-orbit coupling ($\eta = 0$) and (b) with spin-orbit coupling ($\eta = 0.15\ eV$Å). The colors represent the local Berry curvature distribution corresponding to each $\boldsymbol{k}$ point of the bands. A finite SOC explicitly lifts the spin degeneracy of the bands. (b) shows an anti-crossing at the band touching point with SOC of strength $\eta = 0.15\ eV$Å indicating by the sign-change (change of the color) of their Berry curvatures. The other parameters of the Hamiltonian are $v_0 = 2\ eV$Å, $t = 1.5\ eV$Å, $m = 0.1\ eV$, $\zeta_1 = 1$, $\zeta_2 = -1$, $E_1 = 0.02\ eV$, $K_1 = -0.1\pi$, $K_2 = -0.15\pi$, $E_2 = -0.08\ eV$, and $\gamma = 0.05\ eV$. . . . . 110

6.3 (Color online) The non-linear anomalous Nernst coefficient $\Lambda_x$ as a function of chemical potential $E_F$ for different strengths of SOC (a) $\eta = 0$ and (b) $\eta = 0.15\ eV$Å respectively. Insets in (a) and (b) show different Fermi surfaces where the Fermi energies are indicated by magenta dashed line. The color of the insets displays the distribution of Berry curvature weight on the Fermi surface. The color scale is the same as that in Fig. (6.2). Here $T = 50$ K and the other parameters used are the same as in Fig. (6.2). . . . . 111

6.4 (Color online) (a) Non-linear Nernst coefficient $\Lambda_x$ as a function of chemical potential ($E_F$) at different temperatures (T) for spin-orbit coupling $\eta = 0.3eV$Å. The position of the local extreme points of $\Lambda_x$ shifts with increasing temperature. (b) The locus of the local minimum points (indicated by the black dashed line in panel (a)) and the locus the local maximum points (indicated by the white line in panel (a)) are shown for different spin-orbit ($\eta$). In all cases, with increasing temperature, the chemical potential at the local minimum point shows a sudden drop while the chemical potential at the local maximum point decreases almost linearly. . . . . 113

6.5 (Color online) (a) Non-linear Nernst coefficient ($\Lambda_x^T$) at $T = 50$ K with different values of the chemical potential ($E_F$) and SOC strengths ($\eta$). There are two nodes of NLANE coefficient circled by the black dashed line. Clearly, these two nodes behave opposite to each other where this behavior of the NLANE coefficient is related to the band anti-crossing and band inversion near the Dirac nodes situated at $E_F = 0.02\ eV$, and $E_F = -0.08\ eV$ respectively. With increasing the SOC strength the Nernst coefficient at $E_F = 0$ (indicated by the dashed line) goes from positive value (white yellow) to negative value (dark orange) showing an obvious sign change around $\eta = 0.15\ eV$Å. (b) NLANE coefficient at the zero Fermi energy for different temperatures are shown. The magnitude of the Nernst coefficient decreases with increasing the temperature. The strength of spin-orbit coupling, at which all the NLANE coefficient curves intersect, remains unaltered with changing temperature. The other parameters used here are the same as in Fig. (6.3). . . . . 115

6.6 (Color online) (a) Non-linear Nernst coefficient ($\Lambda_x^T$) at $T = 50$ K as a function of chemical potential ($E_F$) and tilt parameter ($t_x$) in the presence of SOC $\eta = 0.2eV$Å. Interestingly, in the absence of tilt, $\Lambda_x^T$ at the non-zero chemical potential becomes finite whereas it vanishes when $E_F$ is at zero energy. (b) $\Lambda_x^T$ at $E_F = 0$ (indicated by the green dashed line in (a)) as a function of tilt parameter for different temperatures. At $t_x = 1.25v_0$, the non-linear Nernst conductivity vanishes in bilayer $WTe_2$ at all temperatures. The other parameters used here are the same as that in Fig. (6.3). . . . . 116

6.7 (Color online) Non-linear Nernst coefficient ($\Lambda_x^T$) at $T = 50$ K as a function of chemical potential ($E_F$) and inter-layer coupling ($\gamma$) in the presence of SOC $\eta = 0.15eV$Å (a) and $\eta = 0.20eV$Å (b). The magnitude of $\Lambda_x^T$ decreases to zero (and stays at zero) when the inter-layer coupling goes over $\gamma = 0.15eV$, in spite of the different spin-orbit coupling in (a) and (b). The insets correspondingly show the values of $\Lambda_x^T$ versus $\gamma$ at $E_F = 0$ (green dashed line in main figure), where the short black lines indicate the point ($\gamma \approx 0.15eV$) above which $\Lambda_x^T = 0$. All the other parameters used here are the same as in Fig. (6.2). . . . . 117

6.8 (Color online) The angular dependence factor $f_1(n_0, \theta)$ as a function of the angle $\theta$ between the temperature gradient and principal axis for different values of $n_0$.The plot in each panel (a) shows the non-scaled curves, where we see the relative magnitude of the $f_1$ for different $n_0$. While all the curves are scaled relatively to the value at $\theta = 3\pi/2$ in panel (b). For a time reversal symmetric system where the linear Nernst response is zero ($n_1 = 0$), a similar angular dependence (given in Eq. (6.37)) of the NLANE is found as that of the NLAHE in the recent work by *Du, et. al, 2018*. . . . . 118

7.1 (Color online) Schematic experimental setup for measuring the non-linear anomalous thermal Hall effect. A transverse thermal gradient ($\Delta T$) can be measured as a second-order response of the longitudinal heat current even in the absence of external magnetic field. The sample breaks inversion but respects time reversal symmetry, so the linear response anomalous thermal Hall current is known to vanish by symmetry. . . . . 123
7.2 (Color online) (a) Berry curvature $\mathbf{\Omega}^{n,s}_{\boldsymbol{k}}$ and (b) modulated Berry curvature $\beta^3(\mathcal{E}_{\boldsymbol{k}}-\mu)^3\mathbf{\Omega}^{n,s}_{\boldsymbol{k}}$ projected on the $\boldsymbol{k}$ space for Hamiltonian given in Eq. (7.17). The black dash lines indicate the Fermi surface at $\mu = 1.5\Delta$. Panel (c) and (d) show the derivative of Fermi distribution function at Fermi energy $\mu = 1.5\Delta$ for $\partial_x f_{\boldsymbol{k}}$ and $\partial_y f_{\boldsymbol{k}}$ respectively. The parameters used here are $n = 1, s = 1, t = 1.1eV, a = 3.19\text{Å}, v = at, \alpha = 0.1v, \Delta = 1.8eV$, $k_{x,y} \in [-0.5\pi, 0.5\pi]$, $\beta = 1(eV)^{-1}$ is considered for (a), (b) and temperature $T = 100K$ is applied for (c), (d). . . . . 127
7.3 (Color online) Non-linear anomalous thermal Hall coefficient $l'_y/(k_BT)^2$ versus chemical potential $\mu$ at different temperatures $T$. The red dotted line represents the analytical results based on the non-linear Wiedemann-Franz law (Eqs. (7.13, 7.14)). The rest of the data points are results of numerical calculations based on Eq. (7.6). The inset is a zoom-in of the plot around $\mu = \Delta$ (black dash line). For $\mu < \Delta$ the numerical results deviate from the modified Wiedemann-Franz law valid in the non-linear regime because of the absence of higher orders temperature contributions (see Eq. (7.13)). Here the unit for the $y$-axes is $\tau k_B^2/\hbar^2$, the other parameters are the same as in Fig. (7.2). . . . . 129
7.4 (Color online) Non-linear thermal Hall coefficient $l'_y$ plotted as a function of $(k_BT)^2$ for different values of the chemical potential. The circles are from numerical calculations based on Eq. (7.6), while the black lines corresponding to each chemical potential are the analytical results based on Eqs. (7.13, 7.14). Here the units for $y$-axes is $\tau k_B^2/\hbar^2$, the applied temperature $T \in [5K, 100K]$ with a unit step $(1K)$, and all other parameters are the same as in Fig. (7.2). 129

# Chapter 1

# Introduction

This first chapter is intended to introduce the central concepts of the topological phenomena in topological condensed matter systems, including Majorana fermions, topological quantum computation, higher-order topology and anomalous topological responses. We begin with introducing the Majorana fermions, which was proposed by Ettore Majorana as fundamental particles in the context of high energy particle physics. Then we talk about the Majorana zero mode, an emergent quasi-particle in topological superconductors, which has been understood as the condensed matter version of the Majorana fermion. Next, we provide an introduction to the topological quantum computation. Different braiding schemes for the Majorana-based topological quantum computation are discussed as well. Majorana zero modes in topological superconductors are non-degenerate and they correspond to the $(N-1)$-dimensional Majorana boundary states of the $N$-dimensional systems. In this chapter, we also introduce the concept of Majorana corner mode, a $(N-2)$-dimensional Majorana excitation in the higher-order topological superfluids. At last, we turn our attention to the anomalous responses in topological insulators and Weyl systems, where we focus on the Berry phase effect on the motions and transport phenomena of Bloch electrons in the external fields. The effects from the Berry curvature and Berry curvature dipole are discussed for the linear and non-linear anomalous transport phenomena, respectively.

## 1.1 Majorana fermions in topological superconductors

### 1.1.1 Majorana fermions as fundamental particles

In an attempt to synthesize special relativity and quantum mechanics, Dirac equation was originally proposed by Paul Dirac in 1928 [1] as a complete quantum description of spin-$1/2$ electron, which reads,

$$i\hbar\frac{\partial}{\partial t}\psi = (c\boldsymbol{\alpha}\cdot\boldsymbol{p} + \beta mc^2)\psi \tag{1.1}$$

Here, $\psi$ is a four-component spinor, $c$ is the speed of light, $\boldsymbol{p} = -i\hbar\boldsymbol{\nabla}$ is the momentum operator. In the Dirac representation, the "gamma" matrices $\boldsymbol{\alpha}, \beta$ written in the format of Kronecker product are given by,

$$\boldsymbol{\alpha} = (\tau_3\otimes\sigma_1, \tau_3\otimes\sigma_2, \tau_3\otimes\sigma_3)\,,\ \ \beta = -\tau_1\otimes\sigma_0 \tag{1.2}$$

where $\tau_i, \sigma_i$ with $i = 0, 1, 2, 3$ are the family $2\times 2$ Pauli matrices. Note that, the Dirac matrices in Eq. (1.2) obey anti-commutations $\{\alpha_i, \alpha_j\} = 0 (i \neq j)$, $\{\alpha_i, \beta\} = 0$, satisfying the Clifford algebra [2]. Provided with the above Dirac matrices, the eigen solutions to the Dirac equation in Eq. (1.1) come as positive and negative pairs $E = \pm\sqrt{\boldsymbol{p}^2c^2 + m^2c^4}$, which satisfy the relativistic energy momentum relation. The positive energies are associated with the states of particles (spin-$1/2$ electrons here), while the negative energy solutions were predicted by Dirac to be attributed to anti-particles, now called positrons, which was soon discovered in experiment four years later [3]. Particles described by the Dirac equation (Eq. (1.1)) are called Dirac fermions, whose anti-particles with opposite energies are distinct from themselves.

In fact, there are many sets of "gamma" matrices that satisfy the Clifford algebra. Another possible representation of these matrices for Eq. (1.1) were given by Ettore Majorana in 1937 [4] as,

$$\boldsymbol{\alpha}_M = (\tau_1\otimes\sigma_1, \tau_3\otimes I_2, \tau_1\otimes\sigma_3)\,,\ \ \beta_M = \tau_1\otimes\sigma_2, \tag{1.3}$$

which is now known as the Majorana representation [5]. The Dirac equation only admits positive energies in the Majorana representation. Interestingly, in this representation the Dirac equation yields a real wave function describing a particle that satisfy the self-conjugate Majorana condition $\psi = \psi^\dagger$, called Majroana fermions, which are different from the Dirac fermions. Assume operator $f^\dagger, f$ respectively creates and annihilates a Dirac fermion while operator $\gamma^\dagger, \gamma$ respectively creates and annihilates a Majorana fermion. The

difference (relation) between Dirac fermions and Majorana fermions can be mathematically presented by,

$$\begin{aligned} f &= (\gamma_1 + i\gamma_2)/\sqrt{2}, \\ f^\dagger &= (\gamma_1 - i\gamma_2)/\sqrt{2} \end{aligned} \tag{1.4}$$

Here, each Dirac fermion is decomposed as two Majorana fermions that obey the anti-commutation $\{\gamma_i, \gamma_j\} = 2\delta_{ij}$. By rewriting the equations in Eq. (1.4) as $\gamma_1 = (f + f^\dagger)/\sqrt{2}, \gamma_2 = i(f^\dagger - f)/\sqrt{2}$, it is obvious to see that $\gamma_1, \gamma_2$ satisfy $\gamma = \gamma^\dagger$.

Majorana fermion, being its own anti-particle, was proposed as a chargeless and spinless fundamental particle, which unfortunately has not yet been experimentally shown to exist. However, Majorana femrions can be understood as collective excitations of a complex many-body ground state [6] and they have been predicted to appear as quasi-particle excitations in various condensed matter systems. The condensed matter version of Majorana fermions will be introduced soon in the following section.

### 1.1.2 Majorana zero modes

Though it was intended to describe the relativistic electrons, Dirac equation can also describe the low-energy dynamics in the non-relativistic condensed matter systems. In the context of condensed matter physics, positive (negative) energy solutions to the Dirac equation are associated with conduction (valence) electrons, which usually are the modified quasi-electrons (holes) rather than the fundamental electrons. Similarly, Majorana fermions can emerge as the quasi-particle excitations, referred to as Bogoliubov quasi-particles, in topological superconductors [7].

In superconducting systems, the Bogoliubov quasi-particles or Bogoliubons are elementary excitations expressed as the linear combinations of positively charged electrons and negatively charged holes [7, 8]. For instance, in superconductors with $s$-wave pairing symmetry, the creation operator $b^\dagger_{\boldsymbol{k}}$ of the Bogoliubov quasi-particle can be written as $b^\dagger_{\boldsymbol{k}} = u_{\boldsymbol{k}} c_{\boldsymbol{k}\uparrow} + v_{\boldsymbol{k}} c^\dagger_{-\boldsymbol{k}\downarrow}$ in the language of second quantization, where $c^\dagger_{\boldsymbol{k}\sigma}, c_{\boldsymbol{k}\sigma}$ create and annihilate an electron with spin $\sigma$, respectively. In the presence of Cooper pairs (energetically favored paired states $c^\dagger_{-\boldsymbol{k}\downarrow} c^\dagger_{\boldsymbol{k}\uparrow}$ , $c_{\boldsymbol{k}\uparrow} c_{-\boldsymbol{k}\downarrow}$) [9, 10], an electron excitation is equivalent to an electron hole excitation. In the superconducting systems, the electronic excitation with energy $E$ ($b^\dagger_{\boldsymbol{k}}(E)$) is correlated with the hole excitation with energy $-E$ ($b_{\boldsymbol{k}}(-E)$) due to the particle-hole symmetry. This indeed renders the superconductors natural platforms to host self-conjugate Majorana fermions ($\gamma = \gamma^\dagger$). When energy $E = 0$, particle and anti-particle states coincide, i.e., $b^\dagger(E = 0) = b(E = 0)$. Therefore, Majorana fermions can likely

be realized as the zero-energy states in superconductors, which normally are bound to topological defects. Note that, the condensed matter version of Majorana fermions require an equal superposition ($|u_{\boldsymbol{k}}| = |v_{\boldsymbol{k}}|$) of an electron and hole state to make $\gamma^\dagger, \gamma$ Hermitian and hence equal to their own anti-particles. Additionally, in contrast to the Bogoliubov quasi-particles operators $b^\dagger, b$, the two equal-weighted components comprising the Majorana fermion operators have same spin projections. Therefore, to realize the zero-energy Majorana bound states (MBSs) or Majorana zero modes (MZMs) in superconductors, the spinless or effectively spinless superconductivity is a key element [6, 11].

How Majorana fermions can emerge in $p$-wave superconductors can be intuitively illustrated by Kitaev's toy model [6], which is a 1-dimensional tight-binding chain with $p$-wave superconducting pairing. Two unpaired Majorana fermions appear when the chain goes through a topological quantum phase transition, shown as the spatially isolated Majorana zero modes localized at opposite ends of the chain. However, electrons in materials have spin $1/2$ and spinless superconducting pairings are rather rare in realistic systems (the majority superconductors found in nature are spin-singlet). This had been an obstacle in searching Majorana fermions in solid state systems, until it was found that the effective $p_x \pm ip_y$-wave superconducting pairing symmetry can possibly be realized in the strong topological insulators with proximity-induced $s$-wave superconductivity [12]. Now various platforms for realizing Majorana zero modes in condensed matter systems have been put forward, including topological insulator-superconductor heterostructures, spin-orbit-coupled semiconductor-superconductor nanowires, and magnetic atom chains in superconducting substrates, etc.

There is a mounting experimentally detected signatures of the existence of the Majorana zero modes in these systems, however, there has been no sufficient evidence for the existence, nor unique confirmation, of the Majorana zero modes in experiments. In Chapter 2, we focus on the model Hamiltonian describing the proximitized nanowires [13, 14, 15], which have been investigated extensively in experiments. We will investigate the properties of Majorana zero modes as well as the low-energy Andreev Bound states based numerically simulations of the model Hamiltonian. In Chapter 3, we revisit the Kitaev chain toy model. An analytical solution to the model Hamiltonian of the finite-length Kitaev chain will be shown and the extended Kitaev chain model by coupling to a quantum dot will also be investigated.

## 1.2 Topological quantum computation

Majorana zero modes have been proposed as the leading candidate for the building block for topological quantum computation [16], owing to their non-Abelian statistic properties and the potentially rich operations generated by braiding. In this section, we discuss how qubits can be made up from Majorana zero modes, and how the logic operations for quantum computation can be realized by Majorana braiding. We also introduce the requirements for realizing quantum computation and the related braiding schemes for Majorana-based topological quantum computation, especially the measurement-only braiding scheme. In the following, we convey these main messages by first introducing the non-Abelian statistic properties of Majorana fermions.

### 1.2.1 Majorana qubit and Majorana braiding

The change of quantum state $|\Psi\rangle$ can be represented by the unitary rotation operator $U$ ($U^\dagger = U^{-1}$). Unlike the bosons and fermions where the quantum state $|\Psi\rangle$ of the system picks up a phase difference ($|\Psi\rangle \rightarrow \pm|\Psi\rangle$) after the exchange of any two particles, Majorana fermions are anyons and they follow non-Abelian statistics. Any exchange or change of order of the exchange of two Majorana fermions will lead to non-trivial rotation operations. The exchange of two non-Abelian anyons is usually called braiding. As shown by Ivanov [17], the result of braiding two Majorana fermions $\gamma_1, \gamma_2$ is,

$$\begin{aligned} \gamma_1 &\rightarrow +\gamma_2, \\ \gamma_2 &\rightarrow -\gamma_1 \end{aligned} \tag{1.5}$$

where the fact that Majorana fermion changes sign i.e., $\gamma \rightarrow -\gamma$ under the change of the phase by $2\pi$ of the superconducting order parameter is considered. Here, $\gamma_1, \gamma_2$ are exchanged in a certain direction (e.g., anti-clockwise) and can be described by the following transformation, $\gamma_1 \rightarrow U_{12}\gamma_i U_{12}^\dagger = \gamma_2, \gamma_2 \rightarrow U_{12}\gamma_2 U_{12}^\dagger = -\gamma_1$, where $U_{12}$ is the braiding operator given as,

$$U_{12} = e^{\frac{\pi}{4}\gamma_2\gamma_1} = \frac{1}{\sqrt{2}}\left(1 + \gamma_2\gamma_1\right) \tag{1.6}$$

Note that, the braiding operation associated with $\widetilde{U}_{12} = \left(1 - \gamma_2\gamma_1\right)/\sqrt{2} = \left(1 + \gamma_1\gamma_2\right)/\sqrt{2}$ is also possible, provided $\gamma_1, \gamma_2$ are exchanged in the direction opposite to that of $U_{12}$ (e.g., clockwise direction). In contrast to the result in Eq. (1.5), the two Majorana fermions are exchanged as $\gamma_1 \rightarrow -\gamma_2, \gamma_2 \rightarrow \gamma_1$ under the braiding

operation of $\widetilde{U}_{12}$.

Consider a system with $2N$ spatially well separated Majorana fermions or Majorana zero modes $\{\gamma_1, \gamma_2, \gamma_3, \gamma_4, ...\gamma_{2N-1}, \gamma_{2N}\}$, each two Majorana fermions ($\gamma_{2j-1}, \gamma_{2j}, j = 1, 2, ...N$) can be paired as a fermionic state ($f_j = (\gamma_{2j-1} + i\gamma_{2j})/2, j = 1, 2, ...N$), giving us $N$ pairs of Majorana fermions or $N$ fermionic states. Every paired state can be either empty ($|0\rangle$) or occupied ($|1\rangle$) by a fermion without costing any energy, it is therefore, we will have $2^N$ possible degenerate quantum states for $N$ pairs of Majoranas. We can represent each such state as

$$|\phi\rangle = |n_1, n_2, n_3, ...n_N\rangle \tag{1.7}$$

where $n_j$ with $i = 1, 2, ...N$ is the occupation number for each paired fermionic state. Note that, $n_j$ is also the eigenvalue of the fermion parity operator defined as $P_j = 2f_j^\dagger f_j - 1 = i\gamma_{2j-1}\gamma_{2j}$. As we see from Eq. (1.5), the fermion parity is not affected by the Majorana braiding operations.

Classically, the basic unit for processing information is a binary bit restricted to the value either $0$ or $1$. In contrast, a quantum bit, or qubit, in general can be any linear coherent superposition of quantum state $|0\rangle$ and $|1\rangle$. Normally, the pure quantum states $|0\rangle$ and $|1\rangle$ are used as computation basis states. This indeed renders the quantum information processing subject to the principle of quantum superposition, endowing quantum computation the massive parallel processing power. In principle, any quantum-mechanical system with two different energy states can be used as a qubit. For instance, the two spin states of an electron, the two polarizations of a single photon or the two energy level states of cold atom in optical lattice.

A semiconductor-superconductor nanowire in topological state, hosting two spatially isolated Majorana zero modes, naturally forms a two-state system. The nanowire now is associated with a regular fermion state comprised of the two Majorana zero modes as have been mentioned earlier, represented by $|0\rangle$ and $|1\rangle = f^\dagger|0\rangle$. However, such two quantum basis states can not be used for coherent superpositions, because linear combinations of states with different fermion parity e.g. $|0\rangle \pm |1\rangle$, violate the superselection rules and are forbidden [18]. This actually accords with the fact that Majorana braiding can not change the fermion parity of system with two Majorana fermion states. Fortunately, it is easy to overcome this drawback.

To define a topological logic qubit, we can use a pair of topological quantum wires i.e., a system with four Majorana zero modes, where the non-trivial effect of Majorana braiding could be also found [18]. For a system with four Majorana fermions $\gamma_{1,2,3,4}$, there are four states on the ground state manifold, namely,

$$|00\rangle, |10\rangle, |01,\rangle, |11\rangle \tag{1.8}$$

Here we assume the first and second digit respectively represents the occupation number $n_j$ of the regular fermion state with $f_j^\dagger = (\gamma_{2j-1} + i\gamma_{2j})/2$ with $j = 1, 2$, i.e., $|10\rangle = f_1^\dagger|00\rangle, |11\rangle = f_2^\dagger|01\rangle = f_2^\dagger f_1^\dagger|00\rangle$. Following the braiding logic given in Eqs. (1.5) and (1.6), the non-Abelian transformations resulted from braiding operations in systems with four Majorana fermions, can be found as [11],

$$\begin{aligned} U_{12}|00\rangle &= \frac{1}{\sqrt{2}}(1+i)\,|00\rangle, \\ U_{23}|00\rangle &= \frac{1}{\sqrt{2}}\left(|00\rangle + i|11\rangle\right), \\ U_{34}|00\rangle &= \frac{1}{\sqrt{2}}(1+i)\,|00\rangle \end{aligned} \tag{1.9}$$

Here each state vector is a $4 \times 1$ ket vector and the braiding operators $U_{ij}$ are $4 \times 4$ matrices which can be written in the basis given by Eq. (1.8). By rewriting the braiding operator $U_{12}$ as $U_{12} = e^{\frac{\pi}{4}\gamma_2\gamma_1} = e^{i\frac{\pi}{4}\left(2f_1^\dagger f_1 - 1\right)}$, the matrix format of $U_{12}$ could be straightforwardly written as [17],

$$U_{12} = \begin{pmatrix} e^{-i\frac{\pi}{4}} & & & \\ & e^{i\frac{\pi}{4}} & & \\ & & e^{-i\frac{\pi}{4}} & \\ & & & e^{-i\frac{\pi}{4}} \end{pmatrix} \tag{1.10}$$

Similarly, $U_{34}, U_{23}$ could be found as,

$$U_{34} = \begin{pmatrix} e^{-i\frac{\pi}{4}} & & & \\ & e^{-i\frac{\pi}{4}} & & \\ & & e^{i\frac{\pi}{4}} & \\ & & & e^{i\frac{\pi}{4}} \end{pmatrix}, U_{23} = \frac{1}{\sqrt{2}} \begin{pmatrix} 1 & 0 & 0 & -i \\ 0 & 1 & -i & 0 \\ 0 & -i & 1 & 0 \\ -i & 0 & 0 & 1 \end{pmatrix} \tag{1.11}$$

Note that, braiding operator $U_{12}, U_{34}$ are diagonal while $U_{23}$ is not. It is the fact that not all the braiding operators are diagonal renders the order of braiding matter a lot, e.g., $U_{12}U_{23} \neq U_{23}U_{12}$ (namely they do not

commute). In general, two braiding operations that involve some same Majorana fermions satisfy

$$[U_{2j-1,2j}, U_{2j,2j+1}] = \gamma_{2j-1}\gamma_{2j+1} \tag{1.12}$$

This in effect represents the non-trivial braiding operations and the non-Abelian statistics of Majorana fermions [11, 17, 18]. On the other hand, two Majorana braiding operations that do not involve any same Majorana fermions indeed commute with each other, for instance, $[U_{12}, U_{34}] = 0$, because both of them are diagonal matrices. Note that, a superposition of states $|00\rangle, |11\rangle$ is explicitly realized by Majorana braiding $U_{23}$. This is allowed now, because the two fermion states being both empty or occupied give an even parity and superconducting condensate conserves fermion number module 2. Therefore, we can define the two basis states as $|\widetilde{0}\rangle = |00\rangle, |\widetilde{1}\rangle = |11\rangle$, with which any general state is expressed as their superpositions. We could also consider the case with a fixed odd parity and define the qubit as $|\widetilde{0}\rangle = |10\rangle, |\widetilde{1}\rangle = |01\rangle$. Since each fermion state is delocalized and composed of a pair of spatially well separated Majorana states, it is unaffected by any local interactions. Non-local encoding of the Majorana zero modes in the topological quantum nonawire allows the storing and processing of information immune to any local perturbations. Qubits made up from Majorana fermions are therefore fundamentally decoherence free, topologically protected from any quantum errors and suitable for fault-tolerent quantum computation.

### 1.2.2 Quantum computation and measurement-based braiding

According to DiVincenzo Criteria [19], there are several minimum requirements for creating a quantum computer, including the conditions for realizing quantum computing and quantum communication. In this thesis, we mainly talk about the conditions for quantum computation. In the context of building qubits from Majorana zero modes hosted in topological semiconductor nanowires, the requirement of *long relevant decoherence times* is satisfied, because Majorana fermions are decoherence free due to their topological properties. *A scalable physical systems with well characterized qubits* can also be realized by building superconducting nanowire networks. The rest of the requirements are significantly important for processing quantum computation, which usually are considered as the three major steps for quantum computation, i.e., (1) initialize the qubits into a predetermined state (*the ability to initialize the state of the qubits to a simple fiducial state*); (2) perform quantum logic operations to braid to qubits (*a "universal" set of quantum gates*) and (3) read out the information encoded in the qubits (*a qubit-specific measurement capability*).

Initializing the qubit states can be controlled via tuning gate potentials or external fields, given a

superconducting nanowire network. The information encoded in the qubits will finally be converted as some observable quantities (e.g., topological charge) that require physical measurements. The quantum logic gates operating on qubits, a quantum-mechanical analog of the classical logic gates for conventional digital circuits, are the building block for quantum circuits. For example, the Pauli-X gate or NOT gate, defined by the Pauli $\sigma_x$ matrix, maps state $|0\rangle$ to $|1\rangle$ and $|1\rangle$ to $|0\rangle$; the Hadamard (H) gate, defined as $H = (\sigma_x + \sigma_z)/\sqrt{2}$, on the other hand can create superposition states by mapping the basis state $|0\rangle, |1\rangle$ into $(|0\rangle + |1\rangle)/\sqrt{2}$ and $(|0\rangle - |1\rangle)/\sqrt{2}$, respectively. These logic gates are all acting with a single qubit, which could be generated by Majorana braiding operations. Majorana braiding can also lead to some other single-qubit gates like $\pi/4$ phase gate. It is computationally sufficient if one can get the braiding-generated gate set comprised of a single-qubit $\pi/8$ phase gate and a two-qubit CNOT gate in system of Majorana fermions [20]. In addition, qubits or Majorana fermions must be braided in order to process the information encoded. Next, we will introduce the Majorana braiding schemes for topological quantum computation.

There are several braiding schemes that utilize the non-Abelian statistics of Majorana fermions, including gate-controlled braiding using junctions of topological nanowires, Coulomb-assisted braiding in Josephson junctions, and measurement-based braiding in superconducting islands coupled to quantum dots. Tremendous experimental progress has been made over the past few years in realizing Majorana zero modes in 1-dimensional semiconductor-superconductor hybrid nanowires, owing to the great possibility of implementing Majorana braiding by tuning the gate voltages of junction-based superconducting nanowire networks. However, this braiding scheme requires "physically manipulating" of individual Majorana zero modes in the coherent topological junctions, which is hard and has not yet been realized in experiments. Further more, actual physical movement of the Majorana fermions will possibly introduce thermal errors into the quantum computation which will restrict the self-correction of the whole quantum computing architecture [21].

In contrast to the gate-controlled braiding, measurement-based braiding is a scheme for "braiding without braiding" [22]. In this braiding scheme, the braiding operations are effectively realized by a sequence of projective parity measurements ($P_{jk} = i\gamma_j\gamma_k$) of a group of Majorana zero modes without any physically movement of the qubits. As have been defined in Eq. (1.6), braiding process for exchanging two Majorana fermions $\gamma_i, \gamma_j$ could be described by operator $U_{ij} = (1 + \gamma_j\gamma_i)/\sqrt{2}$ (one can also use $\widetilde{U}_{ij}$). By using the measurement-only protocol [23], a unitary braiding transformation may be implemented through the

application of a series of projective measurement operator, defined as,

$$\hat{P}_{\gamma_i\gamma_k} = \frac{1}{2}\left(1 - i\gamma_j\gamma_k\right) = \frac{1 - P_{jk}}{2} \tag{1.13}$$

Here operator $\hat{P}_{\gamma_j\gamma_k}$ projects an occupied fermion state (fermion parity $P_{jk} = 1$) back to vacuum. Consider a system with two logic qubits with Majorana zero modes $\gamma_1, \gamma_2, \gamma_3, \gamma_4$. With the help of the ancillary pair of Majorana zero modes $\gamma_a, \gamma_b$, the braiding operation $U_{12}$ can be explicitly expressed as following [22, 24],

$$\begin{aligned}
&\hat{P}_{\gamma_a\gamma_b}\hat{P}_{\gamma_a\gamma_1}\hat{P}_{\gamma_2\gamma_a}\hat{P}_{\gamma_a\gamma_b} \\
&= \frac{1 - i\gamma_a\gamma_b}{2}\frac{1 - i\gamma_a\gamma_1}{2}\frac{1 - i\gamma_2\gamma_a}{2}\frac{1 - i\gamma_a\gamma_b}{2} \\
&= 2^{-4}\left(1 - i\gamma_a\gamma_b\right)\left(1 - \gamma_1\gamma_2 - i\gamma_a\gamma_1 - i\gamma_2\gamma_a\right)\left(1 - i\gamma_a\gamma_b\right) \\
&= \frac{1}{2^{3/2}}U_{12} \otimes \hat{P}_{\gamma_a\gamma_b}
\end{aligned} \tag{1.14}$$

Similarly, we could express Majorana braiding $U_{23}$ as $U_{23} \propto \hat{P}_{\gamma_a\gamma_b}\hat{P}_{\gamma_a\gamma_2}\hat{P}_{\gamma_2\gamma_a}$. In the measurement-based braiding scheme, the topological qubits encoded in the Majorana zero modes can be read out via the change of the total fermion parity of the superconductor island-quantum dot system in the Coulomb-blockade regime. The ground state energy of the system is parity dependent, hence a change of the qubit states is reflected by the shift of the ground state energy, which can be measured by a transmission line resonator coupled with Cooper pair box or transmon [24, 25]. Compared to the braiding with the junctions by manipulating the Majoranas physically, the measurement-based braiding can avoid the possible engineering issues in the fabrications and implementations, and also get rid of the possible thermal errors from the environment. In Chapter 4, we will talk more about the measurement-based braiding for topological quantum computation. Specifically, we will discuss the feasibility of measurement-based braiding in the quasi-Majorana regime.

## 1.3 Higher-order topology

Typically, $D$-dimensional topological insulators/superconductors are characterized by an insulating bulk and stable gapless conducting states localized on $(D-1)$-dimensional boundaries, which constitutes the topological bulk-boundary correspondence. For example, as have been introduced in the previous sections, the zero-dimensional Majorana zero modes localized right at the opposite ends of the 1-dimensional superconducting nanowires are corresponding to a $(D-1)$-dimensional topology. Another example is the

non-degenerate gapless Dirac cones on the 2-dimensional surfaces of the 3-dimensional topological insulators. The robustness of these gapless states are usually promised by the presence of local symmetries, like the time-reversal symmetry $\mathcal{T}$, particle-hole symmetry $\mathcal{P}$ and the chiral symmetry $\mathcal{S}$ ($\mathcal{S} = \mathcal{P}\mathcal{T}$). The conducting $(D-1)$-dimensional states will not be gapped unless certain symmetries are broken in the systems, e.g., the conducting surface states in a strong 3-dimensional topological insulator can not be gapped or localized without breaking the time-reversal symmetry.

In topological crystalline insulators, where crystalline symmetries like mirror, rotation or inversion symmetry are additionally preserved, the bulk-boundary correspondence only works for boundaries which preserve the crystalline symmetry. The bulk-boundary correspondence can be generalized into a version of higher-order, namely, the gapped bulk are associated with protected gapless states of more than one dimension lower. This corresponds to the so-called higher order topology [26, 27, 28]. Higher (second) order topological system is a novel class of topological matters, where the $D$-dimensional bulk as well as the $(D-1)$-dimensional boundaries are gapped, but with robust gapless topological modes hosted on the $(D-2)$-dimensional "edges" defined on the boundary, e.g., corners in 2D systems and hinges in 3D systems. This idea has been used to explain the topologically protected corner modes in quantized electric multipole insulators [29], and the robust 1-dimensional hinge states localized at the edges of the surfaces of 3D crystals of bismuth [30]. Very recently, higher-order topology has also been demonstrated in phononic quadrupole topological insulator [31], twisted bilayer graphene [32] and centrosymmetric transition metal dichalcogenides [33], etc.

Considering of the huge potential of Majorana fermions in topological quantum computation and their emergence as Majorana bound state in topological superconductors, it is a natural question to ask that is there any higher-order topological superconductor can also lead to the emergence of Majorana states? Theoretically, the answer is Yes. It has been proposed that higher-order topological superconductors can be realized by proximitizing 2-dimensional topological insulators with unconventional superconductors like $s_{\pm}$-wave or $d$-wave superconductors [34, 35]. In these systems, the bulk are insulated from being topological insulators, and the conducting edges acquire superconducting gaps due to the proximity effect. Distinct from the non-degenerate Majorana zero modes that breaks time-reversal symmetry in topological nanowires, excitations in the higher-order topological superconductors appear as Majorana Kramer pairs which are protected by time-reversal symmetry. Rather then the more familiar vortex or end modes, the generated gapless Majorana Kramer pairs here are corner modes, where the corners are defined by the points on the edges with zero superconducting order parameter.

Though, in principle, Majorana braiding for topological quantum computation requires non-degenerate Majorana zero modes, braiding with Majorana corner modes which admits non-Abelian statistics is still possible [36, 37]. This indeed makes the Majorana corner modes an alternative candidate for building the qubits for realizing topological quantum computation. However, Majorana corner modes, realized either through defects/impurities/disclinations, or emerging in second order topological superconductors produced using unconventional cuprate ($d$) or iron-based ($s\pm$) superconductors proximity-coupled to a topological substrate have not been realized to date.

Quantum simulation of topological phases with ultra-cold atoms is a rapidly evolving field. There are several remarkable advantages for studying topological phases with cold atoms, including the possibility of engineering single particle Hamiltonians, the high flexibility and controllability of tuning complex many-body interactions, and the feasibility to experimentally probe otherwise inaccessible quantities such as topological invariants, etc. We propose a model of ultra-cold atoms in optical lattices to realize Majorana corner modes and higher order topological superfluids with ordinary $s$-wave superfluidity, which are experimentally realizable, as will be discussed later in Chapter $5$.

## 1.4 Anomalous transport phenomena

In the previous sections, we have introduced the topological excitations in topological superconductors and higher-order topological superconductors, namely, the Majorana zero modes and Majorana corner modes respectively. In this section we will talk about the topological phenomena $-$ anomalous transport phenomena $-$ in topological insulators and Weyl systems.

### 1.4.1 Berry phase effect

During the adiabatic evolution of a quantum state, in addition to the dynamic phase factor, the quantum state acquires an additional geometrical phase $\gamma_n$, called Berry phase [38]. The Berry phase can be expressed as a path integral of a local geometrical vector potential $\boldsymbol{A}_n(\boldsymbol{\mathcal{R}})$ in the $\boldsymbol{\mathcal{R}}$ parameter space, written as,

$$\gamma_n = \oint_{\mathcal{C}} d\boldsymbol{\mathcal{R}} \boldsymbol{A}_n \left(\boldsymbol{\mathcal{R}}\right) \tag{1.15}$$

Here $\boldsymbol{A}_n(\boldsymbol{\mathcal{R}}) = \langle n(\boldsymbol{\mathcal{R}})\left|\frac{\partial}{\partial \boldsymbol{\mathcal{R}}}\right|n(\boldsymbol{\mathcal{R}})\rangle$ is defined as the Berry connection, or Berry vector potential, where $|n(\boldsymbol{\mathcal{R}})\rangle$ represent the basis state that adiabatically moves along a path $\mathcal{C}$ in the parameter space. According to Stokes's theorem, the path integral for Berry phase can in further be rewritten as the following surface integral,

$$\begin{aligned} \gamma_n &= \int_{\mathcal{S}} d\boldsymbol{S} \cdot \boldsymbol{\Omega}_n(\boldsymbol{\mathcal{R}}), \\ \boldsymbol{\Omega}_n(\boldsymbol{\mathcal{R}}) &= \boldsymbol{\nabla} \times \boldsymbol{A}_n(\boldsymbol{\mathcal{R}}), \end{aligned} \tag{1.16}$$

where $\boldsymbol{\Omega}_n(\boldsymbol{\mathcal{R}})$ is the so-called Berry curvature. Note that, the relations between $\boldsymbol{A}_n, \boldsymbol{\Omega}_n$ are exactly analogous to that between the magnetic field $\boldsymbol{B}$ and vector potential field $\boldsymbol{A}$ in electrodynamics. It is therefore, Berry phase is a flux quantity similar as the magnetic flux, and Berry curvature can be viewed as a fictitious magnetic field in momentum space. Berry phase effect is indeed essential for a complete understanding of all the basic phenomena in solid state physics [39].

The motion of the Bloch electrons in momentum space driven by electric filed $\boldsymbol{E}$ and magnetic field $\boldsymbol{B}$ can be described by equation $\dot{\boldsymbol{p}} = e\left(\boldsymbol{E} + \dot{\boldsymbol{r}} \times \boldsymbol{B}\right)$, where $\dot{\boldsymbol{r}} = \boldsymbol{v}$ is the electron velocity in real space. It has been believed [40] that electron velocity $\boldsymbol{v}$ can be simply determined from the Bloch band energy $\varepsilon_{\boldsymbol{k}}$, i.e., $\boldsymbol{v} = \partial\varepsilon_{\boldsymbol{k}}/\hbar\partial\boldsymbol{k}$, until the Berry curvature was clearly found to play an important role in the dynamics of the Bloch electrons. Owing to the non-trivial Berry phase effect, Bloch electrons in the presence of electric field acquire an additional, anomalous velocity that is proportional to the Berry curvature. In the wave packet approach [39], the conventional semi-classical equation of motion for the Bloch electron becomes modified by adding a transverse anomalous term to the velocity, given by,

$$\begin{aligned} \dot{\boldsymbol{r}} &= \frac{1}{\hbar}\frac{\partial\varepsilon_{\boldsymbol{k}}^m}{\partial\boldsymbol{k}} + \frac{\dot{\boldsymbol{p}}}{\hbar} \times \boldsymbol{\Omega}_{\boldsymbol{k}}, \\ \dot{\boldsymbol{p}} &= e\left(\boldsymbol{E} + \dot{\boldsymbol{r}} \times \boldsymbol{B}\right) \end{aligned} \tag{1.17}$$

Here $\varepsilon_{\boldsymbol{k}}^m = \varepsilon_{\boldsymbol{k}} - \boldsymbol{B} \cdot \boldsymbol{m}_{\boldsymbol{k}}$ is the modified electron energy with $\boldsymbol{m}_k$ the orbital magnetic moment. It is obviously shown from Eq. (1.17) that Berry curvature is acting similarly as the magnetic field, i.e., $\dot{\boldsymbol{p}} \times \boldsymbol{\Omega}_{\boldsymbol{k}} \leftrightarrow \dot{\boldsymbol{r}} \times \boldsymbol{B}$. The anomalous velocity supported by the Berry curvature is responsible for a number of anomalous thermoelectric transport phenomena, e.g., the anomalous Hall effect and anomalous Nernst effect.

In fact, if all the Bloch energy states (states $|n(\boldsymbol{\mathcal{R}})\rangle$ are energy states for Bloch electron in Brilouin zone with energy level index $n$ ) are included, the total Berry curvature is identically zero, i.e., $\sum_n \boldsymbol{\Omega}_n(\boldsymbol{k}) = 0$. However, each single energy level has non-trivial Berry phase effect. Note that, to have a non-trivial Berry

curvature ($\boldsymbol{\Omega}(\boldsymbol{k}) \neq 0$), time-reversal and space inversion symmetry can not be simultaneously present in a system. This is because, time-reversal symmetry explicitly respects $\boldsymbol{\Omega}(-\boldsymbol{k}) = -\boldsymbol{\Omega}(\boldsymbol{k})$ while space inversion symmetry leads to $\boldsymbol{\Omega}(-\boldsymbol{k}) = \boldsymbol{\Omega}(\boldsymbol{k})$, and both symmetries being respected renders $\boldsymbol{\Omega}(\boldsymbol{k})$ identically zero.

### 1.4.2 Hall response in the linear and non-linear regime

Generally, the Berry curvature integrated over the entire Brillouin zone, namely, over the filled state, is quantized in the units of $2\pi$. This quantized number is called Chern number [39, 41], corresponding to the net number of monopoles inside the closed manifold. Hence the flux of Berry curvature is also called Chern flux. This quantized flux of Berry curvature is responsible for a number of quantization effect like the quantized adiabatic particle transport and the quantized quantum Hall effect, etc. On the other hand, the Berry phase-supported intrinsic contribution to the anomalous Hall effect is unquantized, which can be given as,

$$\sigma_{xy} = \frac{e^2}{\hbar} \int_{BZ} d\left[\boldsymbol{k}\right] f(\varepsilon_{\boldsymbol{k}}) \boldsymbol{\Omega}_{kx,ky} \tag{1.18}$$

with $f(\varepsilon_{\boldsymbol{k}})$ the Fermi-Dirac distribution function. Note that, anomalous Hall conductivity $\sigma_{xy}$ relies on contributions from non-zero local Berry curvature, instead of a non-zero Chern number (the total Berry curvature flux). Due to the symmetry properties $\mathcal{T}\boldsymbol{\Omega}_{\boldsymbol{k}}\mathcal{T}^{\dagger} = -\boldsymbol{\Omega}_{\boldsymbol{k}}, \mathcal{T}\varepsilon_{\boldsymbol{k}}\mathcal{T}^{\dagger} = \varepsilon_{\boldsymbol{k}}$, $\sigma_{xy}$ identically vanishes in the presence of time-reversal symmetry. Therefore, all the linear anomalous Hall responses including the anomalous Hall, Nernst and thermal Hall effect, must vanish in the systems that preserve time-reversal symmetry as mandated by the Onsager's reciprocity relations [42]. However, non-linear Hall responses have no such restriction.

Very recently, non-linear anomalous Hall effect has been proposed by Inti and Liang in Ref. [43] for the time-reversal invariant materials like Dirac and Weyl materials. Unlike the anomalous Hall effect in the linear-response regime, the non-linear anomalous Hall effect does not require broken time-reversal symmetry but needs inversion symmetry breaking. Rather than directly by the Berry curvature, the non-linear anomalous Hall response is induced by the Berry curvature dipole, which is defined as,

$$D_{ab} = \int d\left[\boldsymbol{k}\right] f_0 \partial_a \boldsymbol{\Omega}_b = -\int d\left[\boldsymbol{k}\right] \frac{\partial f_0}{\partial k_a} \boldsymbol{\Omega}_b \tag{1.19}$$

Two-dimensional transition metal dichalcogenides, topological crystalline insulators, and three-dimensional

Weyl semimetals all are excellent candidate platforms to observe the non-linear Hall response. In some recent electric transport experiments, the non-linear anomalous Hall effect has been successfully observed in the few-layer $WTe_2$ [44, 45].

With the increasing interest in the non-linear properties of topological materials, Berry curvature dipole-related non-linear responses are now being intensively studied in theory as well as in experiments. In Chapter 6 and Chapter 7, within the framework of semiclassical Boltzmann theory, we focus on the non-linear anomalous responses induced by thermal gradient in systems that respect time-reversal symmetry. We propose the non-linear anomalous Nernst effect in the bilayer $WTe_2$ and the non-linear anomalous thermal Hall effect for the transition metal dichalcogenides, respectively. We also make several experimental predictions for these non-linear effects that can be verified in experiments. In addition, we analyze the relations among the anomalous transport coefficients for the non-linear Hall effects in time-reversal invariant systems, including the non-linear anomalous Hall, Nernst and thermal Hall effect. Additionally, for the first time, we find the non-linear analog of the Wiedemann-Franz law and Mott formula for the non-linear anomalous thermoelectric transport phenomena.

# Chapter 2

# Quantized zero bias conductance plateau in semiconductor-superconductor heterostructures without non-Abelian Majorana zero modes

Recent observations of robust zero bias quantized conductance plateaus of height $2e^2/h$ in quantum dot-semiconductor-superconductor nanowires have been interpreted as clear evidence for the presence of non-Abelian Majorana zero modes (MZMs), since other sources of low energy conductance are believed to be unable to produce such quantized plateaus. Based on extensive numerical calculations, we show that in fact quantized conductance plateaus can also arise as a result of *partially separated* Andreev bound states (ps-ABSs), in which the component Majorana modes are somewhat shifted in space without being non-Abelian MZMs. As ps-ABSs can form rather generically, our results suggest that the observation of quantized conductance plateaus does not represent sufficient evidence for the existence of non-Abelian MZMs localized at the opposite ends of a wire.

## 2.1 Introduction

Semiconductor nanowires with proximity induced superconductivity and strong Rashba spin-orbit coupling, which are predicted theoretically [13, 46, 47, 48, 14, 15, 49] to support a pair of mid-gap non-Abelian Majorana zero modes (MZMs) at the opposite ends of a wire [50, 6, 16, 51, 52], have become the leading candidate for the realization of topological quantum computation (TQC) [6, 16] due to the tremendous experimental progress realized in the past few years [53, 54, 55, 56, 57, 58, 59, 60, 61, 62, 63, 64]. The most recent important development of far reaching consequence to TQC has been the observation of quantized zero-bias conductance plateaus in local charge tunneling experiments [64], with the theoretically predicted height ($2e^2/h$) required by topological MZMs [65, 66, 67, 68]. While previous theoretical work on proximitized semiconducting nanowires has shown the formation of zero bias conductance peaks (ZBCPs) even in the absence of MZMs due to disorder [69, 70, 71, 72, 73, 74], non uniform system parameters [75, 76, 77, 78, 79, 80, 81, 82, 83, 84], weak antilocalization [85], and coupling to a quantum dot [86, 87], these peaks of non-Majorana origin *do not* result in a $2e^2/h$–quantized conductance plateau whose height remains constant against variations of the control parameters (e.g., Zeeman field, tunnel barrier height). Note that a quantized conductance plateau does not simply mean the presence of a robust zero-bias conductance peak (of arbitrary height) that sticks at zero energy as a function of the magnetic field, or the realization of a quantized zero-bias peak of height $2e^2/h$ at some specific values of the control parameters, but rather the persistence of a zero-bias peak with a constant quantized height of $2e^2/h$ over a finite range of control parameters such as the magnetic field and the tunnel coupling. This type of feature was so far believed to be associated with the presence of (topological) Majorana zero-modes. Consequently, in the recent experiments [64] the quantized peaks of height $2e^2/h$ and the persistence of the plateaus against the variation of the control parameters have been used as a key evidence for the presence of topologically-protected MZMs localized at the opposite ends of the experimental system. Here, we demonstrate that the quantized conductance plateaus can also have non-Majorana origins, emerging in the topologically-trivial regime.

In this paper we perform detailed numerical calculations of the experimental system [64], which is a quantum dot-semiconductor-superconductor (QD-SM-SC) nanowire heterostructure, and show that quantized conductance plateaus of height $2e^2/h$, which are robust over a large range of Zeeman field and tunnel barrier potential, are also possible due to the presence of low energy Andreev bound states (ABSs) whose component Majorana bound states (MBSs) are somewhat shifted in space: the so-called partially separated ABSs (ps-ABS) introduced in Ref. [88]. The ps-ABSs, on the other hand, are topologically trivial, and cannot be used

in TQC because the separation of the component MBSs, which are localized on the *same* side of the wire, cannot be controlled externally [88]. Essentially, when coupling locally to a ps-ABS one couples strongly to only one of the constituent MBSs (see Fig. 2.1(i)), while the other remains "invisible". We thus arrive at the important result, relevant to the remarkable set of recent experiments [64] and all other tunneling conductance measurements preceding it [53, 54, 55, 57, 58, 59, 60, 61, 62, 63], that the observation of quantized conductance plateaus in local charge tunneling experiments, even if of the theoretically predicted height $2e^2/h$, *cannot* be taken as the clinching evidence for the presence of non-Abelian MZMs, distinguished from other "non-Majorana" sources such as robust low energy ABSs as claimed in the experiments [64].

We interpret the results of this study within a framework based on two observations: i) MZMs and ps-ABSs can be described theoretically using the same modeling of the hybrid structure. However, in the low Zeeman field regime the ps-ABSs are significantly more common, because the parameter region corresponding to inhomogeneous systems that support ps-ABSs is much larger than the parameter region associated with nearly homogeneous systems that host MZMs. ii) The goal of this study is *not* to identify the nature of the low-energy states responsible for the signatures observed experimentally (much less to demonstrate that these states are ps-ABSs). Given the fundamental uncertainty regarding key parameters of the hybrid systems used in experiments, such as, e.g., work function differences and couplings across the SM-SC interface, any attempt to solve these problems purely theoretically would be futile. The answer has to come from experiment. Here, we only show that the signature produced by a ps-ABS in a local tunneling measurement is indistinguishable from the corresponding signature of a MZM, *even if we test the robustness of this signature by varying the control parameters*.

## 2.2 SM-SC heterostructure coupled to a quantum dot

We consider a semiconductor (SM) nanowire with strong spin orbit coupling, proximity coupled to a superconductor (SC) in the presence of an applied magnetic field. A portion of the SM wire is not covered by the SC, which may be thought of as a quantum dot [86, 87, 88], see Fig. 2.1(a). The Bogoliubov-de Gennes (BdG) Hamiltonian for such a one-dimensional QD-SM-SC heterostructure can be written as,

$$\tilde{H} = \left( -\frac{1}{2}\partial_{\tilde{x}}^2 - i\partial_{\tilde{x}}\sigma_y - \tilde{\mu} + V\left(\tilde{x}\right) \right) \tau_z + \Gamma\sigma_x + \Delta\left(\tilde{x}\right)\tau_x \tag{2.1}$$

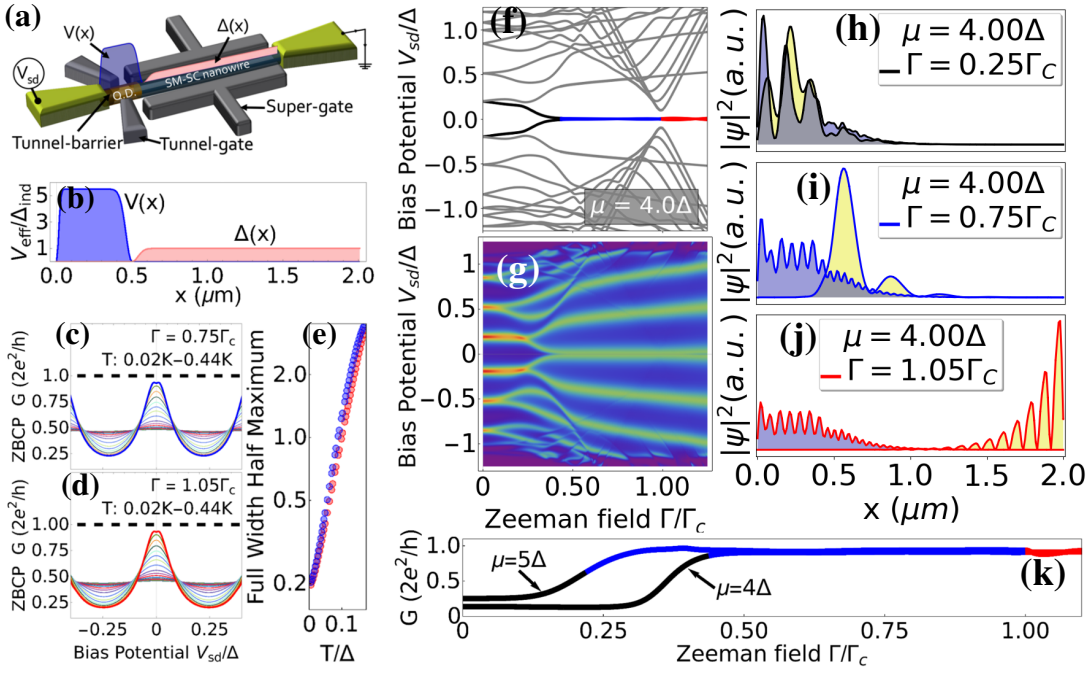


Figure 2.1: (a) Proximitized nanowire junction in which a portion of the semiconductor wire (SM) is not covered by the superconductor (SC), represented by a quantum dot (QD). (b) Quantum dot potential $V(x) = V_{barrier} + V_{dot}$ as described by Eq. 2.2 may form within the QD due to a combination of tunnel coupling to the metallic lead $(V_{barrier})$ as well as application of the tunnel gate potentials $(V_{dot})$. Parameters used here were, barrier potential height $Z = 16\Delta$ and width $x_t = 0.02\mu m$, a quantum dot of width $x_0 \sim 0.5\mu m$ with a potential height $V \sim 5.5\Delta$ which varies over a length scale of $\sigma_V \sim 27.5nm$. Induced pairing $\Delta(x)$ described by Eq. 2.3 is present within the proximitized region of the wire. Here we used $\Delta_{ind} \sim 0.25$meV which varies over a length scale of $\sigma_\Delta \sim 27.5nm$. Robustness of the zero bias peaks to different values of the barrier and dot potentials is shown in Fig. 2.2. (c)-(d) Vertical line cuts from the differential conductance spectra shown in (g) showing a ZBCP quantized to $2e^2/h$ due to the presence of a ps-ABS (blue, Zeeman field $\Gamma < \Gamma_c$ with $\Gamma_c$ the critical field) and a MZM (red, $\Gamma > \Gamma_c$). Temperature dependence of ZBCP from 20 mK to 440 mK in steps of 20 mK shows gradual decrease of the peak height. (e) Full width at half maximum (FWHM) as a function of temperature $T$ for ps-ABS (blue) and MZM (red) of curves taken from (c)-(d). (f) Low-energy spectra as a function of Zeeman field for a nanowire with the potential profile pictured in (b). The Zeeman field $\Gamma > \Gamma_c$ region is marked by the red zero energy mode (MZM), while the blue zero mode marks the region supporting ps-ABSs. (g) Differential conductance spectra as a function of Zeeman field corresponding to energy spectra in (f). (h)-(j) Profiles of lowest energy mode wave functions: (h) A standard ABS consisting of a pair of overlapping MBSs, (i) a ps-ABS consisting of two overlapping MBSs whose separation is on the order of the Majorana decay length $\zeta$, and (j) a pair of non-Abelian MZMs localized at opposite ends of the wire. (k) Zero bias line cuts from conductance spectra showing $2e^2/h$-quantized conductance plateaus against variation of the Zeeman field for two representative values of the chemical potential due to the presence of a ps-ABS (blue) and MZM (red).

with $\tilde{x} = m^*\alpha x$ and $\tilde{H} = (H/m^*\alpha^2)$. Here $\sigma_i$ and $\tau_j$ are the Pauli matrices operating in spin and particle-hole spaces, respectively, $\Gamma$ is the Zeeman field and $\mu$ is the chemical potential. Parameters used were, an effective mass $m^* \approx 0.03m_0$ ($m_0$ being the electron mass), and a Rashba coefficient of $\alpha = 400\ meV \cdot$ Å, consistent with the experiments. All calculations were done at a temperature $T \approx 20$ mK unless otherwise noted. Here $V(\tilde{x}) = V_{barier} + V_{dot}$, in which $V_{barrier}$ represents the potential which arises due to tunnel coupling between the normal lead and the SM wire, and $V_{dot}$ which is due to the tunnel gates shown in Fig. 2.1(b). The potential $V(\tilde{x})$ used throughout this manuscript is of the form

$$V(\tilde{x}) = Z\Theta(x_t - \tilde{x}) + \frac{V}{2}\left(1 - \tanh\left(\frac{\tilde{x} - x_0}{\sigma_V}\right)\right) \tag{2.2}$$

in which $Z$ and $x_t$ are the the height and width of the tunnel barrier $V_{barrier}$ respectively, $V$ is the height of the gate potential $V_{dot}$ within the QD, $x_0$ is the length of the QD, and $\sigma_V$ is the length scale over which $V$ varies. The induced superconducting pair potential is

$$\Delta(\tilde{x}) = \frac{\Delta}{2}\left(1 + \tanh\left(\frac{\tilde{x} - x_0 + \delta_x}{\sigma_\Delta}\right)\right) \tag{2.3}$$

where $\Delta$ is the height of the pairing potential, $\delta_x$ is a parameter that controls the extension of the pairing potential in the QD region due to proximity effect, and $\sigma_\Delta$ is the length scale over which $\Delta$ varies. In Fig. 2.1 we take $V = 5.5\Delta$, $\sigma_V = \sigma_\Delta = 25nm$, $x_0 = 0.5\mu m$, $Z = 16\Delta$, $x_t = 0.02\mu m$, $\Delta = 0.25meV$, and $\delta_x = 4\sigma_\Delta$.

The low-energy spectrum is obtained by numerically diagonalizing the BdG Hamiltonian corresponding to the nanowire. The robustness of the ZBCP is shown for different values of the barrier and dot potentials in Fig. 2.2. Values for the differential conductance $G$ were found by discretizing the Hamiltonian in Eq. 3.5 as follows,

$$\begin{aligned}\hat{H} = \sum_i \{&\psi_i^\dagger \left[(2t - \mu + V(i))\,\tau_z + \Gamma\sigma_x + \Delta(i)\,\tau_x\right]\psi_i \\ &+ \left[\psi_{i+a}^\dagger\left(-t\tau_z + i\alpha\sigma_y\tau_x\right)\psi_i + h.c.\right]\}\end{aligned} \tag{2.4}$$

written in the Nambu basis with $\psi_i = \left(c_{\uparrow i}, c_{\downarrow i}, c_{\uparrow i}^\dagger, c_{\downarrow i}^\dagger\right)$ in which $i$ represents the lattice site and $t = 38\Delta$ is

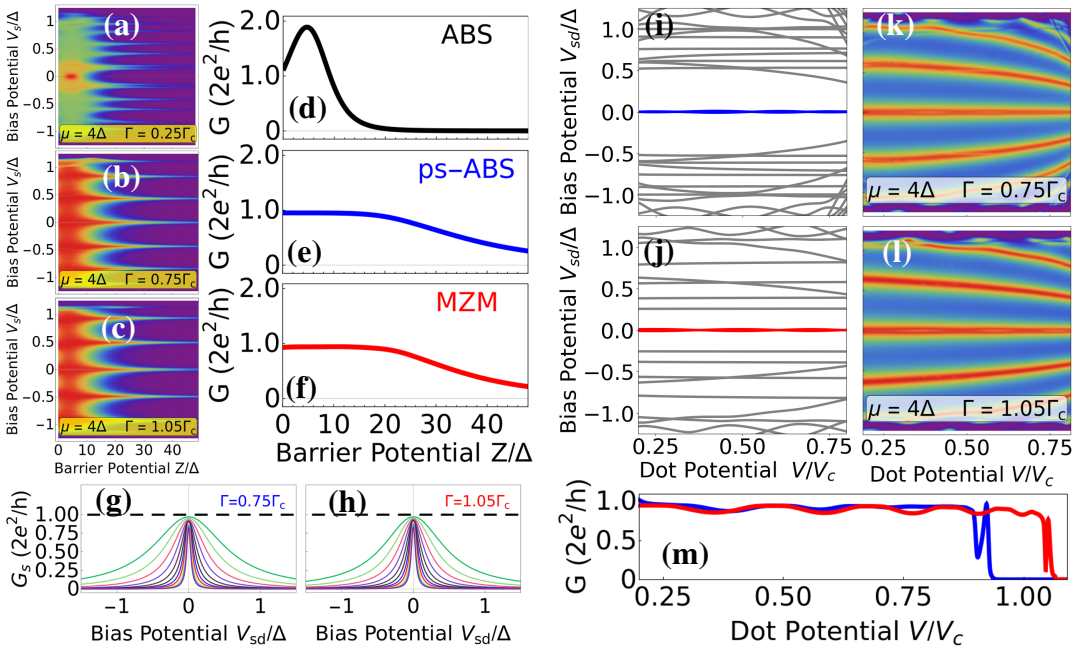


Figure 2.2: (Color online) (a)-(c) Differential conductance as a function of barrier height $Z$ and bias potential associated with a standard ABS ($\Gamma = .25\Gamma_c$) (a), a ps-ABS ($\Gamma = .75\Gamma_c$) (b), and a pair of MZMs ($\Gamma = 1.05\Gamma_c$) (c).(d-f) Zero bias line cuts for (a-c) showing the MZMs and ps-ABSs forming nearly identical profiles which plateau at $2e^2/h$ for a wide range of barrier heights. The standard ABS peak height (d) may take any value between 0 and $4e^2/h$ and quickly goes to 0 with increased barrier height. (g-h) Vertical line cuts from (b) and (c) showing ZBCPs quantized at $2e^2/h$ over a large range of barrier potential heights $Z$ for both ps-ABS and MZM. (i-j) Low energy spectra as a function of quantum dot potential height $V$ associated with potential profile in Fig. 2.1(b) for ps-ABS (blue, $\Gamma < \Gamma_c$) and MZM (red, $\Gamma > \Gamma_c$). Here and in the following plots $V_c = 2\mu$ is taken as the reference dot potential, while the dot potential $V$ is varied between $.25V_c = 2\Delta$ and $V_c = 2\mu = 8\Delta$. (k-l) Plots of differential conductance as a function of dot potential height $V$ and bias potential for values consistent with energy-spectra shown in (i-j). (m) Horizontal zero bias line cuts with (m) corresponding to (k-l) showing a $2e^2/h$-quantized plateau for both ps-ABSs (blue) and MZMs (red).

the hopping matrix element used throughout the calculations. The zero temperature differential conductance

$$G_0(V) = \frac{e^2}{h}(N - R_{\text{ee}} + R_{\text{he}}), \tag{2.5}$$

was found using the S matrix method in KWANT [89], a Python package for transport calculations for systems with tight binding Hamiltonians. Here $N$ is the number of electron channels in the lead, $R_{ee}$ is the total probability of normal reflection and $R_{eh}$ is the total probability of Andreev reflection for an electron in the lead. Finite temperature is represented by broadening the zero temperature conductance through a convolution with the derivative of the Fermi-function in the usual manner, $G\left(V,T\right) = -\int d\epsilon G_0\left(\epsilon\right) f_T'\left(\epsilon - V\right)$.

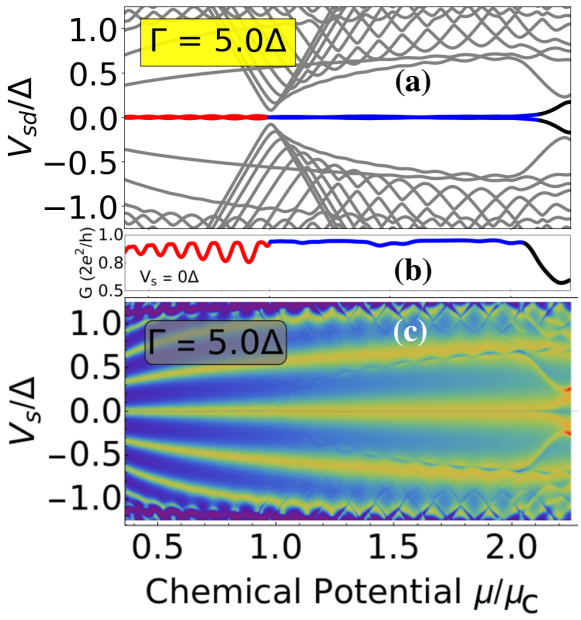


Figure 2.3: (Color online)(a)Low-energy spectra as a function of chemical potential. The red line signifies the topological region supporting MZMs, the blue line shows a non-topological region supporting ps-ABSs which stick to zero energy for a wide range of chemical potential. (b) Zero bias line cut taken from (c) showing a robust $2e^2/h$ quantized conductance plateau forming in the topologically trivial regime due to the presence of a ps-ABS. (c) Differential conductance spectrum as a function of chemical potential for parameter values consistent with Fig. 2.1.

To analyze the low-energy ABSs, we represent the BdG eigenstates $\phi_{\pm\varepsilon}(i)$ of Eq. 2.4 as a pair of overlapping MBSs, $\chi_A(i) = \frac{1}{\sqrt{2}}[\phi_\varepsilon(i) + \phi_{-\varepsilon}(i)]$ and $\chi_B(i) = \frac{i}{\sqrt{2}}[\phi_\varepsilon(i) - \phi_{-\varepsilon}(i)]$. Using this formalism, a standard ABS is defined as a superposition of constituent MBSs that are sitting directly on top of one another (Fig. 2.1(h)), a ps-ABS as a superposition of constituent MBSs that are separated on the order of the Majorana decay length $\zeta$ (Fig. 2.1(i)), while topological MZMs correspond to constituent MBSs separated by the length of the wire (Fig. 2.1(j)). From the wave function profiles, it is straightforward to see that if a ps-ABS is present in the quantum dot region, as in Fig. 2.1(i), a tunnel probe placed on the left hand side of the wire will predominantly couple to a single MBS (purple), making it indistinguishable from a MZM, as in Fig. 2.1(j). Note that in a finite wire the bulk gap does not completely close and thus a ps-ABS can be continuously connected to a pair of non-Abelian MZMs. By contrast, in an infinite (or long) wire, in which the bulk gap closes signaling a TQPT, the ps-ABS and MZMs are separated by a quantum phase transition and only the pair of MZMs for $\Gamma > \Gamma_c$ are topologically non-trivial. Moreover, ps-ABSs cannot be used in TQC, because the separation between the component MBSs in a ps-ABS can not be controlled independently.

## 2.3 Results

In Fig. 2.1(f) we show the low energy spectrum of the QD-SM-SC structure as a function of the applied Zeeman field. A pair of robust zero modes emerge in this plot (blue) well before the bulk band gap has a minimum signaling the TQPT. We associate these modes with ps-ABSs, while the zero energy modes beyond the bulk gap closing (red) are topological MZMs. The corresponding plot of the differential conductance as a function of Zeeman field (Fig. 2.1(g)) shows a robust ZBCP in the topologically trivial regime indistinguishable from the ZBCP in the topological regime. Furthermore, Figs. 2.1(c-e) show an exponential dependence of the ZBCP height and width on the temperature for both MZMs and ps-ABSs. These robust ZBCPs form $2e^2/h$-quantized conductance plateaus both in the topologically trivial and non-trivial regimes (Fig. 2.1(k)), similar to those observed in the experiments [64].

Next, in Fig. 2.2(a-f), we plot the differential conductance as a function of bias potential and barrier potential ($Z$). These results show that while the ZBCP height due to a standard ABS may take any value ($0 - 4e^2/h$) and quickly drops to zero upon increasing the barrier potential (Fig. 2.2(d)), the behavior of the ZBCPs induced by ps-ABSs and MZMs is nearly the same. Indeed, upon varying the barrier height, both the ps-ABS and the MZM induce (practically indistinguishable) quantized zero bias conductance plateaus of height $2e^2/h$ (Fig. 2.2(e-f)). The low energy spectrum as a function of the quantum dot potential $V$ corresponding to the potential profile shown in Fig. 2.1(b) is shown in Fig. 2.2(i) for a ps-ABS (blue, $\Gamma < \Gamma_c$) and in Fig. 2.2(j) for a MZM (red, $\Gamma > \Gamma_c$). The corresponding dependence of the differential conductance shown in panels (k) and (l), respectively, has similar (practically indistinguishable) features. Finally, the ps-ABS and the MZM have nearly identical $2e^2/h$-quantized conductance peaks that are robust against variations of the dot potential, as shown in Fig. 2.2(m).

The dependence of the low energy spectrum on the chemical potential, which experimentally can be controlled by changing the super-gate potential, is shown in Fig. 2.3(a). A robust zero energy mode emerges in the trivial regime (blue) due to a ps-ABS, well before the topologically non-trivial regime (red). This results in a robust $2e^2/h$-quantized conductance plateau as function of the chemical potential (Fig. 2.3(b,c)). As in Ref. [64], the quantized ZBCP exhibits some oscillatory behavior due to peak splitting, with the ZBCP returning to the $2e^2/h$-quantized value but never exceeding it. Finally, SM-SC nanowires require a magnetic field oriented along the wire in order to support topological MZMs [13, 46, 47, 48, 14, 15, 49]. Re-orientating the magnetic field toward the direction of the spin-orbit field should rapidly destroy the MZM-induced ZBCP [61]. The dependence of the differential conductance on the direction of the magnetic field is shown in

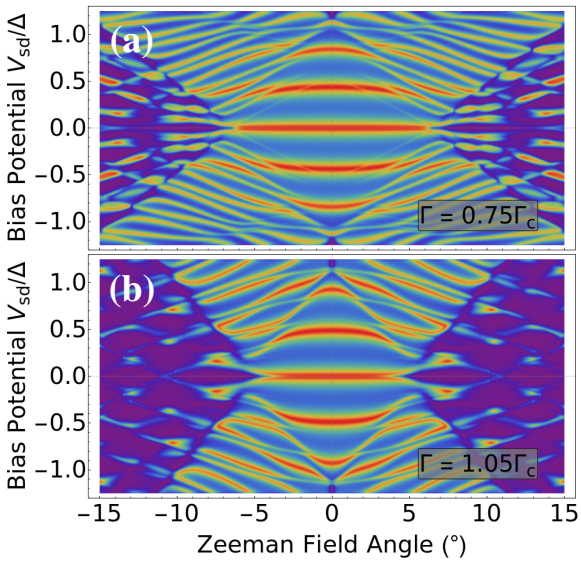


Figure 2.4: (Color online) Differential conductance as a function of the in plane angle of the Zeeman field for the ps-ABS (a) and the MZM (b) shown in Fig. 2.1(i)-(j). A ZBCP appears for a small angle in which the Zeeman field is almost aligned with the wire. As the angle between the wire and the direction of the Zeeman field is increased the ZBCP is destroyed in both cases due to splitting.

Fig. 2.4 for both a trivial ps-ABS (a) and a MZM (b). In both cases the ZBCP is only present for small values of the angle $\phi$, for which the magnetic field is almost aligned with the direction of the wire.

## 2.4 Summary and conclusion

In summary, based on extensive numerical calculations, we show that, quantized zero bias conductance peaks, who's height remains constant at $2e^2/h$ as a function of varying system parameters such as Zeeman field, tunnel barrier height, dot potential, etc. (the so called quantized conductance plateaus [64], can arise as a result of partially separated Andreev bound states, in which the component Majorana bound states are somewhat shifted in space without being topological MZMs. As partially separated Andreev bound states can form generically in the topologically trivial phase, as illustrated in this paper with a step like potential in the quantum dot region which can be induced by tunnel gates, we conclude that the recent experimental observations showing quantized conductance plateaus of height $2e^2/h$ as a function of various control parameters cannot represent definitive evidence for the presence of MZMs. We emphasize that a more "realistic" modeling of the experimental system (which would face major challenges, considering our limited knowledge of key microscopic parameters that characterize the hybrid systems studied experimentally) is not expected to

modify this conclusion. Essentially, when coupling locally to the end of the quantum dot, which may harbor a ps-ABS, one couples much stronger to one of the constituent MBSs than to the other because of the partial separation between the pair of MBSs. Thus, the other constituent MBS basically remains "invisible" to the tunneling lead. For instance, in Fig 1(i) the tunnel lead, which couples from the left end, should couple much more strongly to only one of the MBSs (shown in blue), while coupling to the other MBS (shown in yellow) is strongly suppressed because of partial decoupling of the MBSs. Thus, the local coupling to a ps-ABS is effectively equivalent to the local coupling to a MZM.

In a recent preprint [90] it has been argued (based on a smooth confinement potential scenario similar to that proposed in Ref. [75]) that quantized conductance plateaus can also arise in the trivial regime due to differences in the spin polarization of the constituent MBSs, even if the MBSs are fully overlapping. By contrast, in this paper we find that for a step-like potential in the quantum dot region, the stability of the quantized conductance plateaus is essentially controlled by the separation between the constituent MBSs of a ps-ABS, as shown in Fig. 2.2(p). The details of the relationship between the ps-ABSs found in this paper and the quasi-Majoranas emerging in the presence of a smooth confinement potential as described in Refs. [90, 75], including the effects of spin polarizations and the spatial separation of the component MBSs on the stability of the conductance plateaus, will be addressed in a forthcoming publication. Based on the results of this paper, we conclude that the local charge tunneling measurement, which was, so far, the primary type of probe used in experiments, has exhausted its potential to reveal useful information regarding the distinction of MZMs from low energy ABSs (ps-ABSs in particular), both of which can appear in SM-SC hybrid structures. The next stage must involve non-local probes, such as, for example, the two-terminal charge tunneling measurement [88, 91].

# Chapter 3

# Analytical solution of the finite length Kitaev chain coupled to a quantum dot

We solve analytically the problem of a finite length Kitaev chain coupled to a quantum dot (QD), which extends the standard Kitaev chain problem to the quantum dot-semiconductor-superconductor (QD-SM-SC) nanowire heterostructure currently under intense investigation for possible occurrence of Majorana zero modes (MZMs). As a first step, we obtain the analytical solution of the finite length Kitaev chain *without the quantum dot*, which, to the best of our knowledge, has also not appeared before. Our full solution of the Kitaev chain coupled to a quantum dot reveals the emergence of a robust near-zero-energy Andreev bound state (ABSs) localized in the quantum dot region as the generic lowest energy solution in the topologically trivial phase. By contrast, in the Kitaev chain without the quantum dot such a solution does not exist. The robustness of the ABS in the topologically trivial phase is due to a partial spatial decoupling of the component Majorana bound states (MBSs) over the length of the dot potential. As a result, the signatures of the ABS in measurements that couple locally to the quantum dot, e.g., tunneling measurements, are identical to the signatures of topologically-protected MZMs, which arise only in the topological superconducting (TS) phase of the Kitaev chain.

## 3.1 Introduction

Non-Abelian Majorana zero modes (MZMs) [50, 6, 16], which were theoretically predicted [13, 46, 47, 48, 14, 15, 49] to arise as zero-energy excitations at the edges of low-dimensional spin-orbit coupled semiconductors with proximity induced superconductivity in the presence of a Zeeman field, have emerged [92, 51, 52] as the leading candidate in the creation of topological quantum bits essential to fault-tolerant quantum computation [6, 16]. This research has been bolstered by recent experimental progress leading to observations of key signatures of Majorana zero modes [53, 54, 55, 56, 57, 58, 59, 60, 61, 62, 63, 64] in semiconductor-superconductor (SM-SC) nanowire heterostructures, particularly the emergence of a zero bias conductance peak in the tunneling conductance spectra at a finite magnetic field. Theoretically, such zero bias conductance peaks (ZBCPs) were shown to also arise due to low energy states generated by several different phenomena unrelated to topology [69, 70, 71, 72, 73, 74, 75, 76, 77, 78, 79, 80, 81, 82, 83, 84, 85, 86, 87]. However, the low-energy states of non-topological origins are usually found to generate ZBCPs that are not quantized at peak height $2e^2/h$ and/or are not stable against variations of various experimental control parameters such as magnetic field, chemical potential, and tunnel barrier height. This is the main reason why recent experiments capable of measuring ZBCPs which remain quantized at $2e^2/h$ over a finite range of control parameters [64], as required theoretically for the signatures of topological MZMs [65, 66, 67, 68], have garnered a great deal of excitement [93].

To properly analyze the Majorana zero mode experiments on SM-SC heterostructures, it is useful to note that many of the systems under experimental investigation should be described as a quantum dot-semiconductor-superconductor (QD-SM-SC) nanowire heterostructure (rather than a simple SM-SC heterostructure without the QD as was originally proposed [13, 46, 47, 48, 14, 15, 49]), because a QD is almost inevitably formed in the bare SM wire segment between the normal tunnel lead and the epitaxial SC shell owing to band bending and/or disorder [60, 64]. Therefore, while the topological properties of the theoretically proposed simple SM-SC heterostructure in the presence of spin-orbit coupling and Zeeman field can be described in terms of an effective model consisting of a finite length Kitaev chain [6], the correct effective model for the systems under experimental investigation is a finite length Kitaev chain coupled to a QD, where the QD is defined by a region at the end of the chain in the presence of a local electric potential and vanishing superconducting pair potential $\Delta$. In this paper, we analytically solve this effective model in the long-wavelength, low-energy limit. In addition to providing the analytical solution to a valuable extension of the celebrated Kitaev model (i.e., Kitaev chain coupled to a quantum dot, an extension motivated by ex-

periment), our study allows a qualitative understanding of recent numerical work [88, 94] on proximitized SM-SC heterostructures coupled to a QD, which has shown that it is possible to have quantized ZBCPs of height $2e^2/h$ forming robust plateaus with respect to the experimental control parameters even in the topologically trivial phase.

In this paper we analyze a Kitaev chain of length $L$, characterized by a superconducting pair potential $\Delta$, which is coupled to an end QD of length $x_0$ (see Eq. (3.21)) defined by an effective potential of height $V$ ($V = 0$ in the bulk of the Kitaev chain, see Fig. 3.3). Experimentally, the effective potential in the QD region (which we model, for simplicity, as a step-like potential well of depth $V$) may be induced by a local gate and/or by a position-dependent work function difference between the SM and the SC (which is nonzero in the proximitized segment of the wire and vanishes in the uncovered regions). Note that this type of position-dependent effective potential is manifestly different from the smooth confinement potential at the end of the chain considered in Ref. [75] (see also Ref. [88]). More importantly, the mechanisms for the formation of robust near-zero-energy non-topological ABSs are qualitatively different in the two models. In particular, in the presence of a smooth confinement potential [75, 88] the pair of component MBSs constituting a robust near-zero-energy ABS originates from two *different* spin channels of a confinement-induced sub-band, while in the presence of a step-like potential well in the QD region (Fig. 3.3(a), the component MBSs originate from the *same* spin channel (see Sec. 3.5 and Fig. 3.9). This is why the topological properties of the QD-SM-SC hybrid structure with a step-like potential well can be understood in terms of an effective representation of a Kitaev chain coupled to a QD (since the low-energy physics involves a single spin channel), while the SM-SC heterostructure with smooth confinement potential [75] cannot be analyzed using such a representation (because in this case both spin channels are required).

First, we solve analytically the Hamiltonian for a finite length bare Kitaev chain (i.e. without the quantum dot) and obtain the wave functions corresponding to the lowest energy eigenvalues. To the best of our knowledge, the lowest energy wave functions with eigenvalues $\pm\epsilon$ emerging in the "topological" phase of a finite length Kitaev chain, with the putative Majorana energy eigenvalues $\pm\epsilon$ oscillating with the chemical potential and the chain length $L$, have so far only been estimated perturbatively based on the overlap of end-localized wave functions corresponding to a semi-infinite Kitaev chain or SM-SC Majorana wire [91, 95, 96, 97]. By contrast, our analytical treatment of the finite chain provides non-perturbative solutions for the energy splitting oscillations of the putative Majorana modes (as function of the chain length and chemical potential), as well as the exponential decay of the amplitude of these oscillations with increasing system size. In particular, we show explicitly that the energy splitting oscillations are a direct consequence

of imposing appropriate boundary conditions in a finite system. Next, armed with these solutions, we solve the problem of a finite length Kitaev chain coupled to a quantum dot, where by quantum dot we mean a small region at the end of the chain defined by a local potential well of height $V$ and a reduced (possibly vanishing) induced superconducting pair potential, as suggested by the experimental setups involving semiconductor-superconductor hybrid structures [60, 64]. Our analytical solution of the full problem is characterized by a pair of robust low energy Bogoliubov-de Gennes (BdG) states with energies $\pm\epsilon$ localized in the quantum dot region as the generic lowest energy eigenstates in the topologically trivial phase of the Kitaev chain. We emphasize that no such near-zero-energy robust BdG states exist as low energy solutions in the topologically trivial phase of the finite length Kitaev chain *without* a QD. In the topological superconducting phase, the lowest energy solutions are (topological) MZMs localized at the two ends of the chain. We find that the robustness of the near-zero-energy BdG states $\phi_{\pm\epsilon}$ that emerge in the presence of the QD is due to a partial decoupling of the component Majorana bound states (MBSs), $\chi_A = \frac{1}{\sqrt{2}}\left[\phi_\epsilon + \phi_{-\epsilon}\right]$ and $\chi_B = \frac{i}{\sqrt{2}}\left[\phi_\epsilon - \phi_{-\epsilon}\right]$, over the length of the quantum dot. It follows that such partially-separated ABSs (ps-ABSs), which were first introduced in the numerical study of the SM-SC heterostructure coupled to a QD [88, 94], generate signatures in experiments involving local probes, e.g., in charge tunneling experiments, identical to the signatures of topological MZMs.

The reminder of this paper is organized as follows. In Section 3.2 we provide some preliminaries for the Kitaev chain model with periodic boundary conditions, which is applicable for infinitely long systems. In Section 3.3, we detail the non-perturbative solution of the finite length Kitaev chain (with open boundary conditions). In Section 3.4, we solve the problem of a finite length Kitaev chain coupled to a QD both analytically and numerically (for comparison). First, in Section 3.4 A, we consider the case of no proximity effect in the QD from the adjoining SC, and find that, in this case, near-zero-energy ABSs *do not* exist as low energy solutions in the topologically trivial phase of the Kitaev wire. In Section 3.4 B, we assume a slice of the QD adjoining the SC to be proximitized and show that correct matching of the boundary conditions in the different regions of the Kitaev chain coupled to the QD produces robust near-zero-energy ABSs localized in the QD region as generic low energy solutions in the topologically trivial phase of the bulk Kitaev chain. We also analyze the wave functions of the component MBSs of the low energy ABSs and find that these states are spatially separated by the length of the proximitized region in the QD. We discuss the overlap of the component MBSs and the resultant splitting oscillations of the so-called partially separated ABSs, and find that the splitting is generically lower for these states because of the existence of the adjoining Kitaev chain in which the component MBSs can relax. We end with a summary of the main results and some concluding

remarks in Section 3.5.

## 3.2 Kitaev model preliminaries

The one-dimensional model of topological superconductivity proposed by Kitaev [6] can be derived from the tight binding Hamiltonian for a 1D superconducting wire as follows,

$$H = -\sum_{j=1}^{N} \left[ \mu c_j^\dagger c_j + \left( t c_{j+1}^\dagger c_j - \Delta c_j c_{j+1} + h.c. \right) \right] \tag{3.1}$$

where $t$, $\mu$, and $\Delta$ are the nearest neighbor hopping amplitude, chemical potential, and superconducting pairing potential, respectively, and $c^\dagger$ and $c$ are the second quantized creation and annihilation operators. Introducing the operators $\gamma_{2j-1} = c_j + c_j^\dagger$ and $\gamma_{2j} = i(c_j^\dagger - c_j)$ allows the Hamiltonian $H$ to be rewritten as,

$$\begin{aligned} H = & -i\frac{\mu}{2} \sum_{j=1}^{N} \gamma_{2j-1}\gamma_{2j} \\ & + \frac{i}{2} \sum_{j=1}^{N-1} \left[ (t + |\Delta|)\gamma_{2j}\gamma_{2j+1} + (-t + |\Delta|)\gamma_{2j-1}\gamma_{2j+2} \right] \end{aligned} \tag{3.2}$$

In the limit $\mu = 0$ and $t = |\Delta| > 0$ the Hamiltonian becomes,

$$H = it \sum_{n=1}^{N-1} \gamma_{2n}\gamma_{2n+1}. \tag{3.3}$$

Because $\gamma_1$ and $\gamma_{2N}$ do not appear in the Hamiltonian this represents the topological phase of the wire described in Eq. (3.2), in which a single pair of zero energy MZMs appear at the ends of the wire while the bulk of the wire remains gapped at an energy of $\pm|t|$. More generally, applying periodic boundary conditions, and Fourier transforming the Hamiltonian in Eq. (3.1) into momentum space, the Bogoliubov-de Gennes (BdG) Hamiltonian can be written as (with the lattice constant $a = 1$),

$$\begin{aligned} & H = \int dk \Psi^\dagger(k) H_{BdG} \Psi(k) \qquad \Psi^\dagger = \left( c_k^\dagger, c_k \right) \\ & H_{BdG} = (-2t\cos k - \mu)\tau_z + 2\Delta\tau_y \sin k \end{aligned} \tag{3.4}$$

where $k$ is the momentum and $\tau_z, \tau_y$ are the Pauli matrices operating in the particle-hole space. The bulk band structure for the wire, found by diagonalizing Eq. (3.4) is $E = \sqrt{(2t\cos k + \mu)^2 + 4|\Delta|^2 \sin^2 k}$,

which shows a bulk band gap closure at $k = \{0, \pi\}$ for $\mu = \pm 2t$, representing the topological quantum phase transition (TQPT) as described in the Kitaev model.

In the long wavelength limit near the band gap closure as $k \to 0$, such that $\sin k \to k$ and $\cos k \to \left(1 - k^2/2\right)$, Eq. (3.4) can be rewritten as,

$$\tilde{H}_{BdG} = (-t\partial_x^2 - \tilde{\mu})\tau_z + i\tilde{\Delta}\partial_x\tau_y \tag{3.5}$$

where $\tilde{\mu} = \mu - 2t$ and $\tilde{\Delta} = 2\Delta$. Because the chemical potential is being measured from the bottom of the band ($\tilde{\mu} = \mu - 2t$), the phase transition points in Eq. (3.5) ($\tilde{\mu} = \pm 2t$) are now at $\mu = 0$ and $\mu = 4t$.

Solutions to the eigenvalue equation

$$\tilde{H}_{BdG}\phi\left(x\right) = E\phi\left(x\right) \tag{3.6}$$

are found by applying a trial wave function of the form $\phi\left(x\right) = \left(u\left(x\right), v\left(x\right)\right)^T = \tilde{\phi}\left(x\right)\left(\tilde{u}, \tilde{v}\right)^T$ in which the spatial dependence is fully incorporated in the function $\tilde{\phi}\left(x\right) \propto e^{i\lambda x}$ with $\tilde{u}, \tilde{v}$ being independent of $x$. Substituting the trial function $\phi(x)$ in Eq. (3.6) we find the characteristic equation,

$$E^2 - \left(\lambda^2 - \mu\right)^2 - \Delta^2\lambda^2 = 0 \tag{3.7}$$

along with the following constraint on the spinor degrees of freedom

$$\tilde{v} = i\frac{\lambda^2 - \mu - E}{\Delta\lambda}\tilde{u}. \tag{3.8}$$

Here, all the terms are written in terms of the hopping energy $t$, so all the parameters with dimension of energy are rendered dimensionless in the rest of the paper.

Note that $\lambda$ in the trial wave function $\tilde{\phi}(x)$ is a complex number which can be written as, $\lambda = k + iq$ ($k, q \in \mathcal{R}$). Substituting it back to Eq. (3.7) gives us,

$$\begin{aligned} \left(E^2 - \Delta^2(k^2 - q^2) + 4q^2k^2 - (k^2 - q^2 - \mu)^2\right) \\ -2iqk\left(2(k^2 - q^2) + \Delta^2 - 2\mu\right) = 0 \end{aligned} \tag{3.9}$$

The eigen-energy $E$ being real, it follows that the imaginary part in Eq. (3.9) must vanish,

$$-2iqk\left(2(k^2-q^2)+\Delta^2-2\mu\right)=0 \tag{3.10}$$

There are three possible cases which can be extracted from Eq. (3.10), namely, (a) $q=0$, and $\lambda=k$ is purely real, (b) $k=0$ and $\lambda=iq$ is purely imaginary, and (c) $k,q\neq 0$ with $\lambda=k+iq$ a complex number. Substituting the three solutions to Eq. (3.10), namely, $q=0$, $k=0$, and $2(k^2-q^2)=(2\mu-\Delta^2)$ back in Eq. (3.9) for the cases (a), (b), and (c), respectively, we have,

$$(k^2-\mu)^2+\Delta^2k^2-E^2\equiv 0 \tag{3.11a}$$

$$(q^2+\mu)^2-\Delta^2q^2-E^2\equiv 0 \tag{3.11b}$$

$$(\Delta^2\mu-\Delta^4/4)-4k^2q^2-E^2\equiv 0 \tag{3.11c}$$

We can now solve $k,q$ in a form $k(E),q(E)$ (energy dependent) for each case in Eq. (3.11). However, we can roughly analyze the approximate range of the eigen-energy $E$ in each case before moving on. In case (a), $E^2=(k^2-\mu)^2+\Delta^2k^2$ would give us $|E|\geq|\mu|$ if $\mu\leq 0$. As for $\mu>0$ we have $E^2\approxeq\mu^2+(\Delta^2-2\mu)k^2$ for $k^2\ll\mu$, which would again give us $|E|$ with some value near $\mu$. Similarly in case (b), we have $E^2\approxeq\mu^2+(2\mu-\Delta^2)q^2$ for $q^2\ll\mu$. It follows that both cases (a) and (b) cannot support a low energy solution ($E\ll|\mu|$) appropriate for MZMs in the topological phase. However, in case (c), we can have a solution with low energy-eigenvalue $E$, which is our main interest. In case (c) we have $E^2=\Delta^2(\mu-\Delta^2/4)-4k^2q^2$, which could be tuned to get a near-zero-energy solution independently of $k,q$ in the topological phase. It will indeed provide us with a nontrivial solution in terms of putative Majorana zero modes as discussed below.

## 3.3 Finite length Kitaev chain and splitting oscillations

In order to find the solutions to the full problem of a finite length Kitaev chain coupled to a QD, we first analytically solve the finite length bare Kitaev chain *without* the QD. To the best of our knowledge, these solutions, which reveal the exponential decay and splitting oscillations of the lowest energy eigenvalues with the chain length $L$ and the chemical potential $\mu$ non-perturbatively, have not been written before. Later, we will use these exact solutions to find the solutions for the full problem of the Kitaev chain coupled to a quantum dot by matching the wave functions of the full Bogoliubov-de Gennes equations.

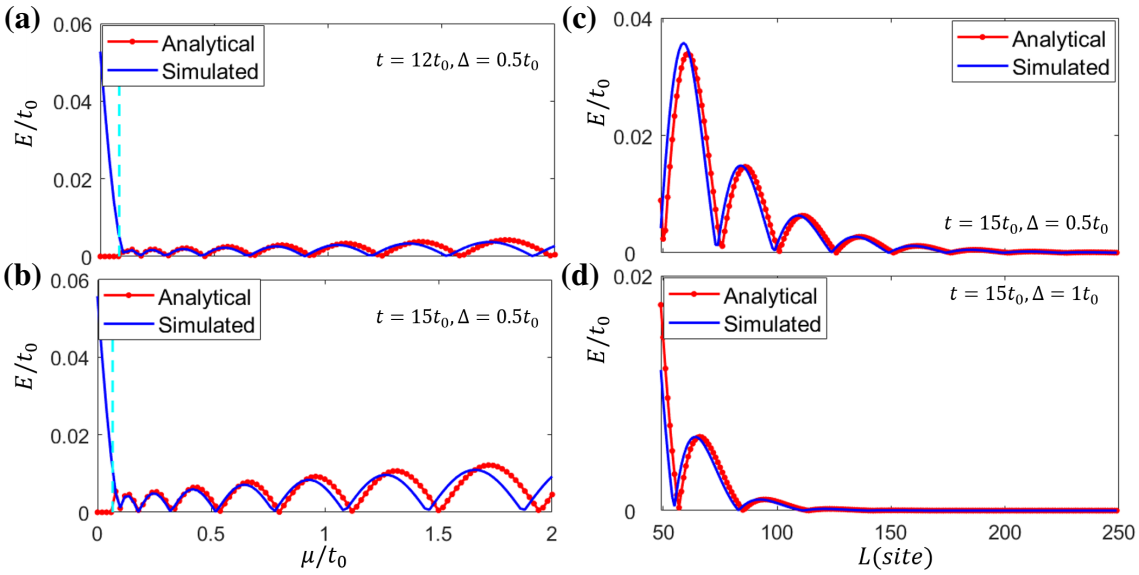


Figure 3.1: (Color online) Lowest-energy spectra for the finite length Kitaev chain in the topological phase $\mu > 0$ as a function of chemical potential $\mu$ in (a)–(b) and Length $L$ in (c)–(d). Analytical results (red dotted line) are based on Eq. (3.18), while the simulation results (blue solid line) are from direct diagonalization of the tight binding hamiltonian in Eq. (3.1) for a finite length $L$. The cyan dashed lines in (a)–(b) show the condition $\mu \geq \Delta^2/4$ discussed below Eq. (3.18), after which the analytical solutions are valid. It shows a lower hopping energy $t$ reduces the energy splitting in (a) relative to that in (b); a higer SC $\Delta$ offers a more effective exponential protection in (d) than that in (c). All of this can be explained by the dependence of the lowest energy $E$ on the parameters $\mu, L$, respectively, through Eq. (3.18). A slight shift of the analytical results relative to the simulation results is caused by the dropped terms for $q$ and $k$ in Eq. (3.18). The other model parameters are $L = 71$ in (a)–(b) and $\mu = 0.25t_0$ in (c)–(d), and $t_0 = 1$.

For a given one-dimensional Kitaev chain in the topological superconducting phase of finite length $L$, to support a pair of low energy solutions at energies $\pm E$, the roots $\lambda_i$ of Eq. (3.7) are necessarily complex (case (c) below Eq. (3.10)). combining Eq. (3.11c) with $2(k^2 - q^2) = (2\mu - \Delta^2)$ (requirement for a complex $\lambda$, discussed in the last section), solutions of the form $\lambda \equiv iq + k$ are found in which

$$\begin{aligned} k &= \frac{1}{\sqrt{2}} \left( (\mu - \Delta^2/2) + \sqrt{\mu^2 - E^2} \right)^{\frac{1}{2}} \\ q &= \frac{1}{\sqrt{2}} \left( -(\mu - \Delta^2/2) + \sqrt{\mu^2 - E^2} \right)^{\frac{1}{2}} \end{aligned} \tag{3.12}$$

When combined with the constraint on the spinor degrees of freedom in Eq. (3.8), and the assumption that $|E| < |\mu|$, the general eigenfunction solution for the Hamiltonian in Eq. (3.5) can be constructed as the linear

combination $\phi(x) = \sum_{i=1}^{4} c_i \phi_i(x)$ such that

$$\begin{aligned} \phi_1(x) &= e^{i\lambda x} \begin{pmatrix} 1 \\ -q\alpha + ik\beta \end{pmatrix} \tilde{u}, \\ \phi_2(x) &= e^{-i\lambda x} \begin{pmatrix} 1 \\ q\alpha - ik\beta \end{pmatrix} \tilde{u}, \end{aligned} \tag{3.13}$$

with $\phi_3(x) = \phi_1^*(x)$ and $\phi_4(x) = \phi_2^*(x)$. The two energy dependent weight components $\alpha, \beta$ are defined as,

$$\alpha \equiv \frac{1}{\Delta}\left(1 + \sqrt{\frac{\mu + E}{\mu - E}}\right); \ \beta \equiv \frac{1}{\Delta}\left(1 - \sqrt{\frac{\mu + E}{\mu - E}}\right) \tag{3.14}$$

The energy $E$ can be found by constructing a matrix equation $\mathcal{A}X = 0$ such that $\mathcal{A}$ consists of the four wave functions $\phi_i(x)$ with the boundary conditions $\phi_{\tilde{u}}(x=0) = \phi_{\tilde{v}}(x=0) = \phi_{\tilde{u}}(x=L) = \phi_{\tilde{v}}(x=L) = 0$ applied, here $\phi_{\tilde{u}}, \phi_{\tilde{v}}$ are the spinor components of $\phi(x)$ and $X = (c_1, c_2, c_3, c_4)^T$. The existence of nontrivial solution for $X$ requires $\mathcal{D}et(\mathcal{A}) = 0$, which yields the transcendental equation

$$k|\beta| \sinh qL = q\alpha |\sin kL| \tag{3.15}$$

Because we are interested in the lowest energy modes such that $E \ll \mu$, Eq. (3.12) is expanded to first order in $E/\mu$, $q \approxeq q_F + \mathcal{O}(E^2)$ and $k \approxeq k_F + \mathcal{O}(E^2)$, resulting in

$$q_F = \Delta/2, \quad k_F = (\mu - (\Delta/2)^2)^{\frac{1}{2}} \tag{3.16}$$

Similar expansion of Eq. (3.14) yields

$$\frac{|\beta|}{|\alpha|} \approxeq \frac{E}{2\mu} \tag{3.17}$$

Combining Eqs. 3.16-3.17 with Eq. (3.15) and solving for $E$, we analytically find the exponentially protected ground state energy solution for a finite 1D $p$-wave superconducting nanowire

$$E \approxeq \frac{4\mu q_F}{k_F} e^{-q_F L} |\sin(k_F L)| + \mathcal{O}(e^{-3q_F L}) \tag{3.18}$$

Results following from Eq. (3.18) are plotted in Fig. 3.1 (dotted lines) and compared with those of a direct numerical diagonalization of the Hamiltonian in Eq. (3.5) (solid lines). Here we note that because $q$

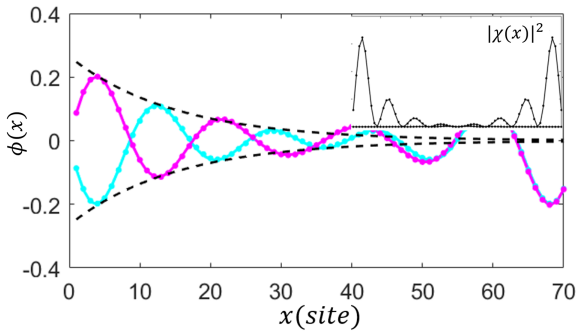


Figure 3.2: (Color online) Lowest energy wave functions $\phi_{\pm E}$ as defined in Eq. (3.19) and its counterpart by particle-hole transformation, for the lowest energy modes of a pure Kitaev chain in the topological regime ($\mu > 0$). The inset shows the corresponding MZMs as defined by Eq. (3.20). The dotted lines correspond to analytical results while the solid lines correspond to numerical simulation. The black dashed line shows the exponential decay envelope of the wave function which is proportional to $e^{-q_F L}$. Parameters used were $\Delta = t_0$, $t = 15t_0$, and $\mu = 2t_0$. In the topological phase the putative MZM wave functions are localized at the two ends of the chain as shown in the inset. No such near-zero-energy subgap state exists as low energy solution in the non-topological phase of the Kitaev chain *without* the quantum dot.

and $k$ shown in Eq. (3.12) are real, the above solution is valid for energy values which are not near the TQPT point, such that $0 \leq E^2 \leq \left(\mu\Delta^2 - \Delta^4/4\right)$, resulting in $\mu \geq \Delta^2/4$. The cyan line in Fig. 3.1(a)-(b) shows this critical value of the chemical potental $\mu$, above which the analytical and simulated results are in close agreement.

Because the Hamiltonian as shown in Eq. (3.6) is real, the non-degenerate eigenfunctions $\phi(x)$ associated with this Hamiltonian must be either purely real or purely imaginary, resulting in $c_{1,2} = \pm c_{3,4}$. In the limit $E \to 0$, the weight coefficients in Eq. (3.14) are $q\alpha \simeq 1$ and $\beta \simeq 0$, hence the spinor part for wavefunction $\phi(x)$ can be written as $(\tilde{u}, \tilde{v})^T = (1, -sign(q))^T$(the spinor term $\tilde{u}$ is incorporated into the normalization factor $c_1, c_2$, and $sign(q)$ is introduced considering of the $\pm\lambda$ in Eq. (3.13)). After applying the boundary conditions $\phi(0) = \phi(L) = 0$, solutions to the eigenvalue equation Eq. (3.6) can be found of the form,

$$\phi(x) = c_1 e^{-q_F x} \sin k_F x \begin{pmatrix} 1 \\ -sign(q) \end{pmatrix} + c_2 e^{q_F (x-L)} \sin\left(k_F (L-x)\right) \begin{pmatrix} 1 \\ sign(q) \end{pmatrix} \tag{3.19}$$

where $c_1$ and $c_2$ are normalization coefficients and $\sin\left(k_F (L-x)\right)$ is taken to satisfy the boundary condition at $x = L$. Because $k_F$ and $q_F$ in Eq. (3.19) are derived from $k$ and $q$ to first order in $E/\mu$ as seen in Eq. (3.16), the two terms in $\phi(x)$ will not simultaneously equal to zero at the boundaries $x = 0$ and $x = L$, but will

when the full expressions for $k$ and $q$ are used.

Due to the particle-hole symmetry ($\tau_x^\dagger \tilde{H}_{BdG}\tau_x = -\tilde{H}_{BdG}$) of the Hamiltonian in Eq. (3.6), if $\phi_E(x) = (u(x), v(x))^T$ is a solution to the BdG equation with energy $E$, then $\phi_{-E}(x) = (v^*(x), u^*(x))^T$ is also a solution with energy $-E$. From these solutions linear combinations of the form, $\chi_A = \frac{1}{\sqrt{2}}(\phi_E(x) + \phi_{-E}(x))$ and $\chi_B = \frac{i}{\sqrt{2}}(\phi_E(x) - \phi_{-E}(x))$, are constructed representing a pair of partially overlapping MBSs. The BdG states $\phi_{\pm E}(x)$ described in Eq. (3.19) are represented as a pair of partially overlapping MBSs of the form,

$$\begin{aligned} \chi_A &= \tilde{c}_1 e^{-q_F x} \sin k_F x \begin{pmatrix} i \\ -i \end{pmatrix} \\ \chi_B &= \tilde{c}_2 e^{q_F(x-L)} \sin\left(k_F(L-x)\right) \begin{pmatrix} 1 \\ 1 \end{pmatrix} \end{aligned} \tag{3.20}$$

where $\tilde{c}_1, \tilde{c}_2$ are the normalization coefficients. Though the Majorana wave functions $\chi_A, \chi_B$ defining bound states at the left and right ends are not exact eigenstates of the BdG Hamiltonian for the finite length Kitaev chain, they are useful in describing the interpolation of a low energy ABS into a pair of MBSs. Fig. 3.2 shows analytical results (dotted lines) based on Eq. (3.19), 3.20 in close agreement with numerical results (solid lines). The left and right MBSs $|\chi_{A/B}|^2$ are spatially protected due to exponential decay (black dashed lines) of the wave functions. Note the boundaries from analytical results now are modified to be consistent with that from numerical simulation, where the boundary condition for the first and last site in TBM is not well defined. We find no near-zero-energy subgap state as low energy solution in the non-topological phase of the Kitaev chain *without* the quantum dot.

## 3.4 Finite length Kitaev chain attached to a quantum dot

The one-dimensional finite length Kitaev chain with a quantum dot attached at the left end of the wire, schematically shown in Fig. 3.3(a), can be modeled with the Hamiltonian,

$$\tilde{H}_{BdG} = -\left(\partial_x^2 + \mu - V(x)\right)\tau_z - i\Delta(x)\,\partial_x \tau_y \tag{3.21}$$

for which $V(x) = V\Theta(x_0 - x)$ in which $V$ can be positive (representing a potential barrier) or negative (representing a potential well) and $\Delta(x) = \Delta\Theta(x - x_0 + \delta_x)$ in which $x_0$ is the length of the QD, and $\delta_x$ is

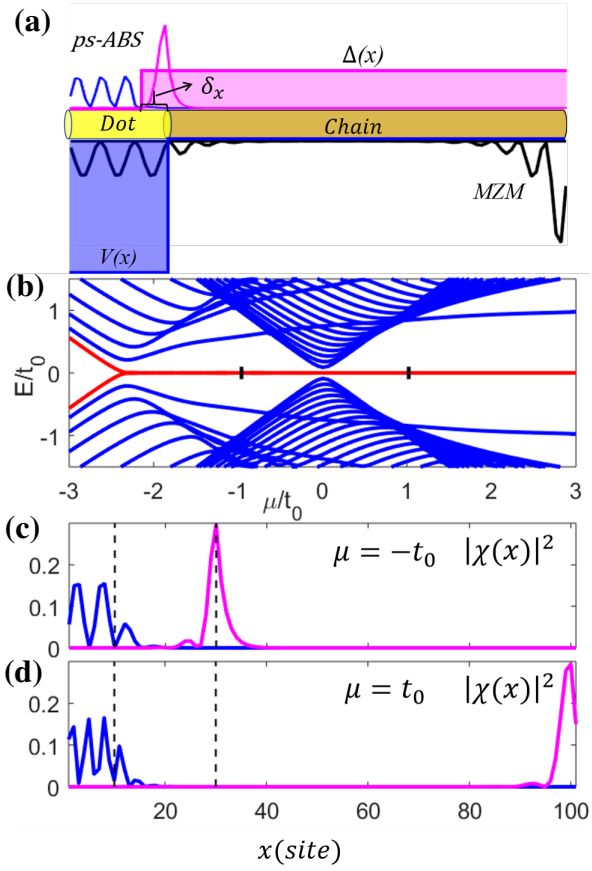


Figure 3.3: (Color online) (a) Schematic of a finite length Kitaev chain in which a fraction of the chain is not covered by the superconductor. This part of the chain (yellow) with vanishing superconducting pair potential $\Delta(x)$, and an effective electric potential $V(x)$ which may be induced by tunnel gates, is called a quantum dot. A proximitized region within the quantum dot (QD) with finite length $\delta_x$ is introduced. We also show the wave functions of the topological MZMs and the partially separated ABSs (in which the component MBSs are spatially separated over the length of the quantum dot), which are the generic lowest energy excitations in the topological and the non-topological phases of the Kitaev chain, respectively. (b) Numerically calculated spectrum of a specific finite length kitaev chain with a potential-well-like QD, where $V = -2.5t_0, \Delta = t_0, x_0 = 30$ , and $\delta_x = 20$ as defined in Eq. (3.21). The spectrum shows a robust near-zero-energy state even before the bulk gap closes around $\mu = 0$, which is present due to the potential-well like QD. The square of the amplitude of the wave functions at zero energy at $\mu = -t_0$ and $\mu = t_0$ (marked by black dots in 3(b)) are shown in (c) and (d), respectively. (c) shows the two component MBSs of the ps-ABS in the topologically trivial phase, while (d) shows the true MZMs in the topoloically non-trivial state that emerges after the bulk gap closing. The vertical black dashed lines in (c) and (d) indicate the boundaries at $x = x_0 - \delta x$ and $x = x_0$ respectively, indicating the spatial separation of the component MBSs of the ps-ABS.

the length of the proximitized region within the quantum dot (shown in Fig. 3.3(a)), caused by the adjacent superconductor. A numerical calculation for a specific model as schematically illustrated in Fig. 3.3(a) with $x_0 = 30, \delta_x = 20, V = -2.5t_0, \Delta = t_0$ is conducted first before we move to the analytical solutions. The numerical results are shown in Fig. 3.3(b), which illustrates the existence of a robust near-zero-energy state as the lowest energy solution even in the topologically trivial phase ($\mu < 0$). The square of the amplitude of the wave functions $|\chi(x)|^2$ of the lowest energy modes at $\mu = \mp t_0$ (marked as black dots in Fig. 3.3(b)) are the ps-ABS state and the MZM, respectively, shown in (c) and (d). In particular, the component MBSs of the ps-ABS are spatially separated by the length of the QD (separation marked by the black dashed lines in (c) and (d), with the right one at $x = x_0$ and the left one at $x = x_0 - \delta_x$). Next we will analytically solve the problem of a Kitaev chain coupled to a QD to understand the origin of the ps-ABS in the topologically trivial phase.

Looking for $E \to 0$ eigen-energy solutions for the Hamiltonian given in Eq. (3.21) we consider the eigenvalue equation given as Eq. (3.6). Uncoupling the near-zero-energy wave function solutions gives,

$$\left(-\partial_x^2 + \Delta(x)\partial_x - \mu + V\left(x\right) - E\right) f = 0 \tag{3.22a}$$

$$\left(-\partial_x^2 - \Delta(x)\partial_x - \mu + V\left(x\right) - E\right) g = 0 \tag{3.22b}$$

in which $f = u + v$ and $g = u - v$, where $u(x)$ and $v(x)$ are the spinor components of $\phi(x)$. The uncoupled equations in Eq. (3.22) are equivalently valid to the coupled BdG equation given by Eq. (3.6) in the near-zero-energy limit. In the limit that the proximitized region within the quantum dot goes to zero ($\delta_x \to 0$) solutions to Eq. (3.22) can be written as,

$$\begin{aligned} f(x) &= f_0(x)\Theta(x_0 - x) + f_1(x)\Theta(x - x_0) \\ g(x) &= g_0(x)\Theta(x_0 - x) + g_1(x)\Theta(x - x_0) \end{aligned} \tag{3.23}$$

where $f_0$ and $g_0$ represent the wave functions within the dot region and $f_1$ and $g_1$ are wave functions within the Kitaev-chain (the case $\delta_x \neq 0$ is discussed in Sec. 3.4.2). The Equations for $f(x)$ and $g(x)$ in Eq. (3.22) are identical except for a change in sign of the superconducting term $\Delta\left(x\right)$. Thus if a solution to $g\left(x\right)$ is found, the corresponding wavefunction $f\left(x\right)$ can be inferred using the relation $f\left(x\right) \propto g\left(-x + dx\right)$ in which $dx$ is a constant shift.

Below we first consider the case where the quantum dot has no proximitized region with non-zero superconducting pair potential adjacent to the SC interface, followed by the case where there is a slice of

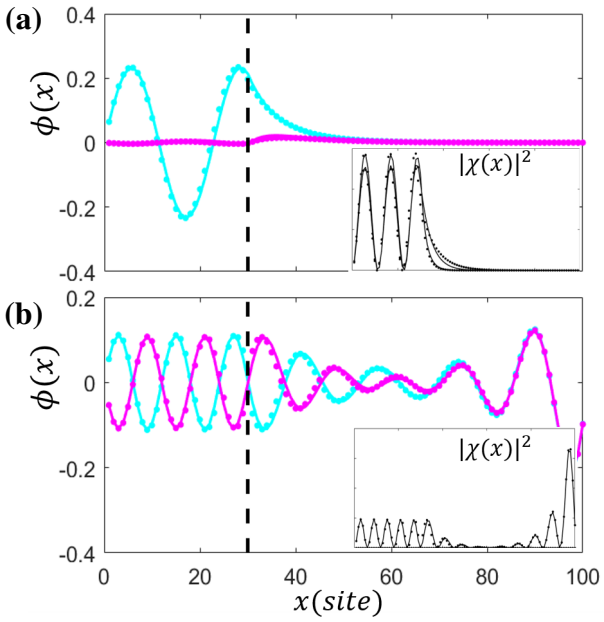


Figure 3.4: (Color online) Wave functions for the lowest energy modes of a QD-Kitaev chain without a proximitized region in the QD ($\delta_x = 0$ in Fig. 3.3) (a) corresponding to Eq. (3.24) for the topologically trivial regime with $\mu = -0.5t_0$, showing a pair of BdG wave functions $\phi_{\pm\varepsilon}$ in which the constituent MBSs are sitting directly on top of each other (see inset); and (b) corresponding to Eq. (3.26) for the topological regime with $\mu = 3.5t_0$ in which a pair of MZMs are separated by the length of the wire (see inset). The insets show the MBSs associated with the low energy BdG wave functions. The dotted lines show the analytical results while the solid lines are from numerical simulations. Because the constituent MBSs are strongly overlapping in (a), there is no robust near-zero-energy ABS in the topologically trivial phase in the absence of a proximitized region ($\delta_x = 0$) in the QD. The black dashed lines mark the QD-SC boundary at $x = x_0$. Parameters used were $V = -1.5t_0$, $\Delta = t_0$ and $t = 10t_0$.

proximitized region within the quantum dot of width $\delta_x$. From our analytical solutions we find that, in the absence of a proximitized region within the QD, there are no robust low energy ABS solutions in the topologically trivial phase, whereas topological MZMs do appear in the topological superconducting phase of Kitaev chain. The low energy partially separated ABSs, on the other hand, are the generic lowest energy solutions localized in the quantum dot in the presence of a slice of proximitized region of width $\delta_x$ adjacent to the SC interface.

### 3.4.1 No Proximity Coupling Within the QD

We first consider the case for which the length of the proximitized region within the QD is zero ($\delta_x = 0$). Assuming a topologically trivial state ($\mu < 0$) within the bulk of the Kitaev chain, and a potential well in the QD region ($V(x) < 0$) the effective chemical potential in the QD is $(\mu - V(x)) \gtrapprox 0$. Under

these conditions the solutions to the Eq. (3.22) for the entire QD-Kitaev chain can be written as

$$\begin{aligned} f_0(x) &= g_0(x) = c_0 \sin(k_0 x) \\ g_1(x) &= c_1(e^{(-\lambda_0+k_1)x} - e^{2k_1 L-(\lambda_0+k_1)x}) \\ f_1(x) &= c_1' \left(e^{(-\lambda_0+k_1)(2L-x)} - e^{(k_1+\lambda_0)x-2\lambda_0 L}\right) \end{aligned} \tag{3.24}$$

with $k_0 \equiv \sqrt{|\mu - V + E|}$, $k_1 \equiv \sqrt{(\Delta/2)^2 - (\mu + E)}$, and $\lambda_0 = q_F$ (defined from Eq. (3.22)). Here the wave vector $k_1$ appearing in the definition of $f_1$ and $g_1$ in Eq. (3.24) describes the topologically trivial state within the Kitaev chain, and thus is not the same as $k$ previously defined for the topological state in Eq. (3.12). For a potential barrier within the QD region $(\mu - V(x) < 0)$ as opposed to a quantum well $(\mu - V(x) > 0)$ the $\sin(k_0 x)$ term as defined in Eq. (3.24) can be replaced by $\sinh(k_0 x)$. The coefficients $c_0$, $c_1$, and $c_1'$ are found by applying the boundary conditions $g_0(x)|_{x_0} = g_1(x)|_{x_0}$, $f_0(x)|_{x_0} = f_1(x)|_{x_0}$, $g_0'(x)|_{x_0} = g_1'(x)|_{x_0}$, and $f_0'(x)|_{x_0} = f_1'(x)|_{x_0}$ resulting in the energy dependent transcendental equations,

$$\begin{aligned} \lambda_0 &= -k_0 \cot k_0 x - k_1 \coth k_1 (L - x_0) \\ \lambda_0 &= k_0 \cot k_0 x + k_1 \coth k_1 (L - x_0) \end{aligned} \tag{3.25}$$

through which the lowest energy $E$ can be found numerically. Note two solutions for E could be found from Eq. (3.25), and we take the lower one as the eigen energy $E$ (actually these two solutions for $E$ are giving an approximately equal value for $k_0, k_1$). Once we know eigen energy $E$, $k_0, k_1$ could be derived, so are the wave functions in Eq. (3.24). For the case in which the Kitaev chain is in the topological phase ($\mu > 0$), wave functions of the form

$$\begin{aligned} f_0(x) &= g_0(x) = a_0 \sin(k_0 x) \\ g_1(x) &= a e^{-q_F(x-x_0)} \sin(k_F(x - L)) \\ f_1(x) &= a' e^{-q_F(L-x)} \sin(k_F(L - x)) \end{aligned} \tag{3.26}$$

can be found, where $a_0$, $a$, and $a'$ are normalization factors. Note wave functions like Eq. (3.19) are used for the topological chain here. The $\sin(k_0 x)$ term within the dot region can again be replaced with $\sinh(k_0 x)$ for values of the chemical potential such that $(\mu - V) < 0$. The wavefunction within the Kitaev chain is expected to be of the same format as that of the pure Kitaev chain in topological phase. Matching the

boundary conditions at $x = x_0$ for $g_0, g_1$ and $f_0, f_1$ respectively gives

$$\begin{aligned} k_0 \cot(k_0 x_0) &= -q_F + k_F \cot(k_F(x_0 - L)) \\ k_0 \cot(k_0 x_0) &= q_F - k_F \cot(k_F(L - x_0)) \end{aligned} \tag{3.27}$$

The above two equations are effectively equivalent for $q_F \ll k_F \cot(k_F(L - x_0))$. Similarly we can take the lower energy solution from Eq. (3.27) as the eigen energy $E$, and then the wave functions given in Eq. (3.26) could be derived. Analytical solutions for the topologically trivial (Eq. (3.24)) and topological (Eq. (3.26)) lowest energy wave functions of a finite QD-Kitaev chian are shown in Fig. 3.4 (dotted lines) to be in close agreement with numerical results (solid lines). The sinusoidal wave within the dot region and the exponentially decaying wave over the Kitaev chain are shown in Fig. 3.4(b) with the black dashed line marking the boundary between the QD and the Kitaev chain. In Fig. 3.4(a) inset, the constituent MBSs are sitting directly on top of each other, resulting in the absence of a robust near-zero-energy ABS in the topologically trivial phase of the Kitaev chain with no proximitized region in the QD ($\delta_x = 0$ in Fig. 3.3).

### 3.4.2 Finite Proximitized Region Within the QD

Now we consider the case in which a finite proximitized region forms within the quantum dot adjacent to the SC interface ($\delta_x > 0$). In this case, the solutions to $\tilde{H}_{BdG}\phi(x) = E\phi(x)$, associated with Eq. (3.21) are found by dividing the QD-Kitaev chain system into three regions as shown in Fig. 3.3: a pure quantum dot ($\Delta = 0, V \neq 0$), a finite proximitized region within the QD located near the QD-SC boundary ($\Delta \neq 0, V \neq 0$), and a finite length Kitaev chain ($\Delta \neq 0, V = 0$). As before we assume that the chemical potential $\mu$ within the bulk of the Kitaev chain is $\mu \lessapprox 0$ such that the chain is in the topologically trivial phase. We also assume a potential well ($V(x) < 0$) within the QD region. It follows that the effective chemical potential within the proximitized region of the QD satisfies $\tilde{\mu} \equiv (\mu - V(x)) \gtrapprox 0$. Under these conditions we will use a sinusoidal wave function $g_0(x)$ in the region covered by the pure QD, the wave function given in Eq. (3.19) for the proximitized region within the QD (call it $g_p(x)$, with "$p$" indicating solution valid in the proximitized region), and the wave function $g_1(x)$ appropriate for topologically trivial phase within the Kitaev chain,

$$g(x) = \begin{cases} a_0 \sin(k_0 x), & (g_0(x)) \\ a_p e^{-\lambda_0 x} \sin(k_p x + \delta\phi), & (g_p(x)) \\ a_1 (e^{(-\lambda_0 + k_1)x} - e^{2k_1 L - (\lambda_0 + k_1)x}), & (g_1(x)) \end{cases} \tag{3.28}$$

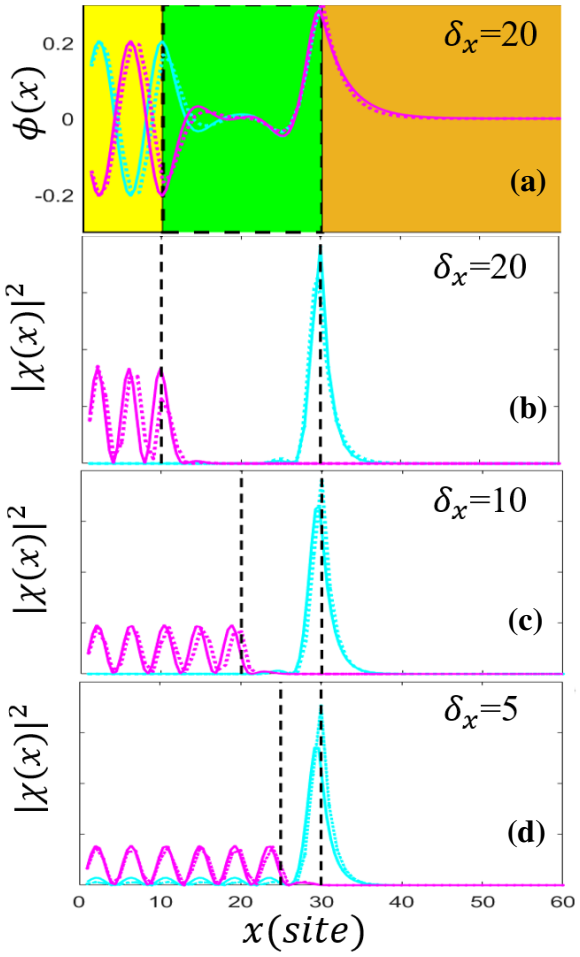


Figure 3.5: (Color online) Wave functions for the lowest energy mode of a Kitaev chain coupled to a QD where the QD contains a proximitized region of finite length $\delta_x$ (see Fig. 3.3)). (a) Wave functions for the lowest energy modes within the bare QD (yellow), the proximitized part of the QD (green), and the bulk Kitaev chian (orange), plotted using analytical results based on Eq. (3.28) (dotted lines) and direct numerical solutions using a tight binding Hamiltonian (solid lines). Here, the parameters are such that the proximitized region of the QD satisfies $\mu - V > 0$, with $V = -2.5t_0$, while the Kitaev chain is topologically trivial with $\mu = -1.25t_0$. (b)-(d) Spatial profiles of the component pair of MBSs of a partially separated ABS for the proximitized regions of various lengths $\delta_x$. (b) shows the MBSs corresponding to the wave functions in (a). Samples are taken for values corresponding to the crossed diamonds in Fig. 3.6(c). The MBSs are separated on the order of the length of the proximitized region $\delta_x$ within the QD, marked by the black dotted lines. The figures illustrate that the ps-ABSs form essentially because the proximitized region in the QD satisfies the effective chemical potential $\tilde{\mu} > 0$, partially decoupling the ABS into a pair component MBSs, which are then spatially separated by the width of the proximitized region. Here the dot length is $x_0 = 30$, the total length of the QD-Kitaev chain is $L = 100$, the hopping energy is $t = 2.5t_0$, and superconducting pairing potential is $\Delta = t_0$.

in which $a_0$, $a_p$, and $a_1$ are normalization factors, $k_p = \sqrt{(\mu + E - V) - (\Delta/2)^2}$ and $k_0$, $k_1$, $\lambda_0$ are as defined earlier. A phase factor $\delta\phi$ is introduced for $g_p(x)$ because there are no fixed boundary values for the region $x \in [(x_0 - \delta_x), x_0]$. Matching the boundary conditions at $x = x_0 - \delta_x$ for $g_0(x)$ and $g_p(x)$ and at $x = x_0$ for $g_p(x)$ and $g_1(x)$ will result in a pair of energy dependent transcendental equations given as Eq.3.29 which can be solved numerically for $E$ and $\delta\phi$.

$$\begin{aligned} \lambda_0 + k_0 \cot(k_0(x_0 - \delta_x)) &= k_p \cot(k_p(x_0 - \delta_x) + \delta\phi) \\ k_p \cot(k_p x_0 + \delta\phi) &= -k_1 \coth(k_1(L - x_0)) \end{aligned} \tag{3.29}$$

Once the eigen energy $E$ is know, wave vectors $k_0, k_p, k_1$ could be derived as well. The coefficients $(a_0, a_p, a_1)$ for the wave functions in Eq. (3.28) are then found by substituting the values $E, \delta\phi$ back into the boundary value equations. The term $e^{-\lambda_0 x}\sin(k_p x + \delta\phi)$ for the proximitized region will show a pair of spatially separated MBSs which are separated by the length of the proximitized region forming inside the QD.

The lowest energy BdG wave functions based on Eq. (3.28), shown in Fig. 3.5(a), illustrate the critical importance of the proximitized region within the QD. When the effective chemical potential within the proximitized region $\tilde{\mu} \gtrapprox 0$, the solution given in Eq. (3.19) is used, implying the formation of a pair of MBSs at the boundaries of the proximitized region. One of this pair of component Majorana bound states can "leak" into the normal part of the QD, while the other bound state remains localized within the QD, effectively separating the MBSs [98, 99]. When the MBSs are separated on the order of the characteristic energy decay length $\zeta \propto q_F^{-1}$ (as defined in Eq. (3.18)) they form a ps-ABS [88, 94] as shown in Fig. 3.5(b)–(d) (where only the first 60 sites of the QD-chain is shown). We now define the overlap between the pair of component MBSs in terms of spatial integral of the product of the absolute values of the wave functions, $\langle\phi_L|\phi_R\rangle = \int dx|\phi_L||\phi_R|$. Plotting this overlap $\langle\phi_L|\phi_R\rangle$ as a function of the length of the proximitized region $\delta_x$ as in Fig. 3.6 shows that if $\delta_x = 0$, as shown in Fig. 3.6(a), there is a strong overlap (in red) throughout the topologically trivial region ($\mu < 0$), signaling the presence of an ABS comprised of a pair of strongly overlapping MBS. On the other hand a proximitized region of finite length $\delta_x \gtrapprox 5$ within the QD allows for the formation of a robust low overlap (in blue) region, even in the topologically trivial regime, signaling the presence of a ps-ABS. As the length of the proximitized region $\delta_x$ increases, the overlap between the left and right MBSs comprising a ps-ABS decreases exponentially (Fig. 3.6(c)) even when the bulk of the Kitaev chain is in the topologically trivial regime.

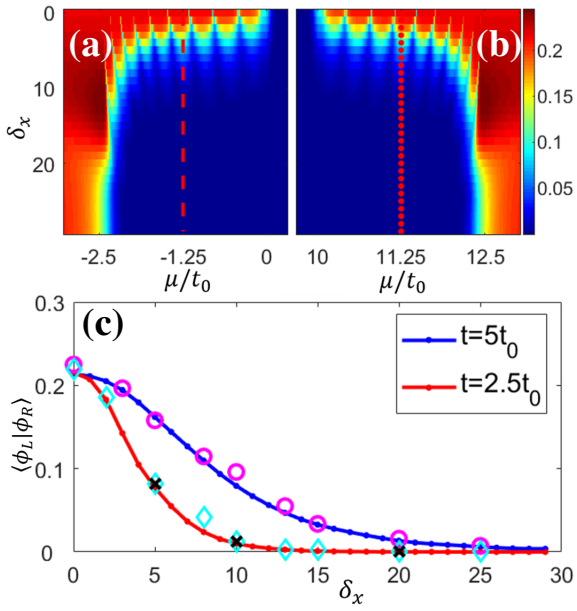


Figure 3.6: (Color online) Overlap between the left and right MBSs $\langle\phi_L|\phi_R\rangle$ of a partially separated ABS, as a function of the width of the proximitized region $\delta_x$ within the QD, and chemical potential $\mu$, for a potential well (a) and a potential barrier (b) in the QD region. Since the mechanism for the formation of the ps-ABS involves the effective chemical potential ($\tilde{\mu} = \mu - V$) in the proximitized part of the QD being in the topological regime, the potential well in the QD region ($V < 0$) works for the bare $\mu < 0$, while the potential barrier in the QD region works for the bare $\mu > 4t$. As the length of the proximitized region $\delta_x$ within the QD approaches zero, the overlap between the left and right MBSs dramatically increases (red). For finite values of the length of the proximitized region $\delta_x \geq 5$ minimal overlap between the left and right MBSs (blue) can be seen within the topologically trivial regime, $\mu \in \{-2.5t_0, 0\}$ (a) and $\mu \in \{10t_0, 12.5t_0\}$ (b) supporting the presence of ps-ABSs. Here $\delta_x = 30$, $L = 100$, and $t = |V| = 2.5t_0$. (c) Overlap between the left and right MBSs as a function of the length of the proximitized region within the dot. The red line corresponds with vertical line cuts taken from (a)(dotted red) and (b)(solid red), and the blue line represents identical values with decreased hopping energy $t$. The cyan diamonds and the magenta circles represent the analytical results. The wave modes for the three black crossed diamonds are given in Fig. 3.5

For a partially proximitized QD of length $x_0 = 30$ attached to a Kitaev chain of length $\delta_L$, in which the effective potential within the proximitized region of the dot is $\tilde{\mu} \gtrapprox 0$ and the Kitaev chain is topologically trivial, the overlap between the left and right MBSs $\langle\phi_L|\phi_R\rangle$ decreases with increasing length of the Kitaev chain $\delta_L$, due to a portion of one of the component MBS leaking into the Kitaev chain. Fig. 3.7 shows results for a partially proximitized ($0 < \delta_x < x_0$) QD of length $x_0 = 30$ attached to a Kitaev chain of length $\delta_L$, in which the effective potential within the proximitized region of the dot is $\tilde{\mu} \gtrapprox 0$ and the Kitaev chain is topologically trivial ($\mu < 0$). As shown in Fig. 3.7(a), the overlap $\langle\phi_L|\phi_R\rangle$ decreases with increasing length of the Kitaev chain $\delta_L$, owing to the fact that one of the component MBS of the ps-ABS can relax into the topologically trivial Kitaev chain. In Fig. 3.7(a) three different $\delta L$ for $t = 5t_0$ and $x_0 = 30$

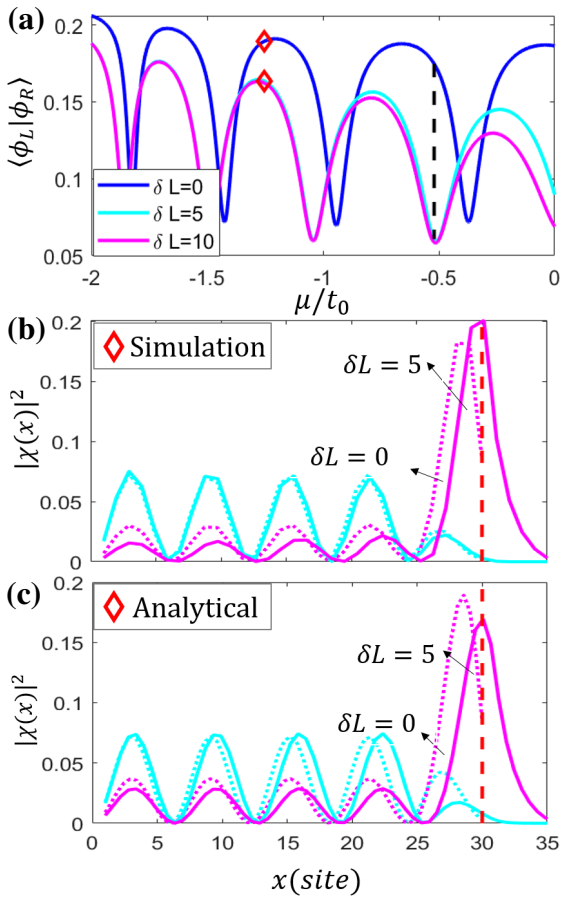


Figure 3.7: (Color online)(a) Overlap of the left and right MBSs $\langle\phi_L|\phi_R\rangle$ of a partially separated ABS as a function of chemical potential $\mu$ for a Kitaev chain of varying length $\delta_L$ coupled to a QD which with a finite proximitized region of length $\delta_x = 5$. Increasing the length of the Kitaev chain $\delta_L$ decreases the overlap between the left and right modes. The overlap value $0.1748$ is significantly reduced to $0.06$ for $\mu$ marked by the black dashed line. (b)-(c) Majorana wave functions for the lowest energy modes of a QD-Kitaev chain associated with red diamonds in (a) for numerical simulation (b) and analytical results based on Eq. (3.26c). Significant portions of the mode distribution leak into the Kitaev chain region $\delta_L$, reducing the overlap between the left and right modes, increasing the robustness of the ps-ABS. Here $t = 5t_0, x_0 = 30, \Delta = t_0, V = -2.5t_0$ were used.

are analyzed, showing a reduction in overlap between the left and right MBSs comprising a ps-ABS with increasing length of $\delta L$. The oscillation of $\langle\phi_L|\phi_R\rangle$ with $\mu$ can be attributed to the oscillation of the wave functions ($\sim \sin(k_F x)$) when the boundary conditions are matched at $x = (x_0 - \delta_x)$ and $x = x_0$. The reduction in overlap between the left and right MBSs is less prevalent between $\delta L = 5$ and $\delta L = 10$ than between $\delta L = 0$ and $\delta L = 5$, signaling that only the part of the Kitaev chain adjacent to the QD-Kitaev chain interface controls the relaxation of the MBS, and the progressive decrease of the wave function overlap in the ps-ABS, as expected. Analytical results for the square of the absolute values of the MBSs associated with the red diamonds in Fig. 3.7(a) are shown and compared to numerical simulation in Fig. 3.7(b)–(c), where a significant fraction of the probability density is shown to leak into the superconducting region of the Kitaev chain. This leads to a lower overlap between the left and right MBSs, decreasing the amplitudes of the splitting oscillations in ps-ABS compared to those for topological MZMs for an equivalent bare (without the quantum dot) Kitaev chain of length $x_0$, as shown in Fig. 3.8.

## 3.5 Discussion and conclusion

In this paper, we have analytically solved the problem of a finite-length Kitaev chain coupled to a quantum dot. This problem, in addition to being a valuable extension of the classic Kitaev chain problem, is an effective representation of a system investigated in recent Majorana experiments: a spin-orbit coupled quandum dot-semiconductor-superconductor hybrid nanowire in the presence of a Zeeman field. Here, the quantum dot is defined by a portion of the SM wire not covered by the epitaxial SC, which can be under an electric potential controlled using external gates. In this paper we take the QD potential as a step-like potential well, as shown in Fig. 3.3(a). The assumption of a step-like potential well in the quantum dot region produces an effective potential profile that is manifestly different from the smooth confinement potential at the end of the SM-SC system as considered in Ref. [75]. Specifically, while the pair of component MBSs that constitute a robust near-zero-energy ABS in the presence of smooth confinement potential [75] originate from two *different* spin channels of a confinement-induced sub-band [100], in the case of a potential well in the QD region, the component MBSs originate from the *same* spin channel as shown in Fig. 3.9(c). The simulation results based on the experimental QD-SM-SC heterostructure with a potential-well like QD are shown in Fig. 3.9. The spectrum shows a robust near-zero-energy state in the topologically trivial phase for values of the magnetic field smaller than the critical field $B_c$ required for a topological quantum phase transition ($B_c = \sqrt{\mu^2 + \Delta_0^2}$, with $\mu = -4t_0, \Delta_0 = t_0$). The square of the amplitude of the wave functions

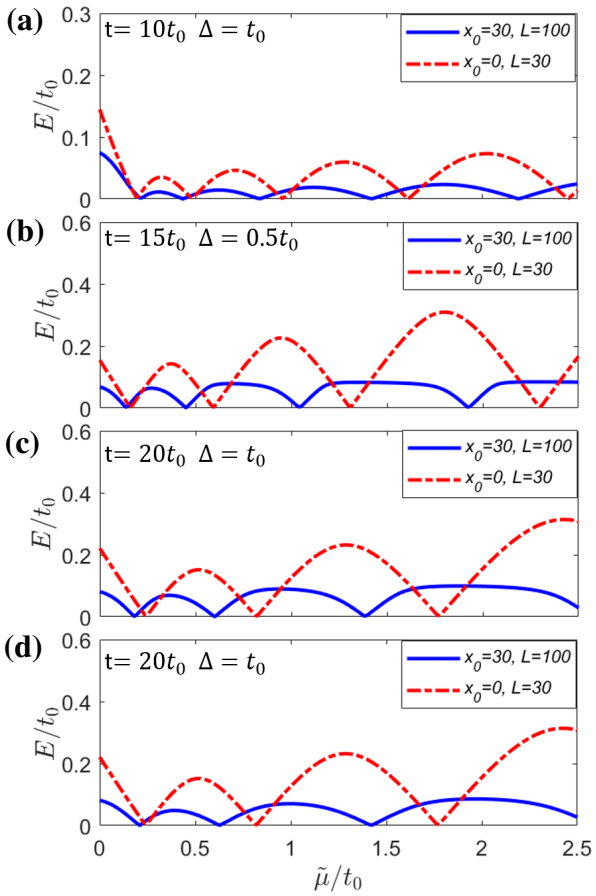


Figure 3.8: (Color online) Lowest energy eigenvalues plotted with effective chemical potential for a Kitaev chain with QD in the topologically trivial phase (solid blue) and bare Kitaev chain of length equal to the QD in the topological phase (dashed red) with different parameters $t, \Delta$, and the length of the proximitized region $\delta_x$. The parameters $x_0 = 30, L = 100$ indicate a dot-chain system with a total length of 100 sites attached to a QD with 30 sites with the effective chemical potential in the QD $\tilde{\mu} = \mu - V$. The parameters $x_0 = 0, L = 30$ indicate a bare Kitaev chain of length 30 sites (and no QD), with the effective chemical potential $\tilde{\mu} = \mu$ ($V = 0$ in the bare chain). We fix $\mu = -0.05t_0$ for the dot-chain system and vary the dot potential $V$ in a range such as $\tilde{\mu} > 0$ within the QD, which varies within the same range as that for the bare Kitaev chain. The lowest energy in the topologically trivial ($\mu < 0$) dot-chain system (i.e., the ps-ABS) shows a significantly suppressed energy splitting as compared to that of the topological ($\tilde{\mu} = \mu > 0$) Kitaev chain of length $x_0$. We have length of the proximitized region $\delta_x = 10$ in (a)-(c), and $\delta_x = 30$ in (d). Parameters $t, \Delta$ are as given.

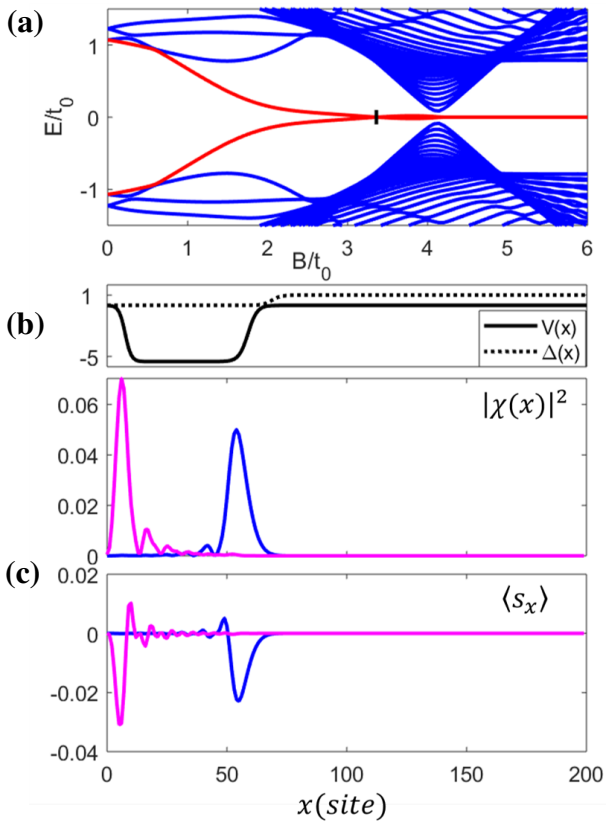


Figure 3.9: (Color online) (a) Energy spectrum for an experimental SM-SC heterostructure attached to a potential well-like QD ($V(x) \leq 0$) where the QD potential and SC pairing potential are given schematically in the top panel in(b) with potential depth $|V(x)_{min}| = 5.5t_0$, and $\mu = -4t_0, \Delta_0 = t_0$. For these parameters the critical phase transition point is $B_c \sim |\mu| = 4t_0$, where the bulk gap closes signifying a topological transition. As can be seen, in the presence of the QD, a robust near-zero-energy state is also present in the topologically trivial phase, i.e., for $B < B_c$. The spatial profile for the amplitude of the square of the wave function at $\mu = 3.4t_0$ is shown in the bottom panel in (b), where we have the two MBS components of a ps-ABS state, separated by the QD size $x_0 \sim 50$. The spin density profile $\langle s_x \rangle$ for the ps-ABS state is plotted in (c), where we see that the two MBS components are characterized by the same spin polarization, i.e., the spin polarizations are mainly in the negative $s_x$ direction in both cases. Here length L=200 sites.

of the component MBSs corresponding to this topologically trivial state for $B = 3.4t_0$ (marked as a black dot in Fig. 3.9 (a)) are plotted in Fig. 3.9 (b). The spin polarization profile of a BdG state could be defined as $\langle s_\nu(x)\rangle = \frac{1}{2}\sum_{s,s'} u_s^*(x)[\sigma_\nu]_{ss'}u(x)_{s'}$, where $u(x)$ is the electron component in the BdG basis, $\nu$ is the $x, y, z$ spin component, $\sigma_\nu$ is the corresponding Pauli matrix [100, 101]. The spin polarizations $\langle s_x\rangle$ of the component MBSs of the ABS for $B = 3.4t_0$ are shown in Fig. 3.9(c). It is clear that the two MBS components of a ps-ABS nucleated in a step-like potential well have the same spin polarization, i.e., the QD-SM-SC hybrid structure with a potential-well like QD supports a ps-ABS state coming from the same spin channel. Consequently, while the topological properties of the QD-SM-SC hybrid structure with local step-like dot potential well can be understood using an effective representation in terms of a Kitaev chain (which has a single spin channel) coupled to a QD, as discussed in the present work, the SM-SC heterostructure with a smooth confinement potential [75] cannot be analyzed within such a representation.

Our key analytical result for the Kitaev chain coupled to a QD is demonstrating the existence of a robust near-zero-energy ABS (localized in the QD region) in the topologically trivial phase ($\mu < 0$) of the Kitaev chain. By contrast, topological near-zero-energy MZMs separated by the chain length $L$ are the lowest energy excitations in the topological superconducting phase ($\mu > 0$) of the Kitaev chain. Our analysis reveals the crucial importance of a slice of the QD being proximitized, which may correspond in the experiments to the potential barrier slightly penetrating into the region covered by the SC. We show that only in the presence of such a slice of proximitized region in the QD, the eigenvalue equation and the boundary conditions admit a robust, near-zero-energy, subgap ABS in the topologically trivial phase of the Kitaev chain. Furthermore, the component pair of MBSs of this topologically trivial ABS are spatially separated by the width of the proximitized part of the QD, leading to the so-called partially separated ABSs (ps-ABS) and the resultant robustness to local perturbations of the zero bias conductance peaks in tunneling measurements [94], as seen in the experiments [64]. For a meaningful comparison with experiment, the properties of the proximitized region (namely, its width and the position-dependence of the induced gap) should be determined by a self-consistent solution of a spinful interacting model of the semiconductor-superconductor nanowire heterostructure coupled to a quantum dot, which is left for future work. On the other hand, performing such a study in the context of the effective model consisting of a spinless Kitaev chain coupled to a quantum dot is not expected to generate experimentally-significant results and is beyond the scope of the present work.

The analytical calculations also reveal that the ps-ABSs appear whenever the effective chemical potential in the proximitized part of the QD $\tilde{\mu} = \mu - V \gtrapprox 0$, allowing the partial decoupling of the component MBSs and nucleating a ps-ABS in the QD, even though the bulk of the Kitaev chain may be in the trivial

phase $\mu < 0$. In the present case, this requires a potential well $V < 0$ in the QD near the Kitaev chain TQPT at $\mu = 0$. Near the Kitaev chain TQPT at $\mu = 4t$, the conditions $\tilde{\mu} = \mu - V \lessapprox 4t$ and $\mu > 4t$ in the bulk of the chain require the presence of a potential barrier ($V > 0$) at the QD. In the analogous spin-full problem of the QD-SM-SC heterostructure the nucleation of a ps-ABS in the proximitized part of the QD can take place in the presence of either a potential well ($V < 0$), or a potential barrier ($V > 0$), but the separation of the component MBSs (hence, the robustness of the ps-ABS) is typically stronger for $V > 0$.[88, 94]. Finally, we also find the important result that the energy splittings in the ps-ABS are significantly suppressed than the energy splittings expected in a bare topological segment of equivalent length (typically, the size of the QD), because the component MBS of a ps-ABS localized near the QD-SC interface can relax into the adjacent Kitaev chain which is in the topologically trivial phase.

# Chapter 4

# Feasibility of measurement-based braiding in the quasi-Majorana regime in semiconductor-superconductor heterostructures

We discuss the feasibility of measurement-based braiding in semiconductor-superconductor (SM-SC) heterostructures in the so-called quasi-Majorana regime $-$ the regime of parameters where the robust zero-bias conductance peaks (ZBCPs) in charge tunneling experiments are due to partially-separated Andreev bound states (ps-ABSs, low energy Andreev bound states in which the component Majorana bound states (MBSs) are separated by a length scale $L^* \lesssim \zeta$ with $\zeta$ the SC coherence length), rather than due to topological Majorana zero modes (MZMs, separated by the length of the wire $\sim L$). In this regime, the ZBCPs may appear to be robust to various perturbations as long as the energy splittings of the ps-ABSs are less than the typical peak width, $\varepsilon_w$, of low-energy conductance peaks ($\varepsilon_w \sim 10 - 20\ \mu eV$). However, the feasibility of measurement-based braiding crucially depends on a different, much smaller, energy scale $\varepsilon_m$ ($\varepsilon_m \sim 0.1\ \mu eV$), given by the typical fermion parity-dependent ground state energy shift due to virtual electron transfer between the SM-SC system in the presence of charging energy and a quantum dot, measurable in a transmon-type measurement, which reveals the fermion parity of a pair of MZMs.

## 4.1 Introduction

Fault-tolerant quantum computation requires the qubits to be protected from quantum errors. Due to their non-Abelian topological properties, Majorana zero modes (MZMs) have been proposed as the ideal qubits for topological quantum computation (TQC) [6, 102, 16]. Non-local encoding of the spatially separated MZMs allows the storing and processing of the quantum information immune to any local perturbations.

Spin-orbit coupled semiconductor nanowires with proximity induced superconductivity were predicted theoretically to support MZMs in the presence of a Zeeman field [13, 48, 46, 14, 47, 15, 49]. In this platform, MZMs arise as the zero-energy excitations localized at the opposite ends of the nanowire. Braiding Majoranas could be possibly implemented by tuning the gate voltage of junctions in the superconducting nonawire networks [20, 103, 104, 105, 106, 107]. Because of this significant advantage, tremendous experimental progress has been made over the past few years in realizing topological MZMs in the one-dimensional SM-SC heterostructures [56, 53, 55, 54, 60, 59, 62, 61, 64]. The most recent significant development involves the observation of the quantized-plateau of height $2e^2/h$ of the ZBCPs in the local charge tunneling experiments of a single topological nanowire [64]. In other recent works [94, 87, 108, 88, 101], however, this experimentally observed strong signature of topological MZMs have been shown to be possible even in a topologically trivial system due to the presence of the so-called partially-separated Andreev bound states (ps-ABSs) or quasi-Majoranas [88]. Therefore, gate-controlled braiding or physically moving the MZMs on the junction-based networks cannot support TQC because the ps-ABSs, which mimic most of the behaviors of topological MZMs in local charge tunneling experiments, do not obey non-Abelian statistics.

In contrast to gate-controlled braiding, measurement-based braiding consists of a sequence of projective parity measurements of a group of MZMs that has the same effect as a braiding operation without actual physical movement of the Majorana fermions [109, 110, 111, 112, 22]. In the measurement-based braiding scheme, quantum information processing could be realized by joint parity measurement of pairs and quartets of MZMs in the Coulomb-blockade regime. By coupling to the probing quantum dots, the ground state energy is shifted and become fermion parity-dependent, which can be read out by suitable energy level spectroscopy. Compared to the braiding with the junctions by manipulating the Majroanas physically, the measurement-based braiding can avoid the possible engineering issues in the fabrications and implementations, and also get rid of the possible thermal errors from the environment [21]. It has been argued in Ref. [90] that the measurement-based braiding scheme even works in the quasi-Majorana (ps-ABSs) regime, because of the exponentially different couplings of the component Majorana bound states (MBSs) of the ps-ABSs to

the external quantum dot. However, in light of the non-topological nature of the quasi-Majoranas (because they appear in the topologically trivial regime, and occur, essentially, on the same side of the wire), a discussion of how sensitive the quasi-Majoranas are to the local perturbations is indispensable for considering their utility in measurement-based braiding.

In the measurement-based braiding scheme, the ability to perform the projective parity measurements rests with non-local couplings to at least a pair of MZMs, instead of coupling to a single one [22, 24]. In this scheme, a quantum dot is coupled to multiple MZMs in a SC island with charging energy. In the presence of charging energy, the virtual transfer of electrons between the island and the quantum dot introduces an energy shift of the island-QD system, which is dependent on the fermion parity of the MZMs. By measuring this ground state energy shift via the frequency shift in a transmon-type measurement, the fermion parity of the MZM system can be identified. Since It can be shown that a sequence of parity measurements of a group of MZMs is equivalent to an effective braiding operation, this process realizes braiding without actually moving the MZMs physically. It is important to emphasize that the parity-dependent energy splittings of the ground state of the MZM island due to virtual electron transfers in the Coulomb blockade regime are required to satisfy the readout condition, i.e, the corresponding frequency shift should fall within the range of the sensitivity of the transmon-type measurements [25, 113, 24]. Therefore, the feasibility of measurement-based braiding through the projective parity measurements crucially depends on the robustness of the energy splittings of the MZM system under consideration.

It has been shown recently that ps-ABSs are quite generic in SM-SC heterostructures and can produce ZBCPs in local charge tunneling experiments which are robust to various perturbations giving rise to quantized conductance plateaus similar to toplogical MZMs [87, 94, 108, 88]. Despite the apparent robustness of the ZBCPs in charge tunneling experiments, the ps-ABSs (or quasi-Majoranas) themselves are not topologically protected. Various local perturbations may produce energy splittings in the low energy spectrum of the ps-ABSs which are sufficient to invalidate measurement-based braiding, in spite of not showing up as splitting of the zero bias peaks in tunneling conductance experiments. For instance, energy splittings induced by perturbations which are less than $\varepsilon_w \sim 10 - 20\ \mu eV$ may be consistent with robust ZBCPs (which typically has the full-width at half maximum comparable to $\sim \varepsilon_w$), but may severely limit the feasibility of measurement-based braiding because the energy scale $\varepsilon_w \gg \varepsilon_m \sim 0.1\ \mu eV$, where $\varepsilon_m$ is the typical fermion parity-dependent energy shift of the SC island due to coupling to external dot which is measured as frequency shifts in transmon type measurements. In this paper we explicitly test the stability of the ps-ABSs in the presence of local perturbations in spin-orbit coupling, Zeeman field, and confinement potential etc. By

comparing with the response of the topological MZMs to similar perturbations, we show that the ps-ABSs are very sensitive to the local perturbations, especially near the region of overlap of the component MBS wave functions. By considering the local deformations described by Eqs. (4.5, 4.6, 4.7) to a system given in Eq. (4.1), we show that the energy splittings of the near-zero energy quasi-Majorana states in the topologically trivial regime can be explicitly lifted to values higher than $\varepsilon_m$, invalidating topologically protected measurement-based braiding, even if such energy splittings can be smaller than the much larger energy scale of ZBCP peak widths $\sim \varepsilon_w$, which may explain the robustness of the quantized conductance plateau due to the ps-ABSs.

The remainder of the article is organized as follows: In Sec. 4.2 we briefly describe the basic idea behind measurement-based braiding. In Sec. 4.3 we introduce the model Hamiltonian (Eq. (4.1)) for the SM-SC heterostructures that host the topological MZMs as well as the topologically trivial ps-ASBs. We also discuss the effects on the ps-ASBs from the confinement potential, effective mass, and spin-orbit coupling strength. In Sec. 4.4, we introduce three different local perturbations in the real system with or without measurement, namely, the deformation in spin-orbit coupling (Eq. (4.5)), Zeeman potential (Eq. (4.6)) and deformation in the confinement potential (Eq. (4.7)). We discuss the stability of the ps-ABSs under the effect of each of these perturbations. Additionally, we also test the susceptibilities to the local perturbations of the topologically trivial ps-ABSs and the topologically non-trivial MZMs. We end in Sec. 4.5 with a discussion and summary of our conclusions.

## 4.2 Measurement-based braiding

In the Coulomb-blockade regime, a finite charging energy can exponentially suppress the quasiparticle exitations from outside the superconducting island. This renders the topological superconductor fermion parity-protected (charge does not change during the process of measurement). The parity of any two MZMs are represented by the eigenvalue of $P_{jk} = i\gamma_j\gamma_k$, and a braiding process for exchanging $\gamma_1$ and $\gamma_2$ could be realized by the operator $P_B(1 \leftrightarrow 2) = (1 + \gamma_1\gamma_2)/\sqrt{2}$. In the language of non-Abelian topology, braiding can be alternatively realized by the topological charge measurement [23, 22]. Therefore, performing a sequence of parity measurement of $i\gamma_3\gamma_4, i\gamma_1\gamma_3, i\gamma_2\gamma_3, i\gamma_3\gamma_4$ is equivalent to $P_B(1 \leftrightarrow 2)$ with only a difference of the normalization factor. Note that, the above procedure for parity measurements or the measurement-based braiding requires the help of the ancillary pair of MZMs ($\gamma_3, \gamma_4$).

The parity measurement is realized in the system of the superconductor island coupled to the quan-

tum dot. Within the context of generic tunneling (with a complex tunneling amplitude) between the SC island and QD, the ground-state energies of the superconductor island-quantum dot system obtain a parity-dependent shift. In addition, the tunneling path a fermion takes in the virtual charging process is expected to be a full loop. Therefore, the parity of the MZMs is reflected by the energy dependence of the system. For example, the dependence of the ground state energy shift on the two-MZM joint parity $p = p_{12}$ and Four-MZM joint parity $p = p_{12}p_{34}$ has been discussed in Ref. [24]. The MZM parity-dependent energy shift can be measured by energy level spectroscopy.

Compared to the typical Cooper pair box quantum bit and the current-biased phase quantum bit, transmon quantum bit has greatly improved insensitivity to charge noise, and stronger coupling to the transmission line resonator [114]. The parity-dependent energy shift discussed early, estimated to be approximately $100\ MHz$, can be observed by the transmon-type measurement. This readout condition of the energy splitting being $\sim 100\ MHz$ can be satisfied for MZMs in the topological regime, because the energy splitting of the MZMs are exponentially suppressed by the length of the nanowire.

Thus, a sufficiently small energy splitting can be reached for the MZMs in the topological regime by increasing the lengths of the nanowires. On the other hand, the component MBSs of the ps-ABSs are separated by a length scale $L^* \sim \zeta$ which can not be easily controlled externally. Here we show that the energy splittings of the ps-ABSs can be made sufficiently small less than $(\sim 100\ MHz)$ provided the confinement potential is sufficiently smooth. However, various local perturbations introduced by the measurement process itself typically increase the energy splittings of the component MBSs. Therefore, it follows that, there are threshold upper limits of the magnitudes of the local perturbations beyond which the measurement-based braiding will not work without error correction in the quasi-Majorana regime of the SM-SC heterostructures.

## 4.3 General properties of quasi-Majoranas

In this section, we consider a perturbation-free quantum dot $-$ semiconductor-superconductor (QD-SM-SC) heterostructure where the QD in a realistic device is a bare SM segment not covered by the superconductivity. Quantum dot confinement potential is expected to naturally arise due to the mismatch of the Fermi energy between the lead and semiconductor [60]. For such a system, we show that the ps-ABSs can generally arise as the lowest energy states in the topologically trivial regime, even with energy splittings below the energy scale $\varepsilon_m$.

A smooth confinement potential is commonly believed to be responsible for the emergence of the

near-zero-energy ABSs in the SM-SC heterostructures in the topologically trivial regime [75, 86, 80, 88]. Recently, it was shown that the topologically trivial near-zero-energy ABSs also exist in the finite-length Kitaev chain attached to a QD with a position-dependent step-like potential [115]. Several types of potential that can induce the low-energy ABSs in the topologically trivial regime have also been discussed recently [101, 88] . In what follows, we discuss the emergence of the near-zero-energy ps-ABSs for a system with a Gaussian confining potential (see Eq. (4.2), Fig. 4.1(b)).

We start with the model Hamiltonian of the one-dimensional QD-SM-SC hybrid nanowire given by

$$\begin{aligned} H = &\left[-\frac{\hbar^2}{2m^*}\partial_x^2 - i\alpha(x)\partial_x\sigma_y - \mu + V(x)\right]\tau_z \\ &+ \Gamma(x)\sigma_x + \Delta(x)\tau_x \end{aligned} \tag{4.1}$$

with $m^*$ the effective mass, $\mu$ the chemical potential, $\alpha(x)$ the spin-orbit coupling (SOC) strength, $V(x)$ the confinement potential, $\Gamma(x)$ the externally applied Zeeman field and $\Delta(x)$ the SC proximitized gap. Here $\sigma_i$ and $\tau_j$ ($i = x, y, z$) are the Pauli matrices operating in the spin and particle-hole spaces, respectively. A position dependence is also considered for the SOC and the Zeeman potential, which will be exploited in Sec. 4.4 to describe local perturbations in these parameters. In this section, we investigate the above Hamiltonian with spatially uniform $\Gamma$ and $\alpha$, but with inhomogeneous confinement potential $V(x)$ and pairing potential $\Delta(x)$, given as,

$$\begin{aligned} V(x) &= V_{max} \times \begin{cases} 1 & \text{if} \quad x < x_V, \\ e^{-\left(\frac{x-x_V}{\delta x_V}\right)^2} & \text{if} \quad x_V < x < L, \end{cases} \\ \Delta(x) &= \Delta_0(1 - e^{-(x-x_\Delta)^2/(\delta x_\Delta)^2}). \end{aligned} \tag{4.2}$$

Here, $x_V$ defines a "flat-top" region with potential $V_{max}$ and $\delta x_V$ describes the smoothness of the decaying potential. Similarly, $x_\Delta$ indicates the length of the bare SM region on the nanowire and $\delta x_\Delta$ controls the smoothness of $\Delta(x)$.

A tight binding model of the QD-SM-SC structure can be written as,

$$\begin{aligned} H_{BdG} = \sum_i \Big\{ &\Psi_i^\dagger \Big[ (2t - \mu + V_i)\,\tau_z + \Gamma_i\sigma_x + \Delta_i\tau_x \Big] \Psi_i \\ &+ \Big[ \Psi_{i+a}^\dagger \left(-t\tau_z + i\alpha_i\sigma_y\tau_x\right) \Psi_i + h.c. \Big] \Big\}, \end{aligned} \tag{4.3}$$

which is written in the discretized Nambu basis with $\Psi_i = \left(c_{i\uparrow}, c_{i\downarrow}, c^\dagger_{i\uparrow}, c^\dagger_{i\downarrow}\right)^T$. Here, $a = 10\ nm$ is the lattice constant, and $c^\dagger_i$ ($c_i$) is the electron creation (annihilation) operator at lattice site $i$. Note that, the position-dependence of the parameters $(\Gamma(x), V(x), \alpha(x), \Delta(x))$ is now reflected by the site-dependence $(\Gamma_i, V_i, \alpha_i, \Delta_i)$ based on $x = ia$. To obtain the low energy spectra and wave functions of the system, we numerically diagonalize the above Hamiltonian, $H_{BdG}\Phi_i = E\Phi_i$.

Consider a positive low energy solution $E = \varepsilon \ll \Delta$ with the eigen function given as $\Phi_{+\varepsilon}(i) = (u_{i\uparrow}, u_{i\downarrow}, v_{i\uparrow}, v_{i\downarrow})^T$. Then, a negative energy solution $E = -\varepsilon$ is guaranteed by the particle-hole symmetry with the eigen function given by $\Phi_{-\varepsilon}(i) = (v^*_{i\uparrow}, v^*_{i\downarrow}, u^*_{i\uparrow}, u^*_{i\downarrow})^T$. To analyze the low-energy Majorana wave functions, we represent the eigenstates $\Phi_{\pm\varepsilon}(i)$ by their linear combinations,

$$\begin{aligned} \chi_A &= \frac{1}{\sqrt{2}}\left(\Phi_{+\varepsilon}(i) + \Phi_{-\varepsilon}(i)\right), \\ \chi_B &= \frac{i}{\sqrt{2}}\left(\Phi_{+\varepsilon}(i) - \Phi_{-\varepsilon}(i)\right). \end{aligned} \tag{4.4}$$

Here $\chi_n$ with $n = A, B$ are the Majorana representations of the wave functions, i.e., the component MBSs, satisfying $\langle\chi_n|H_{BdG}|\chi_n\rangle = 0$ and $\langle\chi_A|H_{BdG}|\chi_B\rangle = i\varepsilon$. In this way, we can express the wave functions with near-zero-energy eigen values as superpositions of MBSs.

In Fig. 4.1(a), we show the low energy spectrum as a function of the applied Zeeman field of the QD-SM-SC hybrid structure. Here, the red lines indicate the lowest energies $\pm E_0$ while the blue lines represent the energies of bulk states. A topological quantum phase transition (TQPT) of the system from a topologically trivial state to topologically non-trivial state is indicated by the bulk gap closing at a critical Zeeman potential $\Gamma_c$ with $\Gamma_c = \sqrt{\Delta^2 + \mu^2}$ i.e., $\Gamma_c \approx 5\Delta$ for $\mu = 5\Delta$. The confinement potential $V(x)$ and the SC-induced pairing potential $\Delta(x)$ are schematically shown in Fig. 4.1(b). In the presence of the quantum dot potential $V(x)$, the near-zero-energy eigenstates (associated with the ps-ABSs) emerge and stay within a considerable range of Zeeman potential in the topologically trivial regime ($\Gamma < \Gamma_c$). The wave functions $\chi_{A,B}$ associated with the near-zero-energy eigenvalues at $\Gamma = 4\Delta$ (green line in panel (a)) are plotted in Fig. 4.1(c) as the red and yellow lines, respectively. The low-energy ps-ABSs are represented as a pair of overlapping MBSs located at the ends of a segment of the wire with a finite quantum dot potential (see $V(x)$ in Fig. 4.1(b)). The two component MBSs of the ps-ABS are partially separated on the order of the length scale of the QD. On the other hand, the MZMs in the topological regime are separated by the length of the nanowire, as shown in Fig. 4.1(d) with $\Gamma = 6\Delta$ (black line in panel (a)).

Note that, in a finite-length wire the lowest energy of the system can not strictly be zero even in

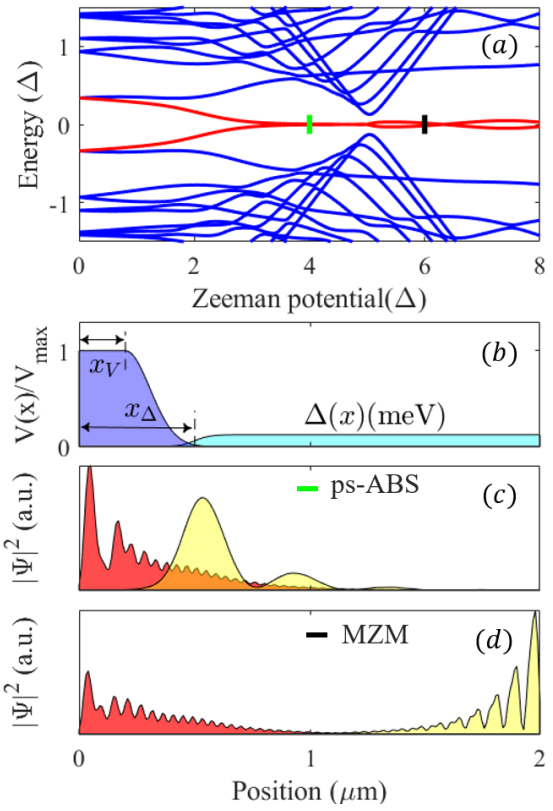


Figure 4.1: (Color online) (a) Dependence of the low energy spectrum on the applied Zeeman field for a system described by the Hamiltonian in Eq. (4.1) with chemical potential $\mu = 5\Delta$. The bulk gap has a minimum at $\Gamma_c \approx \mu = 5\Delta$, the critical field associated with the TQPT. (b) Potential profiles corresponding to Eq. (4.2) with $\Delta_0 = 0.25\ meV, V_{max} = 8\Delta$. (c), (d) Wave functions associated with the near-zero energy eigenstates marked as the green and black lines in panel (a), respectively. The component MBSs of ps-ABS are now separated by QD length scale ($L^* \sim x_\Delta$, the length of the bare SM segment), as shown in panel (c). Here a uniform Zeeman field is applied along the length of the wire and the other parameters are as follows: $m = 0.03m_e, \alpha(x) = \alpha = 0.4\ eV\text{Å}, x_V = 0.20\ \mu m, \delta x_V = 0.15\ \mu m, \delta x_\Delta = 0.10\ \mu m, x_\Delta = 0.50\ \mu m$.

the topological regime. In this sense, the near-zero-energy ps-ABSs can be continuously connected to the topological MZMs when the yellow Majorana mode gradually move towards the right end of the wire with an increasing Zeeman field. The energy splittings of the topological MZMs induced by the finite overlapping between the component MBSs can be exponentially suppressed by increasing the length of the nanowire ($E \sim e^{-L/\zeta}$). Therefore, topological MZMs can satisfy the requirement on the energy splittings with $E \lesssim \varepsilon_w$ for local charge tunneling measurements as well as $E \lesssim \varepsilon_m$ for the measurement-based braiding. In contrast, the length scale of the confinement potential ($L^*$) i.e., the spatial separation between the component MBSs of ps-ABSs (see Fig. 4.1(c)), can not be externally controlled in principle, rendering the ps-ABSs not a natural platform for building a qubit for TQC. However, due to the rapid development in designing the experimental

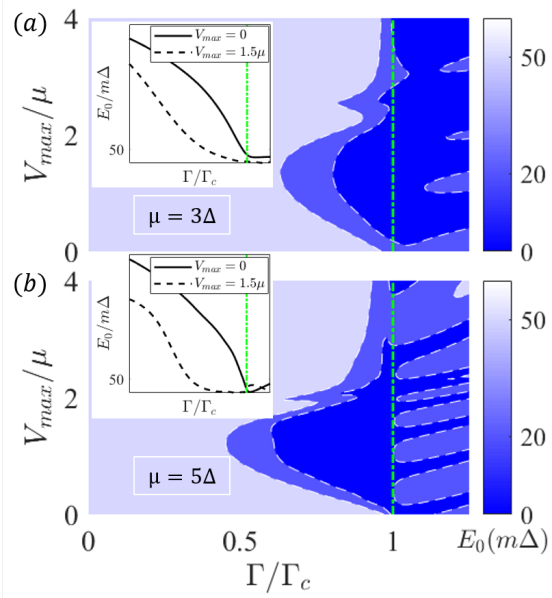


Figure 4.2: (Color online) Lowest energy $E_0$ of Hamiltonian given in Eq. (4.3) as a function of Zeeman potential $\Gamma$ and the maximum potential height of the quantum dot $V_{max}$ with chemical potential $\mu = 3\Delta$ in (a) and $\mu = 5\Delta$ in (b). The green dotted lines represent the critical Zeeman potential of TQPT ($\Gamma/\Gamma_c = 1$). The dark blue regions indicate the ps-ABSs with energy splittings $E_0 \in (0, 20\ m\Delta) < \varepsilon_w$, which are also below the braiding energy scale $\varepsilon_m$. The insets show the lowest energy $E_0$ for system at $\mu = 3\Delta, 4\Delta$ with $V_{max} = 0, 1.5\mu$ respectively. The rest of the parameters used here are the same as in Fig. 4.1.

devices, it may still be possible to produce the topologically trivial ps-ABSs with energy splittings small enough to meet the braiding requirement.

Quantum dot potential ($V(x)$) can affect the emergence as well as the energy splittings of ps-ABSs in the QD-SM-SC systems. It has been discussed in Ref. [90] that the energy splitting of ps-ABSs can be reduced by increasing the smoothness of the confinement potential. In Fig. 4.2, we show the lowest energy $E_0$ of the Hamiltonian in Eq. (4.3) as a function of Zeeman potential $\Gamma$ and quantum dot potential height $V_{max}$ for a fixed smoothness parameter $\delta x_V = 0.15\ \mu m$, where the green dotted lines indicate the critical Zeeman potential for TQPT with $\Gamma/\Gamma_c = 1$. Here, the magnitudes of the energy splittings are represented by the colors with units $m\Delta = 0.25\ \mu eV$. As shown in Fig. 4.2, parameter region with $E_0 \lesssim 20\ m\Delta$, indicated by the dark blue color, appears even in the trivial regime ($\Gamma < \Gamma_c$) for a non-zero $V_{max}$. Trivial systems with parameters within the dark blue regions host ps-ABSs with energy splittings below the energy scale of the charge tunneling experiments ($E_0 < \varepsilon_w \sim 40 - 80\ m\Delta$), which also meet the braiding condition when the energy splittings satisfy $E_0 \lesssim \varepsilon_m \sim 0.4\ m\Delta$. As shown in Fig. 4.2, system with chemical potential $\mu = 5\Delta$ in panel (b) shows a larger blue region that supports ps-ABSs than the system with $\mu = 3\Delta$ as

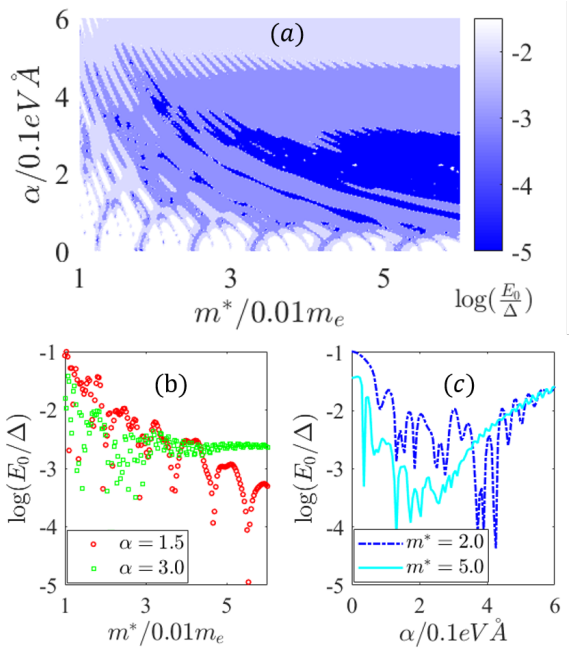


Figure 4.3: (Color online) (a) The logarithm of the lowest energy $E_0$ at $\Gamma = 4\Delta$ ($< \Gamma_c = 5\Delta$) as a function of effective mass ($m^*/m_e \in (0.01, 0.06)$) and spin-orbit coupling strength ($\alpha \in (0, 0.6)$ $eV\mathring{A}$). The dark blue region indicates the trivial states with near zero energy $E_0 \sim 0.1\ m\Delta \lesssim \varepsilon_m$, which in principle can be utilized in measurement-based braiding. Panel (b), (c) show the line-cuts from panel (a), with fixed spin-orbit couplings ($\alpha = 0.15, 0.30$ $eV\mathring{A}$) and fixed effective masses ($m^* = 0.02, 0.05m_e$), respectively. The other parameters used here are the same as in Fig. 4.1

given in panel (a). On the other hand, the energy splittings for the MZMs in the topological state is smaller (see the dark blue region in Fig. 4.1(a) after the green line) in systems at lower chemical potential, which can be attributed to the smaller critical Zeeman field in the system at $\mu = 3\Delta$ than that at $\mu = 5\Delta$. Note that, Fig. 4.2(a), (b) both show a maximum range of Zeeman potential associated with the quasi-Majorana regime with $V_{max} \sim 1.5\mu$. A comparison of $E_0$ versus $\Gamma$ for systems with $V_{max} = 0$ and $V_{max} = 1.5\mu$ is given in the inset for $\mu = 3\Delta, 5\Delta$ in panel (a), (b) respectively.

In realistic experiments, effective mass could be different due to the effect of proximity-induced energy renormalization[101] for a known material. Similarly, due to the non-uniform gate potentials, SOC strength of the system can also be different in experiments[116]. In Fig. 4.3(a), we show the dependence of logarithm of the lowest energy ($\log(E_0/\Delta)$) in a trivial phase ($\Gamma = 4\Delta < \Gamma_c$) on the effective mass ($m^*$) and SOC strength ($\alpha$). Here the effective mass and SOC are taken as $m^* \in (0.01, 0.06)m_e, \alpha \in (0, 0.6)$ $eV\mathring{A}$, respectively. The colors indicate the value of $\log(E_0/\Delta)$, e.g., in Fig. 4.3(a) the dark blue color with scale $-4$

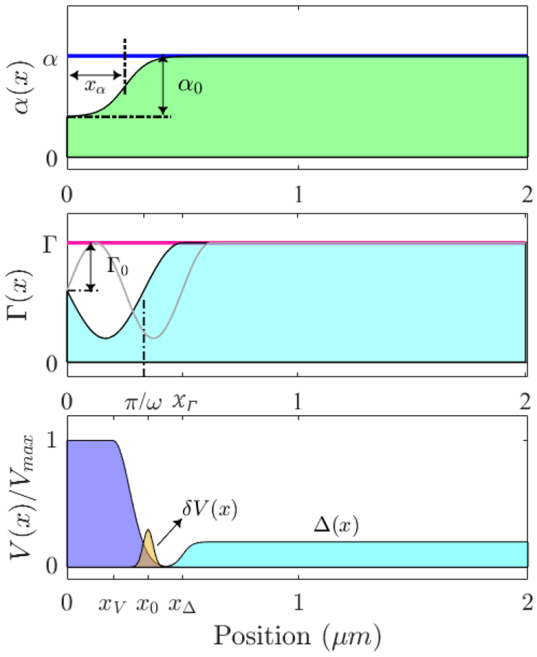


Figure 4.4: (Color online) *Top panel*: spatial profile for spin-orbit coupling strength where the blue line represents a uniform SOC $\alpha$ and the envelop line of the green area represents the position-dependent $\alpha(x)$. *Middle panel*: spatial profile for Zeeman potential where the magenta line represents a uniform Zeeman field $\Gamma$ while the envelop line of the cyan area represents the position-dependent Zeeman potential $\Gamma(x)$. $\Gamma_0$ indicates the twisting amplitude of the Zeeman field (or amplitude of magnetic disorder), $\pi/\omega$ indicates the frequency and $x_\Gamma$ is taken to smoothly connect the twisted region with the uniform region along the direction of the nanowire (see Eq. (4.6)). Here the gray line represents another possible function $\Gamma(x)$. *Bottom panel*: spatial profile for confinement potential where $V(x), \Delta(x)$ are the same as that givn in Fig. 4.1(b) and the orange area represents a local potential disorder $\delta V(x)$ with localization center $x_0$. The length of the nanowire is $L = 2\ \mu m$, and the equations of the spatial profiles in this figure are given in Eqs. (4.5), (4.6), (4.7), respectively.

represents $E_0 \lesssim 0.1\ m\Delta$. Therefore, for systems with parameters $(\alpha, m^*)$ within the dark blue regions, the energy splittings of the topologically trivial ps-ABSs are well within the range of $E_0 \lesssim \varepsilon_m$. In Fig. 4.3(b), we plot the energy splitting $E_0$ as a function of the effective mass for systems with different SOCs ($\alpha = 0.15, 0.30\ eV$Å), indicatng that systems with smaller SOC (red dots) are more sensitive to the variation of the effective mass. Similarly, we show the dependence of $E_0$ on SOC for systems with different effective masses ($m^* = 0.02, 0.05 m_e$) in Fig. 4.3(c). Here we find that systems with small effective mass (blue dashed line) can host ps-ABSs with very low energies ($E_0 \lesssim 0.1\ m\Delta$) for a large SOC, while systems with relatively larger effective mass (cyan solid line) can host ps-ABSs with very low energies for small SOCs. In general, the near-zero-energy ps-ABSs in topologically trivial phase are more favorable for a system with larger effective mass and smaller SOC when the other parameters of the system are fixed.

Based on the discussions above, we find that the low-energy ps-ABSs are quite generic in the QD-SM-SC nanowires investigated in experiments, where a quantum dot is naturally introduced. In addition, the energy splittings of the topologically trivial ps-ABSs are possible to be tuned below the energy scale $\varepsilon_m \sim 0.1\ \mu eV$, as shown in Fig. 4.2 and Fig. 4.3(a). In this sense, these ps-ABSs will not only reproduce the robustness of ZBCPs in the local charge tunneling experiments, but also are possibly applicable for measurement-based braiding in TQC. However, in spite of their sufficiently small energy splittings, the ps-ABSs are topologically trivial, whose energies are sensitively dependent on the local quantities such as the local values of SOC, Zeeman field and confinement potential, etc. Therefore, it is essential to examine the robustness of the energy splitting of the MZM system in the quasi-Majorana regime in the presence of different types of local perturbations.

## 4.4 Stability of quasi-Majoranas in the presence of local perturbations

Partially separated Andreev bound states, or quasi-Majoranas can mimic almost all the behavior of topological Majoranas, including the zero-bias conductance features in the local tunneling experiment and the $4\pi$-Josephson effect [87, 108, 117]. The non-topological quasi-Majoranas are even considered suitable for TQC via measurement-based braiding as long as the corresponding energy splittings are below the energy scale $\varepsilon_m$ [90]. However, it is important to emphasize that, in contrast to the topological MZM modes with spatial separation given by the length of the nanowire, the spatial separation between the component Majorana modes of ps-ABSs are on the order of the length scale of the QD, rendering the ps-ABSs topologically unprotected against local perturbations. In the following, we consider three types of local perturbations as shown in Fig. 4.4, namely, deformations of spin-orbit coupling, local twisting of the applied Zeeman potential, and local perturbation in the confinement potential (defined by Eq. (4.1)). We first show how the near-zero-energy states in the topologically trivial phase are affected by these local perturbations (Secs. 4.4.1,4.4.2, 4.4.3), then discuss the conditions for ps-ABSs admitting measurement-based braiding as long as these perturbations are small (Sec. 4.4.4).

### 4.4.1 Perturbation from step-like spin-orbit coupling

In most of the theoretical calculations, the SOC strength is taken as a constant. However, due to the effect of the gate potentials and the inevitable quantum dot in a realistic device, a non-uniform SOC is possible and can be considered as local perturbation to an ideal system. For example, it has been shown that

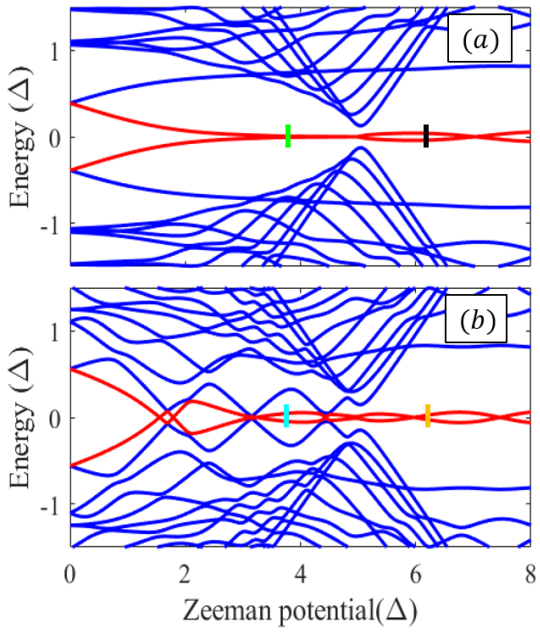


Figure 4.5: (Color online) Low-energy spectrum as a function of Zeeman potential for a system with spin-orbit coupling given as a constant $\alpha$ in panel (a) and a spatially varying function $\alpha(x)$ in panel (b), respectively. A schematic plot of the position-dependent SOC $\alpha(x)$ is given in the top panel of Fig. 4.4. Large energy splitting oscillations (panel (b)) are induced by the presence of the local perturbation in SOC, in contrast to a constant SOC (panel (a)). The wave function profiles associated with the marked lines are given in Fig. 4.6. We consider a system at $\mu = 5\Delta$ with $m^* = 0.03m_e, \alpha = 0.4\ eV\text{Å}, \Delta = 0.25\ meV$, and a confinement potential with $x_V = 0.2\ \mu m, \delta x_V = 0.15\mu m, V_{max} = 6\Delta$. The parameters for $\alpha(x)$ (Eq. (4.5)) in panel (b) is given as $x_\alpha = 0.25\ \mu m, dx_\alpha = 0.02\ \mu m$, $\alpha_1 = 0$, and a symmetric $\alpha(x)$ is applied here. The other parameters used here are: $x_\Delta = 0.5\ \mu m, \delta x_\Delta = 0.15\ \mu m$.

a step-like SOC can lead to decaying oscillations of the energy splitting of MZMs [116]. In this section, we consider a position-dependent SOC described by a function given as

$$\alpha(x) = \alpha_1 + \alpha_0 \frac{1}{2}\left[\tanh\left(\frac{x - x_\alpha}{\delta x_\alpha}\right) - 1\right] \tag{4.5}$$

where $\alpha_1 = \alpha - \alpha_0$ and $\alpha_0, \alpha$ represents the minimum and maximum strength of SOC. Parameter $x_\alpha, \delta x_\alpha$ describe the length scale and the smoothness of the deformation respectively. A schematic plot of the non-uniform SOC is depicted in the top panel of Fig. 4.4. In what follows, we investigate the influence from the spatially varying SOC defined by $\alpha(x)$ in Eq. (4.5) on the near-zero-energy states.

First, we show the dependence of low energy spectrum for a system with spatially uniform SOC namely, $\alpha(x) = \alpha$, on the Zeeman potential in Fig. 4.5(a). Here, $\mu = 5\Delta$, and a quantum dot potential

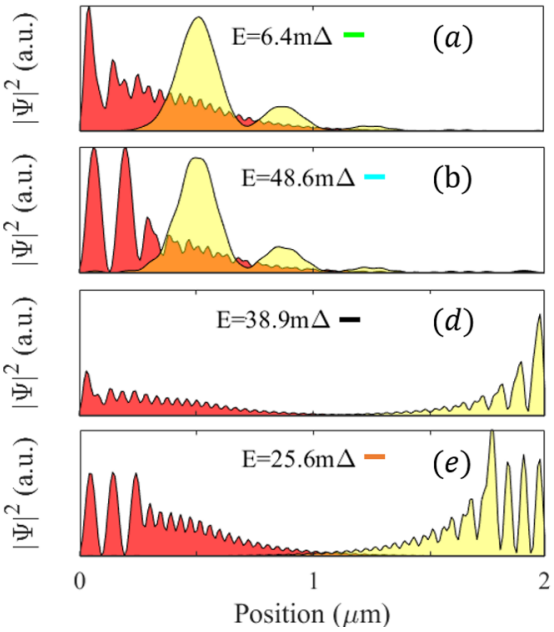


Figure 4.6: (Color online) (a), (b) Wave functions associated with the near-zero energy ps-ABS marked as the green and cyan lines in Fig. 4.5, respectively. Similarly, panel (c), (d) show the wave function profiles for the topological MZMs marked by the black and orange line in Fig. 4.5, respectively. In the presence of a step-like SOC, the splitting energy of the ps-ABS has been increased from $E = 6.4m\Delta$ in (a) to $E = 48.6m\Delta$ in (b), while the splitting energy of the topological MZMs has not been significantly changed ($E = 38.9m\Delta$ in (c) and $E = 25.6m\Delta$ in (d)). Note that, the energy splittings of topological MZMs can be reduced (hence satisfy $E_0 \lesssim \varepsilon_w, \varepsilon_m$) by extending the length of the nanowire, while that of the topologically trivial ps-ABSs can not be controlled externally.

with amplitude $V_{max} = 6\Delta$ is considered. The robust near-zero energy states are present in the trivial region ($\Gamma < \Gamma_c \sim 5\Delta$), with an energy splitting even smaller than that of the topological states ($\Gamma > \Gamma_c$). After we switch on the SOC inhomogeneity described by Eq. (4.5), the ps-ABSs in the trivial regime show visible energy splitting oscillations, as shown in Fig. 4.5(b), while the energy splittings in the topological regime ($\Gamma > 5\Delta$) are not affected significantly.

The wave function profiles corresponding to the marked lines in Fig. 4.5 at $\Gamma = 3.8\Delta$ (green, cyan) and $\Gamma = 6.2\Delta$ (black, orange) are given in Fig. 4.6, along with their corresponding energy splittings. Although the changes in the overlap region (or spatial separation) between the two Majorana components of the ps-ABS (and MZMs in Fig. 4.6(c, d)) can not be observed, the energy splitting associated with the ps-ABS has changed significantly from $E = 6.4\ m\Delta$ ($< \varepsilon_w$) in Fig. 4.1(a) to $E = 48.6\ m\Delta$ ($> \varepsilon_w$) in Fig. (b). On the other hand, the energy splitting for the topological MZMs does not change significantly, as shown in Fig. 4.5(c), (d). Note that, the energy splittings for the topological MZMs can be controllably

reduced by extending the length of the nanowire to be well below the energy scales $\varepsilon_w, \varepsilon_m$.

In Sec. 4.3, we remarked that a system hosting topologically trivial ps-ABSs with energy splittings $E_0 \lesssim \varepsilon_m$ is realizable. In Fig. 4.7, we show similar profiles as those in Fig. 4.5, 6, but for a system with different parameters: bigger effective mass $m^* = 0.05m_e$, smaller SOC strength $\alpha = 0.2\ eV$Å, and bigger smoothness parameter $\delta x_V = 0.30\ \mu m$ of the confinement potential defined by Eq. (4.2). Consequently, the energy splitting associated with the ps-ABSs at $\Gamma = 4\Delta$ (green line in Fig. 4.7(a)) is now sufficiently small to meet the requirement for a transmon readout namely, $E_0 = 0.1\ m\Delta \leq \varepsilon_m \sim 0.4\ m\Delta$, as shown in Fig. 4.7(c). Compared with the wave functions given in Fig. 4.6(a), the component MBSs in Fig. 4.7(c) are now separated more from each other and overlap much less as well. However, the seemingly "robust" near-zero-energy state still suffers from the local perturbation inevitably. As shown in Fig. 4.7(b), the energy splittings are greatly enhanced in magnitude after a step-like SOC is applied. The wave functions of the component MBSs corresponding to the cyan line in Fig. 4.7(b) overlap, as shown in Fig. 4.7(c), and the lifted energy splittings with $E = 43.5\ m\Delta$ now fail to meet the braiding condition.

Next, we show the influence from a local perturbation in the externally applied Zeeman field on the stability of the ps-ABSs in the trivial regime.

### 4.4.2 Perturbation from a twisted Zeeman potential

The semiconductor-superconductor heterostructure is driven into the topological phase when an external Zeeman field parallel to the nanowire is gradually increased. A helical magnetic field that rotates along the wire has been used to generate the topologically non-trivial states in superconducting nanowires without SOC [118]. Also, a twisted Zeeman potential has been used to illustrate the irrelevance of the spin degree of freedom in the emergence of near-zero energy quasi-Majoranas [101]. In this section, we investigate the effect from a locally position-dependent Zeeman field, equivalently acting as a magnetic perturbation, on the energy splitting of topologically trivial ps-ABSs.

We consider a magnetic perturbation localized within the quantum dot region, with which the effective Zeeman field can be described by the following position-dependent function,

$$\Gamma(x) = \big[\Gamma_1 + \Gamma_0 \sin(\omega x)\big]\Theta(x_\Gamma - x) + \Gamma\Theta(x - x_\Gamma) \tag{4.6}$$

with $\Gamma_1 = \Gamma - \Gamma_0$ the Zeeman field magnitude at $x = 0$ and $\Gamma$ the Zeeman field magnitude without any magnetic perturbation. $\omega, x_\Gamma$ indicate the twist period and twisting length scale, respectively. A schematic

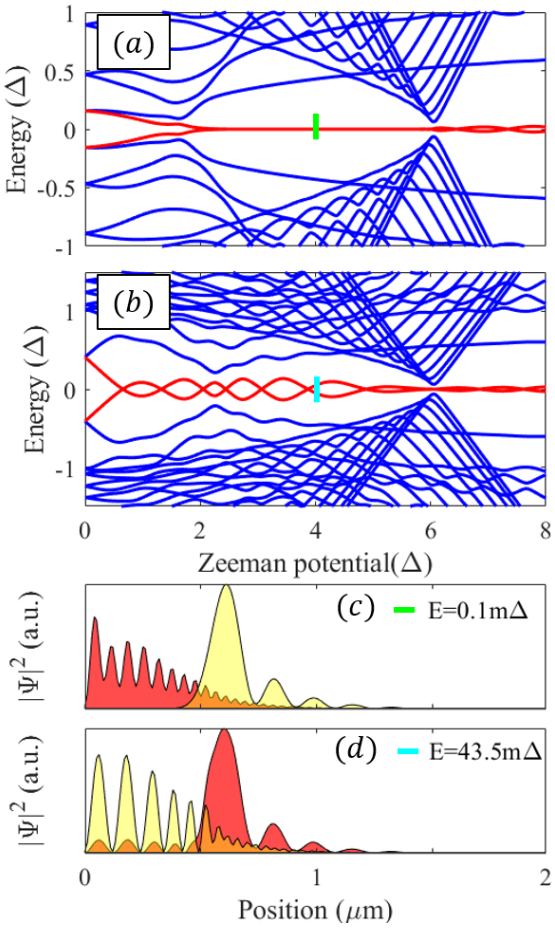


Figure 4.7: (Color online) Low-energy spectrum as a function of applied Zeeman field for a system with SOC given as a constant $\alpha$ in (a) and a spatially varying function $\alpha(x)$ in (b). Panels (c), (d) show the wave functions along with the corresponding energy splittings associated with the green and cyan lines marked in panel (a), (b) respectively. In the presence of local perturbation in SOC, an obvious overlap appears between the two component MBSs, as shown in panel (d). Also, the corresponding energy splitting has been greatly increased from ($E = 0.1\ m\Delta \lesssim \varepsilon_m$) to ($E = 43.5\ m\Delta \sim \varepsilon_w$). In contrast to Fig. 4.5, here we have considered a smoother confinement potential with $\delta x_V = 0.3\ \mu m$, and a position-dependent SOC given with $x_\alpha = 0.55\ \mu m, dx_\alpha = 0.02\ \mu m, \alpha_1/\alpha = 0.2$. The other parameters used are $m^* = 0.05m_e, \alpha = 0.2\ eV\text{Å}, \Delta = 0.25\ meV, \mu = 6\Delta, V_{max} = 8\Delta, x_V = 0.20\ \mu m, \delta x_V = 0.30\ \mu m$.

plot of this position-dependent Zeeman potential is shown in the middle panel of Fig. 4.4. Armed with the position-dependent Zeeman field $\Gamma(x)$, we show how the low energy spectrum is affected by the magnetic field perturbation below.

With a uniform Zeeman potential, $\Gamma(x) = \Gamma$, the system (Eq. (4.1)) hosts robust near-zero energy states even in the trivial regime ($\Gamma < \Gamma_c \sim 5\Delta$), as shown in Fig. 4.8(a). When a local position-dependence is introduced to the applied Zeeman field, namely, $\Gamma(x)$ with $\Gamma_0 = 0.3\Gamma, \omega = -3\pi/100$ (black line in the

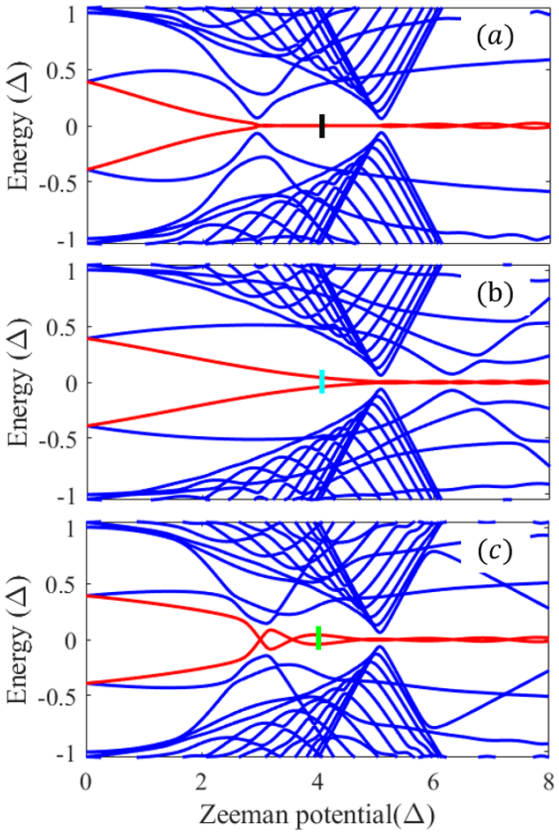


Figure 4.8: (Color online) Dependence of low-energy spectrum on the strength of the applied Zeeman field for a) system with a uniform Zeeman field, b) system with a locally twisted Zeeman field (Eq. (4.6)) with $\Gamma_0/\Gamma = 0.3, \omega = -3\pi/100$, c) system with a locally twisted Zeeman field (Eq. (4.6)) with $\Gamma_0/\Gamma = 0.4, \omega = 4\pi/200$. The twisted Zeeman potentials used here are schematically shown in the middle panel of Fig. 4.4. The chemical potential here is $\mu = 5\Delta$ and the confinement potential is characterised by $x_V = 0.2\ \mu m, \delta x_V = 0.15\ \mu m$ and $V_{max} = 8\Delta$. The other parameters used here are the same are Fig. 4.7.

middle panel of Fig. 4.4), the near-zero energies associated with the trivial ps-ABSs are lifted while the energy splittings in the topological states do not show any significant changes, as shown in Fig. 4.8(b). In Fig. 4.8(c), we show another example of the low energy spectrum for a system perturbed by the position-dependent Zeeman potential $\Gamma(x)$ with $\Gamma_0 = 0.4\Gamma, \omega = \pi/25$ (grey line in the middle panel of Fig. 4.4). Note that, parameter $x_\Gamma$ has been selected accordingly for $\Gamma(x)$ to realize a smooth connection from the twisted region to the constant region of the Zeeman potential for both of these two position-dependent Zeeman fields, as schematically shown in Fig. 4.4.

The wave function profiles, corresponding to the marked lines at $\Gamma = 4\Delta$ in Fig. 4.8, along with their corresponding energy splittings are given in Fig. 4.9. Under the effect of the local perturbation in

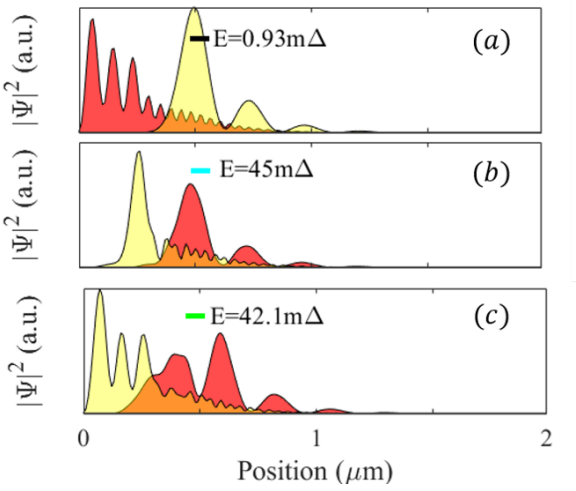


Figure 4.9: (Color online) Majorana wave functions associated with the near-zero energy ABS mode from Fig. 4.8 corresponding to the marked lines. The energy splitting of the trivial ps-ABS in the case of a uniform Zeeman field is small, with $E = 0.93\ m\Delta$ in (a); while as shown in panel (b), (c), in the presence of the twisted Zeeman fields as have been described in Fig. 4.8, the energy splitting has been increased to $E = 45\ m\Delta, 42.1\ m\Delta$, respectively.

Zeeman field, the energy splitting of ps-ABS increases from $E_0 = 0.93\ m\Delta$ ($\sim \varepsilon_m$) in Fig. 4.9(a) to $E_0 = 45\ m\Delta, 42.1\ m\Delta$ in Fig. 4.9(b), (c) respectively. The overlap region of the component MBSs have changed in different ways for Fig. 4.9(b), (c). In Fig. 4.9(b), the increased overlap is because of the rightward movement of the MBS sitting at the left end of the nanowire. In Fig. 4.9(c), on the other hand, the increased overlap is due to the leftward movement of the MBS sitting on the right when we apply a different $\Gamma(x)$ (see grey line in the middle panel of Fig. 4.4). Note that, the perturbation strength for Fig. 4.9(b),(c) are $\Gamma_0/\Gamma = 0.3, 0.4$, respectively, which is a reasonably small deviation from the applied magnetic field strength that might be induced by the measurements. This should be understandable within the context of a position-dependent Zeeman field, since only the region with $\Gamma(x) \geq \Gamma_c$ can host the near-zero-energy states. Though the wave functions and energy splittings for the topological states are not shown here, we have checked that similar susceptibility to the local perturbations in magnetic field is not present for topological MZMs, as is expected for a topological state.

### 4.4.3 Local potential perturbation

We have investigated the effects of perturbations in SOC and externally applied Zeeman field in the previous sections. In this section, we consider the effect from perturbations in the local potential on the energy

splittings of the topologically trivial ps-ABSs. In contrast to the topological MZMs, which are immune to local potential perturbations, the overlap of the component MBSs of the ps-ABS state make them sensitive to local potential perturbations. Here we consider a Gaussian-like potential perturbation localized at $x = x_0$, which can be described by the function

$$\delta V(x) = \delta V e^{-(x-x_0)^2/(\delta x_0)^2} \tag{4.7}$$

with $\delta V$, $\delta x_0$ the magnitude and sharpness of the potential perturbation. A schematic plot of the local potential disorder (shown in orange) is given in the bottom panel of Fig. 4.4. In Fig. 4.10, we show the low energy spectrum as a function of the Zeeman potential for the system without and with the local potential $\delta V(x)$ in panel (a), (b) respectively. Similar to the effect from local perturbations in SOC (Fig. 4.5, 4.7) and the applied Zeeman field (Fig. 4.8), a local potential perturbation $\delta V(x)$ with $\delta V = 0.3V_{max}, x_0 = 0.2\ \mu m$ also leads the topologically trivial ps-ABS split away from near-zero energy. The wave function corresponding to the green line in Fig 10 (a) is given in Fig. 4.10(c), where the component MBSs associated with energy splitting $E_0 = 5.02\ m\Delta$ are partially separated and almost non-overlapping. Perturbed by the local potential $\delta V(x)$, a finite overlap between the component MBSs can be observed in Fig. 4.10(d), which is associated with a significantly increased energy splitting $E_0 = 46.9\ m\Delta$. By contrast, as shown in the low energy spectrum in Fig. 4.10(a, b), the energy splitting in the topological regime does not show any obvious effect of the local potential $\delta V(x)$.

Though we have considered three types of local perturbations in this paper (Fig. 4.4), it is important to note that the perturbations induced by the measurements (or environment) are uncontrolled. Within the framework of these assumed local perturbations, however, it is still possible to identify the perturbation strengths sufficient to split the energy of the ps-ABSs away from the condition $E_0 \lesssim \varepsilon_m$ needed for measurement-based braiding,

### 4.4.4 Energy splitting sensitivity of the quasi-Majoranas to local perturbations

As has been shown above, the energy splittings of the topologically trivial ps-ABSs and topologically protected MZMs react differently to local perturbations. Instead of focusing on the exact value of the energy splittings below a certain estimated limit, in what follows, we now focus on the changes in the energy splitting in response to the local perturbations. More specifically, we analyze the ratio $E_0'/E_0$, where $E_0', E_0$ represent the energy splitting of the ground state with and without the local perturbations, respectively. We

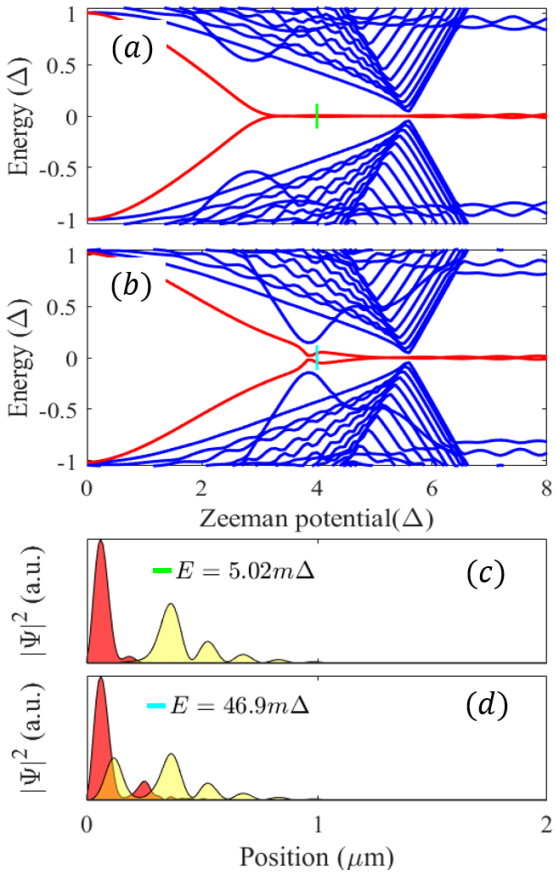


Figure 4.10: (Color online) Dependence of low-energy spectrum on the applied Zeeman field for a) system with a confinement potential (Eq. (4.2)) and without any potential disorder, b) system with a confinement potential (Eq. (4.2)) as well as a local potential disorder, described by Eq. (4.7). Clearly, the trivial near-zero energy splittings in panel (a) have been lifted by the local potential perturbation in panel (b). The wave functions and their corresponding energy splitting associated with the green and cyan line in panel (a), (b) are shown in panel (c), (d) respectively. An obvious overlapping between the component MBSs has been induced by the local potential disorder for ps-ABS in panel (d). The chemical potential is $\mu = 5.5\Delta$, and the local potential disorder is characterized by $\delta V/V_{max} = 0.3, x_0 = 0.2\ \mu m, \delta x_0 = 0.05\ \mu m$. The other parameters used here are $m^* = 0.05m_e, \alpha = 0.15\ eV\text{Å}, V_{max} = 8\Delta$, and $x_\Delta = 0$.

assume that ps-ABSs with perturbed energy splittings $E_0' \geq 10E_0$ are not robust enough in the presence of local perturbations and are not suitable for measurement-based braiding.

For a position-dependent SOC, defined in Eq. (4.5), the deformation amplitude $\alpha_0$, length scale $x_\alpha$ and steepness parameter $\delta x_\alpha$ can all affect the perturbation strength. We consider a system described by the Hamiltonian in Eq. (4.3), with $\mu = 6\Delta$ and confinement potential amplitude $V_{max} = 8\Delta$. In Fig. 4.11(a), we show the logarithm of $E_0'/E_0$ as a function of the strength of the SOC perturbation $(\alpha_0/\alpha)$ with fixed perturbation length scale $x_\alpha = 0.55\ \mu m$. Here the blue line ($\Gamma = 4\Delta$) and the cyan dashed line ($\Gamma = 5\Delta$)

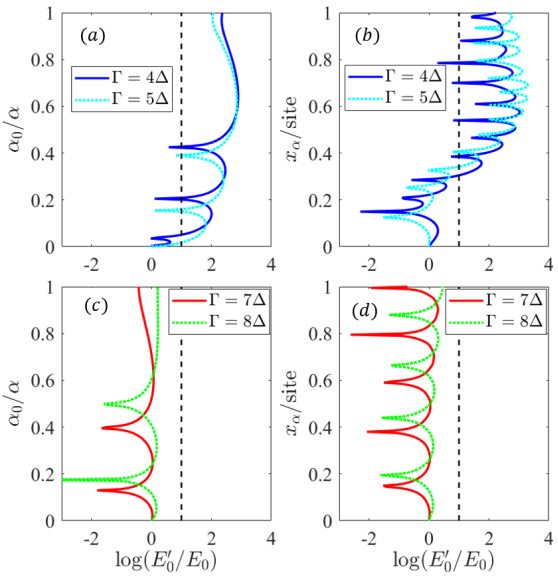


Figure 4.11: (Color online) Dependence of the logarithm of $(E_0'/E_0)$ on the parameters $\alpha_0, x_\alpha$ that characterize the step-like SOC described by the function in Eq. (4.5). Here $E_0', E_0$ are the energy splitting of the system with and without the presence of a local SOC perturbation, respectively. The black dashed lines indicate $\log(E_0'/E_0) = 1$, before which the energy splittings $E_0'$ are considered still applicable for braiding ($E_0' \sim \varepsilon_m$). (a) Energy splittings of the trivial states for systems with a fixed $x_\alpha = 0.55\ \mu m$ for SOC perturbation, here $\log(E_0'/E_0)$ go over the black dashed line ($E_0' > \varepsilon_m$) even at a small perturbation strength $\alpha_0/\alpha \sim 0.05$. (b) Energy splittings of the trivial states for systems with a fixed SOC perturbation strength $\alpha_0/\alpha = 0.30$, in this case a perturbation length scale $x_\alpha \gtrsim 0.35\ \mu m$ is required to break the readout condition for braiding. In contrast, the energy splittings of the topological states satisfy $\log(E_0'/E_0) \approx 0$ for all different values of $\alpha_0$ and $x_\alpha$ of the SOC perturbations, as shown in Fig. (c), (d), respectively. The chemical potential is $\mu = 6\Delta$. The other parameters used here are $m^* = 0.05m_e, \alpha = 0.2\ eV\text{Å}, \Delta = 0.25\ meV$, and the confinement potential is given with $V_{max} = 8\Delta, x_V = 0.20\ \mu m, \delta x_V = 0.30\ \mu m$.

are associated with the energy splitting ratios $E_0'/E_0$ of the trivial states with unperturbed splitting energy $E_0 = 0.09\ m\Delta, 0.04\ m\Delta$, respectively. The black dashed line indicates $\log(E_0'/E_0) = 1$, i.e., $E_0'/E_0 = 10$. As shown in Fig. 4.11(a), energy splittings increase by more than 10 times (across the black dashed line) even with a small perturbation strength $\alpha_0/\alpha \approx 0.05$. However, the topological MZMs, as shown in Fig. 4.11(c), do not show any significant increase in their energy splittings in the presence of SOC perturbation. Instead, the energy splitting ratio of the MZMs follows $\log(E_0'/E_0) \leq 1$ for all the values of $\alpha_0/\alpha$, where $E_0 = 18\ m\Delta, 17.3\ m\Delta$ for $\Gamma = 7\Delta, 8\Delta$, respectively.

Similarly, we show the logarithm of $E_0'/E_0$ as a function of the deformation length scale $x_\alpha$ with a fixed $\alpha_0 = 0.8\alpha$ for the trivial and topological states in Fig. 4.11(b) and 4.11(d), respectively. For the trivial ps-ABSs, as shown by the blue line with $\Gamma = 4\Delta, E_0 = 0.11\ m\Delta$ and the cyan dashed line with $\Gamma = 5\Delta, E_0 = 0.04\ m\Delta$ in Fig. 4.11(b), the values of their corresponding $\log(E_0'/E_0)$ exceed the black

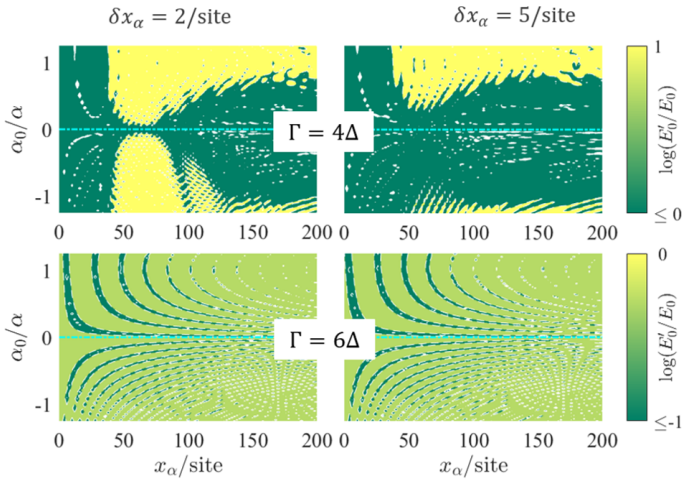


Figure 4.12: (Color online) The logarithm of $(E_0'/E_0)$ (indicated by the colors) as a function of the parameters $\alpha_0$ and $x_\alpha$ that characterize the step-like SOC described by the function in Eq. (4.5). The cyan dashed lines imply the energy splittings ($\log(E_0'/E_0) = 0$) for system without SOC perturbation ($\alpha_0 = 0$). The yellow color implies ps-ABSs with energy splittings $E_0'/E_0 \geq 10$ in the presence of SOC perturbations, which as assumed are not applicable for measurement-based braiding ($E_0' > \varepsilon_m$), as shown in the top panels. However, all of the energy splittings of the topological states satisfy $\log(E_0'/E_0) \lesssim 0$ ($E_0' \lesssim E_0 \sim \varepsilon_m$), as shown in the bottom panels, where nearly no region with yellow color are present. Note that, the threshold amplitude for $\varepsilon_m$ of SOC perturbation is as small as $\alpha_0/\alpha \sim 0.05$ (provided a length scale $x_\alpha \in (50, 80)$site and smoothness parameter $\delta x_\alpha = 0.02\ \mu m$), as shown in the top left panel. A higher threshold perturbation strength $\alpha_0/\alpha \sim 0.25$ (positive $\alpha_0$) is observed in the top right panel, where $\delta x_\alpha = 0.05\ \mu m$. The chemical potential is $\mu = 5\Delta$, the other parameters used here are the same as Fig. 4.11.

dashed line with $x_\alpha \geq 0.35\ \mu m$. On the other hand, for the topological MZMs, as shown by the red line with $\Gamma = 7\Delta, E_0 = 18.1\ m\Delta$ and the green dashed line with $\Gamma = 8\Delta, 17.7\ m\Delta$ in Fig. 4.11(d), the values of the corresponding $\log(E_0'/E_0)$ stay around or below zero ($\log(E_0'/E_0) \lesssim 0$) for all the values considered for $x_\alpha$.

A SOC perturbation with length scale $x_\alpha = 0.55\ \mu m$ and strength $\alpha_0/\alpha \sim 0.05$ is found to be able to split the unperturbed energy by more than 10 times for the topologically trivial ps-ABSs, i.e., $E_0'/E_0 \geq 10$ as shown in Fig. 4.11(a). In Fig. 4.12, we map the logarithm of $E_0'/E_0$ into the $(x_\alpha, \alpha_0)$ parameter space, where the left, right panels are for systems with SOC perturbation with $\delta x_\alpha = 0.02\ \mu m, 0.05\ \mu m$ respectively, and the top, bottom panels are for systems in the trivial and topological state, respectively. The yellow regions in the top panels of Fig. 4.12 indicate energy splittings with $\log(E_0'/E_0) \geq 1$, corresponding to ps-ABSs in the trivial systems which are not applicable for measurement-based braiding. For a stiff step-like SOC with $\delta x_\alpha = 0.02\ \mu m$, SOC perturbations with both positive and negative $\alpha_0$ show a considerable yellow region with enhancement $E_0'/E_0 \geq 10$ on the energy splittings, as shown in the top left panel of Fig. 4.12. A

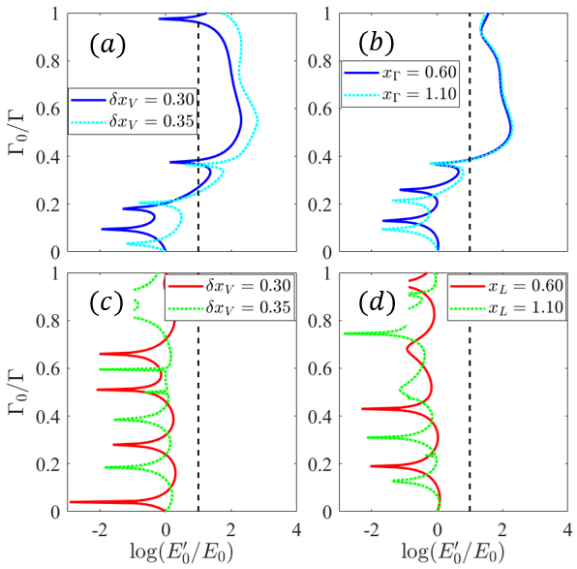


Figure 4.13: (Color online) Similar plot as Fig. 4.11, but is the dependence of the logarithm of $(E_0'/E_0)$ on the parameters $\Gamma_0, x_\Gamma$ that characterize the twisted Zeeman field described by the function in Eq. (4.6). Panels (a), (c) show the value of $\log(E_0'/E_0)$ as a function of $\Gamma_0/\Gamma$ for a system with fixed $x_\Gamma = 0.60\ \mu m$ in trivial states ($\Gamma = 3.5\Delta$) and topological states ($\Gamma = 7.5\Delta$), respectively. Here, two different values of $\delta x_V$, which defines the smoothness of the confinement potential $V(x)$ (Eq. (4.2), are considered. The energy splittings of trivial states, as shown in panel (a), are consistent for braiding ($E_0' \sim \varepsilon_m$) for perturbations in Zeeman field with $\Gamma_0/\Gamma \lesssim 0.30$. On the other hand, a threshold value with $\Gamma_0/\Gamma \sim 0.40$ is observed for measurement-based braiding in quasi-Majorana regime (with ps-ABSs) for topologically trivial systems ($\Gamma = 4.5\Delta$) with fixed $\delta x_V = 0.30\ \mu m$ but with two different length scales $x_\Gamma$, as shown in panel (b). Panel (d) shows the topological case ($\Gamma = 6.5\Delta$) of panel (b), where energy splittings are well below the black dashed line, as expected. The chemical potential is $\mu = 5.5\Delta$, and the other parameters used here are the same as Fig. 4.11.

very small SOC perturbation with $\alpha_0/\alpha \sim 0.05$ can increase the energy splittings of the unperturbed ps-ABS (cyan dashed line) by 10 times, provided the perturbation length scale $x_\alpha \sim 50, 80$sites (1 site $= 0.01\mu m$). On the other hand, for the energy splitting in the presence of SOC perturbation with a smoother step-like $\alpha(x)$ ($\delta x_\alpha = 0.05\ \mu m$), as shown in the top right panel of Fig. 4.12, the yellow region for a negative $\alpha_0$ is now mostly reduced compared with the top left panel in Fig. 4.12. Also, a general higher threshold value with $\alpha_0/\alpha \sim 0.25$ is observed now for increasing the energy splitting by 10 times (yellow regions). As shown in the bottom row of Fig. 4.12, there is no region with $\log(E_0'/E_0) > 0$ and most of the energy splittings in the presence of the SOC perturbation ( $E_0'$) admit $\log(E_0'/E_0) \sim (-1, 0)$.

Based on the results in Fig. 4.11, 4.12, we find that: i) the energy splittings of topologically trivial ps-ASBs can be affected by SOC perturbations with an enhancement $E_0'/E_0 \geq 10$, even with a small perturbation strength ($\sim 0.05$) if the length scale falls within $x_\alpha \sim 50, 80$ sites; ii) either an increase of

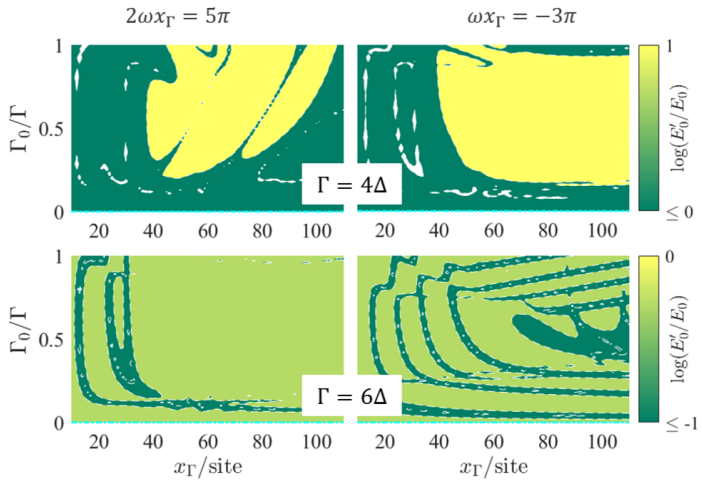


Figure 4.14: (Color online) Similar plot as Fig. 4.12 for $\log(E_0')/E_0$ under the influence of a twisted Zeeman potential (Eq. (4.6)). Here $\Gamma_0/\Gamma$ indicates the perturbation strength from the twisting of the Zeeman field. Length scale $x_\Gamma$ and frequency $\omega$ are varied simultaneously to satisfy $2\omega x_\Gamma = 5\pi$ in the left panels and $\omega x_\Gamma = -3\pi$ in the left panels, respectively. A threshold perturbation amplitude for ps-ABSs admitting braiding is found to be $\Gamma_0/\Gamma \sim 0.25$ for both the two types of the twisted Zeeman field, as shown in the top panels. In addition, the ps-ABSs can not be significantly perturbed in the presence of Zeeman filed perturbation with length scale $x_\Gamma \lesssim 40$sites, in which case, their energy splittings are all consistently below the braiding energy scale $\varepsilon_m$. The chemical potential is $\mu = 5\Delta$, and the other parameters used here are the same as Fig. 4.12.

the smoothness or the length scale of the step-like SOC perturbation will increase the threshold value of the perturbation strength needed to break the condition for measurement-based braiding in the quasi-Majorana regime; iii) the energy splittings of topologically trivial ps-ABSs are more likely to admit braiding in the presence of a negative SOC perturbation.

For a position-dependent Zeeman field, defined by Eq. (4.6), parameters $\Gamma_0, x_\Gamma$ and $\omega$ that describe the perturbation in $\Gamma$ are of interest. In Fig. 4.13(a), we show the logarithm of $E_0'/E_0$ for trivial ps-ABSs ($\Gamma = 3.5\Delta$) with two different smoothness parameters for the confinement potential, namely $\delta x_V = 0.30\ \mu m$ (blue line) and $\delta x_V = 0.35\ \mu m$ (cyan dashed line), where a perturbation strength $\Gamma_0/\Gamma \sim 0.25$ can split the energy from $E_0$ to $E_0' \geq 10E_0$. As expected, the energy splittings of the topological MZMs with $\Gamma = 7.5\Delta$ are immune to the twisted Zeeman potential, as shown in Fig. 4.13(c). Here a period $\omega = 3\pi/100$ is used (the black line in the middle panel of Fig. 4.4). In terms of different $x_\Gamma$ for a fixed $\omega = 3\pi/100$, we show the plot of $\log(E_0'/E_0)$ as a function of $\Gamma_0/\Gamma$ for the trivial state with $\Gamma = 4.5\Delta$ in Fig. 4.13(b), and topological state with $\Gamma = 6.5\Delta$ in Fig. 4.13(d). Here, the threshold value for $E_0' \geq 10E_0$ becomes $\Gamma_0/\Gamma \sim 0.4$ for the trivial ps-ABSs, while the topological MZMs still do not show any significant enhancement of the energy

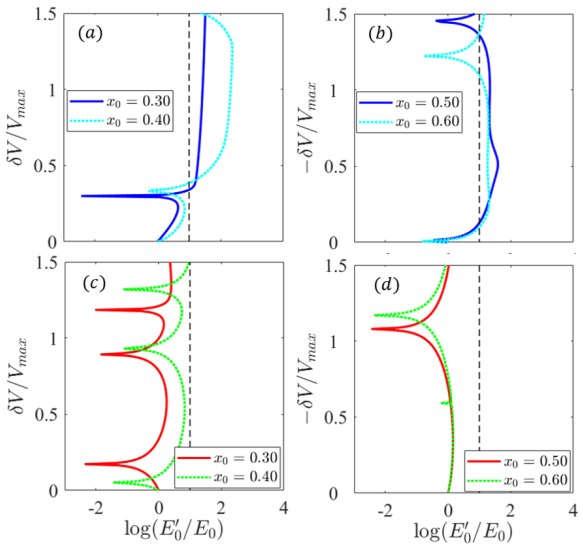


Figure 4.15: (Color online) Dependence of $\log(E_0'/E_0)$ on the perturbation strength $\delta V/V_{max}$ for system perturbed by a local potential perturbation, described by Eq. (4.7). As shown in panel (a) and (b), the energy splittings are generically increased (except for the decrease around $\delta V/V_{max} \approx 0.3$ ) with $\delta V \neq 0$ for the trivial ps-ABSs ($\Gamma = 4\Delta$). On the contrary, the energy splittings for the topological MZMs ($\Gamma = 6\Delta$) do not show this feature, as shown in panels (c), (d). For local perturbations with positive amplitude $\delta V/V_{max} \lesssim 0.40$, the energy splittings are well below the black dashed line, implying their applicability for braiding($E_0' \sim \varepsilon_m$), as shown in panel (a). In the case of a negative potential perturbation, as shown in panel (b), a smaller minimum perturbation strength with $-\delta V/V_{max} \sim 0.10$ is found to be able to increase the energy spitting as $\log(E_0'/E_0) \geq 1$. Panel (c), (d) give energy splittings in the topological case for the system in panel (a), (b), respectively, which are below the black dashed lines (though an enhancement might be present, as shown by the green dotted line in panel (c)). Here, the value of $x_0$ implies the location of the potential disorder, $\mu = 5\Delta$, and the confinement potential is characterized by the same parameters used in Fig. 4.11.

splittings. In Fig. 4.14, we show the $\log(E_0'/E_0)$ as a function of $\Gamma_0, x_\Gamma$ for system applied with a twisted Zeeman field with different periods satisfying $2\omega x_\Gamma = 5\pi$ (left panels) and $\omega x_\Gamma = -3\pi$ (right panels), respectively. The yellow regions (with $\log(E_0'/E_0 \geq 1)$) are present for both cases in the trivial regime, requiring a perturbation strength $\Gamma_0/\Gamma \geq 0.2$. However, in the topological regime, the energy splittings show $\log(E_0'/E_0) \leq 0$ for all the parameter ranges.

Based on the results in Fig. 4.13, 4.14, we conclude that, for the type of perturbation in the Zeeman field analyzed in this paper, i) ps-ABSs can sustain a perturbation in the Zeeman field provided the strength $\Gamma_0/\Gamma \lesssim 0.2$; ii) a higher threshold of the perturbation strength for the topologically trivial phase can be found for $\Gamma(x)$ with different length scales, e.g., for perturbations in the Zeeman field with $x_\Gamma = 50, 60, 80$ sites as shown in the top left panel of Fig. 4.14; and iii) perturbations with $x_\Gamma \leq 40$ in Zeeman potential cannot perturb the energy splittings of the ps-ABSs significantly (more than 10 times), i.e., ps-ABSs in these cases

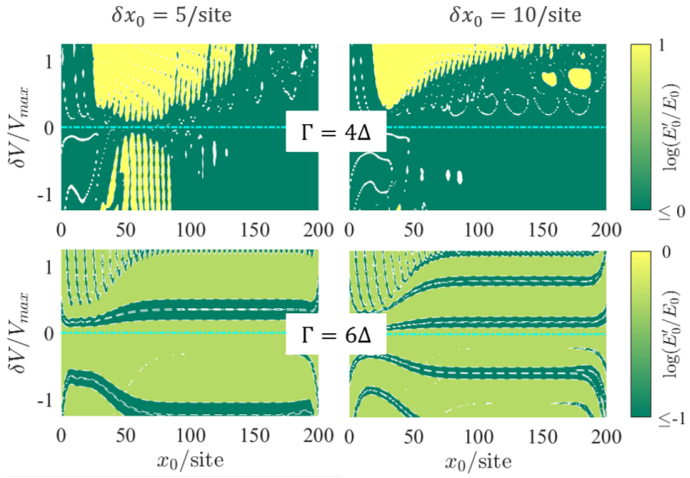


Figure 4.16: (Color online) The energy splittings ($\log(E_0'/E_0)$) under the influence of a local potential perturbation $\delta V(x)$ described by Eq. (4.7). As shown in the top left panel ($\delta x_0 = 0.02\ \mu m$), a threshold amplitude $\delta V/V_{max} \sim 0.10$ for $E_0' \sim \varepsilon_m$ is observed for both positive and negative $\delta V(x)$ if the perturbation is localized around $x_0 \sim (50, 80)$sites (where the component MBSs of ps-ABSs overlap with each other, consistent with the results found in Fig. 4.12). For the system perturbed by potential perturbation with $\delta x_0 = 0.10\ \mu m$, as shown in the top right panel, $\log(E_0'/E_0) \geq 1$ is satisfied at a relatively higher perturbation strength $\delta V/V_{max} \sim 0.3$ for a positive perturbation $\delta V(x)$. For both cases with different values of $\delta x_0$, the energy splittings in the topological states (bottom panels) do not show any significant enhancement ($E_0'/E_0 \geq 10$) as that observed for the trivial states. The parameters used here are the same as Fig. 4.15.

still admit TQC in the measurement-based braiding scheme.

Next, we investigate the sensitivity of the energy splitting to local potential perturbation, which can be described by the function given in Eq. (4.7). We consider both positive and negative local potential perturbations. As shown in Fig. 4.15, the left and right panels are associated with a positive and negative potential disorder, respectively. For the location of the perturbation $x_0 = 0.30\ \mu m$ (blue line) and $x_0 = 0.40\ \mu m$ (cyan dashed line) in Fig. 4.15(a), the energy splitting of ps-ABS can be lifted from $E_0$ to $10E_0'$ by a positive potential perturbation with strength $\delta V/V_{max} \sim 0.35$. In the case of a negative potential perturbation, $\log(E_0'/E_0) \geq 1$ can be satisfied even at a small perturbation strength $-\delta V/V_{max} = 0.1$, as shown in Fig. 4.15(b). On the other hand, a positive potential perturbation (Fig. 4.15(c)) can lift the energy splitting of a topological MZM much more in comparison with the negative potential (Fig. 4.15(d)), though they still satisfy $\log(E_0'/E_0) \leq 0$ at different perturbation strengths. Note that, the locations of the negative perturbations we considered in Fig. 4.15(b, d) are $x_0 = 0.50\ \mu m, 0.60\ \mu m$.

We plot $\log(E_0'/E_0)$ as a function of the potential perturbation parameters $\delta V$ and $x_0$ for different smoothness in Fig. 4.16, where $\delta V(x)$ with $\delta x_0 = 0.05\ \mu m$ (left panels in Fig. 4.16) is a sharp local potential

perturbation and $\delta V(x)$ with $\delta x_0 = 0.10\ \mu m$ (left panels in Fig. 4.16) is a relatively broader local potential perturbation. It is seen, as expected, that the 10-times increase of the energy splittings (yellow) appears at a very small perturbation strength ($\delta V/V_{max} \sim 0.1$), if the perturbation is located around the overlap region of the component MBSs of the ps-ABSs, i.e. $x_0 \sim (0.50 - 0.80)\mu m$ for both positive and negative potential perturbations. On the other hand, for $\delta V(x)$ with $\delta x_0 = 0.10\ \mu m$, a larger threshold value of the perturbation strength is required to split the energy from $E_0$ to $E_0' \geq 10E_0$, while for negative potential perturbation, almost no region with $\log(E_0'/E_0) \geq 1$ is present.

Based on the results in Fig. 4.15, 4.16, we find that, in the presence of a Gaussian-like local potential perturbation, i) the energy splittings of the ps-ABSs satisfy $E_0'/E_0 \geq 10$ even for a small perturbation strength $\delta V/V_{max} \sim 0.1$ if the perturbation is localized around the overlap region of the component MBSs of the ps-ABSs ($x_0 \sim (50 - 80)$ sites); ii) a higher threshold value for the perturbation strength is needed to satisfy $E_0'/E_0 \geq 10$, for either a perturbation with bigger $x_0$ or bigger $\delta x_0$; iii) a broad negative potential perturbation almost can not increase the energy splitting significantly.

It has been discussed in Ref. [90] that a sufficiently smooth confinement potential can host ps-ABSs with energy splitting below the braiding requirement. We test the stability of the seemingly robust ps-ABSs in the presence of local perturbations when the confinement potential is sufficiently smooth. We consider a system described by Eq. (4.3) with $\mu = 5\Delta$ and a confinement potential $V(x)$ with $V_{max} = 8\Delta, x_V = 0.2\ \mu m$. The lowest energy $E_0$ without any perturbations is shown by the contour plot of $\log(E_0)$ as a function of the Zeeman potential and the confinement potential smoothness parameter $\delta x_V$ in Fig. 4.17(a). Here the dark blue region with green index $-4$ indicates the energy splitting $E_0 \sim 0.1\ m\Delta$, which falls within the range of transmon sensitivity and are suitable for measurement-based braiding. It is clearly seen that, the energy splittings for the ps-ABSs in the trivial regime ($\Gamma < \Gamma_c$) are smaller when the confinement potential is smoother ($\delta x_V = 0 \rightarrow 0.50\ \mu m$), while the energy splittings in the topological regime (($\Gamma > \Gamma_c$) ) are not significantly affected by the change of $\delta x_V$. In the presence of local perturbations, the dark blue regions in the trivial regime with energy splitting $E_0' \sim 0.1\ \mu\Delta$ are greatly reduced by local potential perturbations (Fig. 4.17(b, c, d)), perturbations in the step-like SOC (Fig. 4.17(e, f)), and perturbations in the twisted Zeeman potential (Fig. 4.17(g, h)). By contrast, the energy splittings of the topological MZMs do not show any obvious changes under the effects of the local perturbations. However, it is important to note that, in the presence of the perturbations with relatively smaller strengths, as shown in Fig. 4.17(b, c, e, g), the dark blue regions corresponding to a green index -4 are still present, though over a reduced area. Therefore, the topologically trivial ps-ABSs can also be robust in the presence of weak perturbations, rendering the

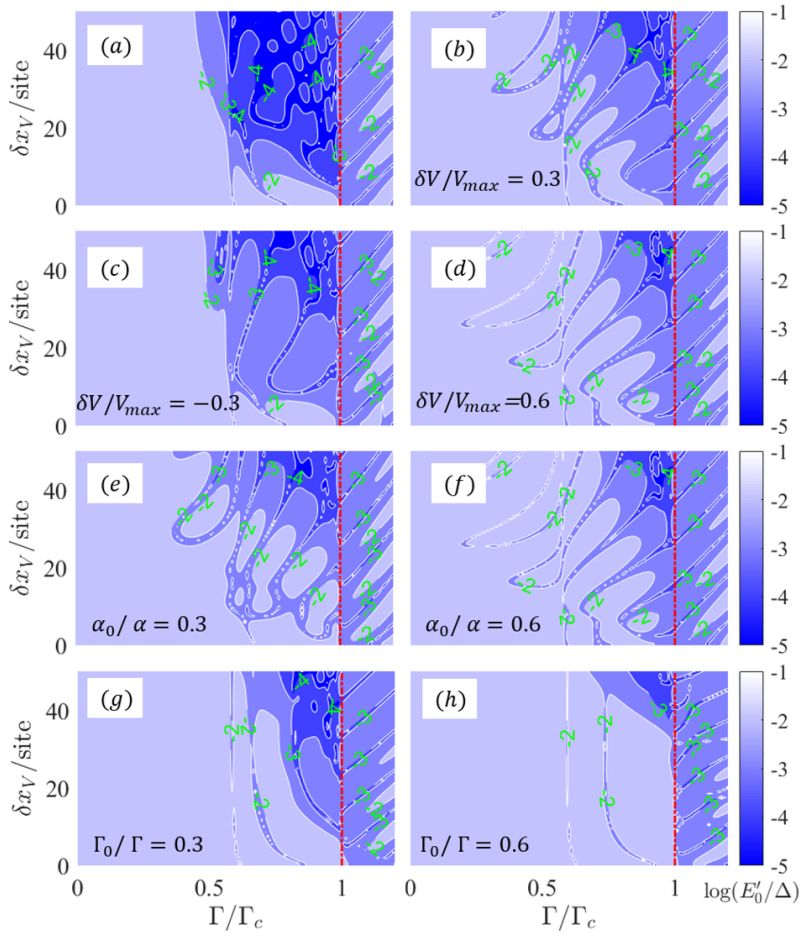


Figure 4.17: (Color online)The logarithm of the lowest energy $E_0$ of the Hamiltonian given in Eqs. (4.1, 4.3) as a function of the applied Zeeman potential ($\Gamma$, $x$-axis) and the smoothness parameter of the confinement potential ($\delta x_V$, $y$-aixs). The values of $\log(E_0)$ (unperturbed) or $\log(E_0')$ (perturbed by local perturbations) are indicated by the colors. Panel (a) shows the $\log(E_0)$ for a system with $m^* = 0.05m_e, \mu = 5\Delta, V_{max} = 8\Delta, \alpha = 0.2\, eV\text{Å}, \Delta = 0.25\, meV$ without the presence of any local perturbations. The dark blue color (with green index $-4$ ) represents energy splittings in the trivial state with $E_0 \lesssim \varepsilon_m$, which satisfy the readout condition in the measurement-based braiding scheme. The energy splittings in the presence of disorder from a local potential are shown in panels (b), (c), (d), where the dark blue region are greatly reduced. Similarly, the energy splittings of the trivial states are all unavoidably enhanced by the local perturbations either from a step-like SOC, as shown in panels (e), (f), or from a twisted Zeeman field, as shown in panels (g), (h). The topologically trivial states that satisfy $E_0 \lesssim \varepsilon_m$ in the unperturbed system in (a) (dark blue regions with index $(-4)$), generally obtain higher energy splittings that fail to meet braiding requirement. In contrast, the energy splittings for the topological states are not showing any evident changes in the presence of the local perturbations. Note that, for systems with a smoother confinement potential ($\delta x_V \gtrsim 0.40\ \mu m$), ps-ABSs in the trivial regime with energy splittings below the energy scale $\varepsilon_m$ for measurement-based braiding still exist in the presence of the local perturbations with relatively weaker strength, as shown in panel (b, c, e, g).

measurement-based braiding scheme realizable even in the quasi-Majorana regime.

Based on our extensive numerical calculations we conclude that the energy splittings for the topological MZMs are robust due to topological protection, and are immune to all types of local perturbations. By contrast, the topologically trivial ps-ABSs are very sensitive to local perturbations, failing to meet the readout requirement in the measurement-based braiding scheme ($E_0 \lesssim \varepsilon_m$) above a threshold strength of the perturbations. This is the case even if the energy splittings are sufficiently small in the unperturbed systems in the presence of sufficiently smooth confinement potentials. However, we also find that, in some cases, the energy splittings of the topologically trivial ps-ABSs may satisfy the braiding requirement $E_0 \lesssim \varepsilon_0$ in the presence of certain types of perturbations when they are sufficiently weak (as shown in Figs. (4.12, 4.14, 4.16, 4.17)).

## 4.5 Discussion and conclusion

In conclusion, we explicitly examine the robustness of the energy splitting of the MZM system in the quasi-Majorana regime, i.e., when the zero-bias tunneling peaks from the nanowire system are from the ps-ABSs rather than topological MZMs. Here by ps-ABSs we mean the low energy ABSs in which the MBSs are separated from each other by a length scale $\sim L^* \lesssim \zeta$ with $\zeta$ being the SC coherent length. These modes, which appear in the system even in a topologically trivial phase, can be contrasted with the topological MZMs which are separated by the length of nanowire $L$. In this paper we show that, it is possible to prepare the SM-SC system in the quasi-Majorana regime with energy splittings $\lesssim \varepsilon_m$, so measurement-based braiding is possible in principle. However, despite the apparent robustness of the ZBCPs in the quasi-Majorana regime to perturbations in local charge tunneling experiments, ps-ABSs are in reality topologically unprotected. Starting with ps-ABSs with energy below $\varepsilon_m$ we identify the maximum amplitudes of different types of perturbations (see Eqs. (4.5, 4.6, 4.7)) that are consistent with energy splittings below $\varepsilon_m$. Since any measurement is expected to generate one or more such local perturbations, we argue that, measurements generating perturbations larger than the threshold amplitudes appropriate for $\varepsilon_m$ can not realize topologically protected measurement-based braiding in SM-SC heterostructures in the quasi-Majorana regime (see Figs. 4.12, 4.14, 4.16). Topological quantum computation (TQC) based on measurement-based braiding in the quasi-Majorana regime thus requires a larger set of error corrections introduced by the measurement processes themselves, while such errors are absent in TQC involving topological MZMs.

# Chapter 5

# Majorana corner modes and higher order topological superfluidity in an attractive Hubbard-Hofstadter model of cold atom optical lattices

Higher order topological superconductors hosting Majorana-Kramers pairs (MKPs) as corner modes have recently been proposed in a two-dimensional (2D) quantum spin Hall insulator (QSHI) proximity-coupled to unconventional cuprate or iron-based superconductors. Here, we show that such MKPs can be realized using a conventional $s$-wave superfluid with a soliton in cold atom systems governed by the Hubbard-Hofstadter model. The MKPs emerge in the presence of interaction at the "corners" defined by the intersections of line solitons and the one-dimensional edges of the system. Our scheme is based on the recently realized cold atom Hubbard-Hofstadter lattice and will pave the way for observing possible higher order topological superfluidity with conventional $s$-wave superfluids/superconductors.

## 5.1 Introduction

$D$-dimensional topological insulators/superconductors (TI/TS) are characterized by a fully gapped bulk spectrum and stable gapless conducting states localized on $(D-1)$-dimensional boundaries [119, 120]. Examples include the 3D strong TI with an odd number of gapless Dirac cones localized on 2D surfaces and the 1D spinless $p$-wave superconductors (SC) with zero-dimensional Majorana zero modes (MZMs) localized near the end points of the system. By contrast, the recently-introduced so-called higher order TI/TS are gapped in the bulk as well as on the $(D-1)$-dimensional boundary, but have robust gapless topological modes on $(D-2)$-dimensional "edges" defined on the boundary, e.g., corners in 2D systems and hinges in 3D systems. This idea has been used to explain the existence of protected low energy corner modes in 2D quantized eletric quadrupole insulators [29, 121, 122, 27, 26, 123, 31, 124, 125] and the existence of 1D protected gapless hinge-modes in 3D crystals of bismuth [30].

It has been recently proposed [126, 34, 35] that zero-dimensional Majorana corner modes (MCMs) in 2D SC systems can be realized from a combination of 2D TI (QSHI) and unconventional (non-$s$-wave) superconductors. Excitations in these systems come in the form of MKPs, which are distinct from non-degenerate MZMs [6, 12, 127, 67, 13, 128, 129, 14, 130, 131, 66] and are protected by time reversal (TR) symmetry [132, 133, 134, 135, 136, 137, 138, 36, 139, 140, 141, 142, 143, 144, 145, 146, 147, 148, 149, 150]. Unfortunately, MCMs proposed in the condensed matter systems [151, 152, 153, 126, 34, 35, 154, 155] have not been realized to date.

In this paper, we propose ultracold atoms in optical lattices as a clean and straightforward route to realize MCMs and higher order topological superfluidity with ordinary $s$-wave superfluids. 2D QSHI Hamiltonians have now been experimentally realized in cold atom systems on square optical lattices [156]. These systems are accurately modeled by a two-component Hofstadter model in a TR invariant scheme where the atoms experience opposite uniform magnetic fields for each of the two components [157, 158, 159, 156, 160, 161, 162, 163]. Furthermore, $s$-wave superfluidity can be induced with an attractive Hubbard interaction arising from a Feshbach resonance between the fermions [164, 165, 166, 167, 168, 169, 170]. Specifically, we study a 2D TR invariant Hofstadter model, $H_0$, with an attractive Hubbard interaction, $H_I$: $H = H_0 + H_I$. The model is characterized by an interaction-controlled phase transition between a QSHI and a superfluid (SF). Above a critical value of the attractive interaction, both the edge and the bulk have a non-zero superfluid order parameter due to BCS-like pairing. Since the edge spectrum is gapped, the 2D superfluid is topologically trivial, according to the conventional (lower order) bulk-boundary correspondence. We show,

however, that the superfluid can host MKPs when a line soliton intersects the edges, changing the sign of the superfluid order parameter [34, 35]. Dark solitons [171], which have been successfully observed recently in Fermi gases [172, 173, 174] using phase imprinting [175], can arise as topological defects where the order parameter vanishes and the phase changes by $\pi$ [176, 177]. Intuitively, the edge states are gapped by the superfluid order parameter, which acts as a Dirac mass. At the intersection of the dark line soliton with the sample edges, the superfluid order parameter (hence the Dirac mass) changes sign, producing a pair of localized zero-dimensional MZMs protected by TR symmetry. Tunneling into the soliton edges can be used to observe these MKPs [176]. We emphasize that the uniform superfluid with no soliton is topologically trivial (in the conventional sense), with the appropriate $\mathcal{Z}_2$ invariant [178] being trivially zero because of the absence of gapless edge modes. Therefore, our work proposes the first cold atom-based realization of $(D-2)$-dimensional MZMs in what is a $D$-dimensional topologically trivial system in the conventional sense and is thus an experimentally realizable higher order topological superfluid.

## 5.2 Non-interacting model and Hofstadter bands

The Hofstadter model [158] describes non-interacting particles on a 2D lattice in the presence of a perpendicular magnetic field $\boldsymbol{B} = B\hat{z}$ given by the vector potential $\boldsymbol{A} = (0, Bx, 0)$. We consider a generalization of the original model that includes a spin-dependent magnetic field:

$$\begin{aligned} H_0 &= -\sum_{i,j,\sigma} \left[ t_x c^\dagger_{i,j,\sigma} c_{i+1,j,\sigma} + t^\sigma_y(i) c^\dagger_{i,j,\sigma} c_{i,j+1,\sigma} + h.c. \right] \\ &+ \sum_{i,j,\sigma} \left( V_{i,j} - \mu \right) c^\dagger_{i,j,\sigma} c_{i,j,\sigma}, \end{aligned} \tag{5.1}$$

where $(i,j)$ labels the sites of a square lattice with lattice constant $a$, $c^\dagger_{i,j,\sigma}$ $(c_{i,j,\sigma})$ creates (annihilates) a particle at $(i,j)$ with spin $\sigma \equiv \{\uparrow, \downarrow\}$, $t_x = t$ and $|t^\sigma_y(i)| = t$ are nearest-neighbor hopping amplitudes along the $x$ and $y$ directions, respectively. We set $t = 1$ and consider i) periodic boundary conditions, ii) a cylindrical geometry (periodic in the $y$-direction and a finite width in the $x$ direction, $L_x = aN_x$), and iii) a rectangular geometry with $L_x = aN_x$, $L_y = aN_y$. The chemical potential is $\mu$, while $V_{i,j}$ is a position-dependent confinement potential. To investigate the effect of soft confinement on $H_0$ in Eq. (5.1), we consider a Gaussian potential characterized by the following spatial dependence for systems with cylindrical

geometries:

$$V(x_i) = V_0 \left( e^{-x_i^2/\delta^2} + e^{-(L_x - x_i)^2/\delta^2} \right), \tag{5.2}$$

and rectangular geometries:

$$V(x_i, y_j) = V_0 \, e^{-d_{ij}^2/\delta^2}, \tag{5.3}$$

where $V_0$ is the amplitude of the confining potential and $d_{ij}$ is the 'distance' to the boundary of a rectangular system defined as

$$\frac{1}{d_{ij}} = \frac{1}{x_i} + \frac{1}{y_j} + \frac{1}{L_x - x_i} + \frac{1}{L_y - y_j} \tag{5.4}$$

Here $\delta$ is a parameter controlling the edge confinement strength. These forms for $V$ induce edge modes used in simulations in this paper where we choose $\delta = 1.5a$ and $V_0 = 5t$.

In the presence of the (spin-dependent) magnetic field, the hopping amplitude $t_y^\sigma(i)$ acquires a spin- and $x$-dependent phase factor $e^{i2\pi\phi_{x_i,\sigma}}$, with $\phi_{x_i,\sigma} = s_\sigma eBax_i/h$. Here, $x_i = ia$ is position along the $x$-direction while $s_\uparrow = 1, s_\downarrow = -1$ correspond to opposite magnetic field orientations for the two spin components, which explicitly restores TR symmetry, in contrast with the original Hofstadter model. We define the number of magnetic-flux quanta per unit cell as $\alpha = (Ba^2)/\phi_0$, with $\phi_0 = h/e$ the magnetic-flux quantum, and we have $t_y^\sigma(\ell) = te^{s_\sigma i2\pi\alpha\ell}$. For $\alpha = p/q$, with $p$ and $q$ primes, the single-particle energy spectrum is given by $q$ sub-bands $\epsilon_{\mathbf{k}n}$, with $n = 0, 1, 2, ..., q-1$. Here, we focus on the case $\alpha = 1/3$. We expect similar physics for other values of $\alpha$ that support QSHI phases.

Eq. (5.1) with $\alpha = 0$ can be written as $H_0(\boldsymbol{k}) = -2t \sum_{k_x,k_y,\sigma} [\cos(k_x) + \cos(k_y)]$ in momentum space with $\mathbf{k} = (k_x, k_y)$. The corresponding energy spectrum has a bandwidth of $8t$ and the system is topologically trivial. To explore a topologically nontrivial regime, we consider $\alpha = 1/3$ and use the Fourier transform $c_{i,j,\sigma} = N_0^{-1/2} \sum_k e^{i\mathbf{kr}} c_{k,\beta,\sigma}$, where $\mathbf{r} = (i, j)$ and $N_0$ is the total number of lattice sites. The field-induced phase factors contained in $t_y^\sigma(\ell)$ give rise to a new periodicity in the $x$-direction: $e^{i2\pi s_\sigma \alpha\ell} = 1, e^{i2\pi s_\sigma/3}, e^{i4\pi s_\sigma/3}$ for $\ell \bmod 3 = 0, 1, 2$, respectively. We label the non-equivalent sites in the $n^{\text{th}}$ magnetic unit cell as $\beta = 0, 1, 2$ and we have $x_\ell/a = \ell(n, \beta) = nq + \beta$. The corresponding first Brillouin zone is

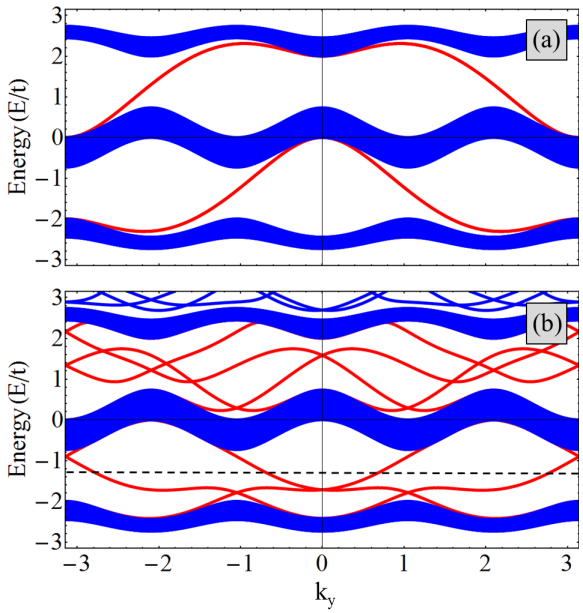


Figure 5.1: Band structure of the non-interacting two-component Hofstadter model, $H_0$, with $\alpha = 1/3$ and periodic boundary conditions in the y-direction. (a) System with $N_x = 92$ and hard confinement in the x-direction. (b) System with $N_x = 92$ and soft (Gaussian) confinement (see Eq. (5.2), (5.3)). The bulk states are shown in blue and the red curves represent the gapless edge modes.

$k_x \in [-\pi/q, \pi/q]$ and $k_y \in [-\pi, \pi]$. After Fourier transforming, we can rewrite $H_0$ as

$$H_0(\mathbf{k}) = \sum_{\mathbf{k}\sigma} \psi^\dagger_{\mathbf{k},\sigma} \begin{pmatrix} h_0 & e^{ik_y} & e^{-ik_y} \\ e^{-ik_y} & h_1 & e^{ik_y} \\ e^{ik_y} & e^{-ik_y} & h_2 \end{pmatrix} \otimes I_2 \psi_{\mathbf{k},\sigma} \tag{5.5}$$

where $I_n$ is the $n \times n$ identity matrix, $\mathbf{k}_\beta = (k_x - \beta 2\pi\alpha, k_y)$, $\psi_{\mathbf{k},\sigma} = (c_{\mathbf{k}_1,\sigma}, c_{\mathbf{k}_2,\sigma}, c_{\mathbf{k}_3,\sigma})^T$, and $h_\beta = 2\cos(k_x - 2\pi\beta\alpha)$, with $\beta = 0, 1, 2$. The corresponding band structure is characterized by $q = 3$ spin-degenerate bands with non-zero Berry curvature $\Omega^\sigma_{\mathbf{k}}$ and non-zero spin-dependent Chern number. Although the total Chern number of a fully-filled band is zero due to TR symmetry [179], the corresponding $\mathcal{Z}_2$ invariant reveals a topological-nontrivial QSHI phase.

The characteristic edge modes can be obtained using a cylindrical geometry with periodic boundary conditions in the $y$-direction. The corresponding band structure for a system with both hard and soft confinement (Eqs. (5.2, 5.3)) is shown in Fig. 5.1. The red lines indicate the (confinement-dependent) gapless edge states, while the (dense) blue lines correspond to the bulk spectrum. When the chemical potential intersects the red

lines, e.g., at $\pm\mathbf{k}_\sigma$, the system supports a pair of gapless edge states $(\mathbf{k}_\uparrow, -\mathbf{k}_\downarrow)$ located along one of the edges and another pair $(-\mathbf{k}_\uparrow, \mathbf{k}_\downarrow)$ located on the other edge. Consequently, if $\mu$ lies within a bulk gap, the system is in a topological QSHI phase with pairs of counter-propagating gapless modes located along the edges.

## 5.3 Attractive interactions

Next, we introduce an attractive interaction described in real space by the Hubbard term

$$H_I = -U \sum_{i,j} n_{i,j,\uparrow} n_{i,j,\downarrow}, \tag{5.6}$$

where $U > 0$ is the magnitude of the on-site attraction. In cold atom systems, the interaction can derive from an attractive Feshbach resonance [167, 170]. We study the effect of this attractive interaction at the mean-field level using a BCS-like approximation. In $k$-space, we have

$$H_I \to \sum_{\mathbf{k},\beta} \left( \Delta^\dagger c_{-\mathbf{k},\beta\downarrow} c_{\mathbf{k},\beta\uparrow} + \Delta c^\dagger_{\mathbf{k},\beta\uparrow} c^\dagger_{-\mathbf{k},\beta\downarrow} \right) + \frac{3N_0}{U} |\Delta|^2, \tag{5.7}$$

where we have introduced a uniform [180] order parameter $\Delta = -(U/N_0) \sum_{\mathbf{k}} \langle c_{-\mathbf{k},\beta\downarrow} c_{\mathbf{k},\beta\uparrow} \rangle$, with $\langle ... \rangle$ indicating the thermal average. At this mean-field level, the total Hamiltonian becomes

$$H_{MF} = \sum_{\mathbf{k}} \Psi^\dagger_{\mathbf{k}} \begin{pmatrix} h_B(\mathbf{k}) - \mu & \Delta \cdot I_3 \\ \Delta^\dagger \cdot I_3 & -h^*_B(-\mathbf{k}) + \mu \end{pmatrix} \Psi_{\mathbf{k}} + \mathcal{E} \tag{5.8}$$

where $\Psi_{\mathbf{k}} = (\psi_{\mathbf{k},\uparrow}, \psi^\dagger_{-\mathbf{k},\downarrow})^T$, and $h_B$ is the matrix in Eq. (5.5), and $\mathcal{E} = -\sum_{\mathbf{k}} \left( 3\mu - 3|\Delta|^2/U + \mathbf{Tr} E_{-\mathbf{k},\downarrow} \right)$ is an energy offset. We solve $H_{MF}$ using a BCS-like self consistent method [165, 166]. We find that the order parameter equation simplifies as:

$$\frac{1}{U} = \frac{1}{3N_0} \sum_{\mathbf{k},\beta} \frac{1}{2E_{\mathbf{k},\beta}} \tanh\left( \frac{E_{\mathbf{k},\beta}}{2k_B T} \right). \tag{5.9}$$

Note the quasiparticle energy $E_{\mathbf{k},\beta} = \sqrt{\epsilon_{\mathbf{k},\beta} + |\Delta|^2}$ is the same for both spin states due to TR symmetry. We also have a self-consistent equation for $\mu$ since now, $\mu$ is determined by the total number of particles $N = \sum_{i,j,\sigma} n_{i,j,\sigma}$, which gives:

$$n = \frac{N}{N_0} = \frac{1}{3N_0} \sum_{\mathbf{k},\beta} \left[ 1 - \frac{\epsilon_{\mathbf{k},\beta}}{E_{\mathbf{k},\beta}} \tanh\left( \frac{E_{\mathbf{k},\beta}}{2k_B T} \right) \right] \tag{5.10}$$

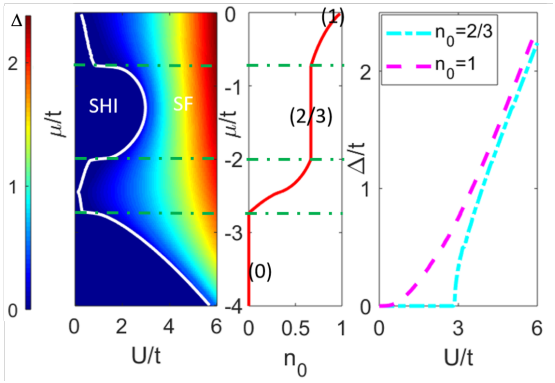


Figure 5.2: (Color online) *Left*: The mean-field phase diagram obtained by plotting the self-consistent value of the pairing order parameter $\Delta$ for $k_BT = 10^{-4}t$. The dashed-white line indicates the phase boundary. *Center*: Chemical potential as function of the filling factor for $\Delta = 0$. *Right*: Mean-field $\Delta$ as function of the interaction strength for two different filling factors. The $n_0 = 1$ line shows $\Delta \neq 0$ (i.e. superfluid phase) all the way to $U \sim 0$, while for $n_0 = 2/3$ one needs $U \sim 3t$ to enter the superfluid phase.. The green dotted lines mark the band edges of the bulk spectrum in Fig. 5.1.

To obtain the phase diagram we self-consistently solve Eqs. (5.9) and (5.10).

The mean-field phase diagram corresponding to Eq. (5.8) is shown in Fig. 5.2. When the chemical potential lies within the bulk gap, the self-consistent value of the s-wave pairing becomes non-zero only above a finite interaction strength $U_c(\mu)$. For $U < U_c(\mu)$ the system is in a QSHI phase with $\Delta = 0$, while $U > U_c(\mu)$ corresponds to the superfluid phase ($\Delta \neq 0$). Note that for $\mu \in [-2t, -0.7t]$, the phase transition from a QSHI state with filling factor $n_0 = 2/3$ to the SF state occurs at a critical interaction on the order of $3t$. On the other hand, at half filling ($n_0 = 1$) $\Delta \neq 0$ for any finite $U$ and the system is in a SF phase. Below, we will show that the SF phase supports MKPs in the presence of a line soliton, when the order parameter changes sign.

## 5.4 Soliton-induced Majorana zero-energy modes

Next, we show that in the presence of a line soliton, MKPs emerge at the "corners" defined by the intersection of the soliton with the edge of the system, which is in a TR symmetric SF phase. In the presence of a dark soliton, the order parameter changes sign, vanishing along a node line. To study the impact of the soliton, we construct the self-consistent BdG formalism in real space. We start by decomposing the Hubbard

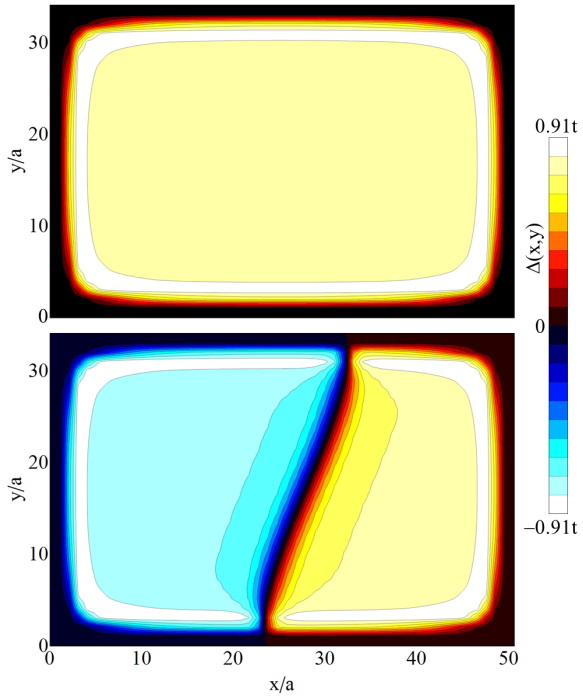


Figure 5.3: Position-dependent pairing potential $\Delta(x, y)$ for a strongly interacting system with $U = 3.5t$, i.e., in the SF phase. The pairing potential is obtained as the self-consistent solution of the mean-field equations (5.12-5.15) for a finite system with $N_x \times N_y = 50 \times 34$ and soft confinement (see Eqs. (5.2, 5.3)) at finite temperature, $k_B T = 0.01t$. The total number of particles is fixed, $N = 800$. *Top*: Self-consistent solution with constant phase. The (self-consistent) chemical potential is $\mu = -1.250t$. *Bottom*: Self-consistent solution with a line soliton. The chemical potential is $\mu = -1.248t$. Note that $\Delta(x, y)$ is nonzero in the bulk – consistent with phase diagram in Fig. 5.2(b) – as well as on the boundary of the system, except along the line soliton.

interaction as:

$$H_I \to \sum_{i,j} \left( \Delta^*_{i,j} c_{i,j,\downarrow} c_{i,j,\uparrow} + \Delta_{i,j} c^\dagger_{i,j,\uparrow} c^\dagger_{i,j,\downarrow} + \frac{|\Delta_{i,j}|^2}{U} \right) \tag{5.11}$$

where the real-space order parameter is defined as $\Delta_{i,j} = -U \langle c_{i,j,\downarrow} c_{i,j,\uparrow} \rangle$.

By combining Eqs. (5.1) and (5.11), we arrive at a real-space mean field approximation to $H$. We can diagonalize this using a Bogoliubov transformation $c_{\mathbf{r},\sigma} = \sum_{n=1}^{2N_0} \left( u^n_{r\sigma} d_n + v^{n*}_{r\sigma} d^\dagger_n \right)$, where $d_n, d^\dagger_n$ are the quasiparticle operators with index $n = 1, 2, ..., 2N_0$, and $u^n_{\mathbf{r}\sigma} = [u_{\mathbf{r}\uparrow}, u_{\mathbf{r}\downarrow}]^T, v^n_{\mathbf{r}\sigma} = [v_{\mathbf{r}\uparrow}, v_{\mathbf{r}\downarrow}]^T$ are the corresponding components for each of the Fermioninc operators in the basis $\psi_{\mathbf{r}} = \left( c_{\mathbf{r}\uparrow}, c_{\mathbf{r}\downarrow}, c^\dagger_{\mathbf{r}\uparrow}, c^\dagger_{\mathbf{r}\downarrow} \right)^T$. The

result is the set of real-space BdG equations:

$$
\begin{aligned}
H_{BdG} &= \sum_{\mathbf{r}\mathbf{r}'} \psi^{\dagger}_{\mathbf{r}} h^{\mathbf{r}\mathbf{r}'}_{BdG} \psi_{\mathbf{r}} + \mathcal{E}', \\
h^{\mathbf{r}\mathbf{r}'}_{BdG} &= \begin{pmatrix} H_0^{\mathbf{r}\mathbf{r}'} & \Delta_{\mathbf{r}\mathbf{r}'} \\ \Delta^{*}_{\mathbf{r}\mathbf{r}'} & -\sigma_y H_0^{\mathbf{r}\mathbf{r}'*} \sigma_y \end{pmatrix}
\end{aligned}
\tag{5.12}
$$

where $\mathcal{E}'$ is the ground state energy, $\sigma_y$ is the usual Pauli matrix, $H_0^{\mathbf{r}\mathbf{r}'}$ are the individual terms in the non-interacting Hamiltonian [Eq. (5.1)], and the matrix $h^{\mathbf{r}\mathbf{r}'}_{BdG}$ satisfies:

$$
\sum_{r'} h^{\mathbf{r}\mathbf{r}'}_{BdG} \begin{pmatrix} u^n_{\mathbf{r}'\sigma} \\ v^n_{\mathbf{r}'\sigma} \end{pmatrix} = E_n \begin{pmatrix} u^n_{\mathbf{r}\sigma} \\ v^n_{\mathbf{r}\sigma} \end{pmatrix}
\tag{5.13}
$$

with $E_n$ the $n_{th}$ excitation energy, and the corresponding eigenvectors are the wave functions in real space. The BdG equations given in Eq. (5.12) and Eq. (5.13) should be solved self-consistently with the number density and s-wave pairing order parameter equations given by [176, 177, 181, 182, 183]:

$$
\langle n_{\mathbf{r}\sigma} \rangle = \sum_{n=1}^{2N_0} \left[ |u^n_{\mathbf{r}\sigma}|^2 f(E_n) + |v^n_{\mathbf{r}\sigma}|^2 f(-E_n) \right]
\tag{5.14}
$$

$$
\Delta_{\mathbf{r}\mathbf{r}'} = -|U| \delta_{\mathbf{r}\mathbf{r}'} \sum_{n=1}^{2N_0} \left[ u^n_{\mathbf{r}\uparrow} v^{n*}_{\mathbf{r}\downarrow} f(E_n) + u^n_{\mathbf{r}\downarrow} v^{n*}_{\mathbf{r}\uparrow} f(-E_n) \right]
\tag{5.15}
$$

where $f(E) = 1/(1 + e^{E/k_B T})$ is the Fermi-Dirac distribution and $E$ is taken relative to the Fermi energy. Eq. (5.14) is constrained by $n_0 = \sum_{\mathbf{r}\sigma} \langle n_{\mathbf{r}\sigma} \rangle / N_0$. As for the pairing order parameter, we first need to choose a set of different values of $\Delta_{\mathbf{r}}$ and self-consistently solve the BdG Hamiltonian in real space for all of the quasiparticle wavefunctions and their corresponding eigen-energies. In the last stage of the calculation we find improved values for $\Delta_{\mathbf{r}}$ from Eq. (5.15) while the chemical potential is adjusted to satisfy the filling factor constraint, based on Eq. (5.14). We do these iterative steps to reach convergence for both Eq. (5.14) and Eq. (5.15). We choose the initial value of the order parameter to be used in the self-consistent scheme as: $\widetilde{\Delta}_{i,j} = \Delta_{i,j} \tanh[(i - 28 + 5\cos[(j-1)\pi/(N_y - 1)])/\xi]$, where $\Delta_{i,j}$ is a constant phase self-consistent solution (i.e. obtained without the soliton) and $\xi = 2.5$. We then solve the BdG equations for $N_x \times N_y = 50 \times 34$ sites and $n_0 = 2/3$.

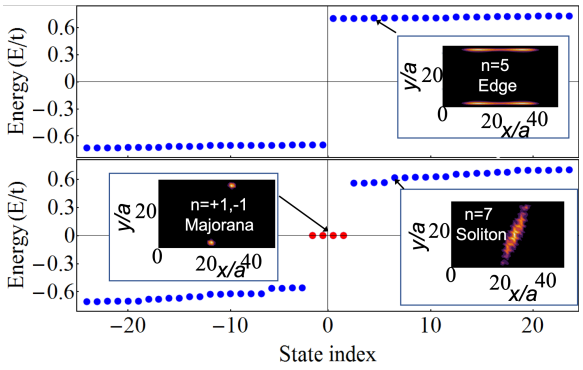


Figure 5.4: *Top*: Low-energy spectrum of the Hofstadter-Hubbard model with strong interaction ($U = 3.5t$) within the mean-field approximation for a system with constant phase pairing potential and parameters corresponding to Fig. 5.3 (top panel). *Bottom*: The same but for parameters corresponding to the bottom panel of Fig. 5.3. Note that in the presence of a line soliton the system hosts two pairs of zero-energy Majorana bound states (red dots). The insets plot the wave functions of the states marked by arrows.

In Fig. 5.3 we show the self-consistent solution for $\Delta(x, y)$ for a system with $U = 3.5t$ without a soliton (top panel) and with a line soliton (bottom panel). Note that $U > U_c(\mu)$, so that, without the soliton, the system is in a SF phase with a non-vanishing order parameter both in the bulk and on the edge. The bottom panel shows that the soliton changes the sign of the order parameter, as expected. The low-energy spectra corresponding to the self-consistent solutions in Fig. 5.3 are shown in Fig. 5.4. The top panel (no soliton) is characterized by a finite quasiparticle gap and low-energy states located along the edges of the system (see inset). The bottom panel, corresponding to a system with a soliton, has four zero-energy states (red circles) representing the MKPs. As shown in the inset, the corresponding wave functions are localized at the intersection of the line soliton with the edges of the system.

Fig. 5.5 plots the same as Fig. 5.3 but for weaker attraction, $U = 2t$. Here we see that, in the weak pairing regime with $U < U_c(\mu)$, the order parameter vanishes in the bulk, but remains finite on the edge, where it changes sign in the presence of a soliton. These edge modes still allow MKPs even for weak pairing. The soliton shown in Fig. 5.5 hosts MKPs at the edge. To see this Fig. 5.6 plots the states in the weak pairing regime as that in Fig. 5.3. Here we also see that the zero-energy states (red circles) correspond to MKPs.

Our results show that MKPs can be induced at soliton edges in a conventional s-wave SF. In the following section, we will show that the line soliton and the corresponding MKPs are robust against small perturbations (e.g., thermal fluctuations and on-site disorder) and are thus topologically robust.

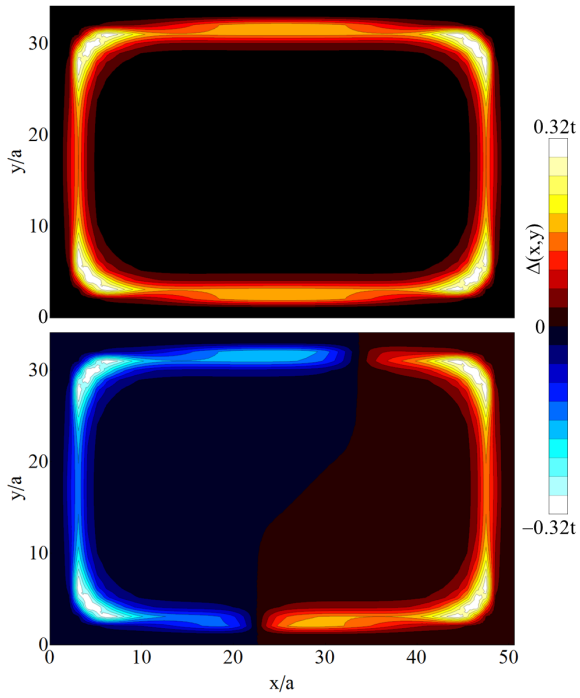


Figure 5.5: The same as Fig. 5.3 but for weak pairing, $U = 2t$ (i.e. in the QSHI phase). *Top*: Self-consistent solution with constant phase. The (self-consistent) chemical potential is $\mu = -1.258t$. *Bottom*: Self-consistent solution with a line soliton associated with a $\pi$ phase change. The (self-consistent) chemical potential is $\mu = -1.255t$. Note that $\Delta(x, y)$ is nonzero only on the boundary of the system (where the low-lying edge modes are located), while the bulk $\Delta(x, y)$ vanished, in agreement with the phase diagram in Fig. 5.2(b).

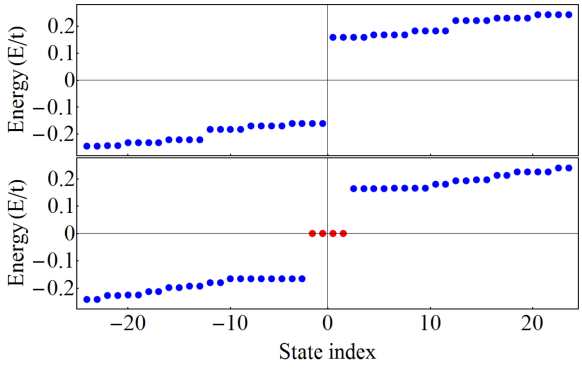


Figure 5.6: Low-energy spectrum of the Hofstadter-Hubbard model within the mean-field approximation for a weakly interacting system ($U = 2t$) with constant phase pairing potential and all other parameters corresponding to Fig. 5.3 (top panel). The bottom plots the same but with a line soliton. The red circles in the bottom panel correspond to MKPs found at the soliton edges in the weak pairing phase.

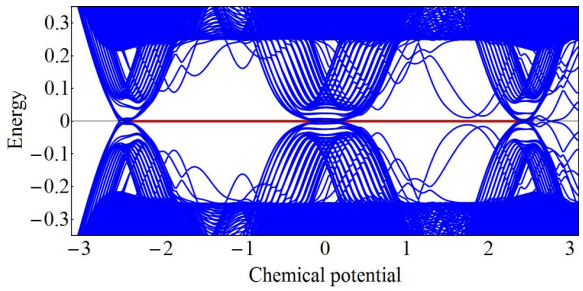


Figure 5.7: Low energy spectrum of the Hamiltonian in Eq. 5.13 as a function of chemical potential in the presence of a soliton (see the initial value of the order parameter $\widetilde{\Delta}_{i,j}$ for the BdG Hamiltonian in Eq. 5.12) for a finite system with $N_x \times N_y = 50 \times 34$ and soft confinement (Eq. 5.3). The red line represents the robust degenerate Majorana zero modes. The rest of parameters used here are the same as in Fig. 5.1.

## 5.5 Connection with higher-order topological superconductors

The relation of the proposed setup with higher order topological superconductors can be argued as follows: In the presence of the superconducting pair potential, i.e, when the system is in the superfluid phase, the edge state spectrum is fully gapped (see Fig. 5.4, top panel). The absence of gapless edge modes in the superfluid phase signals that the two-dimensional time reversal invariant superfluid is topologically trivial (according to the conventional classification). Thus, one would expect an order parameter defect, such as a line soliton, to *not* harbor robust gapless Majorana zero modes of any dimension. Yet, we find that precisely the opposite happens: zero-dimensional MKPs are nucleated at the edges of the 2D trivial superconductor/superfluid whenever the gap changes sign along a line soliton.

Fig. 5.7 shows explicitly the low-energy spectrum of the system as function of the chemical potential (in the presence of a soliton). Here the red line represents the (degenerate) Majorana modes, which have characteristic energies on the order on $10^{-8}t$, orders of magnitude smaller than the thickness of the line. The low-energy modes around $\mu = -2.5t$, $0$, $2.5t$ correspond to states localized along the soliton line when the system is *not* gapped (note that the corresponding spectrum is shown in the paper as Fig. 5.1(b)). Their characteristic energy is small but finite and depends on the characteristic (transverse) length scale $\xi$ of the soliton. The finite energy in-gap modes (blue lines) corresponding to a non-superconducting QSHI phase are edge modes that are highly dependent on the confinement of the cold atom system.

Next, we examine whether the emergence of the MKPs is an effect due to the special properties of the defect (as has been discussed, for instance, in Ref. [184], with defects defined by a Hopf invariant), rather than a property of the underlying superfluid. Consequently, we have considered a “garden variety”

topologically trivial superconductor, that is, an $s$-wave superconductor with the non-superconducting normal state being a two-band Fermi gas. The normal state spectrum of the system (in the stripe geometry) is shown in the Fig. 5.8. There are two bulk bands separated by a gap of about $2t$ and, inside the gap, there are three (degenerate) trivial edge modes. Note that the structure of the spectrum is, basically, the same as that in Fig. 5.1 (with two bands, instead of three), except that the edge modes are now topologically trivial. We also plot the the low-energy spectrum as function of the chemical potential in the presence of supeconducting pairing with a soliton in Fig. 5.9. Note that the only qualitative difference between Fig. 5.9 and Fig. 5.7 is the absence of the Majorana zero modes (red line) in the trivial case. The other types of in-gap states (localized along the soliton or along the physical edge of the system) are present in both systems.

The results allow us to conclude that the presence of the MKPs in the proposed system (where the non-superconducting parent system is a QSHI) is *not* due to some special properties of the defect (as it does not induce MKPs in a topologically trivial superconductor/superfluid), but due to the intrinsic properties of the superfluid. Since this superfluid is topologically-trivial, according to the conventional classification, it must represent a type of higher order topological superfluid. It remains to be shown that the topological robustness of the MKPs induced in the proposed system. We have considered the effect of (potential) disorder. Fig. 5.10 plots the corresponding low-energy spectrum (as function of the chemical potential) where we have applied potential disorder. Here we note that that the Majorana modes are robust (characteristic energies on the order on $10^{-8}t$) within the whole range of parameters characterized by a sizable quasiparticle gap ($0.05t$ and above). By contrast, the low-energy modes localized along the soliton line (which are now clearly gapped) are strongly dependent on the disorder potential. To summarize, the above arguments convincingly

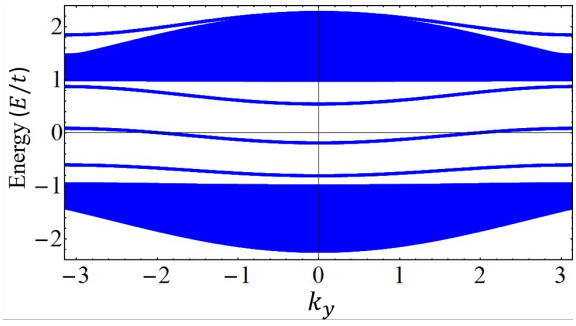


Figure 5.8: The same as Fig. 5.1(a) but with $\alpha = 0$, i.e., the energy eigenvalues for a zero-field hopping model. There is no magnetic field coupling with the spin components, rendering the system a non-interacting two-band Fermi gas. The two bands are separated by a gap of about $2t$, within which the blue lines represent trivial edge modes.

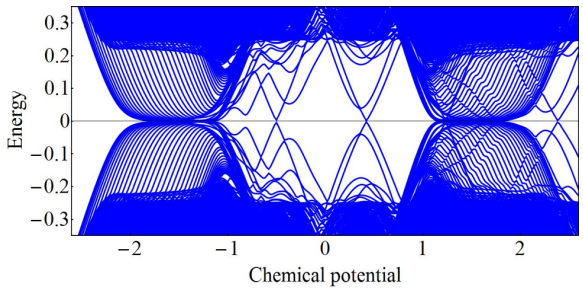


Figure 5.9: The same as Fig. 5.7 but for a trivial superfluid for which the parent system is a two-component Fermi gas, i.e., $\alpha = 0$. We see that this system reveals the same qualitative spectrum as the one in Fig. 5.7 for which the parent system is a QSHI but there is no Majorana zero mode (red line in Fig. 5.7). This shows that the soliton induces (D-2)-dimensional Majorana zero modes *only* when the parent system is a QSHI and not when the non-SF system is a Fermi gas. The parameters used are the same as in Fig. 5.7.

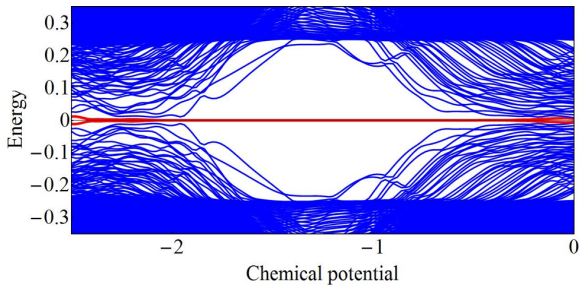


Figure 5.10: The same as Fig. 5.7 but with on-site disorder (with a disorder strength $V_0 = 0.8t$). Here we see that the Majorana zero mode (red line) remains in spite of the applied disorder. Compared with Fig. 5.7, the system now is clearly gapped within the whole range. The other parameters used are the same as in Fig. 5.7.

show that (1) The proposed system is topologically trivial (in the conventional sense), as demonstrated by the absence of gapless edge modes (in the absence of a soliton); the conventional invariant for a time reversal symmetric topological superconductor is trivially zero in this case. (2) In the presence of a topological defect, the proposed system supports MKPs, despite being topologically trivial (in the conventional sense). (3) The presence of the MKPs at the ends of the soliton cannot be attributed to any special property of the defect [185, 184, 186], as demonstrated by the absence of MZMs in "garden variety" superconductors/superfluids in the presence of such soliton. (4) The MKPs induced in the proposed system are robust against disorder. Thus, although the classifications of higher order topological superconductivity/superfluidity is not nearly as well developed as their conventional counterpart, by demonstrating the presence of (D-2)-dimensional topologically protected MZMs in a D-dimensional topologically trivial SC/SF (in the conventional sense), we have presented strong evidence for higher order topological superfluidity in our proposed cold atom system. We have checked that essentially the same arguments apply to the claims of higher order topological

superconductivity in the solid state systems.

## 5.6 Discussion and conclusion

To implement $H_0$ we envision an experimental setup similar to Ref. [156] since this scheme does not rely on the internal atomic structure. We consider a 3D cubic optical lattice were confinement along $z$ separates the system into parallel $x-y$ planes. The 2D Hubbard model then approximates the dynamics of $^{40}$K or $^{6}$Li placed with one atom per site in a deep optical lattice with uniform hopping $t$ if we equally populate two Zeeman levels with opposite magnetic moments. A magnetic field gradient along the $y$-direction creates a splitting (much larger than $t$) between opposite spins in neighboring sites. In addition to the primary lattice beams, a pair of running-wave beams are applied parallel to the $x-y$ bonds of the square lattice to dynamically restore resonant tunneling assuming the running-wave lattice depth is much smaller than the spin splitting. This setup induces the complex spin-dependent phase in Eq. (5.1) in a rotating wave approximation.

To implement $H_I$ we require an attractive Feshbach resonance. For magnetic Feshbach resonances, typical magnetic field gradients ($\sim 10mG/\mu$m) leave the attractive interaction spatially uniform since common resonances occur at relatively high fields ($\sim 400-700G$) and can be broad, as in, e.g., $^{6}$Li. It also safe to assume that close proximity to the Feshbach resonance does not lead to strong heating and loss [187] since the Raman coupling [156] between the same hyperfine states (and neighboring lattice sites) does not induce any new three-body loss channel.

Tuning the chemical potential near zero (Fig. 5.4) allows observation of MZMs. Spatially resolved radio-frequency spectroscopy and probing of the density profile have been proposed as an experimental approach to detect these MZMs [177, 181]. The soliton-induced MZMs can be manipulated by controlling the spatial location of the soliton excitation, which may be beneficial for topological braiding [16, 188] of MZMs.

The essential physics for the creation of MKPs and higher order topological superfluidity in the current system is similar to the proposals for higher order topological superconductors in solid state systems. In both cases, the non-SC "normal" system is a 2D QSHI. This system has counter-propagating Kramer's pairs of gapless edge states (see Fig. 5.1), which can support spin-singlet superconductivity. Furthermore, in both systems introducing superconductivity (by proximity effect in solid state systems and interaction-induced, via Feshbach resonance, in the present work) gaps out the edge modes, which signals that the system is a topologically trivial superconductor/superfluid (because the edge modes are gapped). However, whenever

the superconducting gap changes sign (and thus goes through zero) at a point along the edge, a Kramer's pair of localized MZMs are nucleated by the Jackiew-Rebbi mechanism, which is common to both the solid state proposals and the present work (a Kramer's pair of zero modes is nucleated because the system is time reversal invariant).

The key difference between the solid state case and the current set-up is that in the former system the change of sign of the superconducting gap is proposed to be realized by proximity effect with an unconventional superconductor (such as $d$-wave or $s_{\pm}$wave, which change sign in momentum space), while in our work the change of sign of the superconducting gap is due to a soliton in the $s$-wave superfluid. The other significant difference between the two proposals is that, while the proximity effect of unconventional $d$ or $s_{\pm}$wave superconductivity on QSHI in solid state systems has not yet been demonstrated experimentally (and is probably going to be hard) the main ingredients of the same physics within our proposal, namely, the two-component Hofstadter model (and thus a QSHI, [157, 158, 159, 156, 160, 161, 162, 163]), on-site attractive interactions and non-zero SC pair potential [164, 165, 166, 167, 168, 169, 170], and creation of dark solitons [171, 172, 173, 174], have all been individually realized in the cold atom systems.

# Chapter 6

# Non-linear Nernst effect in bilayer $WTe_2$

Unlike the linear anomalous Nernst effect, the non-linear anomalous Nernst effect (NLANE) can survive in an inversion symmetry broken system even in the presence of time-reversal symmetry. Using semiclassical Boltzmann transport theory, we study the non-linear anomalous Nernst effect that arises as the second-order response function to the applied temperature gradient. We find that the non-linear Nernst current, which flows perpendicular to the temperature gradient even in the absence of a magnetic field, arises due to the Berry curvature of the states near the Fermi surface, and thus is associated with purely a Fermi surface contribution. We apply these results to bilayer $WTe_2$, which is an inversion broken but time reversal symmetric type-II Weyl semimetal supporting chiral Weyl fermions. By tuning the spin-orbit coupling, we show that the sign of the NLANE can change in this system. Together with the angular dependence, we calculate the temperature and chemical potential dependencies of NLANE in bilayer $WTe_2$, and predict specific experimental signatures that can be checked in experiments.

## 6.1 Introduction

The Berry phase effects in anomalous transport phenomena driven by the gradient of temperature or chemical potential is now well-developed theoretically and have been seen in experiments [189, 39, 190, 191, 192, 193, 194]. A nonzero Berry curvature along with the nonuniform statistical distribution of carriers resulting from the external fields have been used to explain the transport anomalies like the anomalous Hall effect (AHE [195, 194, 193, 196, 197, 192, 191, 198, 199, 200] and anomalous Nernst effect (ANE) [201, 202, 203, 204, 205, 206, 207, 208, 209, 210, 211, 212]. These Berry curvature-related topological transport

anomalies are linear responses, which require the breaking of time reversal (TR) symmetry by a complex order parameter or internal magnetization [194, 213, 214, 215, 196, 193, 199]. With the increasing interest in non-linear properties of topological materials [216, 217, 218, 219, 220, 221, 222, 223], the second-order non-linear Hall effect was proposed as a new type of Hall effect that could survive even in the TR invariant systems with broken inversion symmetry [43, 223]. Rather than being induced by the Berry curvature itself, the non-linear response depends on the Berry curvature dipole (BCD), a moment of the Berry curvature over the occupied states [43, 224, 225].

Monolayer transition metal dichalcogenides (TMDCs) have been proposed as the platforms supporting the non-linear Hall effect due to their large spin-orbit coupling and non-centrosymmetric band structure [226, 227, 228]. Recently, it has been reported that the non-linear Hall currents can occur as a second-order response to the applied external electric field in TR invariant but inversion symmetry breaking materials, especially the TMDCs and Weyl semimetals (WSMs) [229, 44, 45, 230]. The underlying physics associated with the non-linear anomalous Hall effect (NLAHE) has been shown to be related to the band structure properties. Several candidate materials with low crystalline symmetries have been proposed to exhibit a finite or enhanced BCD [231, 232, 233, 234, 235].

$WTe_2$ as a type-II WSM exhibiting chiral Weyl Fermions that break Lorentz invariance [236, 237], has attracted tremendous attention in the studies of transport anomalies [238, 239, 240, 241, 242]. The topological properties of $WTe_2$ are caused by its Berry curvature concentrated around the Weyl points with linear band-crossing, acting like monopoles of Berry curvature whose value for the valence band and conduction band are opposite [243]. The nontrivial phenomena in TR invariant systems such as $WTe_2$ requires an asymmetric distribution of the Fermi occupations at $\boldsymbol{k}$ and $-\boldsymbol{k}$. Interestingly, a few-layered $WTe_2$ system, e.g. a bilayer $WTe_2$, intrinsically breaks the inversion symmetry and leaves a nonzero Berry curvature distribution on the Fermi surface. It is the rearrangement of the positive and negative Berry curvature in different momentum that leads to the so-called BCD. Specifically, due to the big net BCD on a given Fermi plane, the bilayer $WTe_2$ system shows a strong non-linear Hall response when a small spin-orbit torque is induced [231, 232, 230]. The strong tunability of bilayer $WTe_2$ by electric gating and/or strain makes the discovery of non-linear phenomena in inversion-symmetry-breaking 2D materials particularly promising.

In the linear regime, the ANE originating from the Berry curvature describes the generation of a charge current in the presence of a transverse temperature gradient and a broken TR symmetry, and vanishes when the TR symmetry is preserved. However, as a counterpart of the NLAHE revealed by charge current, the non-linear anomalous Nernst effect could possibly be non-zero even in the presence of TR symmetry and

measured through the heat transport. Recently the intrinsic non-linear anomalous thermoelectric effects have been proposed for the loop-current model of the cuprate superconductors where the combined TR symmetry and inversion symmetry is retained [244]. However, in this model, the TR symmetry is still broken individually due to the orbital toroidal moment. Very recently, a Hamiltonian of TMDCs under uniaxial strian has been used to demonstrate the NLANE within the two-dimensional TR invariant system with broken inversion symmetry [245]. Here the non-linear anomalous Nernst current is found to have a different temperature dependence in the high and low temperature regimes. In another recent work on non-centro-symmetric crystals [246], the non-linear thermo-electric conductivity has been derived up to the second order to the applied thermal gradient by considering a thermally induced nonlinear perturbation to the Fermi distribution function. In contrast to these works, in this paper we focus on bilayer $WTe_2$, because this system has recently been successfully used to experimentally demonstrate the NLAHE in a TR invariant system [44, 45]. Because of the existence of nonzero NLAHE, we also expect a nonzero NLANE in this system from Onsager reciprocity. Our calculations and results in this paper will thus be of immediate experimental relevance for the demonstration of NLANE in a system that has already been shown to support NLAHE. In the recent experiments of the NLAHE in bilayer $WTe_2$ [45, 44], a transverse voltage drop at the second-harmonic frequencies is found quadratically dependent to the longitudinal driving current. In analogy with the NLAHE, a second-harmonic type response is also possible in principle for the NLANE provided the thermal gradient is time dependent. In what follows, we perform a systematic derivation of the NLANE in a TR invariant but inversion symmetry broken system based on the Boltzmann semiclassical approach. We then provide the general angular dependence of the NLANE response relevant for the Nernst experimental setup (Fig. (6.1)). We apply these results to the case of bilayer $WTe_2$ and make several experimental predictions, including the dependence of the NLANE conductivity on various experimental parameters such as temperature ($T$), chemical potential ($\mu = E_F$), inter-layer coupling ($\gamma$), tilting of the Dirac cones ($t_x$), and spin orbit coupling ($\eta$).

This paper is organized as follows: In Sec. 6.2 we discuss the Boltzmann semiclassical approach to systematically calculate the NLANE response. We derive the general expressions for the NLANE in the presence of a temperature gradient in an appropriate Nernst setup. In Sec. 6.3, we develop the general angular dependence of the NLANE response, where the angle refers to that between the principal axes and applied temperature gradiant (Fig. 6.1(a)). In Sec. 6.5, we apply these general semiclassical results to the specific case of bilayer $WTe_2$ described in Sec. 6.4 and make several experimental predictions. We end with a conclusion in Sec. 6.6.

## 6.2 Semiclassical Boltzmann formalism of non-linear Nernst response

In addition to the band energy, the Berry curvature of the Bloch bands is required for a complete description of the electron dynamics in topological systems. Therefore, the transport properties get substantially modified due to the presence of non-trivial Berry curvature of the Bloch bands [39, 189]. The Berry curvature of the $i^{th}$ band for a Bloch Hamiltonian is defined as

$$\Omega_{i\boldsymbol{k}}^{a'} = -2\epsilon_{a'b'c'} \sum_{j \neq i} \frac{\mathrm{Im}\left(\langle i|\, \partial_{k_{b'}} H\, |j\rangle \langle j|\, \partial_{k_{c'}} H\, |i\rangle\right)}{\left(\varepsilon_{\boldsymbol{k}}^{i} - \varepsilon_{\boldsymbol{k}}^{j}\right)^2} \tag{6.1}$$

where $|i\rangle$ is the eigenvector for the $i^{th}$ band with eigenenergy $\varepsilon_{\boldsymbol{k}}^{i}$ and $\epsilon_{a'b'c'}$ is the Levi-Civita symbol. The general form of the Berry curvature can be obtained using symmetry analysis. From the Eq. (6.1), it is clear that the Berry curvature follows $\boldsymbol{\Omega}_{-\mathbf{k}} = -\boldsymbol{\Omega}_{\mathbf{k}}$ under TR symmetry. On the other hand if the system has spatial inversion symmetry, then it follows $\boldsymbol{\Omega}_{-\mathbf{k}} = \boldsymbol{\Omega}_{\mathbf{k}}$. Therefore, for a system with both TR and spatial inversion symmetry the Berry curvature vanishes identically throughout the Brillouin zone [39]. However, in the presence of broken inversion and/or TR symmetry, the Berry curvature of the Bloch bands can be non-trivial.

In the presence of non-zero Berry curvature, the conventional semiclassical equation of motion for an electron becomes modified by adding a transverse anomalous term to the velocity, given by [189, 39, 247],

$$\begin{aligned} \dot{\boldsymbol{r}} &= \frac{1}{\hbar}\frac{\partial \varepsilon_{\boldsymbol{k}}}{\partial \boldsymbol{k}} + \frac{\dot{\boldsymbol{p}}}{\hbar} \times \boldsymbol{\Omega}_{\boldsymbol{k}} \\ \dot{\boldsymbol{p}} &= e\boldsymbol{E} + e\dot{\boldsymbol{r}} \times \boldsymbol{B}, \end{aligned} \tag{6.2}$$

where $\varepsilon_{\boldsymbol{k}}$ is the energy dispersion for given momentum $\boldsymbol{k}$, and $\boldsymbol{E}, \boldsymbol{B}$ are the external electric and magnetic fields respectively. The above coupled equations for $\dot{\boldsymbol{r}}$ and $\dot{\boldsymbol{p}}$ could be solved together to get [248, 249, 223],

$$\begin{aligned} \dot{\boldsymbol{r}} &= D\left(\boldsymbol{B}, \boldsymbol{\Omega}_{\boldsymbol{k}}\right)\left[\boldsymbol{v}_{\boldsymbol{k}} + \frac{e}{\hbar}\left(\boldsymbol{v}_{\boldsymbol{k}} \cdot \boldsymbol{\Omega}_{\boldsymbol{k}}\right)\boldsymbol{B} + \frac{e}{\hbar}\left(\boldsymbol{E} \times \boldsymbol{\Omega}_{\boldsymbol{k}}\right)\right] \\ \dot{\boldsymbol{p}} &= D\left(\boldsymbol{B}, \boldsymbol{\Omega}_{\boldsymbol{k}}\right)\left[\frac{e}{\hbar}\boldsymbol{v}_{\boldsymbol{k}} \times \boldsymbol{B} + e\boldsymbol{E} + \frac{e^2}{\hbar}\left(\boldsymbol{E} \cdot \boldsymbol{B}\right)\boldsymbol{\Omega}_{\boldsymbol{k}}\right] \end{aligned} \tag{6.3}$$

where $\boldsymbol{v}_{\boldsymbol{k}} = \hbar^{-1}\partial\varepsilon_{\boldsymbol{k}}/\partial\boldsymbol{k}$ is the group velocity, and $D\left(\boldsymbol{B}, \boldsymbol{\Omega}_{\boldsymbol{k}}\right) = \left(1 + e\left(\boldsymbol{B} \cdot \boldsymbol{\Omega}_{\boldsymbol{k}}\right)/\hbar\right)^{-1}$ is the phase space modification factor. Under the relaxation time approximation, the steady state Boltzmann equation is given

by

$$\left(\dot{\boldsymbol{r}}\cdot\boldsymbol{\nabla}_{\boldsymbol{r}}+\dot{\boldsymbol{k}}\cdot\boldsymbol{\nabla}_{\boldsymbol{k}}\right)f_{\boldsymbol{k}}=-\frac{f_{\boldsymbol{k}}-f_0}{\tau}, \tag{6.4}$$

where $\tau$ is the average scattering time between two successive collisions, $f_0=(e^{\beta(\varepsilon_{\boldsymbol{k}}-\mu)}+1)^{-1}$ is the equilibrium Fermi-Dirac distribution function, and $f_{\boldsymbol{k}}$ is the distribution function in the presence of perturbative fields. For simplicity, in what follows we ignore the momentum and band dependence of $\tau$ and treat it to be a constant with $\tau(\mathbf{k})=\tau$.

In this paper we are interested in the NLANE of a TR invariant system where we measure a transverse electric current in response to the second-order of an applied temperature gradient $\boldsymbol{\nabla}T$ in the absence of magnetic field. Substituting $\dot{\mathbf{r}}$ and $\dot{\mathbf{k}}$ with $\boldsymbol{E}=0$, $\boldsymbol{B}=0$ into Eq. $(6.4)$, the Boltzmann equation takes the form

$$\boldsymbol{v}_{\boldsymbol{k}}\cdot\frac{\partial f_{\boldsymbol{k}}}{\partial\boldsymbol{r}}=\frac{f_0-f_{\boldsymbol{k}}}{\tau}. \tag{6.5}$$

Now from the above equation, we can write $f_{\boldsymbol{k}}$ as

$$f_{\boldsymbol{k}}=f_0-\tau v_{a'}\frac{\partial f_{\boldsymbol{k}}}{\partial r_{a'}}, \tag{6.6}$$

where $a'=x,y,z$. For consistency of notation, all the component subscripts in this section indicate the principal axes coordinates. For a system with non-zero Berry curvatures, the complete description of the transport charge current is given by [189],

$$\boldsymbol{j}=-e\int\left[d\boldsymbol{k}\right]\dot{\boldsymbol{r}}f_{\boldsymbol{k}}-\boldsymbol{\nabla}\times\frac{e}{\hbar}\int\left[d\boldsymbol{k}\right]\beta^{-1}\boldsymbol{\Omega}_{\boldsymbol{k}}\log\left(1+e^{-\beta(\varepsilon_{\boldsymbol{k}}-\mu)}\right) \tag{6.7}$$

where the first term is the usual charge current proportional to the carrier's group velocity and the second term is the intrinsic charge current supporting the transport anomaly. From Eq. $(6.7)$, the thermally induced charge current in the presence of a temperature gradient $\boldsymbol{\nabla}T$ can be written as [189],

$$\boldsymbol{j}=-e\int\left[d\boldsymbol{k}\right]f_{\boldsymbol{k}}\boldsymbol{v}_{\boldsymbol{k}}-\frac{\boldsymbol{\nabla}T}{T}\times\frac{e}{\hbar}\int\left[d\boldsymbol{k}\right]\boldsymbol{\Omega}_{\boldsymbol{k}}\Big[\left(\varepsilon_{\boldsymbol{k}}-\mu\right)f_0+\beta^{-1}\log\left(1+e^{-\beta(\varepsilon_{\boldsymbol{k}}-\mu)}\right)\Big]. \tag{6.8}$$

It has been discussed in Ref. [245] that a generalization of the above equation to the nonlinear regime could

be obtained by replacing the equilibrium distribution function $f_0$ by a non-equilibrium distribution function $f_{\mathbf{k}}$. Because of the spatial variation of the temperature, the extra terms contained in $f_{\mathbf{k}}$ will be proportional to the thermal gradient and therefore contribute as the NLANE response. To calculate the general expression for the NLANE coefficient, we assume the distribution function as $f_{\boldsymbol{k}} = f_0 + f_1 + f_2$, where the term $f_n$ is understood to vanish as $(\boldsymbol{\nabla} T)^n$ (for simplicity, $(\boldsymbol{\nabla} T)^n$ is denoted as $\boldsymbol{\nabla}^n T$ in the following). Now the Eq. $(6.6)$ becomes

$$\begin{aligned} f_1 + f_2 &= -\tau v_{a'} \frac{\partial}{\partial r_{a'}} \left( f_0 + f_1 + f_2 \right), \\ f_1 &= -\tau v_{a'} \frac{\partial}{\partial r_{a'}} f_0, \\ f_2 &= -\tau v_{a'} \frac{\partial}{\partial r_{a'}} f_1, \end{aligned} \tag{6.9}$$

where $f_0$ is cancelled. After some straightforward algebra, we can obtain $f_1\left(\boldsymbol{\nabla} T\right)$, and $f_2\left(\boldsymbol{\nabla}^2 T\right)$ as

$$\begin{aligned} f_1 =& \frac{\tau}{\hbar} \left( \frac{\varepsilon_{\boldsymbol{k}} - \mu}{T} \right) \nabla_{a'} T \frac{\partial}{\partial k_{a'}} f_0, \\ f_2 =& -\tau^2 v_{a'} v_{b'} \left( \frac{\varepsilon_{\boldsymbol{k}} - \mu}{T} \right) \frac{\partial f_0}{\partial \varepsilon_{\boldsymbol{k}}} \nabla^2_{a'b'} T \\ &+ \frac{\tau^2}{\hbar^2} \left( \frac{\varepsilon_{\boldsymbol{k}} - \mu}{T} \right)^2 \nabla_{b'} T \nabla_{a'} T \frac{\partial^2 f_0}{\partial k_{a'} \partial k_{b'}} \\ &- \tau^2 v_{a'} v_{b'} \left( \frac{\varepsilon_{\boldsymbol{k}} - \mu}{T} \right) \nabla_{b'} T \nabla_{a'} T \left( -\frac{2}{T} \frac{\partial f_0}{\partial \varepsilon_{\boldsymbol{k}}} \right) \end{aligned} \tag{6.10}$$

where $\nabla_{a'} T = \partial T / \partial r_{a'}$, is the temperature gradient along $r_{a'}$. Substituting the distribution function $f_{\boldsymbol{k}} = f_0 + f_1 + f_2$ into Eq. $(6.8)$, the transport charge current in response to the first-order in $\boldsymbol{\nabla} T$ can be written as

$$\boldsymbol{j}^0 = -\frac{\nabla_{a'} T}{T} \frac{e\tau}{\hbar} \int [d\boldsymbol{k}]\, \boldsymbol{v}_{\boldsymbol{k}} \left( \varepsilon_{\boldsymbol{k}} - \mu \right) \frac{\partial f_0}{\partial k_{a'}} - \frac{\boldsymbol{\nabla} T}{T} \frac{e}{\hbar} \times \int [d\boldsymbol{k}]\, \boldsymbol{\Omega}_{\boldsymbol{k}} \Big[ \left( \varepsilon_{\boldsymbol{k}} - \mu \right) f_0 + \beta^{-1} \sum_n \frac{f_0^n}{n} \Big] \tag{6.11}$$

where the first term of the current ($\boldsymbol{j}^0$) varies linearly with the scattering time $\tau$ and is along the longitudinal direction of applied $\boldsymbol{\nabla} T$. On the other hand, the second term gives the anomalous Nernst-like current along the transverse direction of $\boldsymbol{\nabla} T$ and is independent of $\tau$.

Similarly, we can go further and calculate the non-linear Nernst-like current by extracting the terms depending on second-order in $\boldsymbol{\nabla} T$ after substituting $f_{\boldsymbol{k}}$ into Eq. $(6.8)$. The non-linear response of the charge

current (second-order in temperature gradient) can be written as

$$\begin{aligned}\boldsymbol{j} =& e\tau^2 \int \boldsymbol{v}_{\boldsymbol{k}} \left[d\boldsymbol{k}\right] \Bigg[ v_{a'} v_{b'} \left(\frac{\varepsilon_{\boldsymbol{k}} - \mu}{T}\right) \left(\frac{\partial f_0}{\partial \varepsilon_{\boldsymbol{k}}}\right) \nabla^2_{a'b'} T \\ &+ 2 v_{a'} v_{b'} \left(\frac{\varepsilon_{\boldsymbol{k}} - \mu}{T^2}\right) \left(-\frac{\partial f_0}{\partial \varepsilon_{\boldsymbol{k}}}\right) \nabla_{a'} T \nabla_{b'} T \\ &- \frac{1}{\hbar^2} \left(\frac{\varepsilon_{\boldsymbol{k}} - \mu}{T}\right)^2 \frac{\partial^2 f_0}{\partial k_{a'} \partial k_{b'}} \nabla_{b'} T \nabla_{a'} T \Bigg] \\ &- \frac{e\tau}{\hbar^2} \boldsymbol{\nabla} T \times \int \left[d\boldsymbol{k}\right] \boldsymbol{\Omega}_{\boldsymbol{k}} \frac{\partial f_0}{\partial k_{a'}} \left(\frac{\varepsilon_{\boldsymbol{k}} - \mu}{T}\right)^2 \nabla_{a'} T\end{aligned} \tag{6.12}$$

where the first three terms of the above equation are purely semiclassical and Berry phase independent. In Eq. (6.12), the contributions of the first three terms to the transport current can be distinguished from the last term based on their different orders of $\tau$ dependence, where $\tau$ is approximately picoseconds in experiments. Moreover, under the approximation of constant relaxation time, the first three terms will vanish in a TR invariant system because the integrand is odd under TR symmetry. Therefore, only the last term contributes to the non-linear Nernst-like current, which can be written as [245]

$$\boldsymbol{j} = -\frac{e\tau}{\hbar^2} \boldsymbol{\nabla} T \times \int \left[d\boldsymbol{k}\right] \nabla_{a'} T \frac{\partial f_0}{\partial k_{a'}} \boldsymbol{\Omega}_{\boldsymbol{k}} \frac{\left(\varepsilon_{\boldsymbol{k}} - \mu\right)^2}{T^2}. \tag{6.13}$$

From the above equation, the expression of non-linear Nernst current flowing in the $a$ direction can be written in a compact form as

$$\boldsymbol{j}_{a'} = \epsilon_{a'b'c'} \frac{e\tau}{\hbar^2} \left(\nabla_{b'} T \nabla_{d'} T\right) \boldsymbol{\Lambda}^T_{d'c'}, \tag{6.14}$$

where $\boldsymbol{\Lambda}^T_{d'c'}$, the non-linear anomalous Nernst coefficient, is defined as

$$\boldsymbol{\Lambda}^T_{d'c'} = -\int \left[d\boldsymbol{k}\right] \frac{\left(\varepsilon_{\boldsymbol{k}} - \mu\right)^2}{T^2} \frac{\partial f_0}{\partial k_{d'}} \Omega^{c'}_{\boldsymbol{k}}. \tag{6.15}$$

Clearly, the NLANE coefficient is a pseudotensorial quantity and has a different form compared to the Berry curvature dipole which produces the NLAHE. The non-linear anomalous Nernst conductivity, which is proportional $\boldsymbol{\Lambda}^T_{d'c'}$, is obtained as $\frac{e\tau}{\hbar^2} \boldsymbol{\Lambda}^T_{d'c'}$. Therefore, unlike the linear case, this quantity is found to be a Fermi surface quantity indicating the fact that the main contribution to it comes from the states near the Fermi surface. Moreover, the NLANE coefficient is also linearly proportional to the scattering time whereas the linear

anomalous Nernst coefficient is independent of $\tau$. Interestingly, the NLANE can be finite for a TR invariant system which can be easily checked by looking at Eq. $(6.15)$. In the presence of TR symmetry, $\boldsymbol{\Omega_k} = -\boldsymbol{\Omega_{-k}}$, $\varepsilon_{\boldsymbol{k}} = \varepsilon_{-\boldsymbol{k}}$ and $\partial f_0/\partial k_{d'} = -\partial f_0/\partial\left(-k_{d'}\right)$. Therefore, the integrand of Eq. $(6.15)$ is an even function with respect to $k_{d'}$ which makes the integral finite and results in a non-zero NLANE.

In three-dimension (3D), the Berry curvature $\boldsymbol{\Omega_k}$ is a pseudovector and therefore, the NLANE coefficient ($\boldsymbol{\Lambda}^T_{d'c'}$) becomes a pseudotensor. On the other hand, in the case of a two-dimensional (2D) system, the only nonzero component of the Berry curvature $\boldsymbol{\Omega_k}$ is $\Omega^z_{\boldsymbol{k}}$ $(c' = z)$ which is perpendicular to the $x-y$ plane indicating the fact that the Berry curvature behaves as a pseudoscalar. Therefore, in 2D the pseudotensorial quantity $\boldsymbol{\Lambda}^T_{d'c'}$ is reduced to a pseudovector quantity ($\boldsymbol{\Lambda}^T_{d'}$) confined in the 2D plane with only two independent components ($x$ and $y$ components). Following the above discussion, Eq. $(6.13)$ can be written as

$$\boldsymbol{j} = \frac{e\tau}{\hbar^2}\left(\boldsymbol{\nabla}T\cdot\boldsymbol{\Lambda}^T\right)\boldsymbol{\nabla}T\times\hat{\boldsymbol{z}}. \tag{6.16}$$

It can be shown that the largest symmetry required for a 2D system to get the non-vanishing non-linear anomalous Nernst conductivity (or $\boldsymbol{\Lambda}^T$) is a single mirror line (i.e. a mirror plane that is perpendicular to the 2D system). In a TR invariant 2D system, the presence of single mirror symmetry forces the $\boldsymbol{\Lambda}^T$ to be orthogonal to the mirror plane. Moreover, according to Eq. $(6.16)$, when the applied temperature gradient is aligned with the direction of $\boldsymbol{\Lambda}^T$, we find that the current which flows in the transverse direction of it explicitly originate from $\boldsymbol{\Lambda}^T_{d'}$ [43, 245].

## 6.3 Angular dependence of non-linear anomalous Nernst response

In this section we will study the angular dependence of the NLANE for a Nernst experimental setup which is schematically shown in Fig. 6.1. Angle $\theta$ is due to the misalignment between the temperature gradient $-\boldsymbol{\nabla}T$ (red arrow) and the a-axis of the crystal (black dashed line). In Fig. 6.1(b), $M_a$ is the mirror symmetry line (black long dashed line) along $b-$axis [231, 232, 45]. Based on the analysis in Sec. 6.2, $\Lambda_a$ is the only non-zero component of the NLANE coefficient that is perpendicular to the mirror line $M_a$ as shown in Fig. 6.1(b).

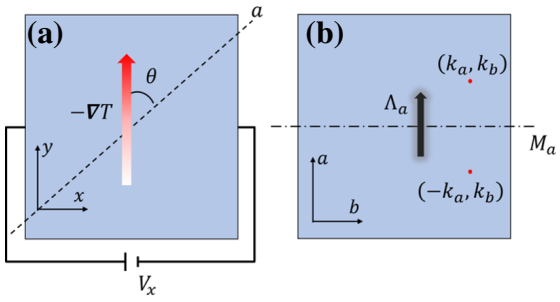


Figure 6.1: (Color online) (a) Schematic experimental setup for measuring the non-linear anomalous Nernst effect in a time-reversal symmetric but inversion symmetry broken system. $V_x$ is measured as the non-linear anomalous Nernst voltage when a temperature gradient ($-\boldsymbol{\nabla} T$, represented by the red arrow) is applied along $y-$direction forming an angle $\theta$ with the principal axis $a$ (black dashed line). (b) $M_a$ is the mirror line which takes $k_a$ to $-k_a$. Due to the mirror symmetry and time reversal symmetry, only the $a-$component (black arrow) of the non-linear anomalous Nernst coefficient ($\boldsymbol{\Lambda}$), which is perpendicular to the mirror line $M_a$, is non-zero.

From Eq. (6.11) we could define the thermo-electric conductivity tensor $\boldsymbol{\alpha}^0$ with components as

$$\begin{aligned} \alpha^0_{aa} &= -e\tau \int [d\boldsymbol{k}]\, v_a^2 \left(\frac{\varepsilon_{\boldsymbol{k}} - \mu}{T}\right)\left(-\frac{\partial f_0}{\partial \varepsilon_{\boldsymbol{k}}}\right), \\ \alpha^0_{ab} &= \frac{e}{\hbar} \int [d\boldsymbol{k}]\, \Omega^c_{\boldsymbol{k}} \left[\left(\frac{\varepsilon_{\boldsymbol{k}} - \mu}{T}\right) f_0 + k_B \sum_n \frac{f_0^n}{n}\right] \end{aligned} \tag{6.17}$$

which represent the longitudinal and transverse components of the thermo-electric conductivity respectively [208, 250, 212]. The linear anomalous Nernst conductivity ($\alpha^0_{ab}$) can also be written in terms of entropy density ($s_{\boldsymbol{k}}$) as $\alpha^0_{ab} = \frac{ek_B}{\hbar} \int [d\boldsymbol{k}]\, \boldsymbol{\Omega}_{\boldsymbol{k}} s_{\boldsymbol{k}}$, where the entropy density is given by $s_{\boldsymbol{k}} = -f_0 \log(f_0) - (1-f_0)\log(1-f_0)$. Now from the linear response theory, we can write

$$\begin{pmatrix} j^0_a \\ j^0_b \end{pmatrix} = \begin{pmatrix} \alpha^0_{aa} & \alpha^0_{ab} \\ -\alpha^0_{ab} & \alpha^0_{bb} \end{pmatrix} \begin{pmatrix} -\nabla_a T \\ -\nabla_b T \end{pmatrix}. \tag{6.18}$$

It is shown in Fig. (6.1) that we are dealing with two sets of coordinates ($(x, y)$ and $(a, b)$) related by angle $\theta$. For this reason, we introduce the transformation matrix $\mathcal{G}(\theta)$ which transforms the principal axes $(a, b)$ coordinates to the $(x, y)$ coordinates in experiment [231]. In the linear regime, both the charge current and

thermal gradient could be transformed by $\mathcal{G}(\theta)$, like

$$\begin{pmatrix} j_a^0 \\ j_b^0 \end{pmatrix} = \mathcal{G}(\theta) \begin{pmatrix} j_x^0 \\ j_y^0 \end{pmatrix}, \mathcal{G}(\theta) = \begin{pmatrix} \cos\theta & \sin\theta \\ -\sin\theta & \cos\theta \end{pmatrix} \tag{6.19}$$

Now under the transformation $\mathcal{G}(\theta)$, we have the thermo-electric conductivity tensor $\widetilde{\boldsymbol{\alpha}}^0 = \mathcal{G}^\dagger \boldsymbol{\alpha}^0 \mathcal{G}$ given by

$$\widetilde{\boldsymbol{\alpha}}^0 = \begin{pmatrix} \alpha_{bb}^0 + \delta\alpha^0 \cos^2\theta & \delta\alpha^0 \sin\theta\cos\theta + \alpha_{ab}^0 \\ \delta\alpha^0 \sin\theta\cos\theta - \alpha_{ab}^0 & \alpha_{bb}^0 + \delta\alpha^0 \sin^2\theta \end{pmatrix} \tag{6.20}$$

where $\delta\alpha^0 = \alpha_{aa}^0 - \alpha_{bb}^0$ is the anisotropy of the thermo-electric conductivity along the principal axes. Now, by definition the corresponding resistivity tensor $\boldsymbol{\nu}$ can be obtained as

$$\begin{pmatrix} -\nabla_x T \\ -\nabla_y T \end{pmatrix} = \frac{1}{\widetilde{\boldsymbol{\alpha}}^0} \begin{pmatrix} j_x^0 \\ j_y^0 \end{pmatrix} = \boldsymbol{\nu} \begin{pmatrix} j_x^0 \\ j_y^0 \end{pmatrix}, \tag{6.21}$$

with

$$\boldsymbol{\nu} = \begin{pmatrix} \nu_{bb}^0 + \delta\nu^0 \sin^2\theta & -\nu_{ab}^0 - \delta\nu^0 \sin\theta\cos\theta \\ -\nu_{ab}^0 + \delta\nu^0 \sin\theta\cos\theta & \nu_{bb}^0 + \delta\nu^0 \cos^2\theta \end{pmatrix} \tag{6.22}$$

where

$$\nu_{ii'}^0 = \frac{\alpha_{ii'}^0}{|\widetilde{\boldsymbol{\alpha}}^0|},\ \delta\nu^0 = \frac{\delta\alpha^0}{|\widetilde{\boldsymbol{\alpha}}^0|},\ |\widetilde{\boldsymbol{\alpha}}^0| = \alpha_{aa}^0\alpha_{bb}^0 + (\alpha_{ab}^0)^2. \tag{6.23}$$

From the Eq. (6.22), the angular dependence of the thermo-electric resistivity in linear regime can be written as

$$\begin{aligned} \nu_{xx} &= \nu_{bb}^0 + \delta\nu^0 \sin^2\theta, \\ \nu_{xy} &= -\nu_{ab}^0 - \delta\nu^0 \sin\theta\cos\theta. \end{aligned} \tag{6.24}$$

Following Eq. (6.16), the non-linear response to the second-order of $\boldsymbol{\nabla} T$ along the principal axes

can be written as,

$$\begin{pmatrix} j_a \\ j_b \end{pmatrix} = \begin{pmatrix} 0 & \alpha_{aab} & 0 & \alpha_{abb} \\ \alpha_{baa} & 0 & \alpha_{bba} & 0 \end{pmatrix} \begin{pmatrix} \nabla^2_{aa}T \\ \nabla^2_{ab}T \\ \nabla^2_{ba}T \\ \nabla^2_{bb}T \end{pmatrix} \tag{6.25}$$

where we have a similar analogy as the non-linear Hall conductivity [231]. Here $\nabla^2_{ii'}T = \nabla_i T \nabla_{i'} T$ for $i, i' = a, b$. Now after the transformation by $\mathcal{G}(\theta)$, the non-linear response tensor in the experimental coordinates can be written as

$$\begin{pmatrix} j_x \\ j_y \end{pmatrix} = \widetilde{\boldsymbol{\alpha}} \begin{pmatrix} \nabla^2_{xx}T \\ \nabla^2_{xy}T \\ \nabla^2_{yx}T \\ \nabla^2_{yy}T \end{pmatrix}, \text{with } \widetilde{\boldsymbol{\alpha}} = \mathcal{G}^{\dagger}(\theta)\boldsymbol{\alpha}\mathcal{G}(\theta) \otimes \mathcal{G}(\theta) \tag{6.26}$$

Therefore, the non-linear Nernst conductivity tensor $\widetilde{\boldsymbol{\alpha}}$ expressed in the experimental coordinates $(x, y)$ takes the form

$$\widetilde{\boldsymbol{\alpha}} = \begin{pmatrix} 0 & \alpha_{xxy} & 0 & \alpha_{xyy} \\ \alpha_{yxx} & 0 & \alpha_{yyx} & 0 \end{pmatrix} \tag{6.27}$$

where all the non-zero terms have an angular dependence given as

$$\begin{aligned} \alpha_{xxy} &= \alpha_{aab}\cos\theta - \alpha_{abb}\sin\theta, \\ \alpha_{xyy} &= \alpha_{aab}\sin\theta + \alpha_{abb}\cos\theta, \\ \alpha_{yxx} &= -\alpha_{xxy}, \alpha_{yyx} = -\alpha_{xyy} \end{aligned} \tag{6.28}$$

Similar to the NLAHE experiment, the measurable quantity in NLANE coefficient experiment is non-linear Nernst voltage. Therefore, we will now derive the angular dependence of the non-linear Nernst voltage which can be directly checked in experiments.

Based on Eq. $(6.21)$ and Eq. $(6.12)$, the non-linear Nernst voltage can be defined as

$$\begin{aligned} V_x =& \nu_{xx} j_x + \nu_{xy} j_y \\ =& \nu_{xx}\left(\alpha_{xxy}\nabla^2_{xy}T + \alpha_{xyy}\nabla^2_{yy}T\right) + \nu_{xy}\left(\alpha_{yxx}\nabla^2_{xx}T + \alpha_{yyx}\nabla^2_{yx}T\right). \end{aligned} \tag{6.29}$$

Assuming the temperature gradiant along the $y$ direction and measuring the non-linear Nernst voltage along the $x$ direction (shown as the schematic setup in Fig. (6.1)), the above equation can be written with the help of Eq. $(6.21)$ as

$$\begin{aligned} V_x =& \nu_{xx}\left(\alpha_{xxy}\nu_{xy}\nu_{yy}+\alpha_{xyy}\nu_{yy}^2\right)\left(j_y^0\right)^2+\nu_{xy}\left(\alpha_{yxx}\nu_{xy}^2+\alpha_{yyx}\nu_{yy}\nu_{xy}\right)\left(j_y^0\right)^2, \\ =& \left(\nu_{xx}\nu_{yy}-\nu_{xy}^2\right)\left(\alpha_{xxy}\nu_{xy}+\alpha_{xyy}\nu_{yy}\right)\left(j_y^0\right)^2. \end{aligned} \tag{6.30}$$

Compare to the case of NLAHE [231], the term $\left(\nu_{xx}\nu_{yy}-\nu_{xy}^2\right)$, which we denote as $\nu'$, is not the same as the determinant $|\boldsymbol{\nu}| = |\widetilde{\boldsymbol{\alpha}}^0|^{-1}$. Substituting all the components in the Eq. (6.30), the non-linear Nernst voltage takes the form

$$\begin{aligned} V_x =& \nu'\left(-\alpha_{aab}\cos\theta+\alpha_{abb}\sin\theta\right)\nu_{ab}^0\left(j_y^0\right)^2 \\ &+\nu'\left(\alpha_{aab}\sin\theta\nu_{bb}^0+\alpha_{abb}\cos\theta\nu_{aa}^0\right)\left(j_y^0\right)^2 \end{aligned} \tag{6.31}$$

Now the linear longitudinal voltage in response to the applied temperature gradiant along the $y$ direction is given by

$$V_y^0 = \nu_{yy}^0 j_y^0 = \left(\nu_{aa}^0\sin^2\theta+\nu_{bb}^0\cos^2\theta\right)j_y^0 \tag{6.32}$$

To get rid of the current dependence $(j_y^0)$ from the above expression, we take the ratio between the non-linear Nernst voltage (Eq. (6.31)) and linear longitudinal voltage (Eq. (6.32)) which takes the form

$$\begin{aligned} \frac{V_x}{\left(V_y^0\right)^2} =& \frac{\nu'\left(-\alpha_{aab}\cos\theta+\alpha_{abb}\sin\theta\right)\nu_{ab}^0}{\left(\nu_{aa}^0\sin^2\theta+\nu_{bb}^0\cos^2\theta\right)^2} \\ &+\frac{\nu'\left(\alpha_{aab}\sin\theta\nu_{bb}^0+\alpha_{abb}\cos\theta\nu_{aa}^0\right)}{\left(\nu_{aa}^0\sin^2\theta+\nu_{bb}^0\cos^2\theta\right)^2}. \end{aligned} \tag{6.33}$$

Replacing the resistivity by the conductivity, the above equation can be rewritten as

$$\begin{aligned} \frac{V_x}{\left(V_y^0\right)^2} =& \frac{\nu''\left(-\alpha_{aab}\cos\theta+\alpha_{abb}\sin\theta\right)\alpha_{ab}^0}{\left(\alpha_{aa}^0\sin^2\theta+\alpha_{bb}^0\cos^2\theta\right)^2} \\ &+\frac{\nu''\left(\alpha_{aab}\sin\theta\alpha_{bb}^0+\alpha_{abb}\cos\theta\alpha_{aa}^0\right)}{\left(\alpha_{aa}^0\sin^2\theta+\alpha_{bb}^0\cos^2\theta\right)^2} \end{aligned} \tag{6.34}$$

where $\nu'' = \alpha_{aa}^0\alpha_{bb}^0-\left(\alpha_{ab}^0\right)^2-\alpha_{ab}^0\delta\alpha^0\sin 2\theta$. To simplify the above equation we now define $n_0 = \alpha_{bb}^0/\alpha_{aa}^0$

and $n_1 = \alpha^0_{ab}/\alpha^0_{aa}$ where $n_0$ represents the conductivity anisotropy ratio along the principal axes. Therefore, the Eq. $(6.34)$ takes the form

$$\frac{V_x}{\left(V^0_y\right)^2} = f_1 \alpha^0_{aa} \alpha_{aab} + f_2 \alpha^0_{aa} \alpha_{abb} \tag{6.35}$$

where the angular dependence factors $f_1$, and $f_2$ can be written in terms of $n_0, n_1$ and $\theta$ as

$$\begin{aligned} f_1 =& \frac{n_0(1 + n_1 \sin 2\theta) + n_1(n_1 + \sin 2\theta)}{\left(\sin^2\theta + n_0 \cos^2\theta\right)^2} \left(n_0 \sin\theta - n_1 \cos\theta\right) \\ f_2 =& \frac{n_0(1 + n_1 \sin 2\theta) + n_1(n_1 + \sin 2\theta)}{\left(\sin^2\theta + n_0 \cos^2\theta\right)^2} \left(n_1 \sin\theta + \cos\theta\right) \end{aligned} \tag{6.36}$$

Eq. $(6.35)$ and $(6.36)$ give the general expressions of angular dependence of the NLANE. Moreover, for the TR invariant system the linear Nernst conductivity vanishes i.e., $n_1 = 0$, then we have

$$\begin{aligned} f_1 &= \frac{n_0^2 \sin\theta}{\left(\sin^2\theta + n_0 \cos^2\theta\right)^2}, \\ f_2 &= \frac{n_0 \cos\theta}{\left(\sin^2\theta + n_0 \cos^2\theta\right)^2} \end{aligned} \tag{6.37}$$

## 6.4 Model Hamiltonian of two-dimensional bilayer $WTe_2$

In this paper, we take the model Hamiltonian of bilayer $WTe_2$ to study the NLANE in this system. The bilayer $WTe_2$, which is created by the stacking of two monolayers [45], preserves the TR symmetry and contains a pair of coupled tilted Dirac nodes. Unlike the monolayer, the inversion symmetry is naturally broken in bilayer case and a tunable spin orbit coupling is allowed via electric gating [236, 243, 237, 231]. The only crystalline symmetry that exists for bilayer $WTe_2$ is the mirror plane symmetry [44]. Therefore, following our analysis in Sec.6.2, the non-linear Nernst conductivity is expected to appear perpendicular to this mirror plane in response to an external temperature gradiant. The model Hamiltonian of bilayer $WTe_2$ can be written as

$$H_C = \begin{pmatrix} H_{K_1} + P \otimes s_x & \gamma \boldsymbol{I}_0 \otimes s_x \\ \gamma \boldsymbol{I}_0 \otimes s_x & H_{K_2} + P \otimes s_x \end{pmatrix} \tag{6.38}$$

where $P = \eta k_x \tau_z$. Here, $\eta$ is the spin-orbit coupling strength, and $\gamma$ is the hybridization strength between the two Dirac cones, whose Hamiltonian is given by,

$$H_{K_i} = t_x \widetilde{k}_x^i + v_0 \left( k_y \sigma_x - \zeta_i \widetilde{k}_x^i \sigma_y \right) + m\sigma_z + E_i \tag{6.39}$$

where $\widetilde{k}_x^i = (k_x - K_i)$ with $K_i$ are the wave vector components of the Dirac point. Here, $t_x$ represents the tilt parameter which tilts the Dirac node along $k_x$ direction, $v_0$ is the velocity, $m$ and $E_i$ are the size of the gap and energy of the Dirac point respectively. The $\sigma_i, s_i (i = 1, 2, 3)$ are the Pauli matrices, and $I_0$ is a $2 \times 2$ unit matrix. $\zeta_i = \pm 1$ is the chirality of the Dirac fermions. $H_{K_i}$ with $i = 1, 2$ describe the individual spinless Dirac fermion from each layer. The time reversal partner of Eq. (6.39) is defined by $H_{K_i}^{TR}(\boldsymbol{k}) = \mathcal{T}^\dagger H_{K_i}(-\boldsymbol{k})\mathcal{T}$ ($\mathcal{T} = \mathcal{K}$ is the TR symmetry operator for spinless fermion, where $\mathcal{K}$ is the anti-Hermitian complex conjugation operator) [251, 252], which could be written as,

$$H_{K_i}^{TR} = -t_x \widetilde{k}_x^{i\prime} - v_0 \left( k_y \sigma_x + \zeta_i \widetilde{k}_x^{i\prime} \sigma_y \right) + m\sigma_z + E_i \tag{6.40}$$

where $\widetilde{k}_x^{i\prime} = (k_x + K_i)$, indicating the time reversal Dirac points of the Hamiltonian in Eq. (6.39) located at $k_x = -K_i$. Therefore, the model Hamiltonian of bilayer $WTe_2$ given in Eq. (6.38) describes only half of the Brillouin zone [231, 44]. However, studying the Hamiltonian in Eq. (6.38) only is sufficient to show the NLANE for bilayer $WTe_2$, since the TR partner of Eq. (6.38) contributes the same to NLANE.

The energy dispersion of bilayer $WTe_2$ in the absence as well as in the presence of spin-orbit coupling (SOC) are shown in Fig. (6.2). The colors associated with each point of the bands represent the weight of the local Berry curvature. In the absence of spin-orbit coupling, the bilayer $WTe_2$, which is a semimetal with a small gap opened by the interlayer coupling, contains four tilted Dirac nodes. In Fig. 6.2(a) we can identify two tilted Dirac cones which carry the opposite Berry curvature because the two layers of the system are related through a mirror reflection. After turned on, the non-zero coupling $\eta$ lifts the spin degeneracy of the bands and splitted the four bands (Fig. 6.2(a)) into eight bands (Fig. 6.2(b)). With increasing the strength of the spin-orbit coupling, the band gap successively shrinks to zero and the system undergoes band inversion and then the band gap reopens again around the Dirac nodes as shown in Fig. 6.2(b). The Berry curvatures of the conduction and valence bands switch their sign due to the band inversion. However, with further tuning SOC, the system could become insulating [239].

It is clearly seen from the Fig. 6.2(a) that the Berry curvature shows finite value only nearby the

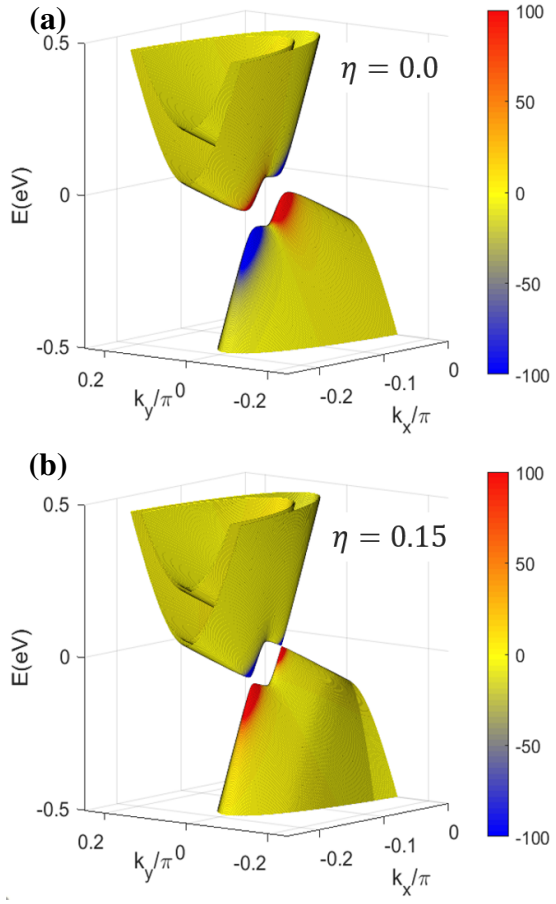


Figure 6.2: (Color online) Energy dispersions of bilayer $WTe_2$ (a) without spin-orbit coupling ($\eta = 0$) and (b) with spin-orbit coupling ($\eta = 0.15\ eV$Å). The colors represent the local Berry curvature distribution corresponding to each $\boldsymbol{k}$ point of the bands. A finite SOC explicitly lifts the spin degeneracy of the bands. (b) shows an anti-crossing at the band touching point with SOC of strength $\eta = 0.15\ eV$Å indicating by the sign-change (change of the color) of their Berry curvatures. The other parameters of the Hamiltonian are $v_0 = 2\ eV$Å, $t = 1.5\ eV$Å, $m = 0.1\ eV$, $\zeta_1 = 1$, $\zeta_2 = -1$, $E_1 = 0.02\ eV$, $K_1 = -0.1\pi$, $K_2 = -0.15\pi$, $E_2 = -0.08\ eV$, and $\gamma = 0.05\ eV$.

band edges in the absence of SOC, which is now asymmetrically distributed at $\boldsymbol{k}$ and $-\boldsymbol{k}$ at the Fermi surface (see insets of Fig. (3)). The sign of the Berry curvature is opposite at any $\boldsymbol{k}$ point for the upper and lower bands. When we turn on the SOC, the bands split and anti-cross with their neighbors due to the hybridization factor $\gamma$. The Berry curvature of the conduction band exchanges sign with the valence band at the band inversion and band anti-crossing. In the presence of spin-orbit coupling, the Berry curvature are intensively concentrated around the Dirac point where the band anti-crossing occurs as shown in Fig. 6.2(b). It has been shown that around the points where the band gaps are almost vanishing, an extremely large Berry curvature

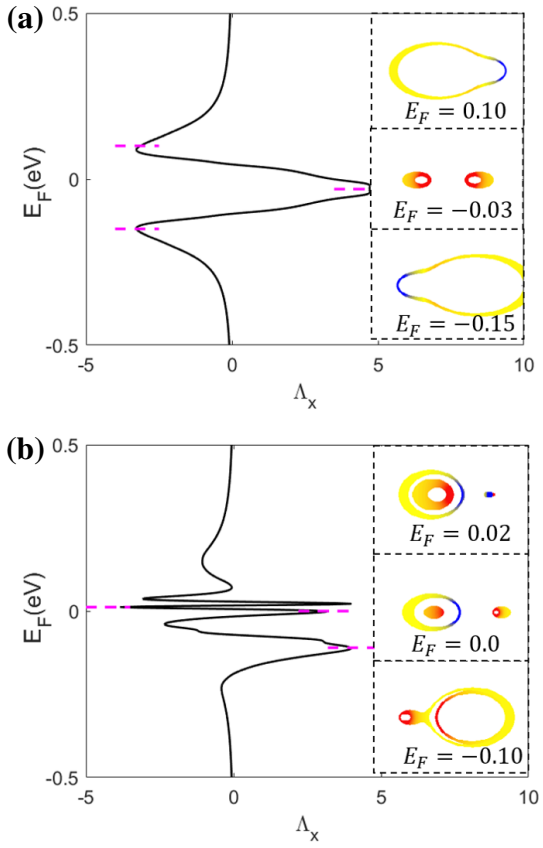


Figure 6.3: (Color online) The non-linear anomalous Nernst coefficient $\Lambda_x$ as a function of chemical potential $E_F$ for different strengths of SOC (a) $\eta = 0$ and (b) $\eta = 0.15\ eV$Å respectively. Insets in (a) and (b) show different Fermi surfaces where the Fermi energies are indicated by magenta dashed line. The color of the insets displays the distribution of Berry curvature weight on the Fermi surface. The color scale is the same as that in Fig. (6.2). Here $T = 50$ K and the other parameters used are the same as in Fig. (6.2).

originates within a small gap region i.e., a large gradiant of the Berry curvature occurs which allows a strong NLAHE in the bilayer $WTe_2$. Therefore, it is expected to get a strong NLANE response in bilayer $WTe_2$ based on Eq. $(6.15)$. We would like to point out that we can get a non-uniform distribution of the Berry curvature at a given Fermi level even without tilting in bilayer $WTe_2$ because the Dirac cones in this system are coupled due to the hybridization factor ($\gamma$) and also situated at different energies, i.e., $E_1 = 0.02$eV, and $E_2 = -0.08$eV.

## 6.5 Results and discussions

Recently, non-linear anomalous Hall effect has been observed experimentally in bilayer $WTe_2$ system due to the nonuniform distribution of the Berry curvature at Fermi surface. It has been shown that the tilted band anti-crossings and band inversions lead to a large Berry curvature dipole which produces the strong non-linear Hall effect in this system. Therefore, it is expected to get a finite non-linear anomalous Nernst signal based on the Eq. $(6.15)$ for the same system. Since the Dirac nodes are tilted along the $k_x$ direction by $t_x$ in this system, the Berry curvature has an asymmetric distribution along $k_x$ direction while symmetric distribution along $k_y$ direction as clearly seen from the figure. Therefore, combing the mirror symmetry and the TR symmetry for the bilayer $WTe_2$ system, only the $\Lambda_x^T$ is nonzero while $\Lambda_y^T = 0$. Note, the component indexes mentioned for $\mathbf{\Lambda}$ is within the principal axes coordinates.

The non-linear anomalous Nernst coefficient $\Lambda_x$ $(a = x)$ at different Fermi energies in the presence as well as absence of spin-orbit coupling are depicted in Fig. $(6.3)$. It is clear from the figure that in the absence of SOC, the magnitude of $\Lambda_x^T$ increases and reaches to a maximum value when the chemical potential approaches towards the band edge. We would like to point out that despite of being the largest Berry curvature at the band edge, the $\Lambda_x^T$ will be zero because the group velocity vanishes at the band edge in the presence of a gap. Now, when we turned on the SOC, band inversions and band anti-crossings occur due to the hybridization factor. Therefore, sharp peaks (divergence like behavior) of the $\Lambda_x^T$ appear at the band inversions which is clearly seen from the Fig. 6.3(b). In particular, with tuning the spin-orbit coupling, the magnitude of the $\Lambda_x^T$ enhances with the shrinking gaps and the divergences appear at the band inversions. A similar dependence of Berry curvature dipole on chemical potential has been obtained recently [231, 232]. The insets in Fig. $(6.3)$ show the Berry curvature distribution at the given Fermi surfaces (indicated by magenta dashed lines). We would like to mention that due to the spin-orbit coupling and hybridizations, the Berry curvature could be significantly large on the Fermi surface in bilayer system compared to the single layer $WTe_2$ system [231].

Now we study the temperature dependence of NLANE using the Eq .$(6.15)$ where the temperature dependence will come from $(-\partial f_{\boldsymbol{k}}/\partial \varepsilon_{\boldsymbol{k}})$ besides the $1/T^2$ factor. Since the Fermi-Dirac distribution function becomes broader for higher temperature, the integrand in Eq. $(6.15)$ collects more contributions and leads to different NLANE coefficients.

The non-linear anomalous Nernst coefficient $\Lambda_x^T$ for different temperatures and chemical potentials is shown in Fig. $(6.4a)$. The white arrow and the black arrow indicate the shift of the local maximum

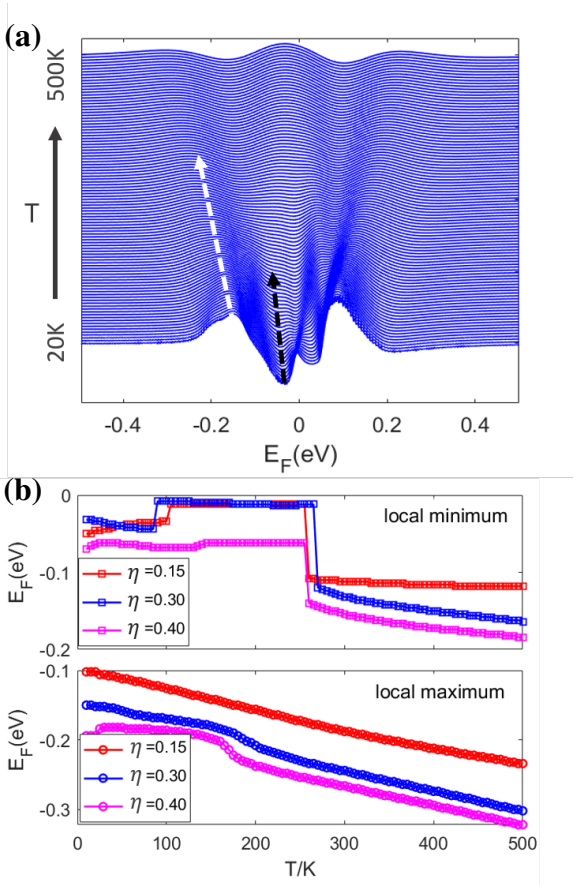


Figure 6.4: (Color online) (a) Non-linear Nernst coefficient $\Lambda_x$ as a function of chemical potential ($E_F$) at different temperatures (T) for spin-orbit coupling $\eta = 0.3eV$Å. The position of the local extreme points of $\Lambda_x$ shifts with increasing temperature. (b) The locus of the local minimum points (indicated by the black dashed line in panel (a)) and the locus the local maximum points (indicated by the white line in panel (a)) are shown for different spin-orbit ($\eta$). In all cases, with increasing temperature, the chemical potential at the local minimum point shows a sudden drop while the chemical potential at the local maximum point decreases almost linearly.

and local minimum value of $\Lambda_x^T$ in $(E_F, T)$ parameter space. The shift of the chemical potential for these extreme points are plotted in Fig. $(6.4b)$. When we increase the temperature from $20K$ to $500K$, there is a linear increasing of the magnitude of the chemical potential of the extreme points far away from the band edge ($E_F \approx 0$). On the other hand, for the extreme points nearby the band edge, there is an obvious drop in chemical potential with increasing the temperature.

This temperature-dependent phenomena could be well explained by the tilted band structure in Fig. $(6.2)$. For the local maximum peak of the NLANE coefficient (bottom in Fig. $6.4\,(b)$), its Fermi energy lies away from the band edge. The broadened Fermi distribution function $f(E_{\boldsymbol{k}}, E_F, \beta)$ moves with the

Fermi energy $E_F$. When the temperature increases, the chemical potential of these extreme points moves away from the band edge resulting in the linear increasing in negative direction of the chemical potential. On the other hand, for the local extreme points nearby the band edge (top in Fig. $6.4\,(b)$), with an increasing temperature the chemical potential of these extreme points do not need to move to reach a minimum or maximum due to the significantly large Berry curvature around the band edge. However, the integrand for the NLANE coefficient will drop suddenly around $T = 250$ K because the width of $(-\partial f_{\boldsymbol{k}}/\partial\varepsilon_{\boldsymbol{k}})$ contains both the positive and negative Berry curvature monopoles. This explains why the chemical potential for the extreme points in Fig. 6.4(b) drops around $T = 250$ K.

Next we study the dependence of NLANE on the spin-orbit coupling because the SOC can affect the band structure as well as the Berry curvature distribution for the bilayer $WTe_2$ system as already discussed in the previous section. The NLANE coefficient as a function of spin-orbit coupling strength $\eta$ and chemical potential $E_F$ is depicted in Fig. $(6.5)$. The colors indicate the magnitude of non-linear Nernst coefficient and the green dashed line is the zero energy level as shown in Fig. $6.5\,(a)$. From the figure we find that there are two nodes circled by the black dashed line in the $(E_F, \eta)$ parameter space around which we can choose a local co-ordinate system. Clearly, these two nodes behave opposite to each other. In the local coordinate system, the node above $E_F = 0$ carries positive conductivity (bright yellow color) in one direction whereas the other node below $E_F = 0$ carries negative conductivity (dark red color) in the same direction and vice-verse in the perpendicular direction. This behavior of the NLANE coefficient is related to the band anti-crossing and band inversion near the Dirac nodes situated at $E_F = 0.02eV$, and $E_F = -0.08eV$ respectively in the system. Clearly, with increasing the SOC strength the non-linear Nernst coefficient for a fixed chemical potential $E_F = 0$ goes from positive value to negative value showing an obvious sign change around $\eta = 0.15$ $eV$Å. The NLANE coefficient at $E_F = 0$ for different temperatures from $T = 20$ K to $T = 120$ K is shown in Fig. $6.5\,(b)$. It is clear from the figure that all the curves intersect around $\left(\eta = 0.15eV\text{Å}\right)$ and the strength of SOC corresponding to the intersection point remains unaltered with changing temperature whereas enhances with increasing the chemical potential ($\eta = 0.12$ $eV$Å and $\eta = 0.16eV$Å for $E_F = -0.08$ $eV$ and $E_F = 0.02$ $eV$ respectively). The magnitude of the NLANE coefficient decreases with increasing the temperature. We find that the strength of spin-orbit coupling at which the NLANE coefficient changes sign shifts towards lower value with increasing temperature. For large value of SOC, the system becomes insulating and $E_F = 0$ lies in the gap. Therefore, the NLANE coefficient at $E_F = 0$ vanishes due to vanishing Fermi surface at large SOC.

For different values of the tilt parameter, the Fermi surface gets reshaped and we have different

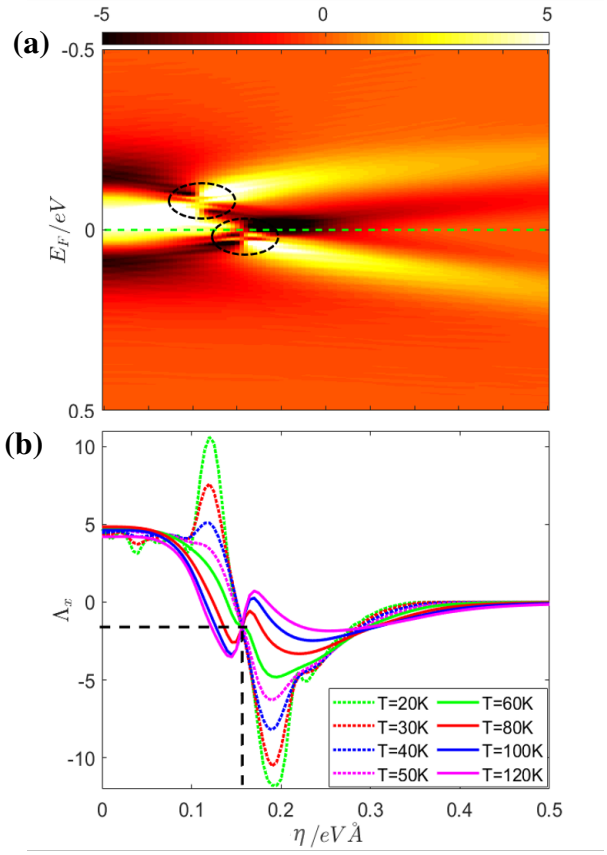


Figure 6.5: (Color online) (a) Non-linear Nernst coefficient ($\Lambda_x^T$) at $T = 50$ K with different values of the chemical potential ($E_F$) and SOC strengths ($\eta$). There are two nodes of NLANE coefficient circled by the black dashed line. Clearly, these two nodes behave opposite to each other where this behavior of the NLANE coefficient is related to the band anti-crossing and band inversion near the Dirac nodes situated at $E_F = 0.02\ eV$, and $E_F = -0.08\ eV$ respectively. With increasing the SOC strength the Nernst coefficient at $E_F = 0$ (indicated by the dashed line) goes from positive value (white yellow) to negative value (dark orange) showing an obvious sign change around $\eta = 0.15\ eV\mathring{A}$. (b) NLANE coefficient at the zero Fermi energy for different temperatures are shown. The magnitude of the Nernst coefficient decreases with increasing the temperature. The strength of spin-orbit coupling, at which all the NLANE coefficient curves intersect, remains unaltered with changing temperature. The other parameters used here are the same as in Fig. (6.3).

Berry curvature distributions at the Fermi surface which result in different Nernst conductivities based on the Eq. (6.15). This fact convinces us to study the dependence of the non-linear Nernst conductivity on the tilt parameter which could be varied by tuning the intrasublattice hoppings [253]. The $x$ component of NLANE coefficient as a function of the tile parameter ($t_x$) for different $E_F$ values is plotted in Fig. 6.6($a$). For bilayer $WTe_2$ system with spin-orbit coupling $\eta = 0.2\ eV\mathring{A}$, the negative non-linear Nernst conductivity arises (shown by the dark red colors) around $E_F = 0$. The dependence of NLANE coefficient on the tilt parameter for different temperatures at zero chemical potential is shown in Fig. 6.6($b$). In the absence of

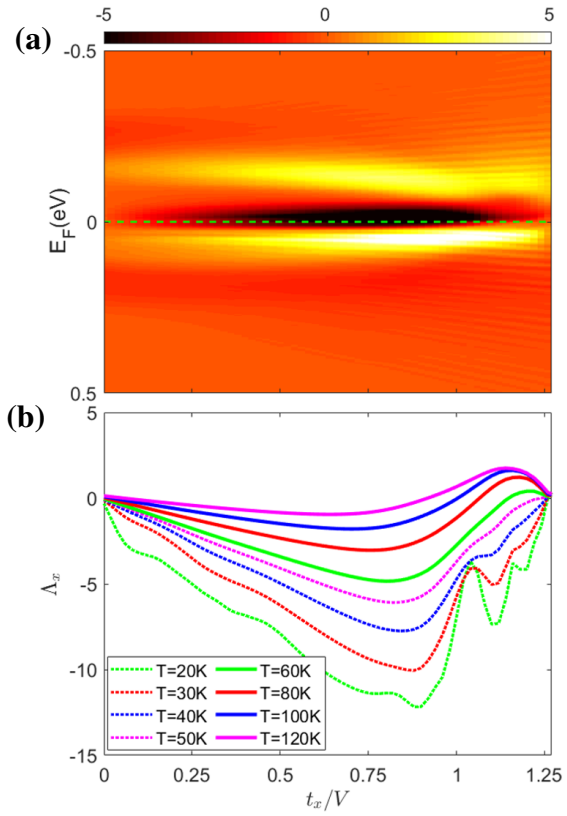


Figure 6.6: (Color online) (a) Non-linear Nernst coefficient ($\Lambda_x^T$) at $T = 50$ K as a function of chemical potential ($E_F$) and tilt parameter ($t_x$) in the presence of SOC $\eta = 0.2eV$Å. Interestingly, in the absence of tilt, $\Lambda_x^T$ at the non-zero chemical potential becomes finite whereas it vanishes when $E_F$ is at zero energy. (b) $\Lambda_x^T$ at $E_F = 0$ (indicated by the green dashed line in (a)) as a function of tilt parameter for different temperatures. At $t_x = 1.25v_0$, the non-linear Nernst conductivity vanishes in bilayer $WTe_2$ at all temperatures. The other parameters used here are the same as that in Fig. (6.3).

tilt, the Berry curvatures distribute symmetrically near the band edge and therefore, the NLANE coefficient vanishes. Now in the presence of tilt $t_x$, the band extrema are shifted from the original $\boldsymbol{K}(-\boldsymbol{K})$ point to opposite directions in $k_x$ axis and makes the Berry curvature distribution asymmetric at the Fermi surface along $k_x$. Therefore, as the Dirac nodes are getting tilted more and more with increasing $t_x$, the magnitude of NLANE coefficient increases and reaches a maximum around $t_x = 0.8v_0$ (near the critical point $t_x/v_0 = 1$ beyond which the Dirac cone becomes overtilted). After that it decreases with further increasing $t_x$ as shown in Fig. 6.6$(b)$. Interestingly, all the curves for different temperatures intersect around $t_x = 1.25v_0$, where the NLANE coefficient also vanishes. Moreover, in the overtilted region, we have a change in sign of the Nernst conductivity from negative to positive for high temperatures as clearly seen from the figure. We consider both the momentum shift ($K_i$) and the energy shift ($E_i$) for the tilted Dirac fermions hybridized via a inter-

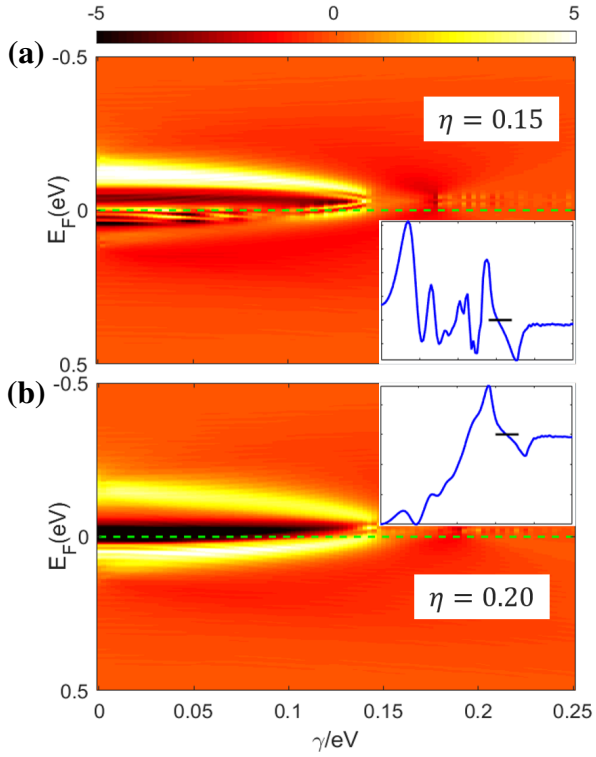


Figure 6.7: (Color online) Non-linear Nernst coefficient ($\Lambda_x^T$) at $T = 50$ K as a function of chemical potential ($E_F$) and inter-layer coupling ($\gamma$) in the presence of SOC $\eta = 0.15eV$Å (a) and $\eta = 0.20eV$Å (b). The magnitude of $\Lambda_x^T$ decreases to zero (and stays at zero) when the inter-layer coupling goes over $\gamma = 0.15eV$, in spite of the different spin-orbit coupling in (a) and (b). The insets correspondingly show the values of $\Lambda_x^T$ versus $\gamma$ at $E_F = 0$ (green dashed line in main figure), where the short black lines indicate the point ($\gamma \approx 0.15eV$) above which $\Lambda_x^T = 0$. All the other parameters used here are the same as in Fig. (6.2).

layer coupling in our model (Eq. (6.38)). Without the inter-layer coupling ($\gamma = 0$), the two uncoupled Dirac fermions contribute independently, not showing any anti-crossings. A small inter-layer coupling between the two monolayers of bilayer $WTe_2$ explicitly breaks the inversion symmetry and opens a tiny gap at the band crossings of the uncoupled systems [44, 231]. The effect of the inter-layer coupling $\gamma$ on the NLANE $\Lambda_x^T$ for different SOC is shown in Fig. (6.7). For both (a) and (b) $\Lambda_x^T$ decreases to zero at all Fermi levels when $\gamma$ goes over $0.15eV$, as shown in the figure. A cross-section of the maps at $E_F = 0$ (green dashed line) is shown in the inset in panel (a) and (b), where the blue line is the value for $\Lambda_x^T$ for varied $\gamma$ and the short black line indicates $\Lambda_x^T = 0$ around $\gamma = 0.15eV$. This could be understood from the band structure based on the Hamiltonian model (Eq. (6.38)) for bilayer $WTe_2$. When the coupling between the Dirac cones for bilayer $WTe_2$ increases, their Dirac points would approach each other and coalesce in momentum space despite the momentum shift $K_i$ and energy shift $E_i$. Therefore, the total NLANE for the system is reduced, due to the

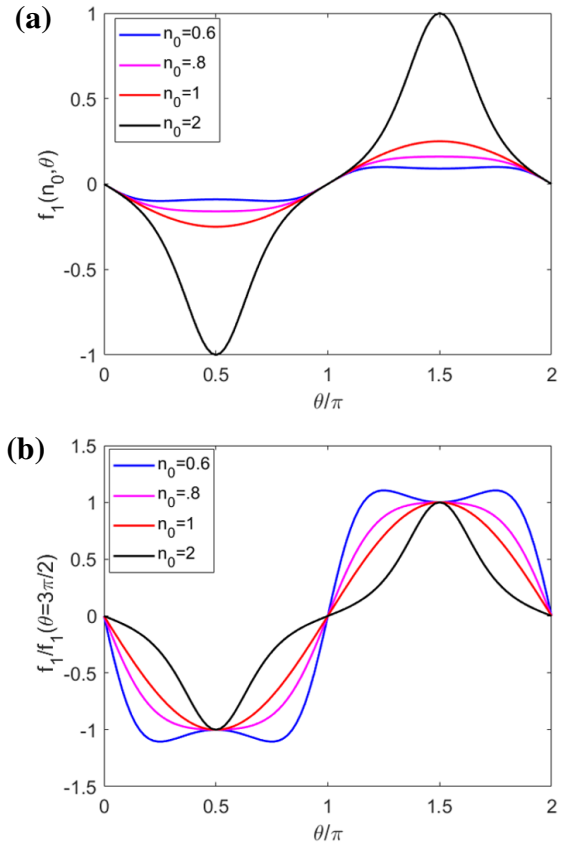


Figure 6.8: (Color online) The angular dependence factor $f_1\,(n_0, \theta)$ as a function of the angle $\theta$ between the temperature gradient and principal axis for different values of $n_0$.The plot in each panel (a) shows the non-scaled curves, where we see the relative magnitude of the $f_1$ for different $n_0$. While all the curves are scaled relatively to the value at $\theta = 3\pi/2$ in panel (b). For a time reversal symmetric system where the linear Nernst response is zero ($n_1 = 0$), a similar angular dependence (given in Eq. $(6.37)$) of the NLANE is found as that of the NLAHE in the recent work by *Du, et. al, 2018*.

decrease of the unevenness of the berry curvature $\boldsymbol{\Omega}(\boldsymbol{k})$ and the Fermi distribution function $f(\boldsymbol{k})$. Increasing $\gamma$ further would open a gap for the system, rendering the whole system insulating and a zero NLANE.

For clarity, we point out that all the components mentioned so far in this section are discussed in the principal axes coordinates, i.e., $t_x$, $\Lambda_x$ are the $a-$component (with $a = x$ is the principal axes) of the tilting and the NLANE coefficient respectively. However, the $x-$component should be distinguished from the $a-$component for the angular dependence analysis based on the setup shown in Fig. (6.1).

In Sec. 6.3, we have systematically derived the general expressions for the angular dependence of the non-linear Nernst voltage (Eq. $(6.35)$) which is tightly connected to the experiments. For a system with given parameters including $\eta, t_x, \gamma$ and $\mu$, the angular dependence of NLANE can be shown by calculating

the angular dependence factors $f_1$ and $f_2$. In Eq. $(6.36)$, the conductivity anisotropy ratios $n_0$ and $n_1$ can be tuned via gate voltage in experiments. In this paper we study the angular dependence of the non-linear Nernst voltage in bilayer $WTe_2$. Considering the presence of time-reversal symmetry and the mirror plane $M_a$ of the bilayer $WTe_2$, the only non-zero component of the NLANE coefficient is $\Lambda_a^T$ which is perpendicular to the mirror plane (as shown in Fig. (6.1)). Therefore, we have $\alpha_{abb} = -\alpha_{bba} = 0$ leading to the fact that we only have to calculate $f_1$ to get the full angular dependence of non-linear Nernst voltage in this system. Note, for Hamiltonian $H_C$ given in Eq. (6.38), both the linear AHE response ($\alpha_{ab}^0$) and the NLANE ($\alpha_{aab}$) are non-zero based on Eq. (6.11) and Eq. (6.13) respectively. Including the contribution of the TR partner of Eq. (6.38), the linear ANE vanishes ($n_1 = 0$) while the total NLANE doubles which is indicated by its coefficient $2\Lambda_a^T$.

Now we consider that the temperature gradient is applied along the $y$ direction and the non-linear Nernst voltage is measured along the $x$ direction in bilayer $WTe_2$ (shown in Fig. (6.1)). For the TR invariant system, $n_1 = 0$ i.e. no linear Nernst response is present, the angular dependence of $f_1$ depends on the anisotropy ratio $n_0$ could be described by Eq. (6.37). The angular dependence factor $f_1\left(n_0, n_1, \theta\right)$ as a function of the angle $\theta$ between the applied temperature gradient and principal axes for different values of $n_0$ with $n_1 = 0$ is depicted in Fig. $(6.8)$. Here, a non-scaled plot is given in (a) where the relative magnitudes for different $n_0$ value are shown correspondingly while in (b) all the curves are scaled by the value at $\theta = 3\pi/2$. In the absence of anisotropy ($n_0 = 1$), the Eq. (6.37) dictates that the angular dependence will be a $\sin\theta$ dependence which is also clearly seen from the figure. When the anisotropy ratio is large ($n_0 > 1$), the angular dependence is deviated from the sine dependence. On the other hand, in the case of small anisotropy ($n_0 = 0.6$), a double-peak line shape appears where the maxima at $\theta = \pi/2, 3\pi/2$ turn into a minima. All these features of the angular dependence of the non-linear Nernst voltage can be checked by tuning the anisotropy ratio through gate voltage in experiments.

## 6.6 Conclusion

In conclusion, we study the nonlinear anomalous Nernst effect of time-reversal invariant but inversion symmetry broken systems, specifically, bilayer $WTe_2$. We have systematically derived the nonlinear Nernst current as a second order response to the temperature gradient through the Boltzmann semiclassical approach. By a symmetry analysis, we show that the transverse nonlinear Nernst response has an explicit origin in a pseudotensorial quantity, $\Lambda_a^T$, which plays a role similar to the Berry curvature dipole

determining the nonlinear anomalous Hall effect in the recent studies. We calculate and make experimental predictions for the NLANE coefficient for its dependence on temperature, spin-orbit coupling, tilting, inter-layer coupling, and chemical potential for the bilayer $WTe_2$, in which signatures of NLAHE have been observed recently. In addition to the Berry curvature dipole contribution, disorder mediated effects such as non-linear side-jump and skew scatterings from impurities that contribute to the non-linear anomalous Hall effect [235, 232, 254, 255, 233], may also contribute to non-linear anomalous Nernst effect. These effects are beyond the scope of this paper and are left for future study.

Through the mapping of NLANE coefficient into the parameter space of chemical potential and spin-orbit coupling $(E_F, \eta)$, we find there are two nodes that could be associated with the Dirac points of the model. Between these two nodes in the parameter space, there is a region where we find the NLANE coefficient changes sign with tuning the spin-orbit coupling. We also show a mapping of the NLANE coefficient into the $(E_F, t_x)$ and $(E_F, \gamma)$ parameter space, where the tilting $(t_x)$ and the inter-layer coupling $(\gamma)$ effect on the NLANE could be observed respectively. We also derive the angular dependence of the NLANE in detail, where the angle is between the applied temperature gradient and the principal axes. Finally we wish to remark that the derivations in this work can also be applied to other $2D$ and $3D$ systems in addition to $WTe_2$. Since NLAHE has already been experimentally observed in bilayer $WTe_2$, we apply the general theoretical framework for NLANE developed in this paper to this system, and make several predictions which can be checked experimentally.

# Chapter 7

# Wiedemann-Franz law and Mott relation for anomalous transport in the non-linear regime

Berry curvature dipole has been shown to produce non-linear anomalous Hall and Nernst effects which are non-zero even in the presence of time-reversal symmetry. Here, within the framework of Boltzmann theory, we predict another Berry curvature induced non-linear response function, namely, the nonlinear anomalous thermal Hall effect as the second-order response of an applied longitudinal temperature gradient. The analytical calculations of the transport coefficients allow us to derive the fundamental relations which can be viewed as the analog of the celebrated Wiedemann-Franz law and Mott relation in the non-linear regime. Our predictions on thermal Hall effect along with the relations among the thermoelectric transport coefficients in the non-linear regime can be directly checked in experiments.

## 7.1 Introduction

Onsager's reciprocity relations mandate that the Hall effect in linear response has to vanish in a time reversal invariant system whereas the non-linear Hall effect has no such restriction [42]. The generalized Onsager's relation appropriate for non-linear current response indicates that in order to get a non-zero DC non-linear conductivity, the current response requires dissipation and should be proportional to the relaxation

time $\tau$ [246]. Unlike the anomalous Hall effect in the linear-response regime [190, 39, 256, 191, 196, 257, 198, 197, 192, 195, 213, 193, 194], the non-linear anomalous Hall effect (NLAHE) does not require broken time reversal symmetry (TRS) but needs inversion symmetry (IS) breaking. The Berry curvature dipole (BCD), which is defined as the first order moment of the Berry curvature over the occupied states, is found to be responsible for NLAHE [216, 43, 45, 44, 235]. Motivated by the idea of NLAHE, another second-order response, non-linear anomalous Nernst effect (NLANE) has been predicted in transition metal dichalcogenides (TMDCs) very recently [246, 245, 258]. Interestingly, these nonlinear responses could manifest distinctive behaviors and have become promising tools for understanding novel materials with low crystalline symmetry in experiments.

In this paper, we first calculate a third non-linear response function, namely, the non-linear anomalous thermal Hall effect (NLATHE) which can be directly observed in experiments. NLATHE refers to the appearance of a transverse thermal gradient as a second order response to an applied longitudinal heat current (Fig. 7.1). Armed with these calculations we then revisit the question of fundamental relations among all three anomalous transport coefficients in the non-linear regime. In linear response theory, the relations among electric, thermo-electric and thermal transport coefficients of metals are encapsulated by the celebrated Wiedemann-Franz law and Mott formula [40]. These formulae in the context of linear anomalous transport coefficients have been studied in topologically trivial and non-trivial materials in theory as well as experiments [189, 259, 39, 260, 209, 261, 208, 262, 263]. While according to the Wiedemann-Franz law, the electric and thermal conductivities (regular or anomalous) are directly proportional to each other, the Mott formula predicts that the Nernst coefficient is proportional to the derivative of the Hall coefficient with respect to the chemical potential (see Eq. (7, 8)). Interestingly, our analytical calculations for all three anomalous transport coefficients allow us to predict fundamentally new relations among the transport coefficients in the non-linear regime. The principal result of this work, other than proposing new experiments to measure the non-linear anomalous thermal Hall effect, is the remarkable prediction that in the non-linear regime, the anomalous Hall and Nernst coefficients are directly proportional to each other (Eq. (7.16)), while the derivative appears in the analog of the Wiedemann-Franz law (Eq. (7.14)). These results should be tested in experiments as confirmation of the intrinsic non-linearity, rather than a more conventional departure from the Wiedemann-Franz law and the Mott formula. We check the validity of our analytical results by full numerical evaluation of the relevant quantities for $MoS_2$, a TR invariant but inversion symmetry broken TMDC that has been intensively studied in experiments recently.

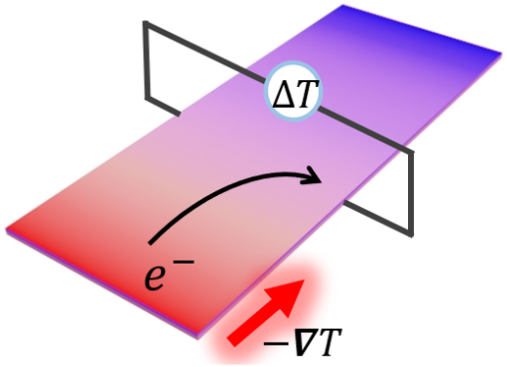


Figure 7.1: (Color online) Schematic experimental setup for measuring the non-linear anomalous thermal Hall effect. A transverse thermal gradient ($\Delta T$) can be measured as a second-order response of the longitudinal heat current even in the absence of external magnetic field. The sample breaks inversion but respects time reversal symmetry, so the linear response anomalous thermal Hall current is known to vanish by symmetry.

## 7.2 Boltzmann theory and anomalous thermal Hall effect in the non-linear regime

The phenomenological Boltzmann transport equation can be written as

$$\{\partial_t + \dot{\boldsymbol{r}}\boldsymbol{\nabla}_{\boldsymbol{r}} + \dot{\boldsymbol{k}}\boldsymbol{\nabla}_{\boldsymbol{k}}\} f(\boldsymbol{k}, \boldsymbol{r}, t) = I_{coll}\{f(\boldsymbol{k}, \boldsymbol{r}, t)\} \tag{7.1}$$

where the collision integral $I_{coll}\{f(\boldsymbol{k}, \boldsymbol{r}, t)\}$ incorporates the effects of electron correlations (inelastic scattering) and elastic scattering from impurities. For the sake of simplicity, we here focus only on the impurity scattering. Invoking the relaxation time approximation, the steady-state solutions to the Boltzmann equation is given by

$$\{\dot{\boldsymbol{r}}\boldsymbol{\nabla}_{\boldsymbol{r}} + \dot{\boldsymbol{k}}\boldsymbol{\nabla}_{\boldsymbol{k}}\} f(\boldsymbol{k}) = -\frac{g_{\boldsymbol{k}}}{\tau} \tag{7.2}$$

where $g_{\boldsymbol{k}} = f(\boldsymbol{k}) - f_0$ is the difference between the perturbed Fermi-Dirac distribution $f_{\boldsymbol{k}}$ and equilibrium Fermi-Dirac function $f_0$. Considering the homogeneous uniform fields, we have dropped the $\boldsymbol{r}$ dependence of $f(\boldsymbol{k}, \boldsymbol{r}, t)$. Here, $\tau$ is the average scattering time between two successive collisions. For simplicity we ignore the momentum dependence of the scattering time $\tau$ and assume it to be a constant for this work.

To find the non-linear anomalous thermal Hall coefficient in the absence of the external fields, we

expand $g_{\boldsymbol{k}}$ as $g_{\boldsymbol{k}} = g^1_{\boldsymbol{k}} + g^2_{\boldsymbol{k}} + ...$, where $g^n_{\boldsymbol{k}}$ is understood as the $n^{th}$ order response to the applied thermal gradient, i.e., $g^n_{\boldsymbol{k}} \propto (\boldsymbol{\nabla} T)^n$. Substituting $f(\boldsymbol{k}) = f_0 + g_{\boldsymbol{k}}$ into the steady-state Boltzmann equation given in Eq. (7.2), we could find the distribution function at the first and second-order in the thermal gradient as,

$$\begin{aligned} g^1_{\boldsymbol{k}} &= \tau \boldsymbol{v}_{\boldsymbol{k}} \frac{(\varepsilon_{\boldsymbol{k}} - \mu)}{T} \frac{\partial f_0}{\partial \varepsilon_{\boldsymbol{k}}} \boldsymbol{\nabla} T, \\ g^2_{\boldsymbol{k}} &= \tau \boldsymbol{v}_{\boldsymbol{k}} \frac{(\varepsilon_{\boldsymbol{k}} - \mu)}{T} \frac{\partial g^1_{\boldsymbol{k}}}{\partial \varepsilon_{\boldsymbol{k}}} \boldsymbol{\nabla} T, \end{aligned} \tag{7.3}$$

where $\mu$ is the chemical potential, $\boldsymbol{v}_{\boldsymbol{k}} = \hbar^{-1} \boldsymbol{\nabla}_{\boldsymbol{k}} \varepsilon_{\boldsymbol{k}}$ is group velocity with $\varepsilon_{\boldsymbol{k}}$ the energy dispersion.

After accounting for both the normal and anomalous contributions, the total thermal current $\boldsymbol{j}^Q_{tot}$ is given by $\boldsymbol{j}^Q_{tot} = \boldsymbol{j}^Q_N + \boldsymbol{j}^Q_E + \boldsymbol{j}^Q_T$, where $\boldsymbol{j}^Q_N$ is the standard contribution to thermal current coming from the conventional velocity $\boldsymbol{v}_{\boldsymbol{k}}$ of the carriers, and $\boldsymbol{j}^Q_E$ is the anomalous thermal current mediated by the Berry curvature $\boldsymbol{\Omega}_{\boldsymbol{k}}$ in the presence of electric field $\boldsymbol{E}$ [189]. In this paper, we are interested in the last term $\boldsymbol{j}^Q_T$ given by [264, 189]

$$\begin{aligned} \boldsymbol{j}^Q_T = &- \frac{k_B^2 T}{\hbar} \boldsymbol{\nabla} T \times \int [d\boldsymbol{k}] \sum_n \boldsymbol{\Omega}^n_{\boldsymbol{k}} \Big[ \beta^2 \left(\varepsilon^n_{\boldsymbol{k}} - \mu\right)^2 f_0 \\ &+ \frac{\pi^2}{3} - \mathrm{In}^2 \left(1 - f_0\right) - 2\,\mathrm{Li}_2 \left(1 - f_0\right) \Big] \end{aligned} \tag{7.4}$$

which describes the transverse thermal response to the applied thermal gradient $-\boldsymbol{\nabla} T$ in the presence of a non-trivial Berry curvature $\boldsymbol{\Omega}_{\boldsymbol{k}}$.

Substituting Eq. (7.3) into the thermal Hall term in Eq. (7.4) (with $f_0$ replaced by $f_{\boldsymbol{k}} = f_0 + g_{\boldsymbol{k}}$)), the non-linear anomalous thermal Hall current flowing along the direction $a$ (second order of $-\boldsymbol{\nabla} T$) can be written as

$$\left(\boldsymbol{j}^Q_T\right)'_a = \epsilon_{abc} \frac{\tau \nabla_b T \nabla_d T}{\hbar^2} \int [d\boldsymbol{k}] \sum_n \Omega^n_{\boldsymbol{k},c} \frac{\left(\varepsilon^n_{\boldsymbol{k}} - \mu\right)^3}{T^2} \frac{\partial f_0}{\partial k_d} \tag{7.5}$$

where the prime on $(\boldsymbol{j}^Q_T)'$ indicates the nonlinear response and $a, b, c, d$ represent the components $x, y, z$, and $n$ is the band index. In this paper we focus on this Berry curvature-dependent anomalous contribution to $(j^Q_T)'_a$ which is non-zero in TRS invariant systems. Note that there is another non-anomalous, Berry curvature-independent contribution to $(j^Q_T)'_a$ which is $\tau^2$-dependent and only exists in the absence of both TRS and inversion symmetries [246], which we ignore. From Eq. (7.5), the non-linear anomalous thermal

Hall coefficient can be written as $\left[(j_T^Q)'_a = \epsilon_{abc} l'_{cd} (\nabla_b T \nabla_d T)\right]$,

$$l'_{cd} = \frac{\tau T}{\hbar^2} \int [d\boldsymbol{k}] \sum_n \Omega^n_{\boldsymbol{k},c} \frac{\left(\varepsilon^n_{\boldsymbol{k}} - \mu\right)^3}{T^3} \frac{\partial f_0}{\partial k_d} \tag{7.6}$$

This is one of the main results of this paper. We find that NLATHE, which is linearly proportional to the scattering time, appears due to the Berry curvature from the states near the Fermi surface. Under TR symmetry, we know $\boldsymbol{\Omega_k} = -\boldsymbol{\Omega_{-k}}$, $\varepsilon_{\boldsymbol{k}} = \varepsilon_{-\boldsymbol{k}}$ and $\partial f_0/\partial k_d = -\partial f_0/\partial\left(-k_d\right)$. Therefore, it is clear from the Eq. (7.6) that NLATHE can survive even in the time-reversal invariant systems.

## 7.3 Analog of Wiedemann-Franz law and Mott relation in the non-linear regime

We now investigate the celebrated Wiedemann-Franz law and Mott relation in the non-linear regime at low temperatures. In the linear response regime, the Wiedemann-Franz law which gives the ratio between thermal conductivity ($\kappa_{ab}$) and electrical conductivity ($\sigma_{ab}$), is given by [265]

$$\frac{\kappa_{ab}}{\sigma_{ab}} = LT \tag{7.7}$$

with $L = \pi^2 k_B^2/3e^2$ the Lorentz number. On the other hand, the Mott relation can be written as [40]

$$\alpha_{ab} = eLT \frac{\partial \sigma_{ab}}{\partial \mu}. \tag{7.8}$$

where $\alpha_{ab}$ is the thermo-electric conductivity. To derive the analog of these formulas in the non-linear regime, we first consider the non-linear anomalous Hall effect. The BCD induced NLAHE at a finite temperature can be written as [43],

$$\chi_{abc} = \epsilon_{acd} \frac{e^3 \tau}{2\hbar^2} D_{bd} \tag{7.9}$$

where $D_{bd}$, the Berry curvature dipole, is defined as

$$D_{bd} = \sum_n \int [d\boldsymbol{k}] \frac{\partial \boldsymbol{\Omega}_{\boldsymbol{k},d}}{\partial k_b} f_{\boldsymbol{k}} = -\sum_n \int [d\boldsymbol{k}] \boldsymbol{\Omega}_{\boldsymbol{k},d} \frac{\partial f_{\boldsymbol{k}}}{\partial k_b} \tag{7.10}$$

Using the Sommerfeld expansion [40], the BCD term ($D_{bd}$) of NLAHE at low temperature can be written as

$$D_{bd}(T,\mu) = G(\mu) + \frac{\pi^2}{6}(k_B T)^2 G^{(2)}(\mu) + \mathcal{O}(T^4) \tag{7.11}$$

where

$$G(\varepsilon) = \int [d\boldsymbol{k}]\delta(\varepsilon - \varepsilon_k)\boldsymbol{\Omega}_{\boldsymbol{k},d}\frac{\partial \varepsilon_{\boldsymbol{k}}}{\partial k_b} \tag{7.12}$$

and $G^{(n)}(\mu) = \partial^n G(\mu)/\partial\mu^n$. Here, the first term $G(\mu)$ is the zero-temperature BCD at Fermi energy $\mu$ whereas the second term shows a $T^2$ temperature dependence of the NLAHE which agrees well with previous experimental results [45]. Similarly, the NLATHE at low temperature can be written as

$$l'_{cd}(T,\mu) = -\frac{7\tau\pi^4 k_B^4}{15\hbar^2}T^2 G^{(1)}(\mu) + \mathcal{O}(T^4) \tag{7.13}$$

with the higher order derivatives $G^{(n)}(\mu)$ (odd number $n \geq 3$) included in $\mathcal{O}(T^4)$.

Now, based on Eqs. (7.11) and (7.13), we can write the Wiedemann-Franz law in non-linear regime as

$$l'_{cd} = -\frac{14}{15}eL_0^2 T^2 \frac{\partial \chi_0(\mu)}{\partial \mu} \tag{7.14}$$

where $\chi_0(\mu) = e^3\tau G(\mu)/2\hbar^2$ denotes the zero temperature NLAHE coefficient given by Eq. (7.9), and $L_0 = k_B^2\pi^2/e^2$. Clearly, unlike the linear response regime, where the thermal Hall coefficient and charge Hall coefficient are directly propotional to each other (see Eq. ( 7.7)), the analog of the Wiedemann-Franz law in the non-linear regime given by Eq. (7.14) shows that the anomalous thermal Hall coefficient is proportional to the *first order derivative* of the anomalous Hall coefficient with respect to the chemical potential. Also, in contrast to the linear regime, the proportionality factor depends on $T^2$, rather then $T$ as in conventional Wiedemann-Franz law. The results in Eq. (7.14) should be taken as a result of the intrinsic non-linearity, rather than a conventional departure from the Wiedemann-Franz law [266, 267, 268, 269, 270, 271, 208, 263, 272].

We could also derive the analog of the Mott formula in the non-linear regime by first writing down the NLANE coefficient [245, 258] as,

$$\alpha'_{cd}(T,\mu) = \frac{e\tau}{\hbar^2}\Big\{\frac{\pi^2 k_B^2}{3}G(\mu) + \frac{7\pi^4 k_B^4}{60}T^2 G''(\mu) + \mathcal{O}(T^4)\Big\} \tag{7.15}$$

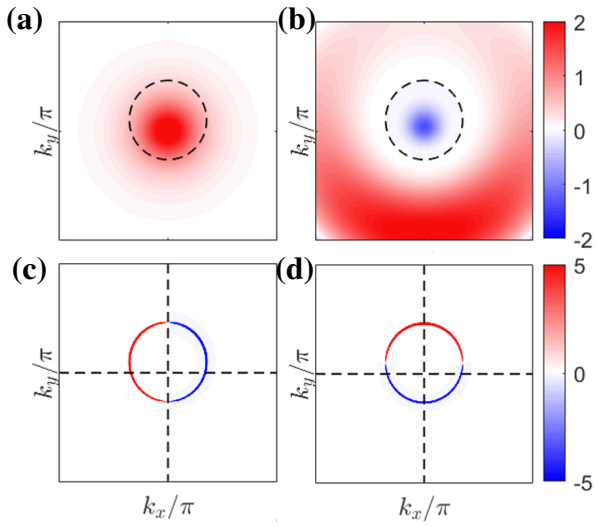


Figure 7.2: (Color online) (a) Berry curvature $\mathbf{\Omega}_{\boldsymbol{k}}^{n,s}$ and (b) modulated Berry curvature $\beta^3(\mathcal{E}_{\boldsymbol{k}}-\mu)^3\mathbf{\Omega}_{\boldsymbol{k}}^{n,s}$ projected on the $\boldsymbol{k}$ space for Hamiltonian given in Eq. (7.17). The black dash lines indicate the Fermi surface at $\mu = 1.5\Delta$. Panel (c) and (d) show the derivative of Fermi distribution function at Fermi energy $\mu = 1.5\Delta$ for $\partial_x f_{\boldsymbol{k}}$ and $\partial_y f_{\boldsymbol{k}}$ respectively. The parameters used here are $n = 1, s = 1, t = 1.1eV, a = 3.19\text{Å}, v = at, \alpha = 0.1v, \Delta = 1.8eV$, $k_{x,y} \in [-0.5\pi, 0.5\pi]$, $\beta = 1(eV)^{-1}$ is considered for (a), (b) and temperature $T = 100K$ is applied for (c), (d).

Based on Eqs. (7.11) and (7.15), the relation between the coefficients of NLANE and NLAHE can be written as

$$\alpha'_{cd}(\mu) = \frac{2}{3} L_0 \chi_0(\mu). \tag{7.16}$$

where we have considered only the first term for $\alpha'_{cd}$ (where the higher-order terms are smaller by the successive higher-order directive of the zero temperature BCD, see Eq. (7.11)). Eq. (7.16) is the Mott relation in the non-linear regime which shows a finite value for the NLANE ($\alpha'$) even at zero temperature. In contrast to the linear regime, where the Nernst coefficient is proportional to the *derivative* of the Hall coefficient (see Eq. (7.8)), in the non-linear regime, the corresponding anomalous coefficients are directly proportional to each other. Therefore, we find that, remarkably, the intrinsic non-linearity introduces a derivative in the Wiedemann-Franz law while it removes the same from the Mott relation. These formulas can be directly tested in experiments in TR invariant but inversion broken systems where the anomalous coefficients are zero in the linear regime by symmetry.

## 7.4 Non-linear transport coefficients for 2D massive Dirac fermions

We consider a model Hamiltonian of tilted 2D Dirac cones [43], which captures the low energy properties of various Dirac materials, such as the surface of topological crystalline insulators and strained transition metal dichalcogenides [273, 274]. The corresponding model Hamiltonian can be written as

$$H_s = s\alpha k_y \tau_0 + v_F \hbar (k_x \tau_y - s k_y \tau_x) + \Delta \tau_z, \tag{7.17}$$

Here, $v_F$ is the Fermi velocity, $\Delta$ is the energy band gap opened at the $\pm\boldsymbol{K}$-valley, $\alpha$ is the tilting parameter and $\tau_{x,y,z,0}$ represent Pauli matrices. The wave vector $\boldsymbol{k}$ is measured from the valley center $\pm\boldsymbol{K}$ with index $s = \pm 1$ (which also indicates the opposite chirality of the Dirac fermions). Note that the Hamiltonian in Eq. (7.17) is TR invariant and the two massive Dirac cones $H_{s=\pm 1}$ are mapped to each other by the TR symmetry.

The low energy dispersion and the corresponding Berry curvature of the Hamiltonian are given as,

$$\begin{aligned} \mathcal{E}^{n,s}_{\boldsymbol{k}} &= s\alpha k_y + (-1)^{n-1}\sqrt{\Delta^2 + (v_F\hbar)^2 \boldsymbol{k}^2}, \\ \Omega^{n,s}_{\boldsymbol{k}} &= (-1)^{n-1} \frac{s(v_F\hbar)^2 \Delta}{2(\Delta^2 + (v_F\hbar)^2 \boldsymbol{k}^2)^{3/2}} \end{aligned} \tag{7.18}$$

It is clear that $\boldsymbol{\Omega}_{\boldsymbol{k}} = -\boldsymbol{\Omega}_{-\boldsymbol{k}}$ is satisfied for $\boldsymbol{\Omega}_{\boldsymbol{k}}$ in Eq. (7.18). The tilting parameter $\alpha$ is required to produce a non-zero Berry curvature dipole contribution which can produce NLAHE, NLANE and NLATHE. In what follows, we use parameters relevant to $MoS_2$, a TR invariant TMDC, to compute the anomalous transport coefficients. For a system tilted along the $k_y$-axis, only the $x$-direction mirror symmetry ($\mathcal{M}_x$) that takes $k_x \to -k_x$ is preserved. As shown as in Fig. 7.2(a), the Berry curvature $\boldsymbol{\Omega}_{\boldsymbol{k}}$ is azimuthally symmetric in $k_x$-$k_y$ plane, whereas in Fig. 7.2(b) the modulated Berry curvature $\beta^3(\mathcal{E}_{\boldsymbol{k}} - \mu)^3 \boldsymbol{\Omega}_{\boldsymbol{k}}$ is only symmetric with respect to $k_x$. Due to the shift of the Fermi surface (black dash line in (a), (b) or the ring in (c), (d)) along $k_y$, the net integral of $\boldsymbol{\Omega}_{\boldsymbol{k}}$ in 2(a) and $\beta^3(\mathcal{E}_{\boldsymbol{k}} - \mu)^3 \boldsymbol{\Omega}_{\boldsymbol{k}}$ in 2(b) over the Fermi surface are non-zero. This explicitly renders the NLATHE a Fermi surface property. Fig. (7.2) shows that the only non-zero component for NLATHE given in Eq. (7.6) is $l'_{zy}$ where $c = z, d = y$ represent $\boldsymbol{\Omega}_{\boldsymbol{k},z}, \partial_y f_0$ respectively.

It has been shown in Ref. [258] that the non-linear anomalous Nernst coefficient has a dependence on the chemical potential similar to that of the non-linear anomalous Hall coefficient studied in the experiments of Ref. [45, 44]. This is consistent with the analog of the Mott formula valid in the non-linear regime given in Eq. (7.16). To verify the relations between the coefficients of anomalous Hall and thermal Hall effects

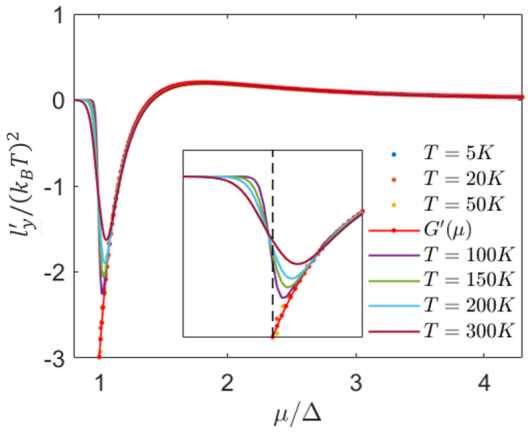


Figure 7.3: (Color online) Non-linear anomalous thermal Hall coefficient $l'_y/(k_BT)^2$ versus chemical potential $\mu$ at different temperatures $T$. The red dotted line represents the analytical results based on the non-linear Wiedemann-Franz law (Eqs. (7.13, 7.14)). The rest of the data points are results of numerical calculations based on Eq. (7.6). The inset is a zoom-in of the plot around $\mu = \Delta$ (black dash line). For $\mu < \Delta$ the numerical results deviate from the modified Wiedemann-Franz law valid in the non-linear regime because of the absence of higher orders temperature contributions (see Eq. (7.13)). Here the unit for the $y$-axes is $\tau k_B^2/\hbar^2$, the other parameters are the same as in Fig. (7.2).

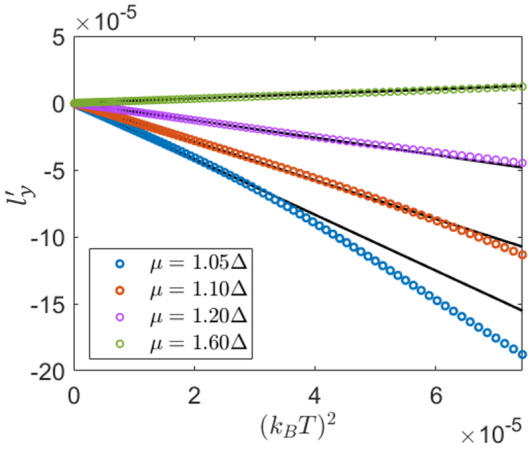


Figure 7.4: (Color online) Non-linear thermal Hall coefficient $l'_y$ plotted as a function of $(k_BT)^2$ for different values of the chemical potential. The circles are from numerical calculations based on Eq. (7.6), while the black lines corresponding to each chemical potential are the analytical results based on Eqs. (7.13, 7.14). Here the units for $y$-axes is $\tau k_B^2/\hbar^2$, the applied temperature $T \in [5K, 100K]$ with a unit step $(1K)$, and all other parameters are the same as in Fig. (7.2).

(namely the Wiedemann-Franz law in the non-linear regime given by Eq. (7.14)), we compare the results for $l'_y$ (index $z$ for $\mathbf{\Omega}_{\boldsymbol{k},z}$ is suppressed in a 2D system) based on Sommerfeld expansion in Eq. (7.13) with that from numerical calculations based on Eq. (7.6). As shown in Fig. 7.3, the analytical results (red dotted

line) from Eq. (7.13, 7.14), coincide with the numerical results (the rest of the data besides the red dotted line) at low temperatures ($T = 5 \sim 50K$). The numerical results and the prediction from the modified Wiedemann-Franz law differ from each other at higher temperatures ($T = 100K \sim 300K$). To verify the quadratic temperature dependence in Eqs. (7.13, 7.14), we plot the NLATHE coefficient $l'_y$ as a function of $(k_B T)^2$ at different chemical potentials in Fig. (7.4). At low temperatures ($T \leq 50K$) the numerical (circles) and analytical (black lines) results are consistent with each other, while they start deviating from each other around $T = 60K$ with $\mu = 1.05\Delta$ (blue circles). The deviations in Fig. 7.3 and Fig. 7.4 are due to the omission of the higher orders terms in temperature ($\mathcal{O}(T^4)$) in Eq. (7.13). These contributions to $l'_y$ can be ignored in the regime of low temperatures. We have checked that our results for NLATHE are robust against all the monotonous modulation of the band gap $\Delta$ such as tuning effect by external field [275], finite temperature effects such as electron-phonon coupling [276], doping effect through the mixing of chalcogens in $MoX_2$(X=S,Se,or Te) [277], etc., as well as strength of the tilting parameter due to uni-axial strain [278, 279, 280, 281].

## 7.5 Conclusions

In conclusion, we study the non-linear anomalous thermal Hall effect of the time reversal invariant but inversion symmetry broken systems, which is attributed to a combined effect from the modulated Berry curvature ($\beta^3(\varepsilon_{\boldsymbol{k}} - \mu)^3 \boldsymbol{\Omega}_{\boldsymbol{k}}$) and the non-equilibrium Fermi distribution ($f_{\boldsymbol{k}}$) purturbed by a thermal gradient ($-\boldsymbol{\nabla} T$). We have systematically derived the transverse non-linear thermal current as a second order response to the longitudinal thermal gradient using the Boltzmann semiclassical approach with a relaxation time approximation. The non-linear anomalous thermal Hall coefficient $l'_{cd}$ is a pseudotensorial quantity, which plays a similar role as the non-linear anomalous Hall coefficient and non-linear anomalous Nersnt coefficient respectively [43, 231, 245, 258]. By Sommerfeld expansion in low temperature regime, we analytically found the non-linear anomalous thermal Hall coefficient, which is shown to have an explicit relation with the zero temperature Berry curvature dipole and a $T^2$ temperature dependence. We also found the analog of the Wiedemann-Franz law and the Mott relation relating the anomalous transverse transport coefficients in the non-linear regime. An important byproduct of these calculations is the realization that the non-linear anomalous Nernst coefficient remains non-zero even in the limit of zero temperature (Eq. (7.15)). We then apply our theoretical derivations to the monolayer $MoS_2$, a TR invariant but inversion symmetry broken TMDC that has been intensively studied recently. Our predictions for the analog of the Wiedeman-Franz law and the

Mott formula relating the anomalous transport coefficients in the non-linear regime can be experimentally verified on inversion asymmetric but time reversal symmetric topological systems where the linear anomalous transport coefficients are identically zero by symmetry. In addition, we make specific predictions for the non-linear anomalous themal Hall coefficient in monolayer TMDCs that can be probed in experiments.

# Chapter 8

# Summary and conclusion

We now summarize the research works of the thesis in this last chapter. This thesis was based on topological condensed matter systems, where specifically we have studied the topological excitations involving Majorana zero modes and Majorana corner modes and the non-trivial topology-manifested anomalous transport phenomena. For the superconducting systems, we have investigated the properties of Majorana zero modes and quasi-Majorana zero modes in 1-dimensional superconducting nanowire. For the topological insulators and Weyl systems, we have studied the Berry curvature dipole-induced non-linear anomalous response in time-reversal invariant systems. We have also proposed an attractive Hubbard-Hofstadter model of ultra-cold atoms in optical lattices as a clean and straightforward route to realize Majorana corner modes and higher order topological superfluids with ordinary s-wave superfluidity. Below, we will summarize the results of each chapter of the thesis.

In Chapter 1, we first introduced the fundamental particle version as well as the condensed matter version of Majorana fermions. We also discussed their non-Abelian statistical properties and how could they be used as qubits for topological quantum computation. Specifically, we introduced in detail about the measurement-only Majorana braiding. In addition, the Berry phase effect on the motions and transport phenomena of electrons, the anomalous Hall responses in the linear and non-linear regime were also discussed. In Chapter 2, we numerically simulated the model Hamiltonian of the realistic 1-dimensional semiconductor-superconductor heterostructures coupled to a quantum dot, investigating the properties of Majorana zero modes. We showed that robust low-energy partially-separated Andreev bound states or quasi-Majoranas in the topologically trivial regime can mimic the behavior of the topological Majorana zero modes, resulting in experimental signatures very similar to those observed in the most recent experiments [64]. In other word,

the local charge tunneling measurements of the superconducting nanowire in the quasi-Majorana regime can also result in a quantized zero-bias conductance peak plateau at height $2e^2/h$ which are robust against various control parameters in experiments. In general, these types of topologically trivial low-energy modes can not be distinguished from the topologically non-trivial Majorana zero modes through any type of local measurement at the ends of the nanowire, provided the energy splittings of these quasi-Majoranas are well below the energy resolutions of the measurements.

As a subsequent work on the studies of realistic quantum dot-semiconductor-superconductor heterostructures in Ref. [94], in Chapter 3, we analytically solved the Kitaev Hamiltonian for Majorana fermions in a finite-length wire, augmented by a coupled quantum dot. We produced the exact results for both the Majorana zero modes in topological phase and the partially-separated Andreev bound states in trivial phase. Note that, to the best of our knowledge, we were the first to analytically solve the Kitaev model for a finite-length 1D $p$-wave superconducting nanowire in this research work, finding the exponentially protected ground state energy solution as $E \approxeq \frac{4\mu q_F}{k_F} e^{-q_F L} |\sin(k_F L)| + \mathcal{O}(e^{-3q_F L})$ (see Eq. (3.18)). Furthermore, we elucidated the formation of partially-separated Andreev bound states in the presence of material imperfections such as external gate voltages and disorder potentials, providing a theoretical support in favor our findings of the numerical results for the hybrid system.

In Chapter 4, we discussed the feasibility of the measurement-based braiding in the quasi-Majorana regime, i.e., using the quasi-Majorana-based qubits. We explicitly examined the robustness of the energy splitting of the Majorana zero mode system in the quasi-Majorana regime. Instead of focusing on the signature of zero-bias conductance peak of the quasi-Majoranas, we turned our attention to the feasibility of measurement-only Majorana braiding in this regime, which crucially depends on a different, much smaller, energy scale $\varepsilon_m \sim 0.1\mu eV$ than the typical peak width $\varepsilon_w \sim 10 - 20\mu eV$ of the low-energy conductance peaks. Based on our extensive numerically calculations, we showed that, it is possible to prepare the semiconductor-superconductor system in the quasi-Majorana regime with energy splittings $\varepsilon \lesssim \varepsilon_w$ as well as $\varepsilon \lesssim \varepsilon_m$, so in principle measurement-based braiding is possible. Considering of the topologically trivial nature of the quasi-Majoranas, we identified the maximum amplitudes of different types of perturbations that are consistent with energy splittings below $\varepsilon_m$. We argued that, measurement inducing perturbations larger than the threshold amplitudes appropriate for $\varepsilon_m$ we found in this work, can not realize the measurement-based braiding for topological quantum computation in the quasi-Majorana regime. Thus, we concluded that, to realize topological quantum computation based on measurement-braiding in the quasi-Majorana regime, a larger set of error corrections is indispensable, while such errors are absent in the topological regime.

In Chapter 5, we proposed an attractive Hubbard-Hofstadter model of ultra-cold atoms in optical lattices as a clean and straightforward route to realize Majorana corner modes and higher order topological superfluids with ordinary $s$-wave superfluidity. We considered a two-fermion Hofstadter lattice along with an attractive Hubbard-type interaction which can be induced by Feshbach resonance. We then solved the self-consistent mean-field equations in both the momentum space and real space to produce the conventional $s$-wave superfluidity. We found that in the presence of a line soliton, the topologically trivial superfluid can support two pairs of Majorana zero modes localized right at the corners defined by the intersections of the line soliton and the edges of the system. We also discussed in detail about the connection of our proposed system with higher-order topological superconductors. The major ingredients in our proposal including a quantum spin Hall insulator and the superconductivity with pairing nodes, have all been individually realized in the cold atom systems. It is this advantage that makes our proposal for realizing the higher-order topological superfluid and Majorana corner modes more experimentally realizable.

In Chapter 6, we studied the non-linear anomalous Nernst effect in bilayer $WTe_2$. Starting with semi-classical Boltzmann approach to linear transport in a system, we first derived the expressions for transport charge current in the presence of thermal gradient $-\boldsymbol{\nabla}T$ in response to the first order as well as the second order in $\boldsymbol{\nabla}T$. For the time-reversal symmetric but inversion symmetry broken model Hamiltonian of the bilayer $WTe_2$, we found that the Nernst current flows perpendicular to the temperature gradient even in the absence of a magnetic field. We showed that the non-zero non-linear anomalous Nernst response is attributed to the Berry curvature of the states near the Fermi surface. We also made several predictions that could be verified in experiments, including the angular dependence, the effects on the non-linear anomalous Nernst coefficient from tilting parameter of the Dirac cones, spin-orbit coupling strength, inter-layer interaction strength, temperature and chemical potential, etc. Because the bilayer $WTe_2$ system has been recently successfully used to demonstrate the non-linear anomalous Hall effect in time-reversal invariant systems [45, 44], our calculations and results in this work thus will be of immediate experimental relevance for the demonstration of the non-linear anomalous Nernst effect.

Another thermoelectric transport phenomena we studied was the non-linear anomalous thermal Hall effect in Chapter 7. Within the framework of Boltzmann transport theory, we first calculated a third non-linear response function, namely, the non-linear anomalous thermal Hall effect, of which we also made experimental predictions for monolayer transition metal dichalcogenides. We then revisited the fundamental relations among all three anomalous transport coefficients in the non-linear regime, namely, the non-linear anomalous Hall, Nernst Hall and thermal Hall coefficients. By doing Sommerfeld expansions, these coefficients were

interestingly found to be related to each other through the Berry curvature dipole and its derivatives with respect to chemical potential. We also predicted the fundamental relations between the non-linear anomalous electric and thermoelectric transport coefficients, which are the analog of the Wiedemann-Franz law and the Mott relation in the non-linear regime. Our results showed that in the non-linear regime, the anomalous Hall and Nernst coefficients are directly proportional to each other (Eq. (7.16)), while the derivative appears in the analog of the Wiedemann-Franz law (Eq. (7.14)). We argued that these results should be tested in experiments as confirmation of the intrinsic non-linearity, rather than a more conventional departure from the Wiedemann-Franz law and the Mott formula. We also checked the validity of our analytical results by full numerical evaluation of the relevant quantities for $MoS_2$, a time-reversal invariant but inversion symmetry broken transition metal dichalcogenide that has been intensively studied in experiments recently.

# Bibliography


[1] Paul Adrien Maurice Dirac and Ralph Howard Fowler. The quantum theory of the electron. *Proceedings of the Royal Society of London. Series A, Containing Papers of a Mathematical and Physical Character*, 117(778):610–624, 1928.

[2] N. G. Marchuk. Dirac gamma-equation, classical gauge fields and Clifford algebra. *arXiv e-prints*, pages math–ph/9811022, Nov 1998.

[3] Jackiw, R. Emergent fractional charge and multiple majoranas. *EPJ Web of Conferences*, 78:01004, 2014.

[4] Ettore Majorana. A symmetric theory of electrons and positrons. *Il Nuovo Cimento*, 14(4):171–184, Apr 1937.

[5] Palash B. Pal. Dirac, majorana, and weyl fermions. *American Journal of Physics*, 79(5):485–498, 2011.

[6] A Yu Kitaev. Unpaired majorana fermions in quantum wires. *Physics-Uspekhi*, 44(10S):131–136, oct 2001.

[7] Yuval Ronen, Yonatan Cohen, Jung-Hyun Kang, Arbel Haim, Maria-Theresa Rieder, Moty Heiblum, Diana Mahalu, and Hadas Shtrikman. Charge of a quasiparticle in a superconductor. *Proceedings of the National Academy of Sciences*, 113(7):1743–1748, 2016.

[8] S. A. Kivelson and D. S. Rokhsar. Bogoliubov quasiparticles, spinons, and spin-charge decoupling in superconductors. *Phys. Rev. B*, 41:11693–11696, Jun 1990.

[9] Leon N. Cooper. Bound electron pairs in a degenerate fermi gas. *Phys. Rev.*, 104:1189–1190, Nov 1956.

[10] J. Bardeen, L. N. Cooper, and J. R. Schrieffer. Theory of superconductivity. *Phys. Rev.*, 108:1175–1204, Dec 1957.

[11] Martin Leijnse and Karsten Flensberg. Introduction to topological superconductivity and majorana fermions. *Semiconductor Science and Technology*, 27(12):124003, nov 2012.

[12] Liang Fu and C. L. Kane. Superconducting proximity effect and majorana fermions at the surface of a topological insulator. *Phys. Rev. Lett.*, 100:096407, Mar 2008.

[13] Jay D. Sau, Roman M. Lutchyn, Sumanta Tewari, and S. Das Sarma. Generic new platform for topological quantum computation using semiconductor heterostructures. *Phys. Rev. Lett.*, 104:040502, Jan 2010.

[14] Roman M. Lutchyn, Jay D. Sau, and S. Das Sarma. Majorana fermions and a topological phase transition in semiconductor-superconductor heterostructures. *Phys. Rev. Lett.*, 105:077001, Aug 2010.

[15] Yuval Oreg, Gil Refael, and Felix von Oppen. Helical liquids and majorana bound states in quantum wires. *Phys. Rev. Lett.*, 105:177002, Oct 2010.

[16] Chetan Nayak, Steven H. Simon, Ady Stern, Michael Freedman, and Sankar Das Sarma. Non-abelian anyons and topological quantum computation. *Rev. Mod. Phys.*, 80:1083–1159, Sep 2008.

[17] D. A. Ivanov. Non-abelian statistics of half-quantum vortices in $p$-wave superconductors. *Phys. Rev. Lett.*, 86:268–271, Jan 2001.

[18] Sergey Bravyi. Universal quantum computation with the $\nu = 5/2$ fractional quantum hall state. *Phys. Rev. A*, 73:042313, Apr 2006.

[19] David P. DiVincenzo. Topics in Quantum Computers. *arXiv e-prints*, pages cond–mat/9612126, Dec 1996.

[20] Jay D. Sau, Sumanta Tewari, and S. Das Sarma. Universal quantum computation in a semiconductor quantum wire network. *Phys. Rev. A*, 82:052322, Nov 2010.

[21] Fabio L. Pedrocchi and David P. DiVincenzo. Majorana braiding with thermal noise. *Phys. Rev. Lett.*, 115:120402, Sep 2015.

[22] Sagar Vijay and Liang Fu. Teleportation-based quantum information processing with majorana zero modes. *Phys. Rev. B*, 94:235446, Dec 2016.

[23] Parsa Bonderson, Michael Freedman, and Chetan Nayak. Measurement-only topological quantum computation. *Phys. Rev. Lett.*, 101:010501, Jun 2008.

[24] Torsten Karzig, Christina Knapp, Roman M. Lutchyn, Parsa Bonderson, Matthew B. Hastings, Chetan Nayak, Jason Alicea, Karsten Flensberg, Stephan Plugge, Yuval Oreg, Charles M. Marcus, and Michael H. Freedman. Scalable designs for quasiparticle-poisoning-protected topological quantum computation with majorana zero modes. *Phys. Rev. B*, 95:235305, Jun 2017.

[25] T. Hyart, B. van Heck, I. C. Fulga, M. Burrello, A. R. Akhmerov, and C. W. J. Beenakker. Flux-controlled quantum computation with majorana fermions. *Phys. Rev. B*, 88:035121, Jul 2013.

[26] Josias Langbehn, Yang Peng, Luka Trifunovic, Felix von Oppen, and Piet W. Brouwer. Reflection-symmetric second-order topological insulators and superconductors. *Phys. Rev. Lett.*, 119:246401, Dec 2017.

[27] Frank Schindler, Ashley M. Cook, Maia G. Vergniory, Zhijun Wang, Stuart S. P. Parkin, B. Andrei Bernevig, and Titus Neupert. Higher-order topological insulators. *Science Advances*, 4(6):eaat0346, Jun 2018.

[28] Eslam Khalaf. Higher-order topological insulators and superconductors protected by inversion symmetry. *Phys. Rev. B*, 97(20):205136, May 2018.

[29] Wladimir A. Benalcazar, B. Andrei Bernevig, and Taylor L. Hughes. Quantized electric multipole insulators. *Science*, 357(6346):61–66, Jul 2017.

[30] Frank Schindler, Zhijun Wang, Maia G. Vergniory, Ashley M. Cook, Anil Murani, Shamashis Sengupta, Alik Yu. Kasumov, Richard Deblock, Sangjun Jeon, Ilya Drozdov, Hélène Bouchiat, Sophie Guéron, Ali Yazdani, B. Andrei Bernevig, and Titus Neupert. Higher-order topology in bismuth. *Nature Physics*, 14(9):918–924, Jul 2018.

[31] Marc Serra-Garcia, Valerio Peri, Roman Süsstrunk, Osama R. Bilal, Tom Larsen, Luis Guillermo Villanueva, and Sebastian D. Huber. Observation of a phononic quadrupole topological insulator. *Nature*, 555(7696):342–345, Mar 2018.

[32] Moon Jip Park, Youngkuk Kim, Gil Young Cho, and SungBin Lee. Higher-order topological insulator in twisted bilayer graphene. *Phys. Rev. Lett.*, 123:216803, Nov 2019.

[33] Zhijun Wang, Benjamin J. Wieder, Jian Li, Binghai Yan, and B. Andrei Bernevig. Higher-order topology, monopole nodal lines, and the origin of large fermi arcs in transition metal dichalcogenides $x\mathrm{te}_2$ ($x = \mathrm{Mo}, \mathrm{W}$). *Phys. Rev. Lett.*, 123:186401, Oct 2019.

[34] Zhongbo Yan, Fei Song, and Zhong Wang. Majorana corner modes in a high-temperature platform. *Phys. Rev. Lett.*, 121:096803, Aug 2018.

[35] Qiyue Wang, Cheng-Cheng Liu, Yuan-Ming Lu, and Fan Zhang. High-temperature majorana corner states. *Phys. Rev. Lett.*, 121:186801, Oct 2018.

[36] Xiong-Jun Liu, Chris L. M. Wong, and K. T. Law. Non-abelian majorana doublets in time-reversal-invariant topological superconductors. *Phys. Rev. X*, 4:021018, Apr 2014.

[37] Konrad Wölms, Ady Stern, and Karsten Flensberg. Braiding properties of majorana kramers pairs. *Phys. Rev. B*, 93:045417, Jan 2016.

[38] Michael Victor Berry. Quantal phase factors accompanying adiabatic changes. *Proceedings of the Royal Society of London. A. Mathematical and Physical Sciences*, 392(1802):45–57, 1984.

[39] Di Xiao, Ming-Che Chang, and Qian Niu. Berry phase effects on electronic properties. *Rev. Mod. Phys.*, 82:1959–2007, Jul 2010.

[40] Neil W. Ashcroft and joint author Mermin, N. David. *Solid state physics*. New York Holt, Rinehart and Winston, 1976. Includes bibliographical references.

[41] D. J. Thouless, M. Kohmoto, M. P. Nightingale, and M. den Nijs. Quantized hall conductance in a two-dimensional periodic potential. *Phys. Rev. Lett.*, 49:405–408, Aug 1982.

[42] L. D. Landau and E. M. Lifshitz. *Statistical Physics (Third Edition)*. Butterworth-Heinemann, Oxford, 1980.

[43] Inti Sodemann and Liang Fu. Quantum nonlinear hall effect induced by berry curvature dipole in time-reversal invariant materials. *Phys. Rev. Lett.*, 115:216806, Nov 2015.

[44] Qiong Ma, Su-Yang Xu, Huitao Shen, David MacNeill, Valla Fatemi, Tay-Rong Chang, Andrés M. Mier Valdivia, Sanfeng Wu, Zongzheng Du, Chuang-Han Hsu, Shiang Fang, Quinn D. Gibson, Kenji Watanabe, Takashi Taniguchi, Robert J. Cava, Efthimios Kaxiras, Hai-Zhou Lu, Hsin Lin, Liang Fu, Nuh Gedik, and Pablo Jarillo-Herrero. Observation of the nonlinear hall effect under time-reversal-symmetric conditions. *Nature*, 565:337–342, Jan 2019.

[45] Kaifei Kang, Tingxin Li, Egon Sohn, Jie Shan, and Kin Fai Mak. Nonlinear anomalous hall effect in few-layer wte2. *Nature Materials*, 18:324–328, Feb 2019.

[46] Sumanta Tewari, Jay D. Sau, and S. Das Sarma. A theorem for the existence of majorana fermion modes in spin–orbit-coupled semiconductors. *Annals of Physics*, 325(1):219 – 231, 2010. January 2010 Special Issue.

[47] Jason Alicea. Majorana fermions in a tunable semiconductor device. *Phys. Rev. B*, 81:125318, Mar 2010.

[48] Jay D. Sau, Sumanta Tewari, Roman M. Lutchyn, Tudor D. Stanescu, and S. Das Sarma. Non-abelian quantum order in spin-orbit-coupled semiconductors: Search for topological majorana particles in solid-state systems. *Phys. Rev. B*, 82:214509, Dec 2010.

[49] Tudor D. Stanescu, Roman M. Lutchyn, and S. Das Sarma. Majorana fermions in semiconductor nanowires. *Phys. Rev. B*, 84:144522, Oct 2011.

[50] N. Read and Dmitry Green. Paired states of fermions in two dimensions with breaking of parity and time-reversal symmetries and the fractional quantum hall effect. *Phys. Rev. B*, 61:10267–10297, Apr 2000.

[51] C.W.J. Beenakker. Search for majorana fermions in superconductors. *Annual Review of Condensed Matter Physics*, 4(1):113–136, 2013.

[52] Steven R. Elliott and Marcel Franz. Colloquium: Majorana fermions in nuclear, particle, and solid-state physics. *Rev. Mod. Phys.*, 87:137–163, Feb 2015.

[53] V. Mourik, K. Zuo, S. M. Frolov, S. R. Plissard, E. P. A. M. Bakkers, and L. P. Kouwenhoven. Signatures of majorana fermions in hybrid superconductor-semiconductor nanowire devices. *Science*, 336(6084):1003–1007, 2012.

[54] M. T. Deng, C. L. Yu, G. Y. Huang, M. Larsson, P. Caroff, and H. Q. Xu. Anomalous Zero-Bias Conductance Peak in a Nb-InSb Nanowire-Nb Hybrid Device. *Nano Letters*, 12(12):6414–6419, Dec 2012.

[55] Anindya Das, Yuval Ronen, Yonatan Most, Yuval Oreg, Moty Heiblum, and Hadas Shtrikman. Zero-bias peaks and splitting in an Al-InAs nanowire topological superconductor as a signature of Majorana fermions. *Nature Physics*, 8(12):887–895, Dec 2012.

[56] Leonid P. Rokhinson, Xinyu Liu, and Jacek K. Furdyna. The fractional a.c. Josephson effect in a semiconductor-superconductor nanowire as a signature of Majorana particles. *Nature Physics*, 8(11):795–799, Nov 2012.

[57] H. O. H. Churchill, V. Fatemi, K. Grove-Rasmussen, M. T. Deng, P. Caroff, H. Q. Xu, and C. M. Marcus. Superconductor-nanowire devices from tunneling to the multichannel regime: Zero-bias oscillations and magnetoconductance crossover. *Phys. Rev. B*, 87:241401, Jun 2013.

[58] A. D. K. Finck, D. J. Van Harlingen, P. K. Mohseni, K. Jung, and X. Li. Anomalous modulation of a zero-bias peak in a hybrid nanowire-superconductor device. *Phys. Rev. Lett.*, 110:126406, Mar 2013.

[59] S. M. Albrecht, A. P. Higginbotham, M. Madsen, F. Kuemmeth, T. S. Jespersen, J. Nygård, P. Krogstrup, and C. M. Marcus. Exponential protection of zero modes in Majorana islands. *Nature*, 531(7593):206–209, Mar 2016.

[60] M. T. Deng, S. Vaitiekenas, E. B. Hansen, J. Danon, M. Leijnse, K. Flensberg, J. Nygård, P. Krogstrup, and C. M. Marcus. Majorana bound state in a coupled quantum-dot hybrid-nanowire system. *Science*, 354(6319):1557–1562, 2016.

[61] Hao Zhang, Önder Gül, Sonia Conesa-Boj, Michał P. Nowak, Michael Wimmer, Kun Zuo, Vincent Mourik, Folkert K. de Vries, Jasper van Veen, Michiel W. A. de Moor, Jouri D. S. Bommer, David J. van Woerkom, Diana Car, Sébastien R. Plissard, Erik P. A. M. Bakkers, Marina Quintero-Pérez, Maja C. Cassidy, Sebastian Koelling, Srijit Goswami, Kenji Watanabe, Takashi Taniguchi, and Leo P. Kouwenhoven. Ballistic superconductivity in semiconductor nanowires. *Nature Communications*, 8:16025, Jul 2017.

[62] Jun Chen, Peng Yu, John Stenger, Moïra Hocevar, Diana Car, Sébastien R. Plissard, Erik P. A. M. Bakkers, Tudor D. Stanescu, and Sergey M. Frolov. Experimental phase diagram of zero-bias conductance peaks in superconductor/semiconductor nanowire devices. *Science Advances*, 3(9), 2017.

[63] Fabrizio Nichele, Asbjørn C. C. Drachmann, Alexander M. Whiticar, Eoin C. T. O'Farrell, Henri J. Suominen, Antonio Fornieri, Tian Wang, Geoffrey C. Gardner, Candice Thomas, Anthony T. Hatke, Peter Krogstrup, Michael J. Manfra, Karsten Flensberg, and Charles M. Marcus. Scaling of majorana zero-bias conductance peaks. *Phys. Rev. Lett.*, 119:136803, Sep 2017.

[64] Hao Zhang, Chun-Xiao Liu, Sasa Gazibegovic, Di Xu, John A. Logan, Guanzhong Wang, Nick van Loo, Jouri D. S. Bommer, Michiel W. A. de Moor, Diana Car, Roy L. M. Op Het Veld, Petrus J. van Veldhoven, Sebastian Koelling, Marcel A. Verheijen, Mihir Pendharkar, Daniel J. Pennachio, Borzoyeh Shojaei, Joon Sue Lee, Chris J. Palmstrøm, Erik P. A. M. Bakkers, S. Das Sarma, and Leo P. Kouwenhoven. Quantized Majorana conductance. *Nature*, 556(7699):74–79, Apr 2018.

[65] K. Sengupta, Igor Žutić, Hyok-Jon Kwon, Victor M. Yakovenko, and S. Das Sarma. Midgap edge states and pairing symmetry of quasi-one-dimensional organic superconductors. *Phys. Rev. B*, 63:144531, Mar 2001.

[66] A. R. Akhmerov, Johan Nilsson, and C. W. J. Beenakker. Electrically detected interferometry of majorana fermions in a topological insulator. *Phys. Rev. Lett.*, 102:216404, May 2009.

[67] K. T. Law, Patrick A. Lee, and T. K. Ng. Majorana fermion induced resonant andreev reflection. *Phys. Rev. Lett.*, 103:237001, Dec 2009.

[68] Karsten Flensberg. Tunneling characteristics of a chain of majorana bound states. *Phys. Rev. B*, 82:180516, Nov 2010.

[69] Dmitry Bagrets and Alexander Altland. Class $d$ spectral peak in majorana quantum wires. *Phys. Rev. Lett.*, 109:227005, Nov 2012.

[70] Jie Liu, Andrew C. Potter, K. T. Law, and Patrick A. Lee. Zero-bias peaks in the tunneling conductance of spin-orbit-coupled superconducting wires with and without majorana end-states. *Phys. Rev. Lett.*, 109:267002, Dec 2012.

[71] Wade DeGottardi, Diptiman Sen, and Smitha Vishveshwara. Majorana fermions in superconducting 1d systems having periodic, quasiperiodic, and disordered potentials. *Phys. Rev. Lett.*, 110:146404, Apr 2013.

[72] Wade DeGottardi, Manisha Thakurathi, Smitha Vishveshwara, and Diptiman Sen. Majorana fermions in superconducting wires: Effects of long-range hopping, broken time-reversal symmetry, and potential landscapes. *Phys. Rev. B*, 88:165111, Oct 2013.

[73] Diego Rainis, Luka Trifunovic, Jelena Klinovaja, and Daniel Loss. Towards a realistic transport modeling in a superconducting nanowire with majorana fermions. *Phys. Rev. B*, 87:024515, Jan 2013.

[74] İ. Adagideli, M. Wimmer, and A. Teker. Effects of electron scattering on the topological properties of nanowires: Majorana fermions from disorder and superlattices. *Phys. Rev. B*, 89:144506, Apr 2014.

[75] G. Kells, D. Meidan, and P. W. Brouwer. Near-zero-energy end states in topologically trivial spin-orbit coupled superconducting nanowires with a smooth confinement. *Phys. Rev. B*, 86:100503, Sep 2012.

[76] D. Chevallier, D. Sticlet, P. Simon, and C. Bena. Mutation of andreev into majorana bound states in long superconductor-normal and superconductor-normal-superconductor junctions. *Phys. Rev. B*, 85:235307, Jun 2012.

[77] Dibyendu Roy, Nilanjan Bondyopadhaya, and Sumanta Tewari. Topologically trivial zero-bias conductance peak in semiconductor majorana wires from boundary effects. *Phys. Rev. B*, 88:020502, Jul 2013.

[78] Pablo San-Jose, Jorge Cayao, Elsa Prada, and Ramón Aguado. Multiple andreev reflection and critical current in topological superconducting nanowire junctions. *New Journal of Physics*, 15(7):075019, jul 2013.

[79] Teemu Ojanen. Topological $\pi$ josephson junction in superconducting rashba wires. *Phys. Rev. B*, 87:100506, Mar 2013.

[80] Tudor D. Stanescu and Sumanta Tewari. Nonlocality of zero-bias anomalies in the topologically trivial phase of majorana wires. *Phys. Rev. B*, 89:220507, Jun 2014.

[81] Jorge Cayao, Elsa Prada, Pablo San-Jose, and Ramón Aguado. Sns junctions in nanowires with spin-orbit coupling: Role of confinement and helicity on the subgap spectrum. *Phys. Rev. B*, 91:024514, Jan 2015.

[82] Jelena Klinovaja and Daniel Loss. Fermionic and majorana bound states in hybrid nanowires with non-uniform spin-orbit interaction. *The European Physical Journal B*, 88(3):62, Mar 2015.

[83] Pablo San-Jose, Jorge Cayao, Elsa Prada, and Ramón Aguado. Majorana bound states from exceptional points in non-topological superconductors. *Scientific Reports*, 6:21427, Feb 2016.

[84] C. Fleckenstein, F. Domínguez, N. Traverso Ziani, and B. Trauzettel. Decaying spectral oscillations in a majorana wire with finite coherence length. *Phys. Rev. B*, 97:155425, Apr 2018.

[85] D I Pikulin, J P Dahlhaus, M Wimmer, H Schomerus, and C W J Beenakker. A zero-voltage conductance peak from weak antilocalization in a majorana nanowire. *New Journal of Physics*, 14(12):125011, dec 2012.

[86] Elsa Prada, Pablo San-Jose, and Ramón Aguado. Transport spectroscopy of $ns$ nanowire junctions with majorana fermions. *Phys. Rev. B*, 86:180503, Nov 2012.

[87] Chun-Xiao Liu, Jay D. Sau, Tudor D. Stanescu, and S. Das Sarma. Andreev bound states versus majorana bound states in quantum dot-nanowire-superconductor hybrid structures: Trivial versus topological zero-bias conductance peaks. *Phys. Rev. B*, 96:075161, Aug 2017.

[88] Christopher Moore, Tudor D. Stanescu, and Sumanta Tewari. Two-terminal charge tunneling: Disentangling majorana zero modes from partially separated andreev bound states in semiconductor-superconductor heterostructures. *Phys. Rev. B*, 97:165302, Apr 2018.

[89] Christoph W Groth, Michael Wimmer, Anton R Akhmerov, and Xavier Waintal. Kwant: a software package for quantum transport. *New Journal of Physics*, 16(6):063065, jun 2014.

[90] A. Vuik, B. Nijholt, A. R. Akhmerov, and M. Wimmer. Reproducing topological properties with quasi-Majorana states. *SciPost Phys.*, 7:61, 2019.

[91] S. Das Sarma, Jay D. Sau, and Tudor D. Stanescu. Splitting of the zero-bias conductance peak as smoking gun evidence for the existence of the majorana mode in a superconductor-semiconductor nanowire. *Phys. Rev. B*, 86:220506, Dec 2012.

[92] T D Stanescu and S Tewari. Majorana fermions in semiconductor nanowires: fundamentals, modeling, and experiment. *Journal of Physics: Condensed Matter*, 25(23):233201, may 2013.

[93] Marcel Franz and Dmitry I. Pikulin. Quantized, finally. *Nature Physics*, 14(4):334–336, Apr 2018.

[94] Christopher Moore, Chuanchang Zeng, Tudor D. Stanescu, and Sumanta Tewari. Quantized zero-bias conductance plateau in semiconductor-superconductor heterostructures without topological majorana zero modes. *Phys. Rev. B*, 98:155314, Oct 2018.

[95] A. A. Zvyagin. Majorana bound states in the finite-length chain. *Low Temperature Physics*, 41(8):625–629, 2015.

[96] Pasquale Marra, Roberta Citro, and Alessandro Braggio. Signatures of topological phase transitions in josephson current-phase discontinuities. *Phys. Rev. B*, 93:220507, Jun 2016.

[97] Corneliu Malciu, Leonardo Mazza, and Christophe Mora. Braiding majorana zero modes using quantum dots. *Phys. Rev. B*, 98:165426, Oct 2018.

[98] E. Vernek, P. H. Penteado, A. C. Seridonio, and J. C. Egues. Subtle leakage of a majorana mode into a quantum dot. *Phys. Rev. B*, 89:165314, Apr 2014.

[99] David A. Ruiz-Tijerina, E. Vernek, Luis G. G. V. Dias da Silva, and J. C. Egues. Interaction effects on a majorana zero mode leaking into a quantum dot. *Phys. Rev. B*, 91:115435, Mar 2015.

[100] Tudor D. Stanescu and Sumanta Tewari. Spin polarization of Majorana zero modes and topological quantum phase transition in semiconductor Majorana nanowires. *arXiv e-prints*, page arXiv:1603.02255, Mar 2016.

[101] Tudor D. Stanescu and Sumanta Tewari. Robust low-energy andreev bound states in semiconductor-superconductor structures: Importance of partial separation of component majorana bound states. *Phys. Rev. B*, 100:155429, Oct 2019.

[102] Sergey B. Bravyi and Alexei Yu. Kitaev. Fermionic quantum computation. *Annals of Physics*, 298(1):210 – 226, 2002.

[103] Jay D. Sau, David J. Clarke, and Sumanta Tewari. Controlling non-abelian statistics of majorana fermions in semiconductor nanowires. *Phys. Rev. B*, 84:094505, Sep 2011.

[104] Jason Alicea, Yuval Oreg, Gil Refael, Felix von Oppen, and Matthew P. A. Fisher. Non-Abelian statistics and topological quantum information processing in 1D wire networks. *Nature Physics*, 7(5):412–417, May 2011.

[105] David J. Clarke, Jay D. Sau, and Sumanta Tewari. Majorana fermion exchange in quasi-one-dimensional networks. *Phys. Rev. B*, 84:035120, Jul 2011.

[106] Bertrand I. Halperin, Yuval Oreg, Ady Stern, Gil Refael, Jason Alicea, and Felix von Oppen. Adiabatic manipulations of majorana fermions in a three-dimensional network of quantum wires. *Phys. Rev. B*, 85:144501, Apr 2012.

[107] David Aasen, Michael Hell, Ryan V. Mishmash, Andrew Higginbotham, Jeroen Danon, Martin Leijnse, Thomas S. Jespersen, Joshua A. Folk, Charles M. Marcus, Karsten Flensberg, and Jason Alicea. Milestones toward majorana-based quantum computing. *Phys. Rev. X*, 6:031016, Aug 2016.

[108] F. Setiawan, Chun-Xiao Liu, Jay D. Sau, and S. Das Sarma. Electron temperature and tunnel coupling dependence of zero-bias and almost-zero-bias conductance peaks in majorana nanowires. *Phys. Rev. B*, 96:184520, Nov 2017.

[109] M. A. Nielsen and Isaac L. Chuang. Programmable quantum gate arrays. *Phys. Rev. Lett.*, 79:321–324, Jul 1997.

[110] Michael A. Nielsen. Quantum computation by measurement and quantum memory. *Physics Letters A*, 308(2):96 – 100, 2003.

[111] Liang Fu. Electron teleportation via majorana bound states in a mesoscopic superconductor. *Phys. Rev. Lett.*, 104:056402, Feb 2010.

[112] Parsa Bonderson. Measurement-only topological quantum computation via tunable interactions. *Phys. Rev. B*, 87:035113, Jan 2013.

[113] Christina Knapp, Michael Zaletel, Dong E. Liu, Meng Cheng, Parsa Bonderson, and Chetan Nayak. The nature and correction of diabatic errors in anyon braiding. *Phys. Rev. X*, 6:041003, Oct 2016.

[114] Jens Koch, Terri M. Yu, Jay Gambetta, A. A. Houck, D. I. Schuster, J. Majer, Alexandre Blais, M. H. Devoret, S. M. Girvin, and R. J. Schoelkopf. Charge-insensitive qubit design derived from the cooper pair box. *Phys. Rev. A*, 76:042319, Oct 2007.

[115] Chuanchang Zeng, Christopher Moore, Apparao M. Rao, Tudor D. Stanescu, and Sumanta Tewari. Analytical solution of the finite-length kitaev chain coupled to a quantum dot. *Phys. Rev. B*, 99:094523, Mar 2019.

[116] Zhan Cao, Hao Zhang, Hai-Feng Lü, Wan-Xiu He, Hai-Zhou Lu, and X. C. Xie. Decays of majorana or andreev oscillations induced by steplike spin-orbit coupling. *Phys. Rev. Lett.*, 122:147701, Apr 2019.

[117] Ching-Kai Chiu and S. Das Sarma. Fractional josephson effect with and without majorana zero modes. *Phys. Rev. B*, 99:035312, Jan 2019.

[118] Morten Kjaergaard, Konrad Wölms, and Karsten Flensberg. Majorana fermions in superconducting nanowires without spin-orbit coupling. *Phys. Rev. B*, 85:020503, Jan 2012.

[119] M. Z. Hasan and C. L. Kane. Colloquium: Topological insulators. *Rev. Mod. Phys.*, 82:3045–3067, Nov 2010.

[120] Xiao-Liang Qi and Shou-Cheng Zhang. Topological insulators and superconductors. *Rev. Mod. Phys.*, 83:1057–1110, Oct 2011.

[121] Wladimir A. Benalcazar, B. Andrei Bernevig, and Taylor L. Hughes. Electric multipole moments, topological multipole moment pumping, and chiral hinge states in crystalline insulators. *Phys. Rev. B*, 96:245115, Dec 2017.

[122] Zhida Song, Zhong Fang, and Chen Fang. $(d-2)$-dimensional edge states of rotation symmetry protected topological states. *Phys. Rev. Lett.*, 119:246402, Dec 2017.

[123] Luka Trifunovic and Piet W. Brouwer. Higher-order bulk-boundary correspondence for topological crystalline phases, 2018.

[124] Taylor L. Hughes Christopher W. Peterson, Wladimir A. Benalcazar and Gaurav Bahl. A quantized microwave quadrupole insulator with topologically protected corner states. *Nature*, 555:346–350, Mar 2018.

[125] Stefan Imhof, Christian Berger, Florian Bayer, Johannes Brehm, Laurens W. Molenkamp, Tobias Kiessling, Frank Schindler, Ching Hua Lee, Martin Greiter, Titus Neupert, and Ronny Thomale. Topolectrical-circuit realization of topological corner modes. *Nature Physics*, 14:925–929, Sep 2018.

[126] Yuxuan Wang, Mao Lin, and Taylor L. Hughes. Weak-pairing higher order topological superconductors. *Phys. Rev. B*, 98:165144, Oct 2018.

[127] Xiao-Liang Qi, Taylor L. Hughes, and Shou-Cheng Zhang. Chiral topological superconductor from the quantum hall state. *Phys. Rev. B*, 82:184516, Nov 2010.

[128] Chuanwei Zhang, Sumanta Tewari, Roman M. Lutchyn, and S. Das Sarma. $p_x + ip_y$ superfluid from $s$-wave interactions of fermionic cold atoms. *Phys. Rev. Lett.*, 101:160401, Oct 2008.

[129] Sumanta Tewari, S. Das Sarma, Chetan Nayak, Chuanwei Zhang, and P. Zoller. Quantum computation using vortices and majorana zero modes of a $p_x + ip_y$ superfluid of fermionic cold atoms. *Phys. Rev. Lett.*, 98:010506, Jan 2007.

[130] Masatoshi Sato, Yoshiro Takahashi, and Satoshi Fujimoto. Non-abelian topological order in $s$-wave superfluids of ultracold fermionic atoms. *Phys. Rev. Lett.*, 103:020401, Jul 2009.

[131] A. Cook and M. Franz. Majorana fermions in a topological-insulator nanowire proximity-coupled to an $s$-wave superconductor. *Phys. Rev. B*, 84:201105, Nov 2011.

[132] Eugene Dumitrescu, Jay D. Sau, and Sumanta Tewari. Magnetic field response and chiral symmetry of time-reversal-invariant topological superconductors. *Phys. Rev. B*, 90:245438, Dec 2014.

[133] Haiping Hu, Fan Zhang, and Chuanwei Zhang. Majorana doublets, flat bands, and dirac nodes in $s$-wave superfluids. *Phys. Rev. Lett.*, 121:185302, Nov 2018.

[134] Xiao-Liang Qi, Taylor L. Hughes, S. Raghu, and Shou-Cheng Zhang. Time-reversal-invariant topological superconductors and superfluids in two and three dimensions. *Phys. Rev. Lett.*, 102:187001, May 2009.

[135] Fan Zhang, C. L. Kane, and E. J. Mele. Time-reversal-invariant topological superconductivity and majorana kramers pairs. *Phys. Rev. Lett.*, 111:056402, Aug 2013.

[136] Chris L. M. Wong and K. T. Law. Majorana kramers doublets in $d_{x^2-y^2}$-wave superconductors with rashba spin-orbit coupling. *Phys. Rev. B*, 86:184516, Nov 2012.

[137] Fan Zhang, C. L. Kane, and E. J. Mele. Topological mirror superconductivity. *Phys. Rev. Lett.*, 111:056403, Aug 2013.

[138] Fan Zhang and C. L. Kane. Anomalous topological pumps and fractional josephson effects. *Phys. Rev. B*, 90:020501, Jul 2014.

[139] Fan Zhang and C. L. Kane. Time-reversal-invariant $Z_4$ fractional josephson effect. *Phys. Rev. Lett.*, 113:036401, Jul 2014.

[140] Zhi-qiang Bao and Fan Zhang. Topological majorana two-channel kondo effect. *Phys. Rev. Lett.*, 119:187701, Oct 2017.

[141] Chao-Xing Liu and Björn Trauzettel. Helical dirac-majorana interferometer in a superconductor/topological insulator sandwich structure. *Phys. Rev. B*, 83:220510, Jun 2011.

[142] Sho Nakosai, Yukio Tanaka, and Naoto Nagaosa. Topological superconductivity in bilayer rashba system. *Phys. Rev. Lett.*, 108:147003, Apr 2012.

[143] Shusa Deng, Lorenza Viola, and Gerardo Ortiz. Majorana modes in time-reversal invariant $s$-wave topological superconductors. *Phys. Rev. Lett.*, 108:036803, Jan 2012.

[144] Sho Nakosai, Jan Carl Budich, Yukio Tanaka, Björn Trauzettel, and Naoto Nagaosa. Majorana bound states and nonlocal spin correlations in a quantum wire on an unconventional superconductor. *Phys. Rev. Lett.*, 110:117002, Mar 2013.

[145] Anna Keselman, Liang Fu, Ady Stern, and Erez Berg. Inducing time-reversal-invariant topological superconductivity and fermion parity pumping in quantum wires. *Phys. Rev. Lett.*, 111:116402, Sep 2013.

[146] Erikas Gaidamauskas, Jens Paaske, and Karsten Flensberg. Majorana bound states in two-channel time-reversal-symmetric nanowire systems. *Phys. Rev. Lett.*, 112:126402, Mar 2014.

[147] Jing Wang, Yong Xu, and Shou-Cheng Zhang. Two-dimensional time-reversal-invariant topological superconductivity in a doped quantum spin-hall insulator. *Phys. Rev. B*, 90:054503, Aug 2014.

[148] Jelena Klinovaja, Amir Yacoby, and Daniel Loss. Kramers pairs of majorana fermions and parafermions in fractional topological insulators. *Phys. Rev. B*, 90:155447, Oct 2014.

[149] Constantin Schrade, A. A. Zyuzin, Jelena Klinovaja, and Daniel Loss. Proximity-induced $\pi$ josephson junctions in topological insulators and kramers pairs of majorana fermions. *Phys. Rev. Lett.*, 115:237001, Dec 2015.

[150] Yingyi Huang and Ching-Kai Chiu. Helical majorana edge mode in a superconducting antiferromagnetic quantum spin hall insulator. *Phys. Rev. B*, 98:081412, Aug 2018.

[151] Jeffrey C. Y. Teo and Taylor L. Hughes. Existence of majorana-fermion bound states on disclinations and the classification of topological crystalline superconductors in two dimensions. *Phys. Rev. Lett.*, 111:047006, Jul 2013.

[152] Robert-Jan Slager, Louk Rademaker, Jan Zaanen, and Leon Balents. Impurity-bound states and green's function zeros as local signatures of topology. *Phys. Rev. B*, 92:085126, Aug 2015.

[153] Wladimir A. Benalcazar, Jeffrey C. Y. Teo, and Taylor L. Hughes. Classification of two-dimensional topological crystalline superconductors and majorana bound states at disclinations. *Phys. Rev. B*, 89:224503, Jun 2014.

[154] Zhigang Wu, Zhongbo Yan, and Wen Huang. Higher-order topological superconductivity: Possible realization in fermi gases and $\mathrm{sr_2ruo_4}$. *Phys. Rev. B*, 99:020508, Jan 2019.

[155] Chen-Hsuan Hsu, Peter Stano, Jelena Klinovaja, and Daniel Loss. Majorana kramers pairs in higher-order topological insulators. *Phys. Rev. Lett.*, 121:196801, Nov 2018.

[156] M. Aidelsburger, M. Atala, M. Lohse, J. T. Barreiro, B. Paredes, and I. Bloch. Realization of the hofstadter hamiltonian with ultracold atoms in optical lattices. *Phys. Rev. Lett.*, 111:185301, Oct 2013.

[157] P G Harper. Single band motion of conduction electrons in a uniform magnetic field. *Proceedings of the Physical Society. Section A*, 68(10):874, 1955.

[158] Douglas R. Hofstadter. Energy levels and wave functions of bloch electrons in rational and irrational magnetic fields. *Phys. Rev. B*, 14:2239–2249, Sep 1976.

[159] Julian Struck, Malte Weinberg, Christoph Ölschläger, Patrick Windpassinger, Juliette Simonet, Klaus Sengstock, Robert Höppner, Philipp Hauke, André Eckardt, Maciej Lewenstein, and L. Mathey. Engineering Ising-XY spin-models in a triangular lattice using tunable artificial gauge fields. *Nat. Phys.*, 9(11):738–743, nov 2013.

[160] Hirokazu Miyake, Georgios A. Siviloglou, Colin J. Kennedy, William Cody Burton, and Wolfgang Ketterle. Realizing the harper hamiltonian with laser-assisted tunneling in optical lattices. *Phys. Rev. Lett.*, 111:185302, Oct 2013.

[161] Colin J. Kennedy, Georgios A. Siviloglou, Hirokazu Miyake, William Cody Burton, and Wolfgang Ketterle. Spin-orbit coupling and quantum spin hall effect for neutral atoms without spin flips. *Phys. Rev. Lett.*, 111:225301, Nov 2013.

[162] Daniel Cocks, Peter P. Orth, Stephan Rachel, Michael Buchhold, Karyn Le Hur, and Walter Hofstetter. Time-reversal-invariant hofstadter-hubbard model with ultracold fermions. *Phys. Rev. Lett.*, 109:205303, Nov 2012.

[163] Gregor Jotzu, Michael Messer, Rémi Desbuquois, Martin Lebrat, Thomas Uehlinger, Daniel Greif, and Tilman Esslinger. Experimental realization of the topological Haldane model with ultracold fermions. *Nature*, 515(7526):237–240, 2014.

[164] Lei Wang, Hsiang-Hsuan Hung, and Matthias Troyer. Topological phase transition in the hofstadter-hubbard model. *Phys. Rev. B*, 90:205111, Nov 2014.

[165] M. Iskin. Hofstadter-hubbard model with opposite magnetic fields: Bardeen-cooper-schrieffer pairing and superfluidity in the nearly flat butterfly bands. *Phys. Rev. A*, 96:043628, Oct 2017.

[166] R. O. Umucal ılar and M. Iskin. Bcs theory of time-reversal-symmetric hofstadter-hubbard model. *Phys. Rev. Lett.*, 119:085301, Aug 2017.

[167] Hans Peter Büchler. Microscopic derivation of hubbard parameters for cold atomic gases. *Phys. Rev. Lett.*, 104:090402, Mar 2010.

[168] J. K. Chin, D. E. Miller, Y. Liu, C. Stan, W. Setiawan, C. Sanner, K. Xu, and W. Ketterle. Evidence for superfluidity of ultracold fermions in an optical lattice. *Nature*, 443:961–964, Oct 2006.

[169] T. Bourdel, L. Khaykovich, J. Cubizolles, J. Zhang, F. Chevy, M. Teichmann, L. Tarruell, S. J. J. M. F. Kokkelmans, and C. Salomon. Experimental study of the bec-bcs crossover region in lithium 6. *Phys. Rev. Lett.*, 93:050401, Jul 2004.

[170] Philipp-Immanuel Schneider and Alejandro Saenz. Two-channel bose-hubbard model of atoms at a feshbach resonance. *Phys. Rev. A*, 87:052712, May 2013.

[171] Mauro Antezza, Franco Dalfovo, Lev P. Pitaevskii, and Sandro Stringari. Dark solitons in a superfluid fermi gas. *Phys. Rev. A*, 76:043610, Oct 2007.

[172] Tarik Yefsah, Ariel T. Sommer, Mark J H Ku, Lawrence W. Cheuk, Wenjie Ji, Waseem S. Bakr, and Martin W. Zwierlein. Heavy solitons in a fermionic superfluid. *Nature*, 499(7459):426–430, 2013.

[173] Mark J. H. Ku, Wenjie Ji, Biswaroop Mukherjee, Elmer Guardado-Sanchez, Lawrence W. Cheuk, Tarik Yefsah, and Martin W. Zwierlein. Motion of a solitonic vortex in the bec-bcs crossover. *Phys. Rev. Lett.*, 113:065301, Aug 2014.

[174] Mark J. H. Ku, Biswaroop Mukherjee, Tarik Yefsah, and Martin W. Zwierlein. Cascade of solitonic excitations in a superfluid fermi gas: From planar solitons to vortex rings and lines. *Phys. Rev. Lett.*, 116:045304, Jan 2016.

[175] J Denschlag. Generating Solitons by Phase Engineering of a Bose-Einstein Condensate. *Science*, 287(5450):97–101, jan 2000.

[176] Yong Xu, Li Mao, Biao Wu, and Chuanwei Zhang. Dark solitons with majorana fermions in spin-orbit-coupled fermi gases. *Phys. Rev. Lett.*, 113:130404, Sep 2014.

[177] Xia-Ji Liu. Soliton-induced majorana fermions in a one-dimensional atomic topological superfluid. *Phys. Rev. A*, 91:023610, Feb 2015.

[178] Shinsei Ryu, Andreas P Schnyder, Akira Furusaki, and Andreas W W Ludwig. Topological insulators and superconductors: tenfold way and dimensional hierarchy. *New Journal of Physics*, 12(6):065010, 2010.

[179] M. Aidelsburger, M. Lohse, C. Schweizer, M. Atala, J. T. Barreiro, S. Nascimbène, N. R. Cooper, I. Bloch, and N. Goldman. Measuring the chern number of hofstadter bands with ultracold bosonic atoms. *Nature Physics*, 11:162–166, feb 2015.

[180] M. Iskin. Attractive hofstadter-hubbard model with imbalanced chemical and vector potentials. *Phys. Rev. A*, 91:053606, May 2015.

[181] Xia-Ji Liu. Impurity probe of topological superfluids in one-dimensional spin-orbit-coupled atomic fermi gases. *Phys. Rev. A*, 87:013622, Jan 2013.

[182] Yong Xu, Chunlei Qu, Ming Gong, and Chuanwei Zhang. Competing superfluid orders in spin-orbit-coupled fermionic cold-atom optical lattices. *Phys. Rev. A*, 89:013607, Jan 2014.

[183] Chunlei Qu, Ming Gong, and Chuanwei Zhang. Fulde-ferrell-larkin-ovchinnikov or majorana superfluids: The fate of fermionic cold atoms in spin-orbit-coupled optical lattices. *Phys. Rev. A*, 89:053618, May 2014.

[184] Zhongbo Yan, Ren Bi, and Zhong Wang. Majorana zero modes protected by a hopf invariant in topologically trivial superconductors. *Phys. Rev. Lett.*, 118:147003, Apr 2017.

[185] Jeffrey C. Y. Teo and C. L. Kane. Topological defects and gapless modes in insulators and superconductors. *Phys. Rev. B*, 82:115120, Sep 2010.

[186] Cheung Chan, Lin Zhang, Ting Fung Jeffrey Poon, Ying-Ping He, Yan-Qi Wang, and Xiong-Jun Liu. Generic theory for majorana zero modes in 2d superconductors. *Phys. Rev. Lett.*, 119:047001, Jul 2017.

[187] R. A. Williams, M. C. Beeler, L. J. LeBlanc, K. Jiménez-García, and I. B. Spielman. Raman-induced interactions in a single-component fermi gas near an $s$-wave feshbach resonance. *Phys. Rev. Lett.*, 111:095301, Aug 2013.

[188] C. Zhang, V. W. Scarola, S. Tewari, and S. Das Sarma. Anyonic braiding in optical lattices. *Proc. Natl. Acad. Sci.*, 104(47):18415–18420, nov 2007.

[189] Di Xiao, Yugui Yao, Zhong Fang, and Qian Niu. Berry-phase effect in anomalous thermoelectric transport. *Phys. Rev. Lett.*, 97:026603, Jul 2006.

[190] Naoto Nagaosa, Jairo Sinova, Shigeki Onoda, A. H. MacDonald, and N. P. Ong. Anomalous hall effect. *Rev. Mod. Phys.*, 82:1539–1592, May 2010.

[191] Y. Taguchi, Y. Oohara, H. Yoshizawa, N. Nagaosa, and Y. Tokura. Spin chirality, berry phase, and anomalous hall effect in a frustrated ferromagnet. *Science*, 291(5513):2573–2576, 2001.

[192] Zhong Fang, Naoto Nagaosa, Kei S. Takahashi, Atsushi Asamitsu, Roland Mathieu, Takeshi Ogasawara, Hiroyuki Yamada, Masashi Kawasaki, Yoshinori Tokura, and Kiyoyuki Terakura. The anomalous hall effect and magnetic monopoles in momentum space. *Science*, 302(5642):92–95, 2003.

[193] Rui Yu, Wei Zhang, Hai-Jun Zhang, Shou-Cheng Zhang, Xi Dai, and Zhong Fang. Quantized anomalous hall effect in magnetic topological insulators. *Science*, 329(5987):61–64, 2010.

[194] Cui-Zu Chang, Jinsong Zhang, Xiao Feng, Jie Shen, Zuocheng Zhang, Minghua Guo, Kang Li, Yunbo Ou, Pang Wei, Li-Li Wang, Zhong-Qing Ji, Yang Feng, Shuaihua Ji, Xi Chen, Jinfeng Jia, Xi Dai, Zhong Fang, Shou-Cheng Zhang, Ke He, Yayu Wang, Li Lu, Xu-Cun Ma, and Qi-Kun Xue. Experimental observation of the quantum anomalous hall effect in a magnetic topological insulator. *Science*, 340(6129):167–170, 2013.

[195] F. D. M. Haldane. Berry curvature on the fermi surface: Anomalous hall effect as a topological fermi-liquid property. *Phys. Rev. Lett.*, 93:206602, Nov 2004.

[196] T. Jungwirth, Qian Niu, and A. H. MacDonald. Anomalous hall effect in ferromagnetic semiconductors. *Phys. Rev. Lett.*, 88:207208, May 2002.

[197] Wei-Li Lee, Satoshi Watauchi, V. L. Miller, R. J. Cava, and N. P. Ong. Dissipationless anomalous hall current in the ferromagnetic spinel cucr2se4-xbrx. *Science*, 303(5664):1647–1649, 2004.

[198] Masaru Onoda and Naoto Nagaosa. Quantized anomalous hall effect in two-dimensional ferromagnets: Quantum hall effect in metals. *Phys. Rev. Lett.*, 90:206601, May 2003.

[199] Gang Xu, Hongming Weng, Zhijun Wang, Xi Dai, and Zhong Fang. Chern semimetal and the quantized anomalous hall effect in $\mathrm{hgcr_2se_4}$. *Phys. Rev. Lett.*, 107:186806, Oct 2011.

[200] Zhenhua Qiao, Shengyuan A. Yang, Wanxiang Feng, Wang-Kong Tse, Jun Ding, Yugui Yao, Jian Wang, and Qian Niu. Quantum anomalous hall effect in graphene from rashba and exchange effects. *Phys. Rev. B*, 82:161414, Oct 2010.

[201] Z. A. Xu, N. P. Ong, Y. Wang, T. Kakeshita, and S. Uchida. Vortex-like excitations and the onset of superconducting phase fluctuation in underdoped la2-xsrxcuo4. *Nature*, 406:486–488, Aug 2000.

[202] Yayu Wang, Z. A. Xu, T. Kakeshita, S. Uchida, S. Ono, Yoichi Ando, and N. P. Ong. Onset of the vortexlike nernst signal above $T_c$ in $\mathrm{la_{2-x}sr_xcuo_4}$ and $\mathrm{bi_2sr_{2-y}la_ycuo_6}$. *Phys. Rev. B*, 64:224519, Nov 2001.

[203] Wei-Li Lee, S. Watauchi, V. L. Miller, R. J. Cava, and N. P. Ong. Anomalous hall heat current and nernst effect in the $\mathrm{cucr_2se_{4-x}br_x}$ ferromagnet. *Phys. Rev. Lett.*, 93:226601, Nov 2004.

[204] Yayu Wang, Lu Li, and N. P. Ong. Nernst effect in high-$T_c$ superconductors. *Phys. Rev. B*, 73:024510, Jan 2006.

[205] Chuanwei Zhang, Sumanta Tewari, Victor M. Yakovenko, and S. Das Sarma. Anomalous nernst effect from a chiral $d$-density-wave state in underdoped cuprate superconductors. *Phys. Rev. B*, 78:174508, Nov 2008.

[206] Chuanwei Zhang, Sumanta Tewari, and S. Das Sarma. Berry-phase-mediated topological thermoelectric transport in gapped single and bilayer graphene. *Phys. Rev. B*, 79:245424, Jun 2009.

[207] Zhen-Gang Zhu and Jamal Berakdar. Anomalous nernst effect in strained graphene coupled to a substrate inducing a time-reversal symmetry breaking. *New Journal of Physics*, 15(7):073028, jul 2013.

[208] Girish Sharma, Pallab Goswami, and Sumanta Tewari. Nernst and magnetothermal conductivity in a lattice model of weyl fermions. *Phys. Rev. B*, 93:035116, Jan 2016.

[209] Rex Lundgren, Pontus Laurell, and Gregory A. Fiete. Thermoelectric properties of weyl and dirac semimetals. *Phys. Rev. B*, 90:165115, Oct 2014.

[210] Ki-Seok Kim, Heon-Jung Kim, and M. Sasaki. Boltzmann equation approach to anomalous transport in a weyl metal. *Phys. Rev. B*, 89:195137, May 2014.

[211] Girish Sharma. Tunable topological nernst effect in two-dimensional transition-metal dichalcogenides. *Phys. Rev. B*, 98:075416, Aug 2018.

[212] Subhodip Saha and Sumanta Tewari. Anomalous nernst effect in type-ii weyl semimetals. *The European Physical Journal B*, 91(1):4, Jan 2018.

[213] Chao-Xing Liu, Xiao-Liang Qi, Xi Dai, Zhong Fang, and Shou-Cheng Zhang. Quantum anomalous hall effect in $\mathrm{hg_{1-y}mn_yTe}$ quantum wells. *Phys. Rev. Lett.*, 101:146802, Oct 2008.

[214] K. Yasuda, R. Wakatsuki, T. Morimoto, R. Yoshimi, A. Tsukazaki, K.S. Takahashi, M. Ezawa, M. Kawasaki, N. Nagaosa, and Y. Tokura. Geometric hall effects in topological insulator heterostructures. *Nature Physics*, 12:555–559, Feb 2016.

[215] A. A. Burkov. Chiral anomaly and diffusive magnetotransport in weyl metals. *Phys. Rev. Lett.*, 113:247203, Dec 2014.

[216] J. E. Moore and J. Orenstein. Confinement-induced berry phase and helicity-dependent photocurrents. *Phys. Rev. Lett.*, 105:026805, Jul 2010.

[217] Steve M. Young and Andrew M. Rappe. First principles calculation of the shift current photovoltaic effect in ferroelectrics. *Phys. Rev. Lett.*, 109:116601, Sep 2012.

[218] Takahiro Morimoto and Naoto Nagaosa. Topological nature of nonlinear optical effects in solids. *Sci. Adv.*, 2(5):e1501524, 2016.

[219] Alexander B. Khanikaev, S. Hossein Mousavi, Wang-Kong Tse, Mehdi Kargarian, Allan H. MacDonald, and Gennady Shvets. Photonic topological insulators. *Nature Materials*, 12:233–239, Dec 2012.

[220] Lei Zhang, Ye-Yan Qin, Zhao-Ji Li, Qi-Pu Lin, Jian-Kai Cheng, Jian Zhang, and Yuan-Gen Yao. Topology analysis and nonlinear-optical-active properties of luminescent metal-organic framework materials based on zinc/lead isophthalates. *Inorganic Chemistry*, 47(18):8286 – 8293, 9 2008.

[221] Liang Wu, S. Patankar, T. Morimoto, N. L. Nair, E. Thewalt, A. Little, J. G. Analytis, J. E. Moore, and J. Orenstein. Giant anisotropic nonlinear optical response in transition metal monopnictide weyl semimetals. *Nature Physics*, 13:350–355, Dec 2016.

[222] Shuqing Chen, Chujun Zhao, Ying Li, Huihui Huang, Shunbin Lu, Han Zhang, and Shuangchun Wen. Broadband optical and microwave nonlinear response in topological insulator. *Opt. Mater. Express*, 4(4):587–596, Apr 2014.

[223] Takahiro Morimoto, Shudan Zhong, Joseph Orenstein, and Joel E. Moore. Semiclassical theory of nonlinear magneto-optical responses with applications to topological dirac/weyl semimetals. *Phys. Rev. B*, 94:245121, Dec 2016.

[224] Yang Zhang, Yan Sun, and Binghai Yan. Berry curvature dipole in weyl semimetal materials: An ab initio study. *Phys. Rev. B*, 97:041101, Jan 2018.

[225] Jorge I. Facio, Dmitri Efremov, Klaus Koepernik, Jhih-Shih You, Inti Sodemann, and Jeroen van den Brink. Strongly enhanced berry dipole at topological phase transitions in bitei. *Phys. Rev. Lett.*, 121:246403, Dec 2018.

[226] Di Xiao, Gui-Bin Liu, Wanxiang Feng, Xiaodong Xu, and Wang Yao. Coupled spin and valley physics in monolayers of $\mathrm{mos}_2$ and other group-vi dichalcogenides. *Phys. Rev. Lett.*, 108:196802, May 2012.

[227] Gui-Bin Liu, Wen-Yu Shan, Yugui Yao, Wang Yao, and Di Xiao. Three-band tight-binding model for monolayers of group-vib transition metal dichalcogenides. *Phys. Rev. B*, 88:085433, Aug 2013.

[228] Xiaodong Xu, Wang Yao, Di Xiao, and Tony F. Heinz. Spin and pseudospins in layered transition metal dichalcogenides. *Nature Physics*, 10:343–350, Apr 2014.

[229] Yang Zhang, Jeroen van den Brink, Claudia Felser, and Binghai Yan. Electrically tuneable nonlinear anomalous hall effect in two-dimensional transition-metal dichalcogenides WTe2 and MoTe2. *2D Materials*, 5(4):044001, jul 2018.

[230] Benjamin T. Zhou, Cheng-Ping Zhang, and K. T. Law. Highly tunable nonlinear hall effects induced by spin-orbit couplings in strained polar transition-metal dichalcogenides. *arXiv:1903.11958*, Dec 2019.

[231] Z. Z. Du, C. M. Wang, Hai-Zhou Lu, and X. C. Xie. Band signatures for strong nonlinear hall effect in bilayer $\mathrm{wte}_2$. *Phys. Rev. Lett.*, 121:266601, Dec 2018.

[232] Z. Z. Du, C. M. Wang, Shuai Li, Hai-Zhou Lu, and X. C. Xie. Disorder-induced nonlinear Hall effect with time-reversal symmetry. *Nature Communications*, 10:3047, Jul 2019.

[233] Cong Xiao, Hailong Zhou, and Qian Niu. Scaling parameters in anomalous and nonlinear hall effects depend on temperature. *Phys. Rev. B*, 100:161403, Oct 2019.

[234] Jhih-Shih You, Shiang Fang, Su-Yang Xu, Efthimios Kaxiras, and Tony Low. Berry curvature dipole current in the transition metal dichalcogenides family. *Phys. Rev. B*, 98:121109, Sep 2018.

[235] S. Nandy and Inti Sodemann. Symmetry and quantum kinetics of the nonlinear hall effect. *Phys. Rev. B*, 100:195117, Nov 2019.

[236] Alexey A. Soluyanov, Dominik Gresch, Zhijun Wang, QuanSheng Wu, Matthias Troyer, Xi Dai, and B. Andrei Bernevig. Type-ii weyl semimetals. *Nature*, 527:495–498, Nov 2015.

[237] Li-kun Shi and Justin C. W. Song. Symmetry, spin-texture, and tunable quantum geometry in a $\mathrm{wte}_2$ monolayer. *Phys. Rev. B*, 99:035403, Jan 2019.

[238] Xiaofeng Qian, Junwei Liu, Liang Fu, and Ju Li. Quantum spin hall effect in two-dimensional transition metal dichalcogenides. *Science*, 346(6215):1344–1347, 2014.

[239] Zaiyao Fei, Tauno Palomaki, Sanfeng Wu, Wenjin Zhao, Xinghan Cai, Bosong Sun, Paul Nguyen, Joseph Finney, Xiaodong Xu, and David H. Cobden. Edge conduction in monolayer wte2. *Nature Physics*, 13:677–682, Apr 2017.

[240] Sanfeng Wu, Valla Fatemi, Quinn D. Gibson, Kenji Watanabe, Takashi Taniguchi, Robert J. Cava, and Pablo Jarillo-Herrero. Observation of the quantum spin hall effect up to 100 kelvin in a monolayer crystal. *Science*, 359(6371):76–79, 2018.

[241] Paul Seifert, Florian Sigger, Jonas Kiemle, Kenji Watanabe, Takashi Taniguchi, Christoph Kastl, Ursula Wurstbauer, and Alexander Holleitner. In-plane anisotropy of the photon-helicity induced linear hall effect in few-layer $\mathrm{wte}_2$. *Phys. Rev. B*, 99:161403, Apr 2019.

[242] Su-Yang Xu, Qiong Ma, Huitao Shen, Valla Fatemi, Sanfeng Wu, Tay-Rong Chang, Guoqing Chang, Andrés M. Mier Valdivia, Ching-Kit Chan, Quinn D. Gibson, Jiadong Zhou, Zheng Liu, Kenji Watanabe, Takashi Taniguchi, Hsin Lin, Robert J. Cava, Liang Fu, Nuh Gedik, and Pablo Jarillo-Herrero. Electrically switchable berry curvature dipole in the monolayer topological insulator wte2. *Nature Physics*, 14:900–906, Sep 2018.

[243] Xiangang Wan, Ari M. Turner, Ashvin Vishwanath, and Sergey Y. Savrasov. Topological semimetal and fermi-arc surface states in the electronic structure of pyrochlore iridates. *Phys. Rev. B*, 83:205101, May 2011.

[244] Yang Gao and Di Xiao. Orbital magnetic quadrupole moment and nonlinear anomalous thermoelectric transport. *Phys. Rev. B*, 98:060402, Aug 2018.

[245] Xiao-Qin Yu, Zhen-Gang Zhu, Jhih-Shih You, Tony Low, and Gang Su. Topological nonlinear anomalous nernst effect in strained transition metal dichalcogenides. *Phys. Rev. B*, 99:201410, May 2019.

[246] Ryota Nakai and Naoto Nagaosa. Nonreciprocal thermal and thermoelectric transport of electrons in noncentrosymmetric crystals. *Phys. Rev. B*, 99:115201, Mar 2019.

[247] Ganesh Sundaram and Qian Niu. Wave-packet dynamics in slowly perturbed crystals: Gradient corrections and berry-phase effects. *Phys. Rev. B*, 59:14915–14925, Jun 1999.

[248] C. Duval, Z. Horvath, P. A. Horvathy, L. Martina, and P. C. Stichel. Berry phase correction to electron density in solids and "exotic" dynamics. *Modern Physics Letters B*, 20(07):373–378, 2006.

[249] Dam Thanh Son and Naoki Yamamoto. Berry curvature, triangle anomalies, and the chiral magnetic effect in fermi liquids. *Phys. Rev. Lett.*, 109:181602, Nov 2012.

[250] Girish Sharma, Christopher Moore, Subhodip Saha, and Sumanta Tewari. Nernst effect in dirac and inversion-asymmetric weyl semimetals. *Phys. Rev. B*, 96:195119, Nov 2017.

[251] Timothy M. McCormick, Itamar Kimchi, and Nandini Trivedi. Minimal models for topological weyl semimetals. *Phys. Rev. B*, 95:075133, Feb 2017.

[252] Vatsal Dwivedi and Srinidhi T. Ramamurthy. Connecting the dots: Time-reversal symmetric weyl semimetals with tunable fermi arcs. *Phys. Rev. B*, 94:245143, Dec 2016.

[253] Lukas Muechler, A. Alexandradinata, Titus Neupert, and Roberto Car. Topological nonsymmorphic metals from band inversion. *Phys. Rev. X*, 6:041069, Dec 2016.

[254] E. J. König, M. Dzero, A. Levchenko, and D. A. Pesin. Gyrotropic hall effect in berry-curved materials. *Phys. Rev. B*, 99:155404, Apr 2019.

[255] Cong Xiao, Z. Z. Du, and Qian Niu. Theory of nonlinear hall effects: Modified semiclassics from quantum kinetics. *Phys. Rev. B*, 100:165422, Oct 2019.

[256] Jinwu Ye, Yong Baek Kim, A. J. Millis, B. I. Shraiman, P. Majumdar, and Z. Tešanović. Berry phase theory of the anomalous hall effect: Application to colossal magnetoresistance manganites. *Phys. Rev. Lett.*, 83:3737–3740, Nov 1999.

[257] Dimitrie Culcer, Allan MacDonald, and Qian Niu. Anomalous hall effect in paramagnetic two-dimensional systems. *Phys. Rev. B*, 68:045327, Jul 2003.

[258] Chuanchang Zeng, Snehasish Nandy, A. Taraphder, and Sumanta Tewari. Nonlinear nernst effect in bilayer $\mathrm{wte}_2$. *Phys. Rev. B*, 100:245102, Dec 2019.

[259] Tao Qin, Qian Niu, and Junren Shi. Energy Magnetization and the Thermal Hall Effect. *Phys. Rev. Lett.*, 107(23):236601, Dec 2011.

[260] Yago Ferreiros, A. A. Zyuzin, and Jens H. Bardarson. Anomalous Nernst and thermal Hall effects in tilted Weyl semimetals. *Phys. Rev. B*, 96(11):115202, Sep 2017.

[261] Takehito Yokoyama and Shuichi Murakami. Transverse magnetic heat transport on the surface of a topological insulator. *Phys. Rev. B*, 83:161407, Apr 2011.

[262] Timothy M. McCormick, Robert C. McKay, and Nandini Trivedi. Semiclassical theory of anomalous transport in type-ii topological weyl semimetals. *Phys. Rev. B*, 96:235116, Dec 2017.

[263] A. Pariari, N. Khan, and P. Mandal. Magnetic field induced drastic violation of Wiedemann-Franz law in Dirac semimetal $Cd_3As_2$. *arXiv e-prints*, page arXiv:1508.02286, Aug 2015.

[264] Doron L. Bergman and Vadim Oganesyan. Theory of dissipationless nernst effects. *Phys. Rev. Lett.*, 104:066601, Feb 2010.

[265] R. Franz and G. Wiedemann. Ueber die wärme-leitungsfähigkeit der metalle. *Annalen der Physik*, 165(8):497–531, 1853.

[266] Rosa López and David Sánchez. Nonlinear heat transport in mesoscopic conductors: Rectification, Peltier effect, and Wiedemann-Franz law. *Phys. Rev. B*, 88(4):045129, Jul 2013.

[267] Ki-Seok Kim. Role of axion electrodynamics in a weyl metal: Violation of wiedemann-franz law. *Phys. Rev. B*, 90:121108, Sep 2014.

[268] Rosa López, Sun-Yong Hwang, and David Sánchez. Thermoelectric effects in quantum Hall systems beyond linear response. In *Journal of Physics Conference Series*, volume 568 of *Journal of Physics Conference Series*, page 052016, Dec 2014.

[269] Liangcai Xu, Xiaokang Li, Xiufang Lu, Clément Collignon, Huixia Fu, Jahyun Koo, Benoît Fauqué, Binghai Yan, Zengwei Zhu, and Kamran Behnia. Finite-temperature violation of the anomalous transverse Wiedemann-Franz law. *arXiv e-prints*, page arXiv:1812.04339, Dec 2018.

[270] Alexandre Jaoui, Benoît Fauqué, Carl Willem Rischau, Alaska Subedi, Chenguang Fu, Johannes Gooth, Nitesh Kumar, Vicky Süß, Dmitrii L. Maslov, Claudia Felser, and Kamran Behnia. Departure from the Wiedemann-Franz law in $WP_2$ driven by mismatch in T-square resistivity prefactors. *npj Quantum Materials*, 3:64, Dec 2018.

[271] Yuval Vinkler-Aviv. Bulk thermal transport coefficients in a quantum hall system and the fundamental difference between thermal and charge response. *Phys. Rev. B*, 100:041106, Jul 2019.

[272] S. Nandy, A. Taraphder, and Sumanta Tewari. Planar thermal hall effect in weyl semimetals. *Phys. Rev. B*, 100:115139, Sep 2019.

[273] Sajedeh Manzeli, Dmitry Ovchinnikov, Diego Pasquier, Oleg V. Yazyev, and Andras Kis. 2D transition metal dichalcogenides. *Nature Reviews Materials*, 2(8):17033, Aug 2017.

[274] Kin Fai Mak and Jie Shan. Photonics and optoelectronics of 2D semiconductor transition metal dichalcogenides. *Nature Photonics*, 10(4):216–226, Apr 2016.

[275] Ashwin Ramasubramaniam, Doron Naveh, and Elias Towe. Tunable band gaps in bilayer transition-metal dichalcogenides. *Phys. Rev. B*, 84:205325, Nov 2011.

[276] Sefaattin Tongay, Jian Zhou, Can Ataca, Kelvin Lo, Tyler S. Matthews, Jingbo Li, Jeffrey C. Grossman, and Junqiao Wu. Thermally driven crossover from indirect toward direct bandgap in 2d semiconductors: Mose2 versus mos2. *Nano Letters*, 12(11):5576–5580, 2012. PMID: 23098085.

[277] Christopher R. Ryder, Joshua D. Wood, Spencer A. Wells, and Mark C. Hersam. Chemically Tailoring Semiconducting Two-Dimensional Transition Metal Dichalcogenides and Black Phosphorus. *arXiv e-prints*, page arXiv:1603.08544, Mar 2016.

[278] Habib Rostami, Rafael Roldán, Emmanuele Cappelluti, Reza Asgari, and Francisco Guinea. Theory of strain in single-layer transition metal dichalcogenides. *Phys. Rev. B*, 92:195402, Nov 2015.

[279] Riccardo Frisenda, Matthias Drüppel, Robert Schmidt, Steffen Michaelis de Vasconcellos, David Perez de Lara, Rudolf Bratschitsch, Michael Rohlfing, and Andres Castellanos-Gomez. Biaxial strain tuning of the optical properties of single-layer transition metal dichalcogenides. *arXiv e-prints*, page arXiv:1703.02831, Mar 2017.

[280] Joolee Son, Kyung-Han Kim, Y. H. Ahn, Hyun-Woo Lee, and Jieun Lee. Strain engineering of the berry curvature dipole and valley magnetization in monolayer $\mathrm{mos}_2$. *Phys. Rev. Lett.*, 123:036806, Jul 2019.

[281] Shahnaz Aas and Ceyhun Bulutay. Strain dependence of photoluminescence and circular dichroism in transition metal dichalcogenides: a k · p analysis. *Optics Express*, 26(22):28672, Oct 2018.